UCLA
UCLA Electronic Theses and Dissertations

Title
Algorithms for Rapid Characterization and Optimization of Aperture and Reflector Antennas

Permalink
https://escholarship.org/uc/item/4mx9393h

Author
Densmore, Arthur Charles

Publication Date
2014

Peer reviewed|Thesis/dissertation

eScholarship.org Powered by the California Digital Library
University of California

UNIVERSITY OF CALIFORNIA

Los Angeles

Algorithms for Rapid Characterization and Optimization of Aperture and Reflector Antennas

A dissertation submitted in partial satisfaction of the

requirements for the degree of Doctor of Philosophy

in Electrical Engineering

by

Arthur Charles Densmore

2014

ABSTRACT OF THE DISSERTATION

Algorithms for Rapid Characterization and Optimization of Aperture and Reflector Antennas

by

Arthur Charles Densmore

Doctor of Philosophy in Electrical Engineering

University of California, Los Angeles, 2014

Professor Yahya Rahmat-Samii, Chair

Aperture and reflector antennas play a key role in the communication industry, and methods of enhancing the speed of their analysis and measurement can benefit industry as well as promote better understanding of software modeling through faster visualization. This dissertation addresses such methods. Use of the three-parameter aperture distribution, unified for both sum and difference patterns, provides fast calculation of the aperture radiation characteristics through the use of closed form equations. All reflector antenna systems require a feed to illuminate the reflector, and the feed aperture field integration and spherical wave expansion methods serve as means to trade accuracy for compute speed. The mode matching method of cylindrical corrugated feedhorn analysis is shown to be accelerated by nearly two orders of magnitude with the use of optimized computer math libraries. The Gaussian beam method is shown to improve computational speed by up to two orders of magnitude compared to brute force physical optics integration, and the Levin method up to three orders of magnitude acceleration. The use of graphics processors accelerates the physical optics compute speed by two orders of magnitude or more. The use of the sun as a source of radio flux provides a quick means of measuring receive G/T, for which the results of a Ka-band solar flux study are reported.

The dissertation of Arthur Charles Densmore is approved.

Chris Anderson

Yuanxun Wang

Yahya Rahmat-Samii, Committee Chair

University of California, Los Angeles

2014

To my father and mother

TABLE OF CONTENTS

LIST OF FIGURES

LIST OF TABLES

LIST OF SYMBOLS

θ ..... Theta, angle from boresight of an antenna or feed (similar to spherical latitude)

ϕ ..... Phi, 2D cylindrical or 3D spherical angle (longitude), complementary to rho or theta

ρ ..... Rho, radial distance in 2D cylindrical coordinates

r ..... Distance in spherical coordinates, from antenna to field observation point

$\bar{r}$ ..... 3D vector from origin near antenna to field observation point

$\hat{r}$ ..... 3D unit vector from antenna to field observation point

r' ..... Distance from origin near reflector to a point on reflector surface

$\bar{r}'$ ..... 3D vector from origin near reflector to a point on reflector surface

η ..... Eta, free space impedance

λ ..... Wavelength (wave velocity / frequency)

$\bar{\mathrm{A}}$ ..... Magnetic vector potential (Vs/m)

ds' ..... Element of surface area (of reflector surface in PO integrals)

$D_{i,j}$ ..... Differential matrix (Chebyshev)

$\bar{E}$ ..... Electric field vector (V/m)

exp[z] ..... Natural exponential functions

ε ..... Permittivity

$\bar{\mathrm{F}}$ ..... Electric vector potential (As/m)

pFq($g_1 \ldots g_p; h_1 \ldots h_q; z$) ..... Hypergeometric series

γ ..... Radial mode coefficient for cylindrical wave propagation equations

$\bar{H}$ ..... Magnetic field vector (A/m)

$H_\nu(z)$ ..... Struve function of order υ

i or j ..... Imaginary component, positive square root of negative one

$I_\nu(z)$ ..... Modified Bessel function of first kind and order υ

$\bar{\bar{I}}$ ..... Unit dyad $\left(\hat{r}\hat{r}\cdot + \hat{\theta}\hat{\theta}\cdot + \hat{\phi}\hat{\phi}\cdot\right)$

$J_\nu(z)$ ..... Bessel functions of first kind and order υ

$\bar{J}$ ..... Electric current vector (A/m)

$\bar{J}^{\mathrm{PO}}(\bar{r}')$ ..... Physical optics current on reflector surface

k ..... Wave number ($2\pi / \lambda$)

$\bar{\mathrm{M}}$ ..... Magnetic current

$P_\nu^m(x)$ ..... Associated Legendre polynomials

μ ..... Permeability

ω .....Natural frequency, radians per second

Λ ..... Propagation mode parameter

ACRONYMS AND ABBREVIATIONS

AFIM.....Aperture field integration method

AUT ..... Antenna under test

AVX.....Advanced Vector Extensions

BLAS ..... Basic linear algebra subprograms (math library, netlib.org)

CAD ..... Computer analysis and design

clMAGMA..... OpenCL port of the MAGMA math library for heterogeneous systems

dBi.....Decibels isotropic gain

dBp..... Decibels wrt peak level (of antenna pattern)

DSP .....Digital signal processing unit

FFT..... Fast Fourier Transform

FNBW .....First null beamwidth (antenna pattern characteristic)

FOQRP..... First-order quadratic radial phase

FSS..... Frequency selective surface

GB ..... Gaussian beam

G/T ..... Gain over system-noise-temperature ratio (Receive performance metric)

GPU..... Graphics processor unit (integrated with or plugs into computer motherboard)

GPGPU ..... General Purpose computing on Graphics Processor Units

HPBW ..... Half power beamwidth (antenna pattern characteristic)

LAPACK..... Linear algebra package (math library, www.netlib.org)

LNA ..... Low-noise amplifier

MAGMA..... Matrix Algebra on GPU and Multi-core Architectures (http://icl.cs.utk.edu/magma/)

MoM ..... Method of moments

OpenCL..... Open Computing Language (for CPU, GPU and/or DSP)

PMQRP ..... Perimeter-matched quadratic radial phase

PO ..... Physical optics

PSO ..... Particle swarm optimization

PSLL ..... Peak sidelobe level (antenna pattern characteristic)

SIMD..... Single instruction multiple data

SFU ..... Solar flux unit (10e−22 $W \cdot m^{-2} / Hz$)

SSE..... Streaming SIMD Extensions

SWEX ..... Spherical wave expansion

wrt ..... with respect to

ACKNOWLEDGEMENTS

I would like to thank my academic advisor, Professor Yahya Rahmat-Samii, for this opportunity to pursue a PhD, for his guidance of the research, and for sharing his insightful intuition with me. I would like to thank Professors Chris Anderson, Tatsuo Itoh, and Yuanxun Wang, for serving on the committee and the ideas they inspired. I'd also like to acknowledge helpful discussions on many topics related to this research with fellow UCLA ARAM PhD students Shenheng Xu, Harish Rajagopalan, Tim Brockett, Ilkyu Kim, and Joshua Kovitz, as well as Gerry Seck of L3 Communications, Inc. Thanks for all your encouragement.

This work was funded in part by financial tuition support from L3 Communications' Datron Advanced Technology Division.

VITA

2013-2014	Teaching Assistant: 2013 UCLA Henry Samueli Excellence in Teaching Award
1987-2012	Electrical Engineering positions at several companies: Jet Propulsion Laboratory (Pasadena, CA), KVH Industries (Middletown, RI), Malibu Research Associates (Calabasas, CA), L-3 Communications (Simi Valley, CA), and United Research (Thousand Oaks, CA)
1995	U.S. Patent 5,398,035 "Satellite-tracking millimeter-wave reflector antenna system for mobile satellite-tracking," A. Densmore, V. Jamnejad and K. Woo.
1987	Masters degree in Electrical Engineering, California Institute of Technology (Pasadena, CA)
1986	Bachelors degree in Electrical Engineering, Summa Cum Laude, California State Polytechnic University (Pomona, CA)

PUBLICATIONS AND PRESENTATIONS

- A. Densmore and Y. Rahmat-Samii, "OpenCL GPU 100x Acceleration of Physical Optics," Antennas and Propagation Society International Symposium (APSURSI), IEEE, Memphis, Tennessee, July 6-12, 2014.
- A. Densmore and Y. Rahmat-Samii, "Three-Parameter Elliptical Aperture Distributions for Difference Patterns by Particle Swarm Optimization," Antennas and Propagation Society International Symposium (APSURSI), IEEE, Memphis, Tennessee, July 6-12, 2014.
- A. Densmore and Y. Rahmat-Samii "Three-Parameter Elliptical Aperture distributions for Sum and Difference Antenna Patterns Using Particle Swarm Optimization," *Progress in Electromagnetic Research*, Vol. 143, 709-713, 2013.
- A. Densmore, G. Seck and Y. Rahmat-Samii, "Ka-band Solar Flux Study for G/T Measurement," URSI National Radio Science Meeting, U. Colorado at Boulder, January 4-7, 2012.
- A. Densmore, Y. Rahmat-Samii and G. Seck, "Corrugated-Conical Horn Analysis Using Aperture Field with Quadratic Phase," *IEEE Trans. Antennas Prop.*, Vol. 59, No. 9, pp 3453-3457, Sept. 2011• A. Densmore and Y. Rahmat-Samii, "Analysis of Corrugated Horns Using a Novel Augmentation of the Aperture Mode with Quadratic Phase," URSI National Radio Science Meeting, U. Colorado at Boulder, January 5-8, 2011.
- A. Densmore and Y. Rahmat-Samii, "Particle Swarm Optimized Three-Parameter Aperture Distribution for Antenna Synthesis," Antennas and Propagation Society International Symposium (APSURSI), IEEE, Toronto, Ontario, Canada, July 11-17, 2010.
- A. Densmore and Y. Rahmat-Samii, "Particle Swarm Optimization of Optimal Three-Parameter Aperture Distribution for Antenna Applications," URSI National Radio Science Meeting, U. Colorado at Boulder, January 6-9, 2010.

- A. Densmore and Y. Rahmat-Samii, “Estimating Circularly Polarized Squint in an Offset Reflector: A Simplified Approach with an Intuitive Understanding,” URSI National Radio Science Meeting, U. Colorado at Boulder, January 6-9, 2010.
- Y. Rahmat-Samii and A. Densmore, "A History of Reflector Antenna Development: Past, Present and Future," SBMO/IEEE MTT-S Internat. Microwave and Optoelectronics Conf. (IMOC), Brazil - Pará - Belém, November 3-6, 2009.
- A. Densmore and J. Huang., "Mobile Satcom Antenna Developments and Land and Aeronautical Field Trial Results," in *IEE 5th Intl. Conf. on Sat. Sys. for Mobile Comm. and Navigation Proceedings*, London, England, May 13-15, 1996.
- A. Densmore and M. Guler, "An Aeronautical-Mobile 20/30 GHz Satellite-Tracking Antenna for High Data Rate Satcom," in *IEEE AP-S Symposium Proceedings*, Baltimore, Maryland., July 21-26 1996.
- M. Agan and A. Densmore., "Aeronautical Satellite Communications at T1 Data Rates," in *AIAA 16th International Comm. Satellite Systems Conf. Proceedings*, Wash. D.C., February 25-29, 1996.
- M Agan and A. Densmore, "ACTS Broadband Aeronautical Terminal," in *Proc. Int. Mobile Sat. Conf.*, Ottawa, Canada, JPL June 6-8, 1995, Pub. No. 95-12.
- A. Densmore, "K/Ka-band Antenna for Broadband Aeronautical Mobile Application," in *IEEE AP-S Symposium Proceedings*, pp. 1032-1035, Seattle, Wash., June 19-24, 1994.
- A. Densmore and M. Agan, "NASA's K/Ka-band Broadband Aeronautical Terminal for Duplex Satellite Video Communications," in *IEEE National Telesystems Conference Proceedings*, pp. 165-168, San Diego, Calif., May 26-27, 1994.
- A. Densmore and V. Jamnejad, "A Satellite-Tracking K and Ka Band Mobile Vehicle Antenna System," *IEEE Trans. Veh. Technol.,* Vol. VT-42, No. 4, pp. 502-513, November 1993.
- A. Densmore and V. Jamnejad, "K- and Ka-band Satellite-Tracking Small Reflector Antenna System for Mobile Satellite Service," *IEE European Conference on Satellite Communications Proceedings,* Manchester, England, UK, November 1993.
- V. Jamnejad and A. Densmore, "A Small 20/30 GHz Reflector Antenna System for ACTS Mobile Terminal Experiment," in *Proceedings of the 2nd Internat. Conf. on Universal Personal Comm.*, Ottawa, Ontario, Canada, October 1993.
- A. Densmore, *et al.*, "Land Mobile Satellite Antenna Development at JPL," in *Proceedings of the Univ. of Illinois Symposium on Antenna Applications*, Monticello, Illinois, September 22-24, 1993.
- J. Huang, V. Jamnejad and A. Densmore, "Mobile Antenna Development at JPL," in *Progress in Electromagnetic Research Symposium Proceedings*, Pasadena, Calif., July 12-16, 1993.
- A. Densmore, *et al.*, "K/Ka-Band Antenna System for Mobile Satellite Service," in *IEEE Antenna Propag. Soc. Intern. Symp. Dig.*, Ann Arbor, Mich., June 1993.
- A. Densmore, *et al.*, "K- and Ka-Band Mobile-Vehicular Satellite-Tracking Reflector Antenna System for the NASA ACTS Mobile Terminal," in *Proc. Int. Mobile Sat. Conf.*, JPL Pub. No. 93-9, June 1993.
- A. Tulintseff, A. Densmore, *et al.*, "An Active K/Ka-band Antenna Array for the NASA ACTS Mobile Terminal," in *Proc. Int. Mobile Sat. Conf.*, JPL Pub. No. 93-9, June 1993.
- J. Huang, A. Densmore, A. Tulintseff and V. Jamnejad, "Downsizing Antenna Technologies for Mobile and Satellite Communication," in *IEEE Antennas Propag. Soc. Intern. Symp. Dig.*, Ann Arbor, Mich., June 1993.

- A. Densmore, V. Jamnejad, A. Tulintseff, R. Crist, T.K. Wu and K. Woo, "Two K/Ka-Band Mechanically-Steered, Land-Mobile Antennas for the NASA ACTS Mobile Terminal," in NASA's *ACTS Prog. Conf. Proc.*, Wash. D.C., November 1992.
- A. Densmore, *et al.,* "The ACTS Mobile Terminal Reflector Antenna System," in *SATCOM Quarterly,* Vol. 7, JPL Publication No. 410-33-7, October 1992.
- R. Crist, A. Densmore, *et al.*, "Millimeter-Wave T/R System for ACTS Mobile Terminal," in *Proc. of Military Microwave Conf.*, London, England, October 14-15, 1992.
- A. Densmore, *et al.,* "Mobile Satellite Vehicular Antenna Development at JPL," in *Proceedings of the NASA Space Communications Symposium*, Cleveland, Ohio, October 1992.
- A. Densmore and J. Huang, "A Low Cost, Conformal Vehicular Antenna System for Mobile Satellite Service," in *SATCOM Quarterly*, Vol. 4, JPL Publication No. 410-33-4, January 1992.
- A. Densmore, *et al.,* "Commercial Applications of NASA's ACTS Mobile Terminal mm-Wave Antennas," in NASA's *Technology 2001* Conf. Proceedings, JPL Pub. No. D-9147, December 1991.
- J. Huang and A. Densmore, "Microstrip Yagi Array Antenna for Mobile Satellite Vehicle Application," *IEEE Trans. Antennas Prop.*, Vol. AP-39, No. 7, pp. 1024-1030, July 1991.
- Krisher, T.P., J.D. Anderson, D.D. Morabito, S.W. Asmar, S.E. Borutzki, M.L. Delitsky, A.C. Densmore, P.M. Eshe, G.D. Lewis, M.J. Mauer, D.C. Roth, Y.H. Son, T.R. Spilker, D.N. Sweetnam, A.H. Taylor, G.L. Tyler, D.L. Gresh and P.A. Rosen, "Radio Range Measurements of Coronal Electron Densities at 13 and 3.6 Centimeter Wavelengths During the 1988 Solar Conjunction of Voyager 2," *ASTROPHYSICAL JOURNAL*, Vol. 375, pp. L57-L60, July 10, 1991.
- A. Densmore and J. Huang, "Microstrip Yagi Antenna for Mobile Satellite Service," in *IEEE Antenna Propagat. Soc. Symposium Dig.*, Vol. 2, June 1991, pp. 616-620.
- A. Densmore, "Performance Evaluation of the Antennas Used for the JPL Land Mobile Satellite Field Experiment in Australia," Technical Feature Article in *MSAT-X Quarterly*, No. 24, JPL Publication No. 420-13-24, July 1990, pp. 2-10.
- K. Woo, A. Densmore, *et al.*, "Performance of a Family of Omni and Steered Antennas for Mobile Satellite Applications," in *Proc. Int. Mobile Sat. Conf.*, JPL Pub. No. 90-7, June 1990, pp. 540-546.
- J. Huang, A. Densmore, D. Pozar, "Microstrip Yagi Array for MSAT Vehicle Antenna Application," in *Proceedings of the 2nd International Mobile Satellite Conference* (IMSC 1990), June 1990, pp 554-559.
- A. Densmore, "A Software Phase-Locked Loop Code for Phase Allan Variance and Amplitude Stability Analysis of Precision Calibration Tones," JPL *TDA Progress Report 42-93*, Vol. Jan.-Mar 1988, NASA JPL Publication, pp. 207-213

CHAPTER 1 INTRODUCTION

This dissertation contributes to the field of rapid algorithms for the characterization and optimization of aperture and reflector antennas. The characterization of aperture and reflector antennas must be accomplished rapid enough to satisfy the needs of communication system designers and planners. Those needs include the antenna designer's ability to process a range of configurations to find a balance of possibly competing performance requirements before incorporating such a design into a proposal or passing the antenna design on to manufacturing or into a system design cycle. The faster a candidate antenna design characterization is completed the more rapidly an optimization process utilizing it can converge to a satisfactory solution and the larger the number of specialized features that can be considered in the optimization. Specialized algorithms can help to accelerate this overall process by exploiting unique features of, and relationships between, antenna characterization methods. Those features have evolved along with the development of the reflector antenna.

1.1 APERTURE ANTENNAS

An aperture antenna is a planar model of antenna field distributions over a given aperture area. The aperture field distributions determine the radiation pattern and characteristics for the given aperture antenna by utilizing the Schelkunoff field equivalence principle [1]–[4], which in general represents the fields from sources within a closed surface — such as a metallic feed with

a radiating aperture — by electromagnetic currents that equivalently represent the aperture fields and are tangent to the closed surface. Reflectors, and even phased arrays, are example topologies than an aperture antenna design may represent. With a realistic model of aperture fields associated with a given topology, a particular aperture distribution may be designed to suit the needs of a given system design, leaving the implementation of the resulting aperture field distribution to be designed subsequently, using a topology to be chosen during that subsequent design. Staging the overall antenna design in this manner allows the system-level design to proceed quicker by postponing some of the physical implementation details.

1.2 HISTORY OF REFLECTOR ANTENNAS

Reflector antennas are commonly constructed as a surface of revolution defined by a curve consisting of a conic section, including the parabola, ellipse and hyperbola. A very common example of a reflector antenna is found in a flashlight. The reflector antenna has seen a wide range of applications throughout history mainly because as newer antenna typologies have been developed the reflector continues to provide the highest gain, widest bandwidth, best angular resolution, and lowest costs among available topologies.

After the close of the Renaissance the parabolic reflector greatly enhanced science discoveries with its application to astronomy. In 1663 a Scottish mathematician, James Gregory, at the age of 24, published a treatise entitled *Optica Promota*. In this he gave a description of a compound reflecting telescope, the Gregorian, employing two concave specula (metal mirrors) [5]. Sieur Cassegrain, a Frenchman, in 1672 designed a distinct compound reflector, differing from Gregory's in that it employed a convex hyperbolic secondary, placed inside the focus of the

parabolic primary reflector. While the Gregorian can provide higher magnification the Cassegrain is more compact. In the same year, 1672, Newton designed and constructed his telescope with two reflectors, a parabolic primary and a flat secondary, which became popular with amateur astronomers.

In 1888 Hertz used a dipole-fed cylindrical parabolic antenna along with a spark-gap generator and similar detector to verify the existence of electromagnetic waves predicted by Maxwell's theory. Nobel laureate Marconi also started his experiments using a cylindrical parabola, as described in his first patent in 1896.

The strong push for the development of RADAR in WWII led to a unified treatment of reflector antennas, documented in Silver's twelfth volume of the MIT Radiation Laboratory Series [6]. Silver's twelfth volume documents many antenna characterization algorithms and has timelessly continued to serve as a standard reference for antenna methods. Subsequently Ruze studied the effects of the random surface roughness on reflector antenna gain and showed that there is a smallest wavelength at which the gain of any particular antenna reaches a maximum.

Many astronomical objects are not only observable in visible light but also emit significant radiation at radio frequencies. Jansky was the first to detect radio emission from the Milky Way Galaxy. In 1937 the first radio telescope was used for astronomical research. The 64 meter diameter radio astronomy antenna at Parkes in Australia was completed in 1961, and its success lent support to NASA's case to the US Congress for funding of a Deep Space Network of antennas, now including JPL's 70 m in Goldstone, California [7].

The largest fully steerable reflector antenna is currently the 110 m Green Bank Telescope (GBT) at the National Radio Astronomy Observatory in Green Bank, West Virginia (Fig. 1-1). The GBT is an offset (asymmetrical) reflector antenna in order that its feed and support arm do not block the projected main aperture. The largest reflector antenna in the world is the Arecibo 300 m [8] (Fig. 1-2), located in Puerto Rico. It includes specialized feeds that compensate for the reflector's spherical shape and use it to steer the antenna beam.

Fig. 1-1. The Green Banks 110 m radio telescope is the largest fully steerable antenna. (Photo from www.gb.nrao.edu.)

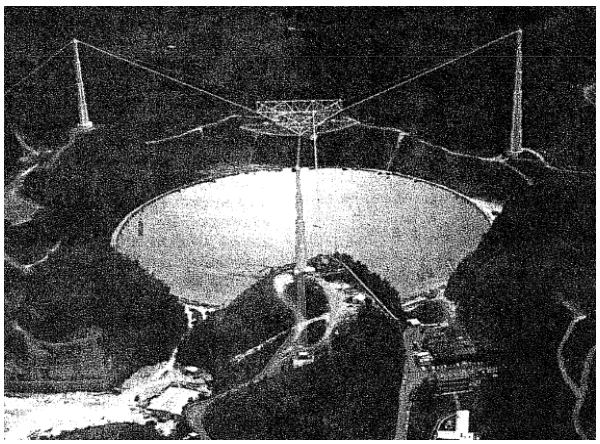

Fig. 1-2. The Arecibo 300 m radio telescope is the largest single-aperture telescope in the world. (Photo from Love [8].)

On May 20, 1996, the crew of the Space Shuttle Endeavor released a Spartan Free-Flyer Spacecraft into orbit carrying a container about half the size of an office desk. It was comprised

of a 14 m inflatable reflector, supported by a 15 m diameter torus and connected to the Spartan via three 30 m long struts.

Inertially stabilized reflector antennas in operation on cars, trains, airplanes and boats support commercial and private use for reception of a range of services via geostationary satellites, including Dish ™ and DirecTV™, which use circularly polarized signals. A two-axis inertial sensor can be mounted on the mobile reflector, with its third axis aligned with the view to the satellite, in order to keep the reflector pointed at the satellite as the mobile vehicle moves underneath the stabilized (tracking) antenna (Fig. 1-3 and Fig. 1-4). Incorporating an additional third axis inertial sensor allows the tracking of linearly polarized signals while the antenna remains pointed at the satellite signal source.

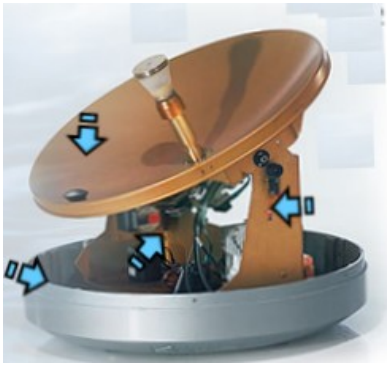

Fig. 1-3. 30 cm diameter Ku-band maritime-mobile satcom tracking reflector antenna system. (Photo from www.kvh.com)

Fig. 1-4. 45 & 30 cm diameter Ka-band aeronautical mobile satcom tracking reflector antenna systems. (Photo from www.L-3com.com Datron division)

An offset reflector antenna configuration displaces the feed outside the projected main aperture, which provides the advantages of low sidelobes and high efficiency — due to the lack of blockage of the projected aperture (as viewed from the direction of the satellite for the roof-mounted reflectors shown in Fig. 1-5). With an offset reflector linear polarized cross-polarization is higher in the plane perpendicular to the direction of feed offset and circular polarization (CP) exhibits a beam squint [9] in that same plane. Computerized algorithms that can characterize sidelobe and cross-polarization levels and beam squint rapidly help meet the needs of antenna and system designers.

Fig. 1-5. Residential offset reflector Satcom antennas. (Photo from www.reformation.org.)

Some of the material in this section is reproduced from a portion of one of the author's previous publications [10].

1.3 LITERATURE REVIEW

The literature provides a history of techniques and algorithms provided to increase the speed at which an antenna's radiation pattern may be computed. A common choice for diffraction analysis (characterizing the radiation pattern) of a reflector antenna is the physical optics (PO), and PO is the method utilized in this dissertation. With PO the reflector surface supports a

current determined by the magnetic field incident on the reflector surface, $\bar{J} = 2\hat{n} \times \bar{H}$, which according to Maxwell's equations represents the discontinuity from the incident field outside the reflector to the absence of field inside the reflector material (assumed perfectly electrically conducting: PEC). The PO method assumes an abrupt transition from the said surface current covering the portion of the reflector that is illuminated, by the fields from the feed, to an absence of surface current in any portion of the reflector surface that is not directly illuminated by the feed (by line-of-sight). Other methods of diffraction analysis include geometric optics (GO), the geometrical theory of diffraction (GTD), and the physical theory of diffraction (PTD). GO effectively involves ray bouncing and localized quadratic surface approximation; although it fails in caustic direction, e.g., the main beam. GTD is a method of accounting for diffraction from the reflector edges, which supplements GO. PTD provides a means of accounting for edge currents and so complements PO. In the far field the PO integral has the form of (1.1) [11], where Fig. 1-6 depicts each of the spatial vectors.

$$I_{\text{far field}} = \frac{-jk\eta}{4\pi r} \exp[-jkr] \left\{ \hat{\theta}\hat{\theta} \cdot + \hat{\phi}\hat{\phi} \cdot \right\} \iint \bar{J}(\bar{r}\,') \exp[jk\bar{r}\,' \cdot \hat{r}] ds' \tag{1.1}$$

The speed of a diffraction analysis algorithm is compared in this dissertation to that of brute force, where brute force PO involves dividing the reflector surface area into small patches, each one-tenth of a wavelength on a side (electrically small), and summing the contribution from each partition to the overall far field antenna pattern integral. The brute force method is accurate but requires a considerable amount of compute time for a practical antenna. A few decades ago this brute force compute time for a practical antenna took several hours. The subsequent computer hardware speed improvements have significantly reduced that compute time, according to

Moore's law, which has since flattened out. New hardware architectures, such as multi-core processors and the use of graphics processors for general purpose computing, have attempted to recover the growth of Moore's law, but new architectures require new compute algorithms. The flattening out of Moore's law and the introduction of new computer architectures have spurred the development of new algorithms to continue to improve the speed of diffraction analysis of reflector antennas.

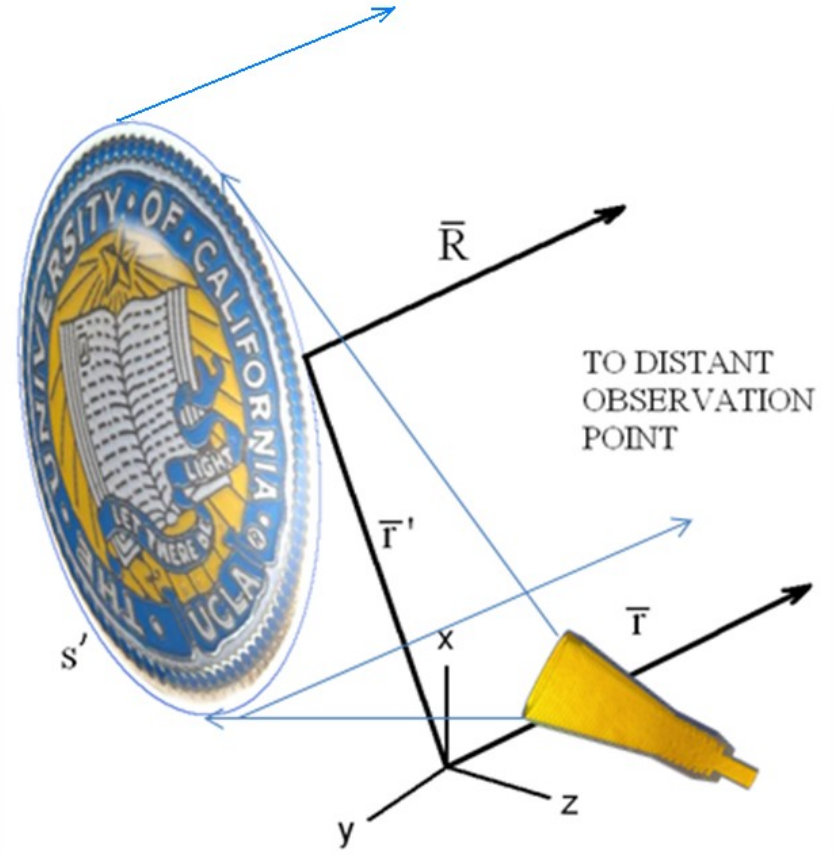

Fig. 1-6. Geometry for PO calculation of reflector far field radiation pattern.

1.3.1 Adaptive Sampling

Burkholder and Lee [12] show that the brute force numerical evaluation of the physical optics integral may be accelerated by an order of magnitude or more in the main beam with an adaptive quadrature method by varying the sampling density according to the variation of the integrand. The variation of the integrand is determined by the gradient of the phase, which in some regions may require far fewer points-per-wavelength than the standard Nyquist sampling rate. This technique involves nonuniform sampling of the aperture, which has been addressed by Rahmat-Samii and Cheung [13].

Table 1-1. Acceleration of brute force by adaptive sampling wrt one-tenth wavelength sampling.

SAMPLING INTERVAL (λ)	MAXIMUM PATTERN ANGLE (DEG)	ACCELERATION FACTOR
0.1	90	1
0.25	80	6
0.65	45	41
0.98	30	90
2.9	10	630

1.3.2 FFT

Craig and Simms [14] demonstrate the use of the Fast Fourier Transform (FFT) to calculate aperture radiation patterns in the main beam region and recognize that by neglecting the depth and curvature of the reflector surface, the aperture field method approximates the physical optics integral as a two-dimensional Fourier integral that can be efficiently evaluated by a very rapid 2D FFT. When the depth (curvature) of the reflector surface is accounted for the PO surface integral does not represent a Fourier integral and so the FFT cannot be so directly and efficiently used, but with a series approximation of the integrand it can be computed by a series of FFTs. Thereby accuracy is traded for speed. Craig and Simms also point out that the aperture field

integral fails to account for the asymmetry in the main beam of an offset reflector in the offset plane — one of the compromises of using the rapid FFT technique. The inability of the aperture field method to account for this asymmetry in the physical optics integral for an offset reflector is discussed by Rahmat-Samii [15]. Lam, Lee, Hung, and Acosta [16] compare the calculation of a reflector antenna pattern by the "brute force" FFT method to geometric optics (GO), geometrical theory of diffraction (GTD) and Fourier-Bessel techniques. Lam, *et al.*, also report that the reflector curvature prohibits direct use of the FFT for accurate calculation of the PO integral, but that a total of 4MN one-dimensional FFTs serve to compute the physical optics integral, where M and N represent the respective orders of sine series approximations of the integrand in the two dimensions of the aperture plane. They report that the FFT compute time is comparable to the other methods. Nezhad, Firouzeh and Mirmohammad-Sadeghi present a method for use of FFT with shaped reflector antennas [17] using the approximate aperture field method. This neglects the curvature of the reflector surface, thereby providing an approximation of the physical optics integral valid for the main beam region that is computed very rapidly. Boag [18]–[20] presents a method for fast evaluation of a radiation pattern using a multi-level algorithm similar to the fast Fourier transform.

One of the issues with the use of the FFT is that the number of usable far field observation angles covering the hemisphere is at most equal to the number of aperture sample points. The discretization of the aperture, relative to the wavelength, determines the discretization of the far field observation angle. At spatial aperture sampling of half wavelength the number of far field points equals the number of aperture sample points; although, when the spatial sampling is one-tenth wavelength, to correspond with the brute force method, the number of usable far field

angular points produced by the FFT is reduced by a factor of five: The angular points outside this range do not represent physical angle. Thus the angular sampling of the main beam far field may not be sufficient for some studies. With a one-dimensional FFT, with an even number M spatial samples taken regularly along the span, the angular pattern samples calculated by the FFT correspond to the angles $u(m) = \sin\left[\theta(m)\right] = \left[\frac{-M}{2}, \frac{-(M-1)}{2}, \ldots, 0, \ldots, \frac{M-2}{2}\right]\lambda/(Md)$, where d is the spacing between spatial samples, which with the brute force physical optics integral is one-tenth wavelength. The acceleration that the FFT method can provide over brute force though is limited by the fact that its computation requires that the vector value of the integral be numerically calculated at each of many points throughout the aperture. On the other hand, an advantage of the 2D FFT is that it provides a rapid means of estimating the full hemispherical coverage of an antenna pattern, calculating the radiated fields in many directions all at once. The Jacobi-Bessel expansion method [21], [22] also provides a similar benefit. Such rapid calculations can be quite suitable for computer graphics to overlay a 3D rendering of the radiation pattern onto a 3D model of the antenna.

1.3.3 Quadrature Methods

Duan presents in Appendix D of [23] an efficient Gaussian quadrature for super quadratic apertures that avoids oversampling in the central region. Duan's method is similar to that offered by Jamnejad [24] for circular apertures, which claims an acceleration of compute time by a factor of four to seven compare to schemes to do not avoid the central crowding.

Ludwig's method [25], [26] of reducing the number of points required to numerically evaluate a double integral provides an effective compute speed acceleration of four to eight. It involves

discretization of the integration surface into rectangular patches and determining the coefficients to best fit a plane, in the mean-square sense, to the values of the integrand at the corners and thereby is a linear patch technique. Pogorzelski [27] extended Ludwig's method [25] to a triangular patch instead of Ludwig's rectangular patches, and Santos [28] simplified Pogorzelski's triangular extension by using area coordinates and an equation that only has to be calculated once for each triangular subregion. Meng, Nan and Changhong [29] provide a method for overcoming a potential problem of a singularity occurring in Ludwig's original or triangularized method.

Crabtree [30] presents a biquadratic surface patch technique that provides more than a magnitude of acceleration of compute speed over brute force by approximating the physical optics integral with surface patches over which the amplitude and phase are each approximated by quadratic functions, and Parks [31] investigates its application. Pogorzelski [32] provides a method of quadratic phase approximation with Chebyshev expansion of the amplitude function and shows that the quadratic method provides about 20 dB reduction in error with comparable compute time compared to the linear phase method.

Levin [33], [34] presents an efficient method of integrating rapidly oscillating functions by transforming the original problem into the solution of an ordinary differential equation, for single integral, or a partial differential equation for multiple integrals, and Durgun [35] applied it to the evaluation of physical optics integrals. Xiang [36] offers a new efficient Levin method. Li has improved the Levin method so that collocation basis functions are not required, by using Chebyshev-Lobatto (Gauss-Lobatto) nodes and the Chebyshev differential matrix [37], and improving its accuracy by revealing the utility of using the truncated singular value

decomposition method instead of more standard matrix solution methods [37]–[42] to accomplish the Levin collocation. The compute speed is also improved by avoiding some of the computations that are required to produce the Levin method solution.

Ehrenmark [43] provides a three-point numerical quadrature method, comparing it to the Levin method, and claims it can be implemented in minutes by the average user; whereas, more sophisticated methods may require hours of preparation by a specialist before a computer run can be done.

1.3.4 Asymptotic Methods

1.3.4.1 Asymptotics with NURBS

Saez de Adana, Gutierrez, Gonzalez, Catedra and Lozano published their book, "Practical applications of asymptotic techniques in electromagnetics" [44] which deals with physical optics for parametric non-uniform rational B-spline (NURBS) surfaces and summarizes the GO/GTD and PO/PTD techniques. Acceleration techniques addressed include the elimination of hidden surfaces and an angular Z-buffer algorithm based on the light buffer technique used for computer graphics.

1.3.4.2 Method of Stationary Phase

Zhang, Yu, Zhou and Cui [45] study the use of the stationary phase method applied to physical optics problems with nearby stationary points, to provide compute time independent of frequency. Some practical notes regarding the implementation of this technique are presented in the appendix section 8.5.

1.3.4.3 Numerical Theory of Diffraction

Vico-Bondia, Ferrando-Bataller and Valero-Nogueira [46], [47]develop a new fast physical optics technique called the numerical theory of diffraction (NTD) for integrals with a saddle stationary phase point, based on a new approach for the quadratic fast physical optics developed by Catedra [48]. The surface is broken into triangular subregions. The NTD is based on a decomposition of each quadratic triangular patch into different contributions that extends the asymptotic contribution for high frequencies, which allows for neglecting all the triangles where no high frequency phenomena take place and provides for compute time being independent of frequency. The Zhang, Xu and Cui [49] elaborate on the NTD method, showing that higher-order poles have no contribution.

1.3.4.4 Steepest Descent Path

Wu, Jiang, Sha and Chew [50], [51] use the numerical steepest descent path method to analyze the highly oscillatory physical optics integral on smooth conducting parabolic surfaces, including both monostatic and bistatic cases. Chou and Chou [52] present an approach using steepest descent method for the synthesis of shaped reflectors. It discretizes the surface into small patches and uses grid nodes as synthesis variables and provides and advantage of providing closed-form expressions for the derivatives of a cost function.

1.3.5 Line-integral Boundary Diffraction

Albani [53] presents a formulation to reduce 2D aperture radiation integrals to 1D line integrals for physical optics scattering from flat plates. The integrand of the line integral along the rim of the aperture is free from singularities.

1.3.6 Blunt Approximation methods

Arias-Acuna, Garcia-Pino and Rubinos-Lopez [54] present accelerated approximation methods by blunt approximation methods for physical optics integration and method of moment solutions of dual reflectors that trade accuracy for compute speed. They also utilize precomputation of complex exponentials to improve speed by an additional factor of two to three.

1.3.7 Approximating Dual Reflector with Equivalent Single Paraboloid

Rusch, Prata, Rahmat-Samii and Shore [55] show that the radiation pattern of a dual reflector system can be adequately represented by that of an equivalent single reflector for the main beam and first sidelobes. Since the full analysis of a dual reflector system requires substantially more compute time than that for a single reflector this is a viable means of accelerating the computation of dual reflector main beam patterns.

1.4 DISSERTATION OUTLINE

This dissertation contributes to the field of the analysis of aperture and reflector antennas with means and algorithms to speed up the computations. Very compact closed-form equations that can be quickly calculated are provided for the cylindrical mode matching of feedhorns. Closed-

form equations for the rapid calculation of the radiation properties of three-parameter aperture distributions are presented. Asymptotic methods of Gaussian beam and Levin quadrature are discussed in detail. The new OpenCL language is used to harness the compute power of graphics processors, and potentially other, processors in heterogeneous computer architectures to accelerate antenna calculations by more than two orders of magnitude. The new MAGMA math library is ported to the Windows ™ compute platform using the AMD HD5850 GPU.

Chapter two discusses computer hardware and software architecture factors that affect the speed at which antenna analysis codes run. Parallel processing techniques are discussed including OpenMP, MPI, and GPUs. CPU acceleration methods of SSE, AVX and the software method of C++ extension templates and the eager versus lazy numerical evaluation models are discussed.

Chapter three overviews several optimization methods, and discusses particle swarm optimization in particular. Examples are presented, including a multi-objective optimization of a novel multi-band FSS subreflector.

Chapter four discusses the three-parameter aperture distribution, generalized for sum or difference pattern, where the speed advantage is provided by closed-form equations of the radiation characteristics. Examples of particle swarm optimized patterns are provided, and the far field polarization orientation equations for a general radiating aperture are derived.

Chapter five discusses several methods for the analysis of the radiation from a corrugated feedhorn, which is a common type of feed used for reflector systems. The methods include aperture field integration, spherical wave expansion, and cylindrical mode matching, including the use of optimized math libraries that accelerate the matrix arithmetic involved in the mode

matching. The particle swarm optimization method is used in a multi-objective optimization to effectively design a smoothly profiled corrugated horn.

Chapter six discusses several methods for the characterization of a reflector system radiation pattern. These methods include brute force, Gaussian beam, Levin method and the application of the new OpenCL computer language to harness the power of graphical processors.

Chapter seven discusses methods for rapidly estimating system-level characterizations of circularly-polarized squint and gain over temperature ratio. The results of a study of the Ka-band flux emitted by the sun (which doesn't vary much with time) are presented, from which the calibration is obtained to accomplish the gain-over-temperature ratio measurements for the characterization of the receive sensitivity of a receive antenna system.

Chapters eight and nine respectively contain the appendices referenced in the individual chapters and the literature references cited throughout the document. Chapter eight includes a brief user manual for the UCLA ARAM CYL_MM Windows ™ software developed to support this dissertation and which created the cylindrical mode matching results and 3D graphics presented through this dissertation.

CHAPTER 2 COMPUTER AND SOFTWARE ARCHITECTURE

The speed of computation depends largely on the computer architecture, including the central processor hardware and any supplemental processors included in the system architecture; e.g., graphics processors. The list of capabilities incorporated into the state of the art processors and the programming languages to control them continue to increase, and several such capabilities over the past ten years or so have been found to offer a significant capability to accelerate the kind of computations typically involved in reflector antenna analysis and are addressed in this chapter.

2.1 PARALLEL PROCESSING

The incorporation of more than a single processor to complete some computational workload is in general referred to as parallel processing, of which there are several forms. Here we discuss OpenMP, MPI and GPGPU. The potential for parallel processing to accelerate the execution of a given compute code depends on how the routine that that code represents is organized and what fraction of it can be parallelized. Highly parallelizable routines can be accelerated the most by parallel processing; whereas, routines that require mainly a serial implementation are not accelerated much at all by parallel processing. In 1967 Gene Amdahl recognized that the

potential for parallel processing to accelerate a computer code depends on what fraction of the routine is able to be parallelized. Amdahl's law is depicted in Fig. 2-1.

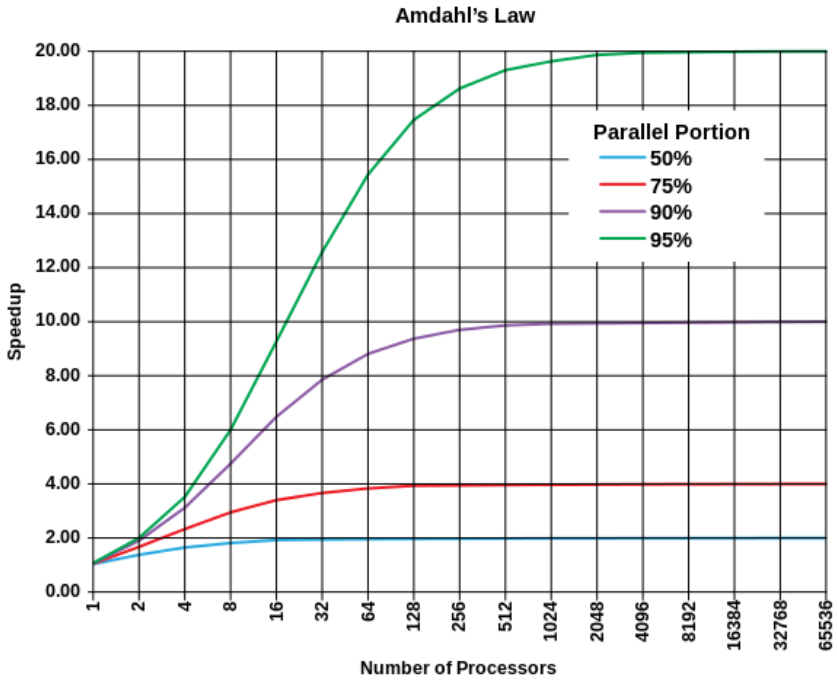

Fig. 2-1. Amdahl's law of the acceleration of computer code by parallel processing (from Wikipedia).

2.2 OPENMP

OpenMP is an application program interface created to support multi-platform shared memory multiprocessor coding. The first version of the OpenMP specification was published in 1997. Basically, it harnesses the power of multiple processors (mutli-core) available in a computer architecture that otherwise would not be utilized, since the default runtime mode of a program is single-threaded, using only a single processing core. OpenMP provides a set of compiler directives — meaning the compiler must support OpenMP, and all recent versions do — that affect the runtime behavior. Thus OpenMP provides programmers with a simple interface for developing code for parallel processing. By combining OpenMP with the MPI (message passing

interface) application program interface, the power of OpenMP can be applied to distributed-memory computer architectures as well.

OpenMP parallel codes utilize multithreading. A section of code that has been parallelized with the use of OpenMP directives — e.g., a *for* loop — first has a master thread assigned, which then forks a specified number of slave threads. An example C compiler directive is "#pragma omp parallel." The master and slave threads then all compute their assigned tasks, and when finished the master thread resumes control of the program. If the total number of master and slave threads does not exceed the number of processing cores available in the computer architecture then all threads will run in parallel, simultaneously. If the number of threads exceeds the number of available processing cores then some threads will have to wait their turn to be executed, and this case is referred to as *hyper-threading*, which is usually not as fast as avoiding hyper-threading.

The number of threads used in the execution of the sections of code parallelized by OpenMP is determined either by set values coded by the programmer into the OpenMP compiler directives, or by environment variables in the computer system, set by the user or system administrator. For example, the system environment variable OMP_NUM_THREADS sets the number of threads used at runtime. Note that the Intel MKL math library incorporates OpenMP, and the number of parallel threads it uses at runtime is set by the system environment variable MKL_NUM_THREADS. Of course, if the number of threads set by any such variable exceeds the number of processing cores in the computer architecture then only the actual number of cores will be used as the number of threads.

There are usually an optimum number of threads for maximum compute speed, depending on the algorithm that is being parallelized. This optimum number of threads will also depend on the computer architecture, such as whether all cores are contained in a single CPU or in multiple CPUs, and the memory bandwidth that exists in the computer architecture. A parallelized algorithm may run slower as additional threads are used above the optimum number of threads.

Special features are incorporated to handle the sharing of limited system resources simultaneously by a number of threads. An example is if all threads must each access the same memory location. These special features help avoid situations such as a racing condition by use of the compiler directive clause *critical*, which causes multiple threads to each take their turn, sequentially running the specified section of code instead of running simultaneously. Data reduction is another important issue address by these special features provided by OpenMP.

2.3 MPI

MPI stands for message passing interface and provides a means of communication between networked compute nodes in a distributed memory compute model, where multiple compute nodes, each with their own dedicated memory, cooperate to accomplish some computing task. It was introduced in 1994 and is a computer language-independent protocol used to program parallel computers, and it is a portable model, meaning that the code is compatible with and can be run on a range of different compute platforms; thus it can harness a wide range of computational power together. The time spent computing on each node in between MPI message passing events must significantly exceed the time spent sending the messages through the network in order to maximum overall computational efficiency. Computations in between

message passing should therefore span several seconds or more on each node for highest efficiency. Although originally intended for distributed memory models, it functions in shared memory models as well, providing communication between the processing units — thereby, an MPI code intended for use in a distributed memory model can be first tested on a shared memory system, on which the programmer has immediate control of all resources.

The MPI communication between compute nodes often takes the form of TCP/IP (transmission control protocol / internet protocol), but not necessarily. A MPI code incorporates all communication between all nodes. The one code is distributed among the different compute nodes and then simultaneously run on all of them. So the MPI code represents a master plan of all the communication that will take place between any of the nodes involved. MPI code entries are basically meant to specify that some particular node will send a message to another node (or nodes), and that that other node will receive the message. Such an example is provided by the following two lines of MPI code.

```
MPI_Send ( data_i, count, MPI_INT, node, tag, MPI_COMM_WORLD);

MPI_Recv ( data_i, count, MPI_INT, node, tag, MPI_COMM_WORLD, &stat);
```

The first line sends a message from one node to another, and in that line the count of the length of the message and the type of data it represents (integer: MPI_INT) is specified. The second line corresponds with the first. The first line runs only on the compute node that is assigned to send the message, and the second line runs only on the compute node assigned to receive the message. When each compute node runs the one common MPI code it is assigned a unique compute node identifier, and the MPI code is written to assign specific tasks to specific compute

nodes. Special features are also provided in MPI, similar to those mentioned for OpenMP, to provide for data reduction and other special circumstances. The startup time of a MPI code depends on how many compute nodes are involved, and one limitation of MPI is that no breaks from compute loops, e.g., *for* loops, are allowed.

2.4 SSE2-SSE5

Streaming SIMD Extensions (SSE) provide a notable increase in computational efficiency by utilizing the Single Instruction Multiple Data model, whereby a single instruction acts on multiple data loaded into the one instruction set and expanded registers associated with SSE. SSE2 and later versions act on integer as well as floating point values. Optimized math libraries, such as Intel's MKL library, make extensive use of a CPU's SSE capabilities. SSE3 added instructions to add and subtract multiple values stored within a single extended size register. SSE2 was introduced in 2001, SSE3 in 2004, SSE4 in 2007, and SSE5 in 2011.

2.5 ADVANCED VECTOR EXTENSIONS

AVX was introduced in 2011 and extends the SIMD register on the CPU from 128 to 256 bits. It introduced a three-operand SIMD instruction format and the capability for expressions such as $c = a + b$ use a non-destructive three-operand form to preserve the two source operands. It increases parallelism and throughput in floating point SIMD calculations.

2.6 C++11 EXTENSION TEMPLATES

The C++ language by default uses what's called the eager evaluation model, whereby each individual operation within a mathematical expression is evaluated as soon as possible, which

leads to the storage of partial results in temporary objects. This eager evaluation is inefficient when relatively large memory objects (matrices) are involved in the calculations. A more computationally efficient alternative is to delay the evaluation of the operations within a mathematical expression until the result is needed; thereby avoiding the intermediate calculation and storage of temporary memory, and this alternative method is what's called the lazy evaluation model. By applying template metaprogramming tools in C++ this "lazy," yet more computationally efficient method can be achieved, using a technique called *C++ expression templates,* and it was first described by Veldhuizen [56]. CPU and also GPU code can benefit from the computational efficiency of the lazy model [57], for applications involving large data models. Expression templates create objects with a custom, unique *C++ type* that specifies the particular algorithm to be computed, and that *type* is interpreted at compile-time to generate an efficient algorithm implementation of the whole expression, thereby minimizing the inefficiencies of temporary calculation and intermediate storage. The lazy evaluation model appears to have a direct analogy in the *just in time* business production strategy that strives to maximize a business' return on investment with the reduction of in-process inventory and the carrying costs associated with that inventory. The 2011 release of the C++11 language standard provides a new *r-value reference* feature that incorporates *move semantics* and may functionally supersede the *expression templates* functionality in a more compact manner.

2.7 GRAPHICS PROCESSORS

General purpose computing on graphics processing units is referred to as GPGPU. The acronym GPU was coined in 1999 to distinguish the graphics processor topology from the central

processor unit (CPU) when general programming capabilities were first included into the graphics processor design The next year, 2000, GPU architectures began incorporating a programmable shader unit, which provided new capabilities that have enabled the evolution of GPGPU [58]. In 2002 Mark Harris coined the acronym GPGPU, when it was an obscure research topic addressed by only a few researchers, and in 2003 he founded the website www.gpgpu.org. Soon after high-level shading languages came into use with DirectX9, to replace former assembly code, which involved much more intricate software coding. In 2004 the PCIe PC bus replaced the slower AGP bus, for video cards, and the enhanced speed of the PCIe bus is what the GPU relies on in the transfer of data to and from the CPU. The fundamental data structure in a CPU system is a one-dimensional array, and the fundamental data structure in a GPU system is a two-dimensional array, called a texture. A GPU kernel represents a code fragment, which accomplishes a portion of an overall computational task that in a traditional (single-threaded) CPU program would be accomplished by an unfragmented single set of code.

Graphics processors are multi-core devices primarily developed to speed up the display of graphics in real time. The website www.gpgpu.org is a source of GPGPU news and information. Specialized languages have been developed for GPGPU coding of GPUs, including Brook, CUDA, OpenCL and OpenACC.

The graphics processing unit (GPU) was originally developed to speed up graphical displays, but it has proven to be useful in speeding up scientific computing as well. One of the first publications describing the use of a graphics processor to antenna computations was by J.S. Asvestas in 1995 [59]. Over the past decade clever methods have been developed to utilize the GPU as a general-purpose graphics processing unit (GPGPU) to accelerate computations,

including electromagnetic problems, traditionally handled by a CPU. The key difference between the GPU and CPU that determines the computational speed advantage is a difference in architecture: Single Instruction Multiple Data (SIMD). With SIMD hundreds if not thousands of parallel GPU processors execute the same instructions on data that is stored in the GPUs high-speed memory banks. The largest manufacturers of GPUs are NVIDIA, AMD (ATI), and Intel. NVIDIA provides their own software language, CUDA [60], to program only their GPUs for GPGPU computing, as well as supporting OpenCL. AMD had provided GPU drivers to support Stanford's Brook [61] language since 2003, the first attempt at a GPGPU language, as well as an extension to the Brook language customized for AMD GPUs, Brook+, and in 2011 switched to providing GPU drivers only for the now industry-standard OpenCL GPGPU language.

2.7.1 OpenCL

OpenCL [62] is a universal GPGPU programming language, originally trademarked by Apple, Inc, subsequently adopted by the entire industry, and is currently under development and managed by the Khronos group (www.khronos.org/opencl/). OpenCL is considered the open standard for parallel programming of heterogeneous systems, and it's intended for any brand of GPU: NVIDIA or AMD — the idea is that OpenCL code can be run on a heterogeneous system, whether the computing engines include CPUs, GPUs, DSPs, or a heterogeneous combination of computing engines. In 2008 the Khronos group published the first specification of the OpenCL language. Some limitations of OpenCL are that the current version 2.0 does not support recursion, so a subroutine cannot call itself. Also, complex variable type is not native in OpenCL, so complex arithmetic must be specially handled.

2.7.2 OpenACC

In 2012 a new GPU programming language became available: OpenACC, which is intended to allow existing CPU code to be simply revised to offload sections of the CPU code that can be computed in parallel, e.g., *for* loops, to a GPU for processing considerably faster than can be done on the CPU. OpenACC relies on a collection of compiler directives being added to existing C, C++ or FORTRAN code to specify loops and regions of code in to be offloaded from the host CPU to an attached GPU (www.openacc-standard.org), and in this regard the coding implementation of OpenACC is similar to that of OpenMP (http://openmp.org/wp/).

2.7.3 GPU Double-Precision Support

GPU support for double-precision computing is usually only provided in the upper-end GPU models, and on those models only a limited percentage (about 20%) of the chip's real estate is allocated to double-precision processing units (since the primary market for GPUs is graphics, which has no need for double-precision). If a matrix is ill-conditioned it may solve faster, or only when, using double- than single-precision arithmetic [63]: Note that the truncated singular value decomposition method helps to solve ill-conditioned matrices [42].

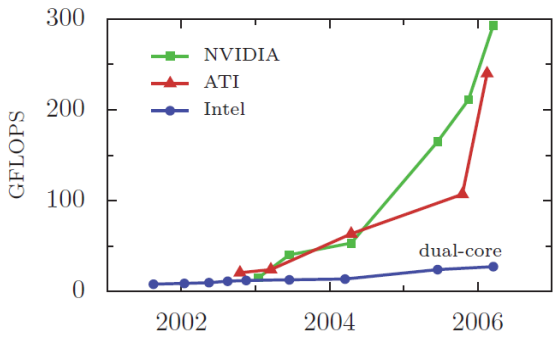

Fig. 2-2. Timeline of GPU versus CPU Compute Speed (adapted from **[64]**).

2.7.4 MAGMA

In 2009 the University of Tennessee, which had decades previously developed the highly efficient LINPACK and LAPACK libraries [65] for CPU code, effectively joined the competing forces of the CPU and GPU by releasing their first beta version of their new MAGMA library (Matrix Algebra on GPU and Multi-core Architectures), to simultaneously harness the unique strengths of both CPU and GPU to try to solve matrix problems as fast as possible. MAGMA version 1.0 was released in 2011, coded only in the CUDA language customized for NVIDIA GPUs. In 2012 MAGMA was ported to the OpenCL language as clMAGMA release version 1.0 in late 2012, supporting both AMD and NVIDIA GPUs, and part of the work of this dissertation involved porting clMAGMA to Windows ™: That port is documented on the MAGMA User Forum:http://icl.cs.utk.edu/magma/forum/viewtopic.php?f=2&t=437&sid=939ece890958f1fe1ab170fae738e4c9, http://icl.cs.utk.edu/magma/forum/viewtopic.php?f=2&t=727, and http://devgurus.amd.com/message/1299829#1299829, and results of the GPU acceleration speed achieved in comparison with CPU implementations of a few key BLAS and LAPACK routines are summarized in Table 2-1 below.

The MAGMA web site states, “The MAGMA project aims to develop a dense linear algebra library similar to LAPACK but for heterogeneous/hybrid architectures, starting with current ‘Multi-core + GPU’ systems. The MAGMA research is based on the idea that, to address the complex challenges of the emerging hybrid environments, optimal software solutions will themselves have to hybridize, combining the strengths of different algorithms within a single framework.”

The recently-introduced Matrix Algebra for GPU and Multi-core Architectures (MAGMA) and clMAGMA libraries provide similar functionality for systems with a GPU as the BLAS and LAPACK do for a CPU, but with significant potential for further accelerating matrix algebra computations due to the use of the GPU. Fig. 2-3 presents the potential of the GPU to accelerate computational speed beyond the CPU alone — the graph shows a GPU/CPU speed advantage about an order of magnitude for matrix size around 2000. Current GPUs of moderate capability and cost provide more than 1000 processing units and 1 GB or more of high-speed memory.

Table 2-1. GPU acceleration of clMAGMA versions of BLAS GEMM & LAPACK GESV subroutines versus CPU (AMD HD5850 hosted on Intel Core 2 Quad Q8200 running Windows ™).

Netlib subroutine	Matrix Size	Acceleration Factor of GPU vs. CPU
BLAS SGEMM	200	1
DGEMM	300	1
CGEMM	150	1
ZGEMM	100	1
SGEMM	4000	30
DGEMM	4000	22
CGEMM	4000	20
ZGEMM	3000	10
LAPACK SGESV	1000	1
DGESV	800	1
CGESV	500	1
ZGESV	500	1
SGESV	4000	5
DGESV	3000	3+
CGESV	3000	5
ZGESV	2000	3+

MAGMA and clMAGMA are provided in the form of a source code that must be compiled. I have gotten MAGMA compiled and working on the UCLA Hoffman2 general cluster (NIVIDA Tesla Fermi C2070 GPUs) and clMAGMA working on a few desktop PCs (AMD HD5850 and HD6850 GPUs). My testing indicates a clMAGMA (GPU) to LAPACK (CPU) matrix solving execution speed advantage of about an order of magnitude for matrix size about 2000. Below matrix size of a few hundred the CPU is faster, especially when supported by CPU hardware-optimized LAPACK library such as AMD's ACML or Intel's MKL.

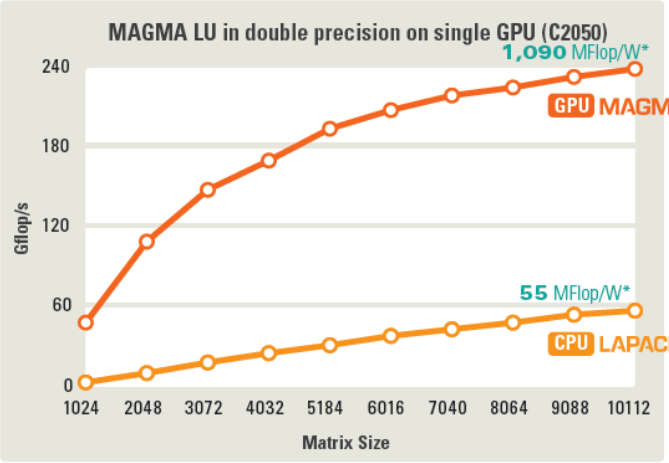

Fig. 2-3. MAGMA's advertized CPU+GPU speed enhancement over CPU alone (from http://icl.cs.utk.edu/magma/overview/index.html).

2.8 CONCLUSION

The capabilities of the computer architecture, and the computer language features to control the hardware have a significant a significant impact on the rapidity of any compute algorithm. Through a balanced use of parallel processing and full utilization of the features of the processing cores and language extensions (SSE, SSE2, SSE3, SSE4, SSE5, AVX, extension templates, r-value references, and OpenCL for GPGPU) the characterization and optimization of aperture and reflector antennas can be suitably accelerated.

CHAPTER 3 METAHEURISTIC OPTIMIZATION

Optimization techniques used in the electromagnetic engineering community are often metaheuristic because of the complexity of the tradeoffs involved. Metaheuristic methods involve stochastic optimization to distinguish global from local optimal solutions, as opposed to classical optimizers that are meant to produce exact solutions for simpler classical models with local extrema, which if applied to real-world engineering problems tend to get stuck on local optimum solutions.

A basic overview of metaheuristic methods is provided in [66]. Such methods include Ant Colony Optimization [67], Covariance Matrix Adaptation Evolution Strategy (CMA-ES) [68], Genetic Algorithms (GA) [69], Invasive Weed Optimization (IWO) [70], PSO [71]–[76], Simulated Annealing [77], and Tabu Search [78]. Among these optimization techniques, the PSO is a practical balance between model simplicity and robust, rapid, global solution convergence.

Optimization can pertain to a system with one or more variables with one or more optimization objectives, goals, or constraints. With only one objective the optimization can evaluate it with a fitness function. If there are multiple (competing) objectives evaluation of the optimality becomes more complicated. There are generally two approaches to multi-objective optimization:

1) combining fitness functions and 2) referring to a Pareto front [76], [79], [80]. A classical way of combining multiple objectives into a single fitness function is a weighted sum of fitness functions — one from each objective — where the result of the overall optimization can depend on the choice of weighting. An example is given in (3.1) of section 3.1, which involves the two competing objectives of peak sidelobe level and first-null beamwidth. Pareto optimality represents the trade-off between multiple goals: A solution is Pareto optimal when it is not possible to improve one goal without degrading at least one of the others. Optimization by Pareto front involves more intensive numerical investigation to determine the actual boundary of optimality between competing objectives, and a few examples of Pareto fronts are given below. The Pareto front provides the bottom line optimum tradeoff between the competing fitness functions, which is then used to narrow down the optimization process to provide a particular design using that knowledge. In general there is no singly optimal solution to a multi-objective optimization: The set of Pareto optimal multi-objective solutions is called a Pareto front.

3.1 PARTICLE SWARM OPTIMIZATION

The Particle Swarm Optimization (PSO) algorithm is similar to the concept of a swarm of bees in a field, effectively communicating their individual findings and so guiding the swarm as a whole ever closer to a suitable location to converge upon. A PSO algorithm directs the search and evaluates a fitness function, customized for the particularly specified goal(s), to evaluate the merit of each candidate solution considered by any member of the swarm. Example PSO convergence plots are shown in Fig. 3-1 and Fig. 3-2, using respective fitness functions given by (3.1) and (3.2), and each with twenty agents per swarm and thirty swarm trials per iteration.

These two are comparable since they both have the same goal of -40 dB PSLL; although, one is for a sum pattern and the other for a difference pattern. Note that the convergence plot in Fig. 3-1 involves a fitness function that is not conditional; whereas, that in Fig. 3-2 is conditional: In the former case the average fitness is considerably larger than in the latter; although, the rate of convergence appears to be a bit faster in the former than the latter.

$$\text{fitness\_11a} = \left(\text{PSLL}\left(\text{dB}\right) - \text{goal}\right)^2 + \text{FNBW}\left(u\right)/2 \tag{3.1}$$

$$\text{fitness\_11b} = \begin{cases} \text{FNBW}\left(u\right)/2, & \text{if PSLL} \le \text{goal;} \\ 999, & \text{otherwise.} \end{cases} \tag{3.2}$$

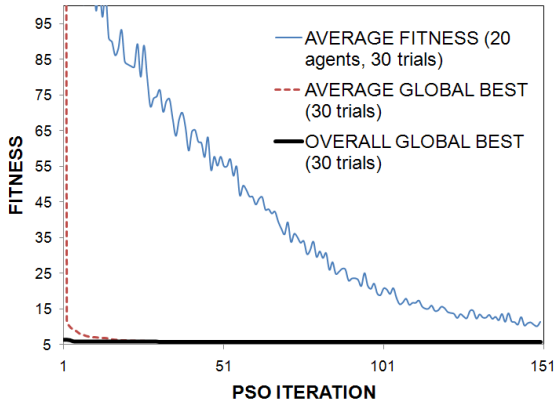

Fig. 3-1. PSO convergence for design of 3PS pattern with -40 dB PSLL and minimum FNBW, reproduced courtesy of The Electromagnetics Academy [81].

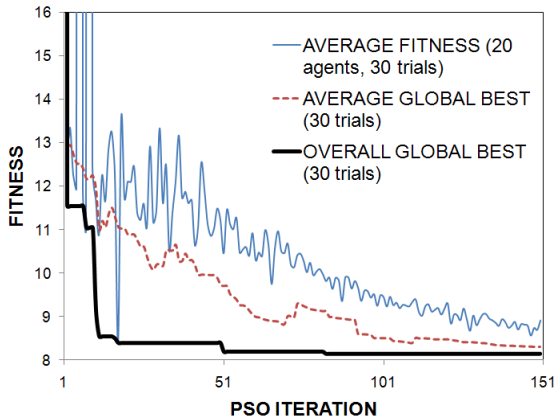

Fig. 3-2. PSO convergence for design of 3PD pattern with -40 dB PSLL and minimum FNBW, reproduced courtesy of The Electromagnetics Academy [81].

The position, in model parameter space, of the search agent (swarm member) with the best fitness value among the swarm at any iteration is the *global best* for that iteration. Each search agent moves about the parameter space and its flight path is pulled toward that global best. It is also pulled toward its own *personal best* location, and its flight path is also affected by its own inertia and random motion.

Consider the flight trajectory of any particular swarm member ("search agent," or "bee") in the PSO model *n*-dimensional parameter space, letting $n = 2$ here for simplicity. Applying real-world physics and assuming each bee naturally counteracts the force of gravity, we imagine that each bee has some linear momentum that Newton's Law preserves until external forces are applied or the bee alters its path. External winds and individual bee behavior combine to provide a seeming randomness to the individual flight paths. By means of the waggle dance a bee communicates to its hive-mates in which direction with respect to the Sun and how far it flew to reach the food source it found. So we can imagine that each bee's flight path is affected by 1) Newton's Law, 2) random motion, 3) its own knowledge of the best place at which it has found food (personal best, or p_{best}), and 4) the best overall location found by any member of the swarm (the global best, or g_{best}). This is represented by (3.3) for the motion of any PSO search agent. v_n represents the search agent's velocity vector in the current (n^{th}) iteration, x_n represents its current position vector, w is the momentum factor, c_1 and c_2 effectively represent *spring constants* pulling the search agent respectively towards its personal and the overall swarm's global best locations, and rand() is a strictly-positive valued random number function ranging between the zero and one. Δt is a discrete step representing the time between iterations.

$$x_{n+1} = x_n + v_n \Delta t, \text{ and } v_{n+1} = w v_n + c_1 \text{rand}() \left(p_{\text{best}} - x_n \right) + c_2 \text{rand}() \left(g_{\text{best}} - x_n \right) \qquad (3.3)$$

The fitness function used to evaluate the merit of the search agent's current location in parameter space can represent the merit with respect to one or more complementary goals. With a single goal, such as beamwidth, the fitness function can be simply a function of beamwidth that PSO will strive to minimize. The fitness function can also represent multiple complementary goals by combining fitness functions for each of the goals into a single fitness value, where the respective weighting of each factor affects the outcome of the optimization process. An effective technique for handling multiple goals in an optimization makes use of a *Pareto front* [80]. Pareto optimality represents the trade-off between multiple goals: A solution is Pareto optimal when it is not possible to improve one goal without degrading at least one of the other, and a set of Pareto optimal solutions determines the Pareto front.

3.1 IMPLEMENTATION

The particle swarm optimization can be implemented in regular code (C/C++, FORTRAN) single-threaded, or accelerated by parallel processing. Generally the majority of the compute time of a PSO optimization run is spent calculating the fitness function of the optimization loop. This means that parallel processing techniques can be used to accelerate PSO by calculating the fitness functions for several different parameter permutations all at the same time. The previously discussed techniques of OpenMP, MPI and OpenCL are well suited in this regard, where OpenCL allows harnessing the power of graphics processors. The acceleration factor is maximized on graphics processors by writing the PSO code, including the fitness function calculations, so that all the PSO computations remain resident on the graphics processor as long as possible and having the graphics processor communicate with the host computer only at first

to receive the tasks instructions and then at the end to report the final results back to the host computer for archiving the results.

3.2 MULTI-PARAMETER PSO OF MULTIBAND FSS SUBREFLECTOR

The results of an example application of PSO to produce an optimized design of a four-band multi-layer frequency selective surface (FSS) subreflector are presented below, wherein nearly twenty design parameters were involved in the optimization in order to specify the respective thicknesses of ten internal material layers, including dielectric and honeycomb sheeting, and the dimensions of the frequency selective conductive elements arranged in a spatially periodic hexagonal pattern on four different intermediate material interfaces within the multi-layer construction. At every step of the optimization a combined fitness function for the candidate set of design parameters, chosen by the optimizer, is determined by comparing the response of the subreflector over specified relative frequency bandwidths (10–20%) in four different frequency bands (S-band, X-band, Ku-band, and Ka-band) and over the angular range of 10–40 deg, which is the angular range that the rays from the feedhorn make wrt the subreflector surface normal for this particular example. The electromagnetic response of the FSS subreflector is evaluated by a Floquet mode analysis of the periodic, multi-layer structure calculated using the QDAS software provided by Steatite Q-par Antennas (http://www.q-par.com/capabilities/software/fss-demo-software-download).

The combined fitness function is defined to minimize the S-band transmission loss while simultaneously minimizing the reflection loss in the X-, Ku- and Ka-bands. Different shapes for the periodic elements were considered (square, cross, etc.) and the tripole element yielded the

best results. A unique part of this design is that the layering is asymmetrical. Subreflectors are often constructed symmetrically, such that the material layering and FSS sheets are identical when entering the subreflector from either side, with an odd number of layers so that one material layer occupies the center. It was recognized for this design exercise that the transmission properties are naturally independent of the direction of wave travel (due to the principle of reciprocity), and that the reflection loss requirements only applied to reflection from one particular side of the subreflector. Thereby the optimizer was set free to evaluate asymmetrical material layer thickness profiles, as well as an asymmetrical layup of the FSS sheets (periodic arrays of conductive elements). The asymmetrical design provides the benefit of minimizing the overall subreflector thickness.

The optimized shapes of the conductive FSS element sheets chosen by the optimizer are indicated below, in order of the reflective side inward toward the other side of the subreflector multi-layer construction.

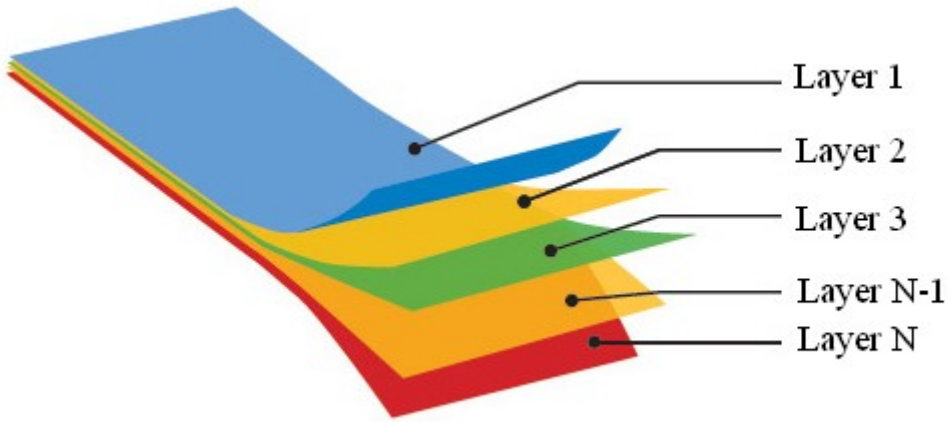

Fig. 3-3. Multi-layered subreflector construction, from www.appliedbpc.com.

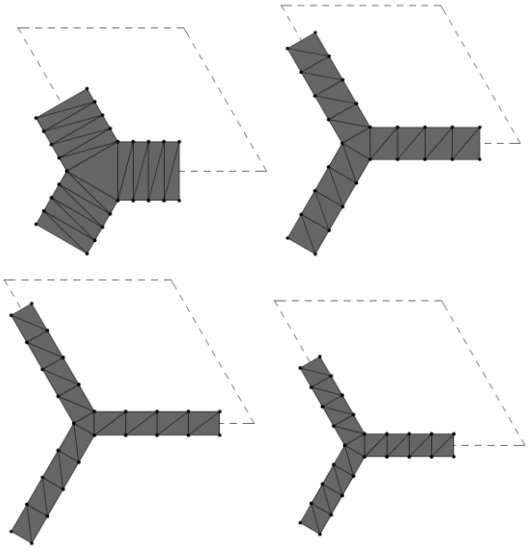

Fig. 3-4. The relative shapes of the four different periodic FSS elements, each individually repeated on a different FSS sheet within the multi-layer subreflector. The dashed rhombus represents the unit cell in the respective periodic FSS sheet.

Fig. 3-5 provides a sample full spectral response of the FSS subreflector for an intermediate design from the optimizer: after the optimizer has run for a while but not yet converged on the final solution — this indicates the complexity of the problem of achieving minimum loss across several specific frequency bands. The S-band transmission and X-, Ku- and Ka-band reflection losses of the fully optimized multi-band subreflector are indicated in Fig. 3-6 through Fig. 3-9 below versus frequency and incidence angle. Only the horizontal central third of the indicated frequency plots represent the frequency bands evaluated by the optimizer fitness function: The additional left and right thirds of the plots are included to indicate the trend of the subreflector frequency response so that the effects of manufacturing tolerance might be considered.

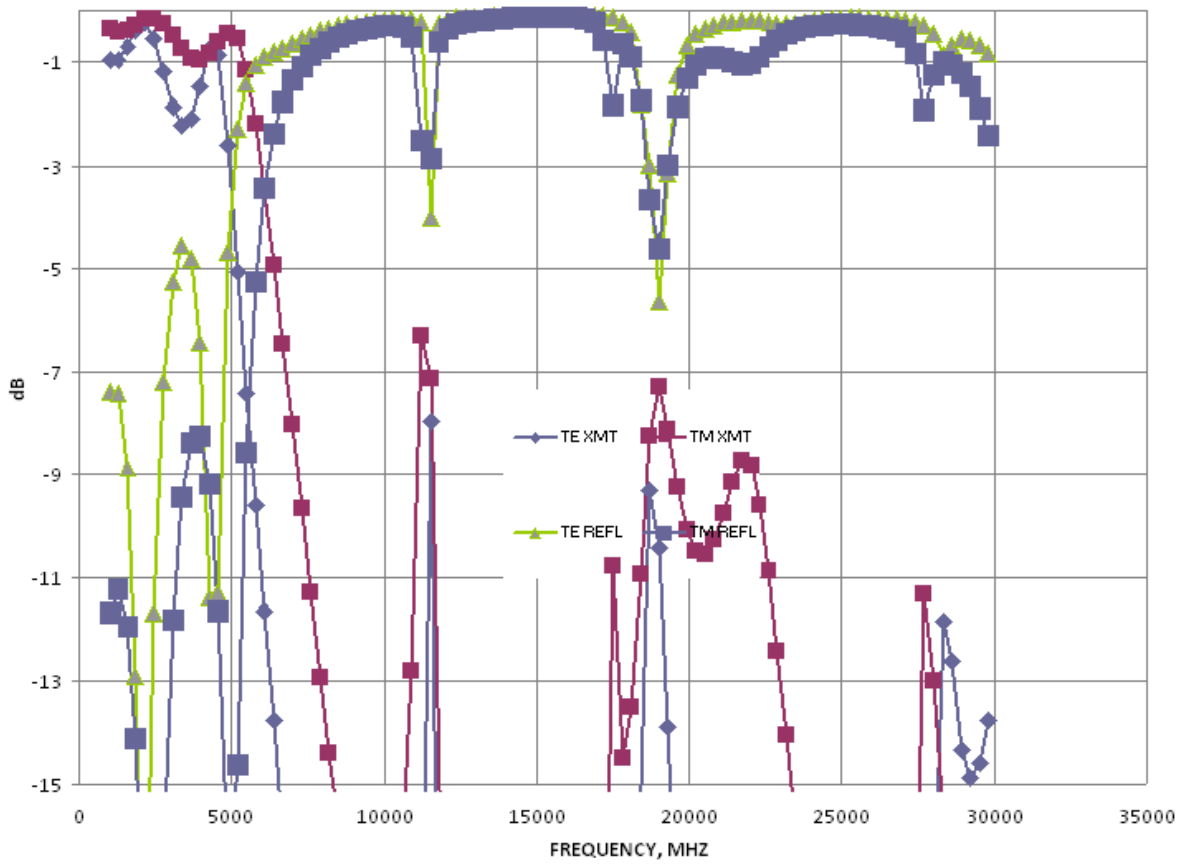

Fig. 3-5. Intermediate optimizer result: Full spectral response of FSS after the optimizer started by not yet converged on the solution. This indicates the complexity of the problem of achieving minimum loss across several frequency bands, showing that an initial design can have very significant losses.

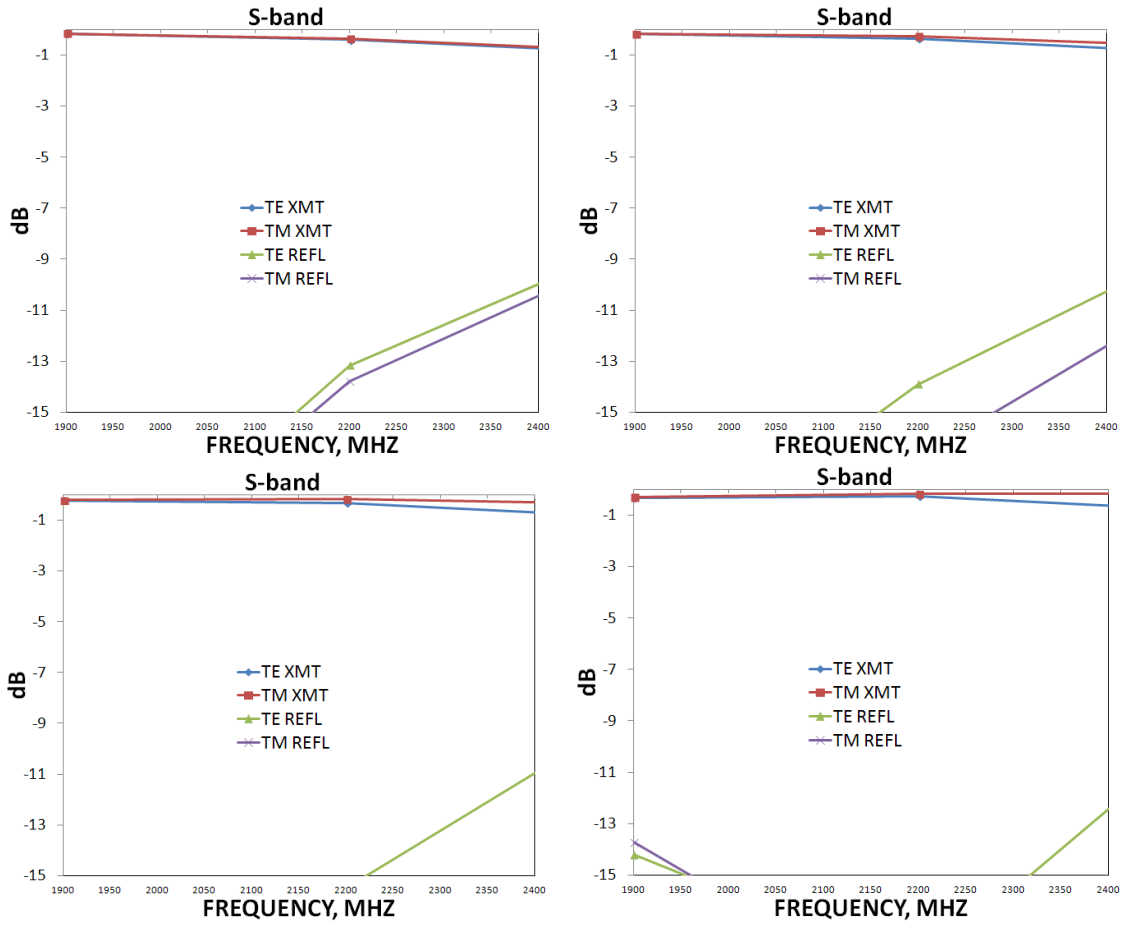

Fig. 3-6. Fully optimized design: S-band transmission response of PSO optimized multi-layer FSS subreflector at incidence angles of 10 deg (top left), 20 deg (top right), 30 deg (bottom left), and 40 deg (bottom right).

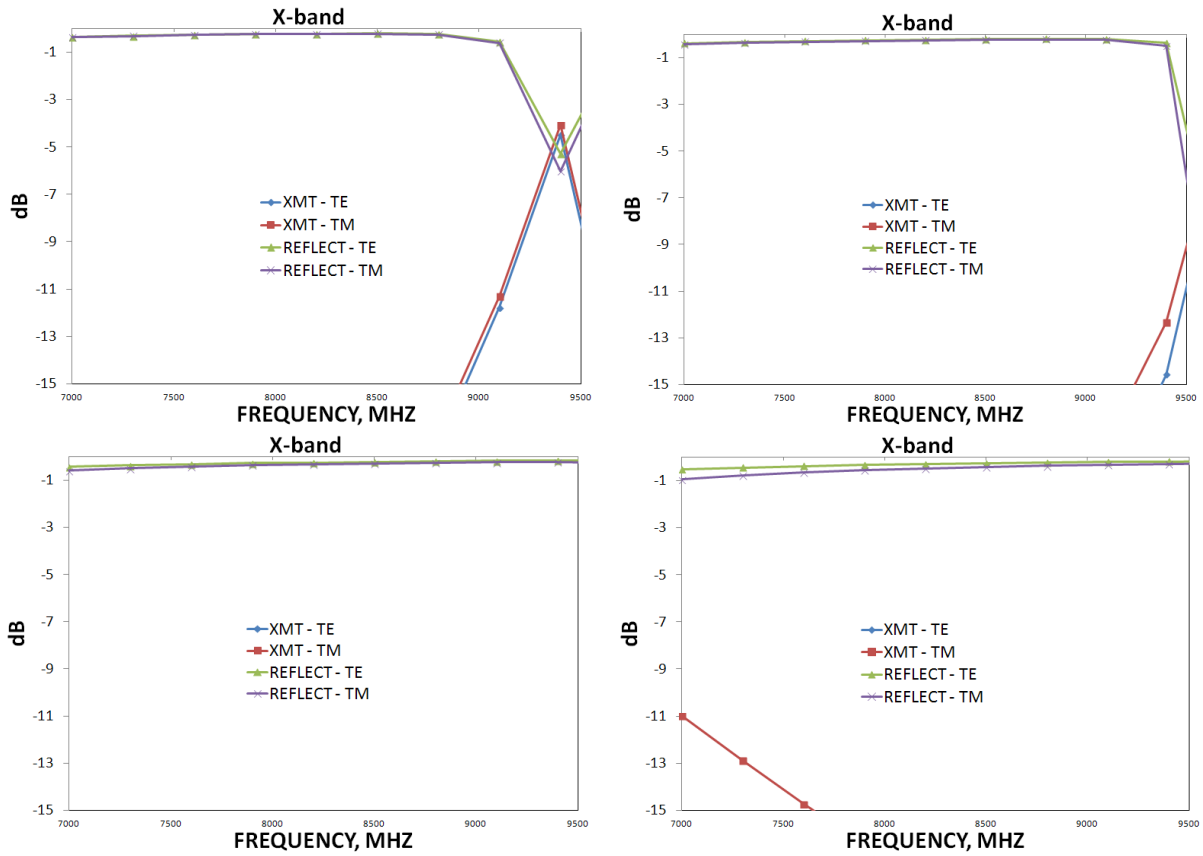

Fig. 3-7. X-band reflection response of PSO optimized multi-layer FSS subreflector at incidence angles of 10 deg (top left), 20 deg (top right), 30 deg (bottom left), and 40 deg (bottom right).

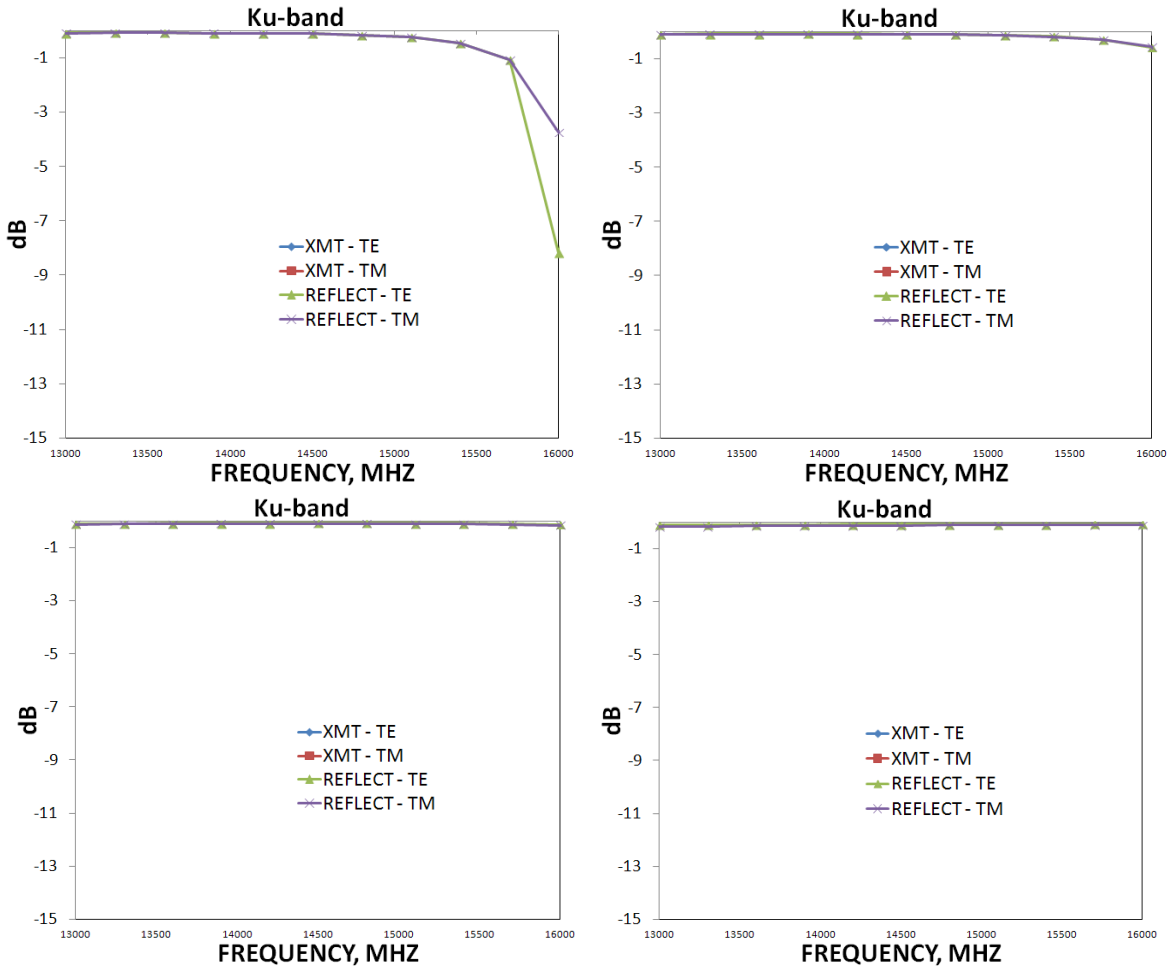

Fig. 3-8. Ku-band reflection response of PSO optimized multi-layer FSS subreflector at incidence angles of 10 deg (top left), 20 deg (top right), 30 deg (bottom left), and 40 deg (bottom right).

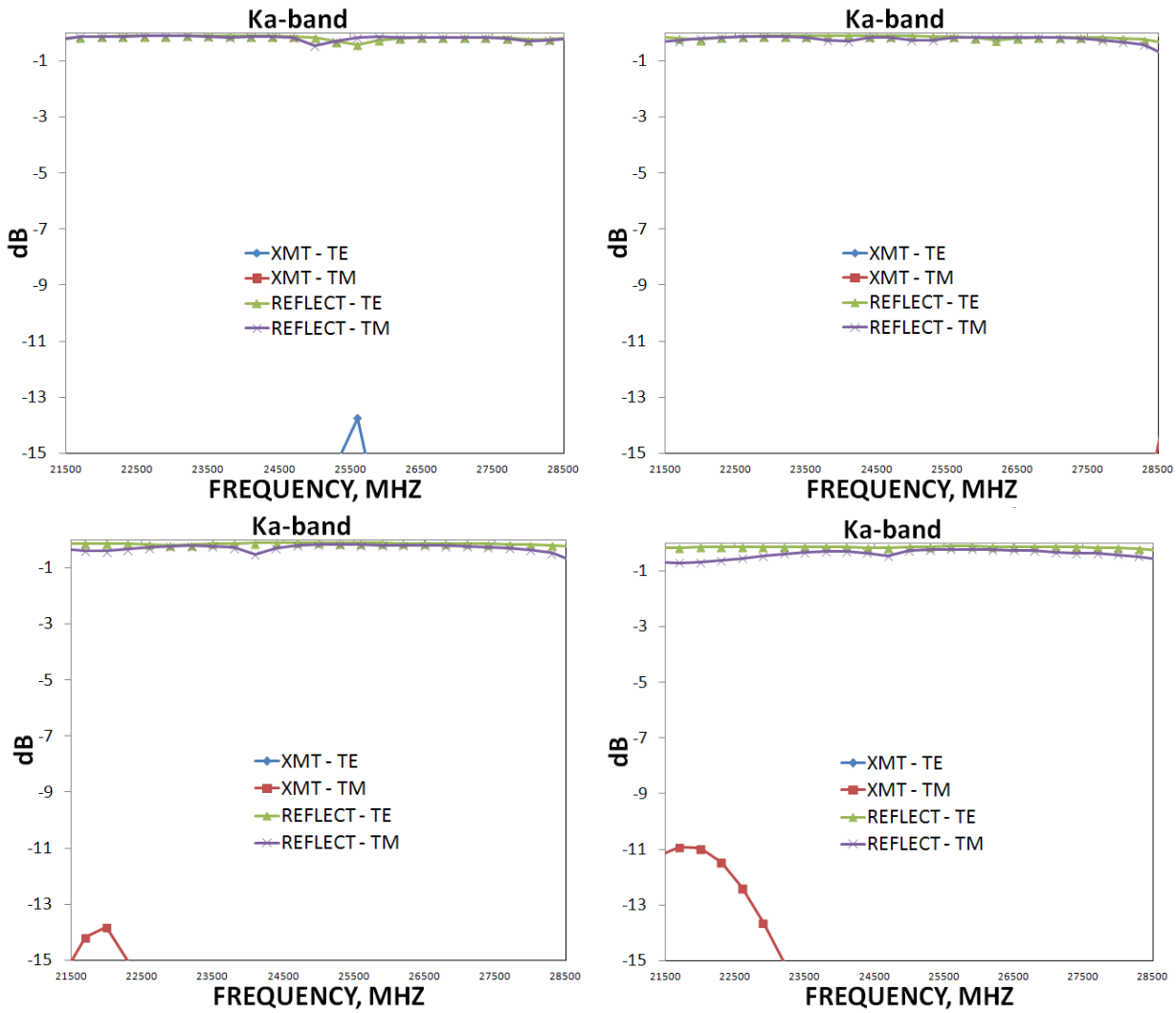

Fig. 3-9. Ka-band reflection response of PSO optimized multi-layer FSS subreflector at incidence angles of 10 deg (top left), 20 deg (top right), 30 deg (bottom left), and 40 deg (bottom right).

3.3 CONCLUSION

Metaheuristic optimization is utilized to solve real-world engineering problems in which there may be a complex relationship between local optima and a desired global optimum. The literature reports that the method of particle swarm optimization (PSO) provides a reasonable balance between accuracy of locating a global optimum and the speed of solution convergence. A set of examples were discussed that indicate that PSO is able to provide good rates of convergence toward a stable solution and also handle real-world design optimizations with a

relatively large number of design parameters. With these observations and example demonstrations in mind, the method of PSO is the primary optimization technique utilized in this dissertation.

CHAPTER 4 THREE-PARAMETER APERTURE DISTRIBUTIONS

This chapter presents a unified analysis of the three-parameter aperture distributions for both sum and difference antenna patterns, suitable for communications or telemetry applications with either a stationary or tracking antenna, and with the parameters automatically determined by Particle-Swarm Optimization (PSO). The optimizations involve multiple objectives, for which Pareto efficiency concepts apply, and are accelerated by compact, analytical closed-form equations for key metrics of the distributions, including the far field radiation pattern and detection slope of the difference pattern. The limiting cases of the three-parameter distributions are discussed and shown to generalize other distributions in the literature. A derivation of the generalized vector far fields provides the background for the distribution study and helps clarify the definition of cross-polarization in the far field. Examples are given to show that the three-parameter (3P) distributions meet a range of system-level constraints for various applications, including a sidelobe mask for satellite ground stations and maximizing pointing error detection sensitivity while minimizing clutter from sidelobes for tracking applications. The equations for the relative angle sensitivity for the difference pattern are derived. A study of the sensitivity of the 3P parameter values is presented.

4.1 INTRODUCTION

There are many methods of antenna synthesis, each of which is developed in response to a given class of problems. This chapter provides a unified method for antenna pattern synthesis for the broad classes of antennas having a single main beam, with some constraint on the sidelobe levels, and including tracking antennas. This 3P unification provides closed-form equations for key metrics associated with each aperture distribution, including the radiation patterns for both sum and difference patterns, allowing quick calculation analytically rather than by brute force integration.

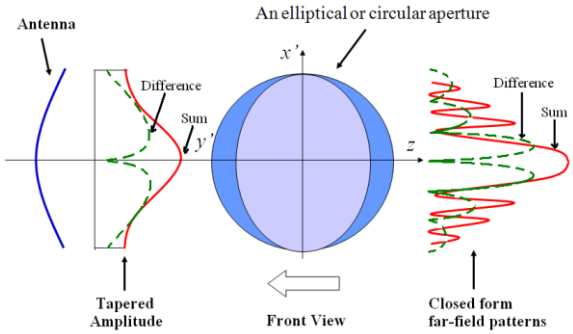

Fig. 4-1. Elliptical aperture geometry, with generic sum and difference patterns, reproduced courtesy of The Electromagnetics Academy [81].

Consider an elliptical aperture as shown in Fig. 4-1. An antenna's radiation characteristics are largely determined by its aperture fields, which are respectively determined by the antenna's design and construction. When a realistic, comprehensive model of aperture field distribution is available with a relatively small number of parameters, the overall antenna design process can be effectively divided into two sequential steps: first identifying an aperture distribution model that meets the given system-level design constraints (considering antenna system metrics such as beamwidth, sidelobe level, and pointing error detection sensitivity) and subsequently designing the antenna to provide the chosen aperture distribution. Ideally such a model would provide

analytical relationships between the aperture parameters and the system metrics, and this chapter provides those relationships as equations for the 3P distribution, generalized for sum and difference patterns. The three parameters are α, β, and *c*. With just a few parameters for the aperture distribution the top-level antenna system design can be completed quickly.

The 3P distribution, as originally published [82], applies only to sum patterns. Here we extend it to include difference patterns as well and analyze both the sum and difference distributions in a unified manner. The 3P distributions provide considerable flexibility, as the remainder of this chapter shows: The 3P sum distribution generalizes several other distributions in the literature, including Hansen's 1P distribution [83], the parabolic 2P, and the Bickmore-Spellmire 2P: all as discussed in [82]. These other distributions are represented by limiting cases of the 3P general distribution, as discussed below. What is meant by a sum pattern is the radiation pattern from the fields in the entire aperture, all in phase (adding constructively). On the other hand, the difference pattern negates the sign of the fields on one side of the aperture so as to cancel out the fields on the other side and produce a difference pattern null in the central direction that coincides with the sum pattern's main beam. Antenna tracking systems track the null in the difference pattern to keep the main (sum) beam peaked on the signal.

An antenna's radiation pattern is determined from the aperture fields by the field equivalence principle according to Maxwell's equations. A radiation pattern varies in shape as a function of distance from the aperture: reactive near field zone closest to the antenna, radiating near field (Fresnel zone) and radiating far field (Fraunhofer) zone. Beyond a certain distance from the aperture, which depends on the antenna size, the radiation pattern remains effectively constant in shape. In this analysis the true (infinitely distant) far fields are considered. The radiation

characteristics of taper efficiency, beamwidth, sidelobe level, and the asymptotic trend of the far-out sidelobe levels are addressed for the 3P distributions.

The 3P model assumes a planar aperture, and there are several methods by which to synthesize planar apertures, *e.g.*, [84] chapter 7, [83], or [85] chapter 6, that must relate the aperture parameters to a given set of design constraints. A manual design of an aperture distribution can require considerable time, and as Hansen mentions [83] can result in a suboptimal result. An optimizer that automatically searches the available range of distribution model parameter values can significantly reduce the time and effort required to meet particular design constraints — even finding unexpected solutions that might be missed if designed manually.

Metaheuristic optimization is discussed, identifying the common methods currently in use, followed by a discussion of the fundamentals of the PSO algorithm [71]–[76], and several examples are given for 3P distributions designed by PSO to meet common design constraints, which can involve multiple competing factors. Multiple-objective optimization is addressed from the perspective of Pareto efficiency [76]. The PSO algorithm serves the purposes of 3P distribution design quite well, as the examples reveal.

A number of mathematical appendices are included at the end, in which the closed form equations discussed in the body of the text are each derived, in order to make the chapter more complete. The following special functions are used:

$J_\nu(z)=$ Bessel function of the first kind, of order ν

$I_\nu(z)=$ modified Bessel function of the first kind, of order ν.

$\mathrm{H}_\nu(z)=$ Struve function, of order ν.

${}_pF_q(g_1,\ \ldots\ ,g_p;h_1,\ \ldots\ ,h_q;z)=$ generalized hypergeometric series.

For example,
$$ {}_2F_1(a,b;c;x)=\sum_{n=0}^{\infty}\frac{(a)_n(b)_n}{(c)_n}\frac{x^n}{n!}\ , \tag{4.1}$$

where $(a)_0=1$ is the simplest Pochhammer symbol, and the general Pochhammer symbol is $(a)_n=a(a+1)\ \ldots\ (a+n-1),\ n=1,\ 2,\ 3,\ \ldots$

4.2 FROM APERTURE DISTRIBUTIONS TO FAR FIELDS

In this section the aperture geometry is summarized, a set of equations that represent the vector far fields in a general form are derived (applicable to both sum and difference, and providing insight regarding the issue of the definition of cross-polarization), basic concepts pertaining to antenna radiation patterns are presented, including directivity, and the particulars regarding both sum and difference distributions are discussed, relating the model equations presented here to real-life applications.

4.2.1 Aperture Geometry

Consider an elliptical aperture with major and minor axes, *a* and *b*, centered about the origin in the *xy*-plane bounded by

$$\left(\frac{x}{a}\right)^2+\left(\frac{y}{b}\right)^2=1 \tag{4.2}$$

Any point inside the planar aperture is represented by a relative radial term, *t,* an angle, ψ, and a vector, $\bar{\rho}'$.

$$\bar{\rho}' = \hat{x}\,x' + \hat{y}\,y', \text{ where } x' = at\cos\psi,\ y' = bt\sin\psi,\ t \in [0,1],\ \psi \in [0,2\pi] \tag{4.3}$$

4.2.2 Generalized Vector Far fields

This section reviews the construction of the vector far field equations for an elliptical aperture distribution. The time-convention is $\exp[j\omega t]$, where $j = \sqrt{-1}$. The real-valued aperture distribution function $Q(t,\psi)$ represents the magnitude and sign of unidirectional (*e.g., x*- or *y*-directed) aperture fields, $\bar{E}_{ap}$ and $\bar{H}_{ap}$, assuming transverse electromagnetic mode (TEM) [11], with constant aperture phase other than a possible sign reversal defined by the distribution. The assumption of TEM mode in the aperture imposes

$$\eta\bar{H}_{ap} = \hat{n} \times \bar{E}_{ap}, \tag{4.4}$$

where η is the free-space impedance and $\hat{n}$ is the outward aperture surface normal vector — the *z*-axis here. The aperture distribution defines the aperture fields as a function of the aperture coordinates according to (4.5), where $\hat{p}$ is the polarization orientation of the electric field in the aperture, and η is the impedance of free space.

$$\bar{E}_{ap}(t,\psi) = \hat{p}\,Q(t,\psi)\sqrt{2\eta}, \tag{4.5}$$

The Schelkunoff field equivalence principle [1] relates the aperture field, given by the distribution, to equivalent electric and magnetic currents tangential to the aperture and related to vector potentials. The vector potentials then determine the radiating far fields associated with the

given aperture distribution. The equivalent currents relate to the aperture fields by the following equations.

$$\bar{J}_{eq} = \hat{n} \times \bar{H}_{ap} \quad \text{and } \bar{M}_{eq} = -\hat{n} \times \bar{E}_{ap} \tag{4.6}$$

Following (6-95), (6-101), and (6-102) from [11] the radiated electric far field, $\bar{E}_{ff}$, is proportional to the magnetic and electric vector potentials as given by the equations below, where the magnetic vector potential in the far field is $\bar{A}_{ff}$, the electric vector potential $\bar{F}_{ff}$, μ free-space permeability, ε free-space permittivity, $k = 2\pi / \lambda$, λ is the wavelength, and ds' the elemental aperture surface area. The vector from the origin in the center of the aperture to a given far field observation point is $\bar{r}(r, \theta, \phi)$, with corresponding unit vector $\hat{r}$.

$$\bar{E}_{ff} = \bar{E}_{A\,ff} + \bar{E}_{F\,ff} \approx j\omega\,(-\bar{A}_{ff} + \eta\,\hat{r} \times \bar{F}_{ff})\,, \tag{4.7}$$

where

$$\bar{A}_{ff} = \frac{\exp[-jkr]}{4\pi r} \mu \iint \bar{J}_{eq} \exp\left[jk(\bar{\rho}' \cdot \hat{r})\right] ds'\,, \tag{4.8}$$

and

$$\bar{F}_{ff} = \frac{\exp[-jkr]}{4\pi r} \varepsilon \iint \bar{M}_{eq} \exp\left[jk(\bar{\rho}' \cdot \hat{r})\right] ds'\,. \tag{4.9}$$

These equations reduce in the far field to

$$\bar{E}_{ff} = \frac{jk \exp[-jkr]}{4\pi r} \iint \left[\eta\left(-\hat{n} \times \bar{H}_{ap}\right) + \hat{r} \times \left(-\hat{n} \times \bar{E}_{ap}\right)\right] \exp\left[jk(\bar{\rho}' \cdot \hat{r})\right] ds'\,. \tag{4.10}$$

Working out the math for the two primary polarizations yields a conditional equation:

$$\bar{E}_{ff} = \frac{jk \exp[-jkr]}{4\pi r} (1 + \cos\theta) \sqrt{2\eta}\, T \begin{cases} \hat{\theta}\cos\phi - \hat{\phi}\sin\phi, & \hat{p} = \hat{x}; \\ \hat{\theta}\sin\phi + \hat{\phi}\cos\phi, & \hat{p} = \hat{y}. \end{cases} \text{ and } \bar{H}_{ff} = \hat{r} \times \frac{\bar{E}_{ff}}{\eta} \tag{4.11}$$

Note that the equation for $\bar{E}_{ff}$ shows that the $\hat{\theta}$ and $\hat{\phi}$ TEM spherical components of the far field radiated from a TEM aperture are related via sine and cosine, which is a definition of a Huygens source [86] (18), for which the Ludwig third definition of cross-polarization [87] applies. Equation (4.11) is derived in Appendix 8.1.

T in the equation for $\bar{E}_{ff}$ is defined as

$$T(\theta,\phi) = \iint Q(t,\psi)\exp\left[jk(\bar{\rho}'\cdot\hat{r})\right]ds', \tag{4.12}$$

or $$T(\theta,\phi) = \int_0^{2\pi}\int_0^1 Q(t,\psi)\exp\left[jk\left(at\cos\psi\sin\theta\cos\phi + bt\sin\psi\sin\theta\sin\phi\right)\right]abt\ dtd\psi\ . \tag{4.13}$$

Substituting

$$u(\theta,\phi) = kB(\phi)\sin\theta\,, \tag{4.14}$$

where $$B(\phi) = \sqrt{a^2\cos^2\phi + b^2\sin^2\phi}\ , \tag{4.15}$$

and $$\Phi(\phi) = \arctan\left[\left(b\sin\phi\right)/\left(a\cos\phi\right)\right]\ , \tag{4.16}$$

and noting that $u(\theta,\phi)$ is the normalized radian angle, simplifies (4.13) to

$$T(u) = \int_0^{2\pi}\int_0^1 Q(t,\psi)\exp\left[jut\cos(\psi-\Phi)\right]abt\ dtd\psi\ . \tag{4.17}$$

In order to generalize for both sum and difference patterns, Q is defined by (4.18), where $R(t) \geq 0$ and n is zero for sum patterns or unity for difference patterns. $\psi = \Delta$ is the orientation of the plane perpendicular to the aperture in which the difference pattern is intended.

$$Q(t,\psi) = R(t)\cos\left[n(\psi-\Delta)\right];\ n = 0 \text{ or } 1 \tag{4.18}$$

With the help of (3.915.2) in [88], (4.17) reduces to

$$T(u)\Big|_{n=0 \text{ or } 1} = 2\pi abj^n \cos\left[n(\Delta-\Phi)\right]\int_0^1 R(t)J_n(ut)t\,dt\,. \tag{4.19}$$

Equation (4.19) is derived in the appendix (8.27). The superscript *norm* is used to denote normalization by aperture area; *e.g.*,

$$T_S^{\text{norm}} = T_S/(\pi ab)\,. \tag{4.20}$$

The above equations specify the form of the vector far fields in spherical coordinates for a general elliptical aperture distribution *Q*. $n=0$ produces a sum pattern and $n=1$ a difference pattern. If the aperture is electrically large (yielding a pattern with a narrow beamwidth centered at $\theta=0$) then the $(1-\cos\theta)$ term, referred to as *element factor* of a Huygens source, can be neglected: In that case a study of the radiation patterns associated with various aperture distributions can focus entirely on *T*, the radiation pattern *space factor*, and that is the path taken in this analysis.

In the remainder of this chapter the properties of the space factor are studied for two distinctly different types of distributions: that for producing a radiation pattern with a main beam central peak (referred to as a sum pattern and commonly used for data communications), and also that for producing a radiation pattern with a central null (referred to as a difference pattern and typically used to detect antenna pointing error for tracking). The distribution and space factor functions associated with the sum pattern type are respectively distinguished as Q_S and T_S; whereas, those for the difference pattern type as Q_D and T_D.

4.2.3 Radiation Pattern Characteristics

In reference to the radiation patterns there are a few terms to define. A *sum* pattern has a central peak on-axis (zero angle), and a *difference* pattern has a central null. The angular width of a sum pattern's main beam at the points where the radiated power pattern drops to half its peak value is the *half-power beamwidth*, or HPBW. A radiation pattern from an aperture with uniform phase typically has *pattern nulls* at regular angular intervals off-axis. The angular distance between the two first off-axis nulls, one on each side of the axis, is the pattern's *first-null beamwidth* (FNBW). Other than the main central beam of a sum pattern — or dual off-axis main beams of a difference pattern — the sub-beams between the off-axis nulls are the *sidelobes*, and the level of the highest sidelobe in the pattern, with respect to the level of the main beam(s), is the *peak sidelobe level* (PSLL). *Taper* (or illumination) *efficiency*, e_t, is defined by (4.21), which for an aperture with uniform-phase and zero cross-polarization is the ratio of the effective radiating area to the physical area. Zero cross-polarization occurs when the aperture fields, all throughout the aperture, are all oriented in the same direction, as given in (4.5).

$$e_t = \frac{\left|\iint Q\,ds\right|^2}{A_{\text{ap}} \iint |Q|^2\,ds} \tag{4.21}$$

Equation (14) in [82] gives the taper efficiency as the ratio of the squared magnitude of the aperture-area-normalized on-axis space factor divided by the aperture-area-normalized area integral of the square of the distribution.

Aperture *directivity* is $4\pi r^2$ times the ratio of the power radiated in one direction to the total power radiated in all directions. The directivity is approximated in [82], for electrically large apertures, by (4.22), where P_{ap} is the total TEM aperture power.

$$D(\theta,\phi) \to D_0 \frac{\left|T^{\text{norm}}\right|^2}{P_{\text{ap}}^{\text{norm}}} \left(\frac{1+\cos\theta}{2}\right)^2, \tag{4.22}$$

where

$$D_0 = \pi ab \frac{4\pi}{\lambda^2}, \tag{4.23}$$

and

$$P_{\text{ap}}^{\text{norm}} = \frac{P_{\text{ap}}}{\pi ab} = \frac{\frac{1}{2}\iint \left|\bar{E}_{\text{ap}} \times \bar{H}_{\text{ap}}\right| ds'}{\pi ab} = \frac{\iint |Q|^2 \, ds'}{\pi ab}. \tag{4.24}$$

Borrowing terminology from antenna array theory, the T term in (4.11) is referred to as the radiation pattern's *space factor* [89], and the $(1+\cos\theta)$ term in (4.11) as the *element factor*, or obliquity factor, of a Huygens source [90]. The aperture-power normalized directivity pattern of an electrically large aperture (with narrow beamwidth), for sum or difference in general, is thereby approximated by $\left|T^{\text{norm}}\right|^2 / P_{\text{ap}}^{\text{norm}}$, the squared magnitude of the area-normalized space factor divided by the area-normalized aperture power.

A simple normalization is suitable to provide a basic comparison of the radiation patterns among candidate aperture distributions. Since sidelobe level with respect to the beam peak is typically one of the most significant requirements for an antenna, a suitable normalization is simply with respect to the peak of the sum pattern, so that all normalized sum patterns peak at unity (zero dB). Difference patterns, on the other hand, don't have a main beam peak: A natural alternative normalization for a difference pattern is with respect to the peak of its matching sum pattern,

which places the difference pattern's dual peaks at a level of about -2 dB. The difference patterns plotted in the figures simply normalize to the pattern peak in order emphasize the relative sidelobe levels. The matching sum pattern results from a hypothetical aperture distribution equal to the absolute value of the difference pattern's aperture distribution, and its on-axis peak value is denoted $T_{|D|}(0)$, defined in (4.25). $R_{\mathrm{D}}(t)$ is a difference pattern's radial distribution according to (4.18).

$$T_{|D|}(0) = \iint |Q_{\mathrm{D}}|\, ds' = \int_0^{2\pi} \int_0^1 R_D(t) \left|\cos(\psi - \Delta)\right| abt\, dt d\psi = 4ab \int_0^1 R_D(t)\, t\, dt \tag{4.25}$$

Equation (4.26), the taper efficiency of a difference pattern, is constructed using (4.21), (4.24), and (4.25).

$$e_{t\mathrm{D}} = \frac{\left[T_{|D|}^{\mathrm{norm}}(0)\right]^2}{P_{\mathrm{apD}}^{\mathrm{norm}}} \tag{4.26}$$

One of the most important features of the difference distribution is the slope of its radiation pattern about its central null. That slope determines the sensitivity of its detection of pointing error and is the primary coefficient in any feedback tracking control system that uses the antenna pointing error detected by this slope. Equation (4.27) represents the slope normalized by aperture area.

$$S^{\mathrm{norm}} = \left.\frac{dT_{\mathrm{D}}^{\mathrm{norm}}(u)}{du}\right|_{u=0} \tag{4.27}$$

For the purpose of comparing slopes among candidate aperture distributions it's appropriate to further normalize S^{norm} by $\sqrt{P_{\mathrm{apD}}^{\mathrm{norm}}}$ or $T_{|\mathrm{D}|}^{\mathrm{norm}}(0)$. Normalizing with respect to the square root of

the area-normalized aperture power would effectively reduce the slope by the taper efficiency; whereas, the normalization of (4.28) by the peak of the matching sum pattern sets the (dual) peaks of all difference patterns at the same level of about -2dB and so provides normalization independent of the taper efficiency. Bayliss [91] suggests comparing distributions by *relative angle sensitivity*, defined as normalizing by the maximum possible slope. The relative angle sensitivity, based on normalization by the matching sum pattern, is defined in (4.29), where $S_{\mathrm{MAX}}^{\mathrm{normT}}$ is the maximum matching-sum-pattern-normalized angle sensitivity for the class of aperture distributions in consideration.

$$S^{\mathrm{normT}} = S^{\mathrm{norm}} / T_{|\mathrm{D}|}^{\mathrm{norm}}(0) \tag{4.28}$$

$$S^{\mathrm{relative}} = S^{\mathrm{normT}} / S_{\mathrm{MAX}}^{\mathrm{normT}} \tag{4.29}$$

4.3 SUM AND DIFFERENCE PATTERNS

The terms 3PS and 3PD distinguish between a 3P distribution intended respectively for a sum and difference pattern. This section introduces the basic sum and difference patterns and then addresses the unique details of the general sum and difference patterns respectively. The distribution functions are identified, the radiation patterns developed, the asymptotic sidelobe behavior recognized, the equation for the total aperture power derived, and the limiting cases of the distributions are presented. Pareto fronts for the limiting cases describe the unique characteristics of each. For the difference pattern the normalization of the central slope is discussed, and the relative angle sensitivity derived.

4.3.1 Basic Sum and Difference Patterns

The simplest aperture distribution that produces a sum pattern is a constant, and in that case the resulting space factor T is solved with the help of [88] (5.52.1) as

$$T_S^{\text{norm}}\Big|_{Q_S=1} = 2\frac{J_1(u)}{u}. \tag{4.30}$$

The simplest elliptical aperture distribution that produces a *difference* pattern effectively involves the difference rather than the sum of the fields on either side of the aperture. Distinguishing respective sides implies the choice of a particular ϕ angle, in which phi-plane *pattern cut* the difference pattern is intended, and that angle is defined as $\phi = \Delta$. The line that divides the two halves of the aperture is at an angle perpendicular to Δ. Instead of simply negating the sign of the fields on one half of the aperture, the method given in [85] is used to create a difference pattern from a radial aperture distribution: by multiplying the radial distribution by $\cos\psi$. In this manner, the simplest example of a distribution that produces a difference pattern is a constant times $\cos\psi$, in which case (4.31) is the space factor for the resulting difference pattern, determined using [88] (6.561.1), where $\mathrm{H}_0(z)$ and $\mathrm{H}_1(z)$ are respectively the Struve functions of order zero and one.

$$T_D^{\text{norm}}\Big|_{Q_D=\cos(\psi-\Delta)} = j\pi\cos(\Delta-\Phi)\frac{J_1(u)\mathrm{H}_0(u)-\mathrm{H}_1(u)J_0(u)}{u} \tag{4.31}$$

Equation (4.31) is derived in the appendix (8.31).

4.3.2 Sum Pattern Distributions (3PS)

The 3PS distribution, introduced in [82], is defined over an elliptical aperture, depicted in Fig. 4-1. Each unique 3P distribution is represented by a triplet of parameter values: α, β and c. For the 3PS distributions these three parameters represent respectively: α) the *tail* shape, β) *steepness,* and c) *pedestal* height of the distribution. Each 3P distribution has a characteristic radiation pattern that is conveniently expressed by a modest closed-form equation. The fact that the 3P distribution has a closed-form radiation pattern equation provides faster convergence for any optimization algorithm that utilizes it: In each cycle of an iterative optimization the candidate three-parameter distribution is quickly evaluated (in closed-form) as the optimization algorithm proceeds. Without the closed-form radiation equation the far field radiation pattern of the distribution would have to be computed by numerical integration, which tends to require substantially more compute time.

The 3P sum distribution is defined in [82] as $Q(t)$ and here renamed $Q_S(t)$.

$$Q_S(t) = c + (1-c)\left(\sqrt{1-t^2}\right)^{\alpha} \frac{I_\alpha\left(\beta\sqrt{1-t^2}\right)}{I_\alpha(\beta)}, \tag{4.32}$$

where the domains of the three parameters (α, β, c) are $\alpha \geq 0$, $\beta \geq 0$, $0 \leq c \leq 1$. The far field radiation integral for the 3P sum distribution is solved in closed form using [88] (6.683.2).

$$T_{\mathrm{S}}^{\mathrm{norm}}(u) = 2c\frac{J_1(u)}{u} + (1-c)\frac{2\beta^{\alpha} J_{\alpha+1}\left(\sqrt{u^2-\beta^2}\right)}{I_\alpha(\beta)\left(\sqrt{u^2-\beta^2}\right)^{\alpha+1}} \tag{4.33}$$

Equation (4.33) is derived in the appendix (8.35). The asymptotic behavior of T_S for large u describes the level of the far-out sidelobes, and for the 3PS distribution that behavior is in (4.34). Note that for large argument, z, $J_\nu(z) \to z^{-1/2}$.

$$T_{\mathrm{S}}(u)\Big|_{u\to\infty} \to \begin{cases} u^{-3/2}, & c \neq 0; \\ u^{-3/2-\alpha}, & c = 0. \end{cases} \tag{4.34}$$

The normalization of the 3P sum distribution is discussed in [82], where the choice is made to normalize by the square root of the normalized aperture power integral. The equation for the aperture area normalized power integral is

$$P_{\mathrm{apS}}^{\mathrm{norm}} = c^2 + 4c(1-c)\frac{I_{\alpha+1}(\beta)}{\beta I_\alpha(\beta)} + \frac{(1-c)^2}{2\alpha+1}\left(1 - \frac{I_{\alpha+1}^2(\beta)}{I_\alpha^2(\beta)}\right). \tag{4.35}$$

Equation (4.35) is derived in the appendix (8.43). The limiting cases for the 3PS distribution are discussed in [82] and become the Bickmore-Spellmire distribution when $c = 0$, the parabolic 2P model when $\beta = 0$, and the 1P model when $\alpha = 0$ and $c = 0$. These three limiting cases are given respectively by (4.36), (4.37), and (4.38), and several example distributions for each case are displayed respectively in Fig. 4-2 to Fig. 4-4.

$${}_{\text{B-S}}Q_S(t) = \left(\sqrt{1-t^2}\right)^\alpha \frac{I_\alpha\left(\beta\sqrt{1-t^2}\right)}{I_\alpha(\beta)} \tag{4.36}$$

$${}_{\text{2P}}Q_S(t) = c + (1-c)\left(1-t^2\right)^\alpha \tag{4.37}$$

$${}_{\text{1P}}Q_S(t) = \frac{I_0\left(\beta\sqrt{1-t^2}\right)}{I_0(\beta)} \tag{4.38}$$

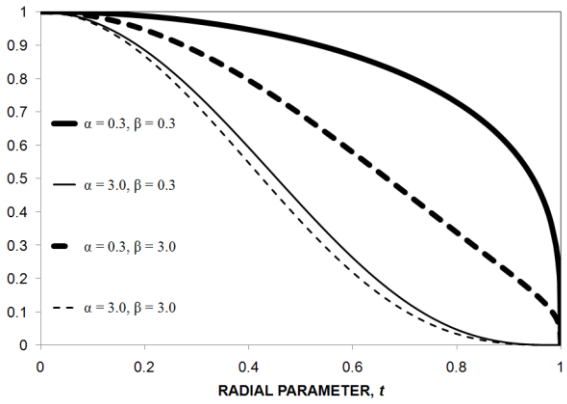

Fig. 4-2. Example distributions for 3PS limiting case of $c = 0$, reproduced courtesy of The Electromagnetics Academy [81].

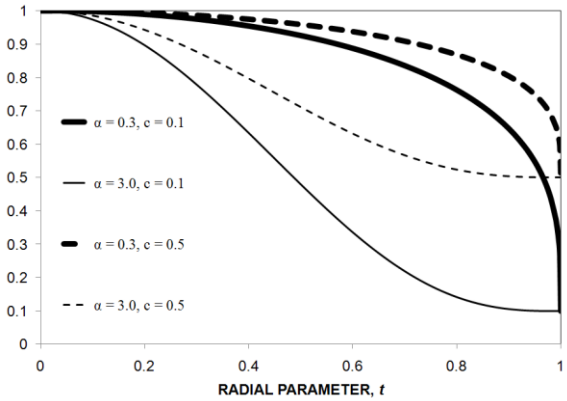

Fig. 4-3. Example distributions for 3PS limiting case of $\beta = 0$, reproduced courtesy of The Electromagnetics Academy [81].

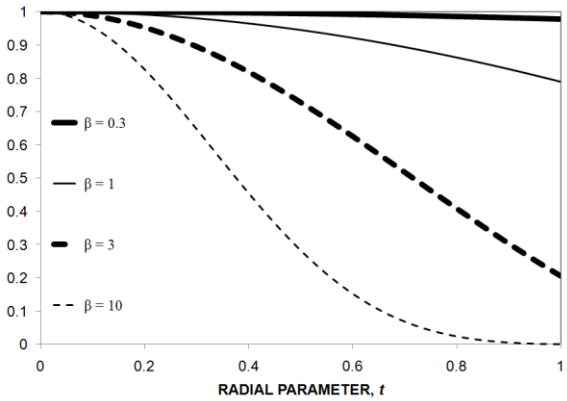

Fig. 4-4. Example distributions for 3PS limiting case of $\alpha = c = 0$, reproduced courtesy of The Electromagnetics Academy [81].

Since the broad classes of antennas that the 3P distributions apply to are mainly concerned with tradeoffs between directivity and PSLL, an appreciation of the main distinctions between the

three limiting cases can be obtained by considering the uniquely different tradeoff that each case provides between PSLL and FNBW/2, the angle (u) at which the first off-axis null occurs, which is an indirect measure of directivity. A multi-objective optimization, such as a tradeoff between PSLL and FNBW, is effectively summarized by a Pareto front [79]. Pareto fronts for the radiation patterns of these three limiting cases of the 3PS distribution are given by the perimeters of sample-population areas presented respectively in Fig. 4-5 and Fig. 4-6. The case of $c=0$ appears as essentially a fan sector and fills the region between the curves, and that of $\beta=0$ has particularly detailed features. For reduction of the radiation pattern (4.33) in the limiting case of $\beta\to 0$, note that

$$\lim_{\beta\to 0}\left[\beta^{\alpha}/I_{\alpha}(\beta)\right]=2^{\alpha}\Gamma(\alpha+1)\,. \tag{4.39}$$

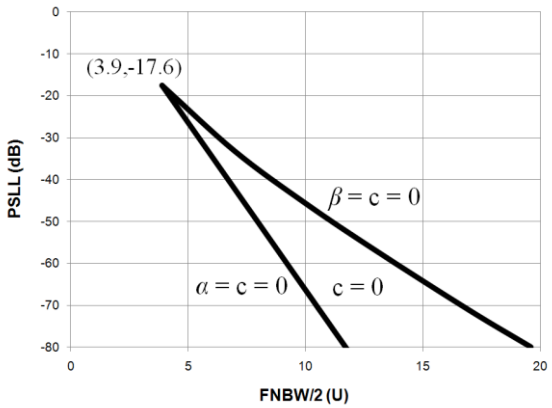

Fig. 4-5. PSLL versus FNBW/2 Pareto fronts for 3PS limiting cases of $c=0$, $a=c=0$, and $\beta=c=0$, reproduced courtesy of The Electromagnetics Academy [81].

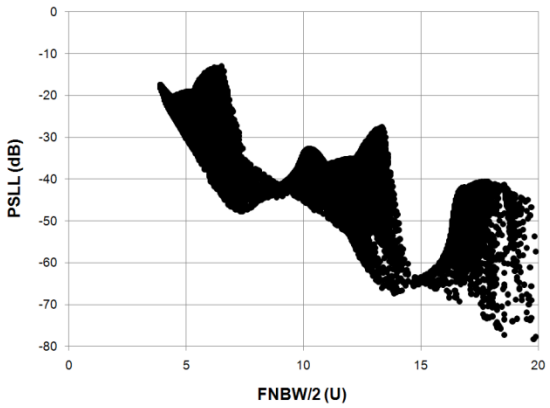

Fig. 4-6. PSLL versus FNBW/2 Pareto front for 3PS limiting case of $\beta = 0$, reproduced courtesy of The Electromagnetics Academy [81].

4.3.3 Difference Pattern Distributions (3PD)

The most commonly referenced distribution for a difference pattern appears to be that of Bayliss [91], which presents a two-parameter circular aperture distribution as an analog to the Taylor $\bar{n}$ sum distribution [90]. Section IV in [83] references the discussion in [85] of a circular Bayliss distribution based on multiplying by $\cos\psi$. This is a natural method of producing a difference pattern, judging by the fact that the higher-order mode (HE_{21}) linearly-polarized fields in the mouth of a large corrugated horn (commonly used for detecting tracking error in satellite earth stations) have the $\cos\psi$ dependence [92]. A difference pattern distribution for a line source is suggested in [93] as a complement to the 3P sum distribution in [82]. That suggestion is basically to multiply the radial $Q(t)$ distribution in [82] by t. Heeding that suggestion, along with the $\cos\psi$ factor, the 3P difference pattern distribution reviewed in this chapter for a general elliptical aperture is defined as

$$Q_{\mathrm{D}}(t,\psi) = \cos(\psi - \Delta)\left\{c + (1-c)t\left[Q_{\mathrm{S}}(t)\Big|_{c=0}\right]\right\}, \tag{4.40}$$

or
$$Q_D(t,\psi)=\cos(\psi-\Delta)\left\{c+(1-c)t\left(\sqrt{1-t^2}\right)^{\alpha}\frac{I_{\alpha}\left(\beta\sqrt{1-t^2}\right)}{I_{\alpha}(\beta)}\right\}. \tag{4.41}$$

The 3P difference pattern far field is solved using [88] (3.915.2, 6.561.1, and 6.682.2):

$$T_{\mathrm{D}}^{\mathrm{norm}}(u)=2j\cos(\Delta-\Phi)\left\{c\frac{\pi}{2u}\left[J_1(u)\mathrm{H}_0(u)-\mathrm{H}_1(u)J_0(u)\right]+(1-c)\frac{u\beta^{\alpha}J_{\alpha+2}\left(\sqrt{u^2-\beta^2}\right)}{I_{\alpha}(\beta)\left(\sqrt{u^2-\beta^2}\right)^{\alpha+2}}\right\}. \tag{4.42}$$

Equation (4.42) is derived in the appendix (8.52). The asymptotic behavior of T for large u describes the level of the far-out sidelobes, and for the 3P difference distribution that behavior is given in (4.43). This is steeper than for the sum distribution when c = 0.

$$T_{\mathrm{D}}(u)\Big|_{u\to\infty}\to\begin{cases}u^{-3/2}, & c\neq 0;\\ u^{-5/2-\alpha}, & c=0.\end{cases} \tag{4.43}$$

On-axis field strength of the matching sum pattern corresponding to the absolute value of the 3PD distribution, solved using [88] (6.683.6), is

$$T_{|D|}^{\mathrm{norm}}(0)=2\left\{\frac{c}{\pi}+(1-c)\sqrt{\frac{2}{\pi}}\frac{I_{\alpha+3/2}(\beta)}{\beta^{3/2}I_{\alpha}(\beta)}\right\}. \tag{4.44}$$

Equation (4.44) is derived in the appendix (8.58). The total aperture power in the 3PD distribution is similarly found:

$$P_{\text{apD}}^{\text{norm}} = \frac{c^2}{2} + \frac{2c(1-c)}{\beta^{3/2}}\sqrt{\frac{\pi}{2}}\frac{I_{\alpha+3/2}(\beta)}{I_\alpha(\beta)} + \frac{(1-c)^2}{2}\left[\frac{1-\frac{I_{\alpha+1}^2(\beta)}{I_\alpha^2(\beta)}}{2\alpha+1} - \frac{\beta^{2\alpha}\,{}_2F_3\left(\begin{matrix}[2\alpha+2,\alpha+1/2];\\ [2\alpha+1,2\alpha+3,\alpha+1];\\ \beta^2\end{matrix}\right)}{2^{2\alpha+1}(\alpha+1)\Gamma^2(\alpha+1)I_\alpha^2(\beta)}\right] \tag{4.45}$$

Equation (4.45) is derived in the appendix (8.64). The limiting cases for the 3PD distribution that correspond to the same aforementioned cases as for 3PS, (4.36)-(4.38), are presented in (4.46)-(4.48), and example distributions for each case are displayed respectively in Fig. 4-7 - Fig. 4-9.

$${}_{c=0}R_D(t) = t\left(\sqrt{1-t^2}\right)^\alpha \frac{I_\alpha\left(\beta\sqrt{1-t^2}\right)}{I_\alpha(\beta)} \tag{4.46}$$

$${}_{2\text{P}}R_{\text{D}}(t) = c + (1-c)\,t\left(1-t^2\right)^\alpha \tag{4.47}$$

$${}_{1\text{P}}R_{\text{D}}(t) = t\frac{I_0\left(\beta\sqrt{1-t^2}\right)}{I_0(\beta)} \tag{4.48}$$

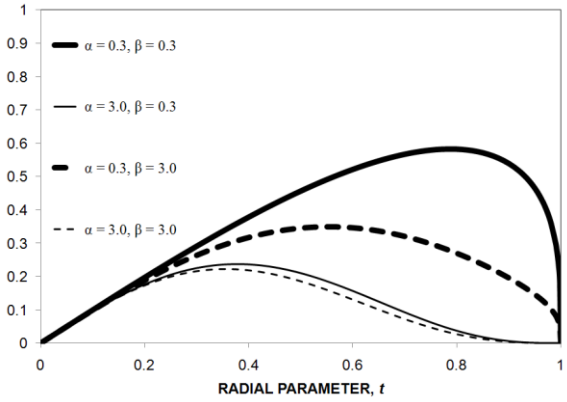

Fig. 4-7. Example distributions for 3PD limiting case of $c = 0$, reproduced courtesy of The Electromagnetics Academy [81].

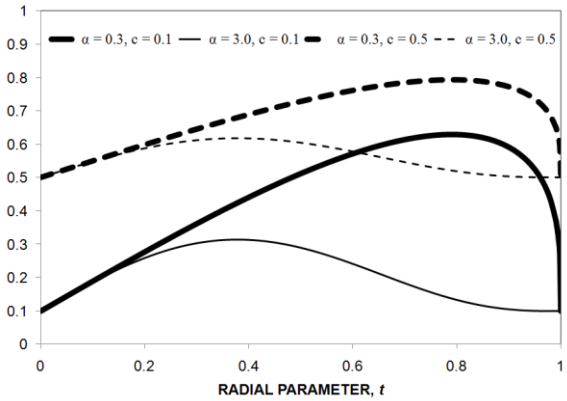

Fig. 4-8. Example distributions for 3PD limiting case of $\beta = 0$, reproduced courtesy of The Electromagnetics Academy [81].

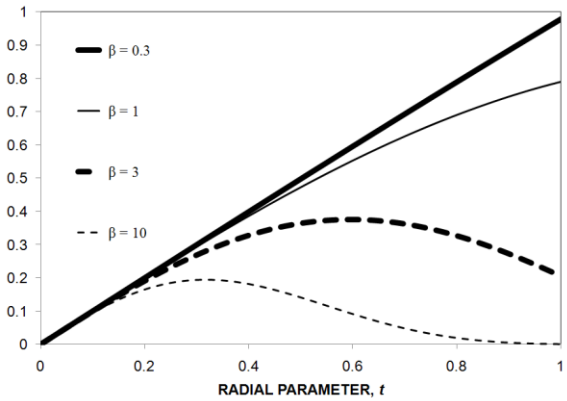

Fig. 4-9. Example distributions for 3PD limiting case of $\alpha = c = 0$, reproduced courtesy of The Electromagnetics Academy [81].

Pareto fronts that reveal the uniquely different tradeoff that each case provides between PSLL and FNBW are presented in Fig. 4-10 and Fig. 4-11. The case of $c = 0$ appears as a fan sector,

and that of $\beta = 0$ has particularly detailed features. Pareto fronts revealing the tradeoffs between PSLL and relative angle sensitivity are presented in Fig. 4-12 and Fig. 4-13. The case of $c = 0$ is similar in shape to the former set of Pareto fronts; although, in Fig. 4-12 what was in Fig. 4-10 a nearly straight fan sector is seen to be significantly curved.

$$S^{\text{norm}} = 2j\cos(\Delta - \Phi)\left\{\frac{c}{6} + \frac{(1-c)I_{\alpha+2}(\beta)}{\beta^2 I_\alpha(\beta)}\right\} \tag{4.49}$$

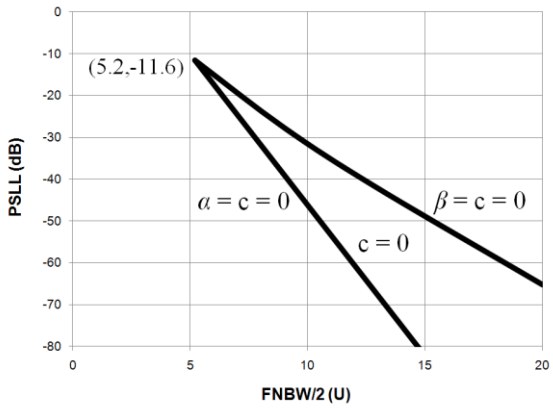

Fig. 4-10. PSLL versus FNBW/2 Pareto fronts for 3PD limiting cases of $c = 0$, $\alpha = c = 0$, and $\beta = c = 0$, reproduced courtesy of The Electromagnetics Academy [81].

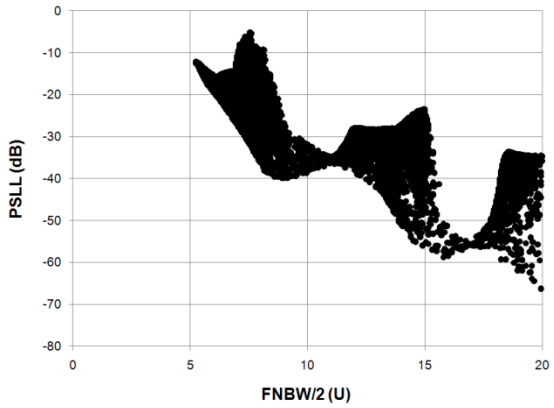

Fig. 4-11. PSLL versus FNBW/2 Pareto front for 3PD limiting case of $\beta = 0$, reproduced courtesy of The Electromagnetics Academy [81].

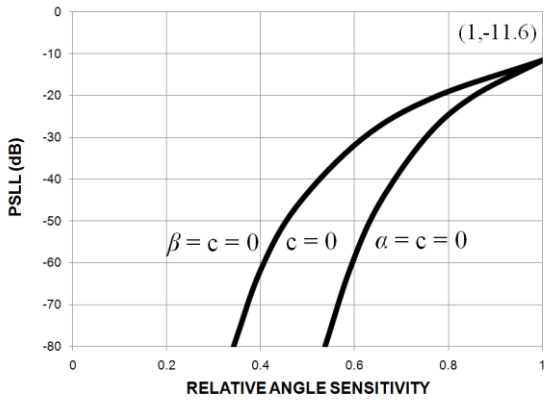

Fig. 4-12. PSLL versus relative angle sensitivity Pareto fronts for 3PD limiting cases of $c = 0$, $\alpha = c = 0$, and $\beta = c = 0$, reproduced courtesy of The Electromagnetics Academy [81].

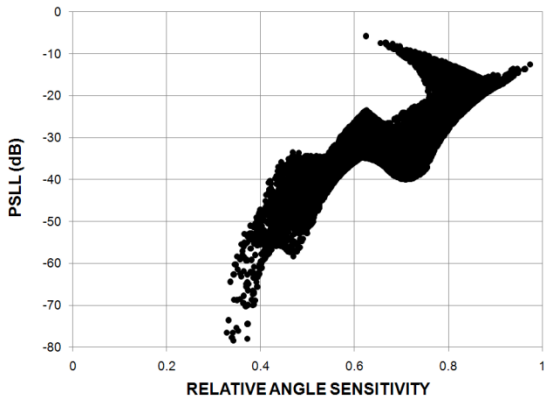

Fig. 4-13. PSLL versus relative angle sensitivity Pareto front for 3PD limiting case of $\beta = 0$, reproduced courtesy of The Electromagnetics Academy [81].

Equation (4.49) is derived in the appendix (8.75). The aperture area normalized slope of the 3PD pattern is presented in (4.49). Further normalizing by the peak of the matching sum pattern and also the maximum possible slope results in the *relative angle sensitivity* of the distribution, given in (4.51). The maximum matching-sum-pattern-normalized angle sensitivity, $S_{\mathrm{MAX}}^{\mathrm{normT}}$, for a 3PD pattern occurs in the limit as all three of the 3P parameters approach zero, in which case the 3PD distribution has a triangular shape peaking at the aperture edge.

$$S_{\mathrm{MAX}}^{\mathrm{normT}} = \frac{\lim\limits_{\alpha=\beta=c\to 0} S^{\mathrm{norm}}}{\lim\limits_{\alpha=\beta=c\to 0} T_{|D|}^{\mathrm{norm}}(0)} = \frac{\sqrt{\pi}}{2}\frac{\Gamma\left(\frac{5}{2}\right)}{\Gamma(3)} \tag{4.50}$$

$$S^{\text{relative}} = S^{\text{normT}} / \left[\frac{\sqrt{\pi}}{2} \frac{\Gamma\left(\frac{5}{2}\right)}{\Gamma(3)} \right] \tag{4.51}$$

4.4 PARTICLE SWARM OPTIMIZATION FOR 3P

The goal for the 3P distribution is to provide an antenna aperture distribution that provides specified radiation pattern characteristics, such as beamwidth, PSLL, taper efficiency, sidelobe level limit (mask) as a function of angle, and for the difference pattern: relative angle sensitivity. These characteristics are translated into a fitness function for the optimizer, which by convention the PSO minimizes. Throughout the optimization process the PSO varies the 3P parameter values automatically, within any parameter value constraints imposed on the algorithm. Convergence is faster when any of the 3P parameters are constrained to within a range known to provide the desired solution.

Several examples of the application of PSO to the 3P distributions are given. Two examples of the design of 3PS distributions by PSO are presented: maximizing aperture taper efficiency while satisfying a sidelobe mask, and minimizing the beamwidth with the peak sidelobe level (PSLL) set to a target value. A study of the sensitivity of the 3P parameter values is presented, followed by examples of 3PD distributions design by PSO for a range of PSLL constraints. An example multi-objective PSO application for the design of a corrugated horn is provided in section 5.4.

4.4.1 Example 1: 3PS Maximum Gain with a Sidelobe Mask

The first example maximizes the gain with a sidelobe constraint. Given a uniform phase aperture, which the 3P distribution assumes, maximum gain is associated with peak taper efficiency. A formal constraint for the sidelobes of a geostationary satellite ground station antenna is the FCC 25.209 mask [94], which starts at 1.5 deg from beam peak with sidelobe directivity constraint of twenty-nine decibels isotropic gain minus twenty-five decibels times the base ten logarithm of the pattern angle in degrees (for conventional Ku- or Ka-band geostationary service ground stations). The conditional fitness function which PSO minimizes for this example is

$$\text{fitness\_12} = \begin{cases} -e_t, & \text{if all sidelobes below the mask;} \\ 999, & \text{otherwise.} \end{cases} \tag{4.52}$$

If any sidelobe exceeds the mask then the candidate 3P distribution is deemed out-of-bounds and discarded with a very large fitness value. This out-of-bounds treatment is the same as how search agents that wander outside an acceptable range of parameter values can be dealt with in the PSO algorithm by applying *invisible boundaries* [72]. Fig. 4-14 shows the 3P distribution and radiation pattern from this PSO run, which yields 3P parameter values of alpha = 1.9389, beta = 1.6928, and c = 0.5581. The locus of the sidelobe peaks is seen to follow the mask, and a 96.6% taper efficiency is achieved with an aperture diameter of 68 wavelengths.

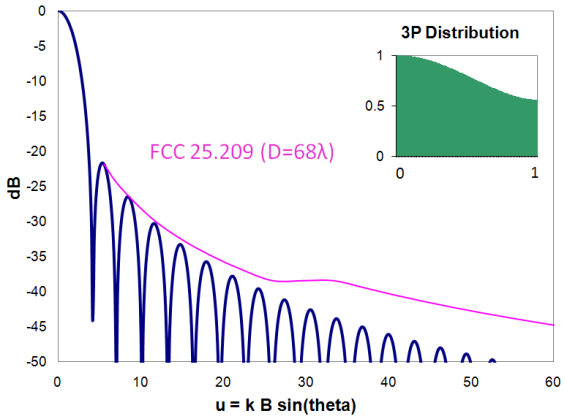

Fig. 4-14. PSO 3PS radiation pattern achieving maximum taper efficiency while also meeting a sidelobe mask, reproduced courtesy of The Electromagnetics Academy [81].

4.4.2 Example 2: 3PS Minimum Beamwidth with Specified PSLL

The second example provides a 3P antenna aperture distribution that achieves a radiation pattern with sidelobe level (PSLL) less than –30 dB peak while minimizing beamwidth. For this example the fitness function is the square of the difference between the PSLL and the goal, in dB, plus the angle, *u*, of the first null.

$$\text{fitness\_13} = \left(\text{PSLL} - \text{goal}\right)^2 + \text{FNBW}/2\,, \tag{4.53}$$

where the PSLL goal is -30 dB peak. The 3P parameters produced by one PSO run meeting these constraints are alpha = 2.002, beta = 2.877, and c = 0.306, and the resulting radiation pattern and 3P distribution are shown in Fig. 4-15. This figure also superimposes (light shading) the uniform-amplitude aperture radiation pattern for comparison — in which case the sidelobes would be considerably higher than that provided by the optimized 3P distribution.

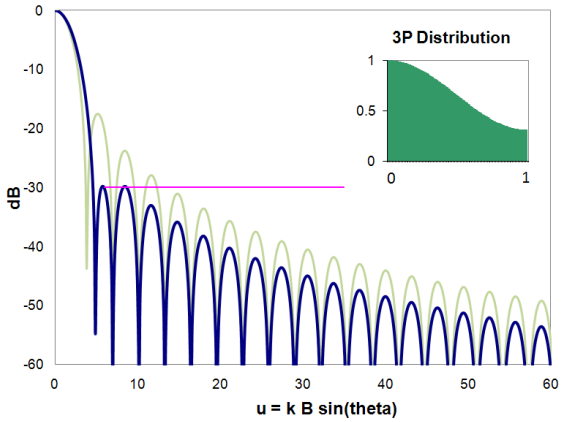

Fig. 4-15. PSO 3PS distribution and radiation pattern achieving PSLL of -30 dB peak with minimum beamwidth, reproduced courtesy of The Electromagnetics Academy [81].

4.4.3 Example 3: 3PS Family of PSO Solutions

PSO typically yields a family of solutions, the family of which is related to a Pareto front. Fig. 4-16 shows such a family, with a PSLL of -40 dB. The selected family of solutions is: 1) alpha = 2.2390, beta = 0.5625, c = 0.139, 2) alpha = 1.2196, beta = 3.7930, c = 0.1015, and 3) alpha = 0.6207, beta = 4.5970, c = 0.0757. This family represent only three of many PSO solutions that were found to meet the given requirements, and these three were chosen because of the substantial variation in their alpha parameter values, to show that the combination of a high alpha value and low beta value can provide a similar distribution as the combination of a low alpha value and high beta. There is little difference between the distributions of each of these family members, as the inset distribution shows (since they all meet the same design requirements). The fitness function is given by (4.53).

4.4.4 Example 4: 3P Pattern Sensitivity to Variation of Parameter Values

A practical design must account for implantation error, and so a sensitivity analysis was conducted to determine how sensitive the 3P distribution might be to variations in each of the

parameter values. The first PSO family member 3PS solution in Fig. 4-16 is used as the basis for the parameter sensitivity analysis. Fig. 4-17 shows that a 10% variation in the alpha parameter value can cause as much as 5-10 dB variation in the level of the first sidelobe. Fig. 4-18 shows that the beta parameter value is the least sensitive to variation of its value: Only a few dB variation in the level of the first sidelobe level result from a significant variation in the beta value from -100% to +300%. Fig. 4-19 shows that the 3P *c*-parameter has intermediate sensitivity. The level of the first sidelobe level varies several dB with a 10% variation in the value of the c-parameter value. The corresponding variations in 3PD patterns are comparable to those given here for 3PS.

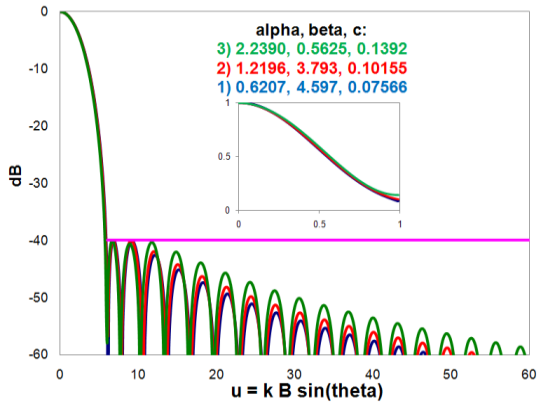

Fig. 4-16. PSO 3PS distributions and radiation patterns for a family of PSO solutions all achieving PSLL of -40 dB peak with minimum beamwidth, reproduced courtesy of The Electromagnetics Academy [81].

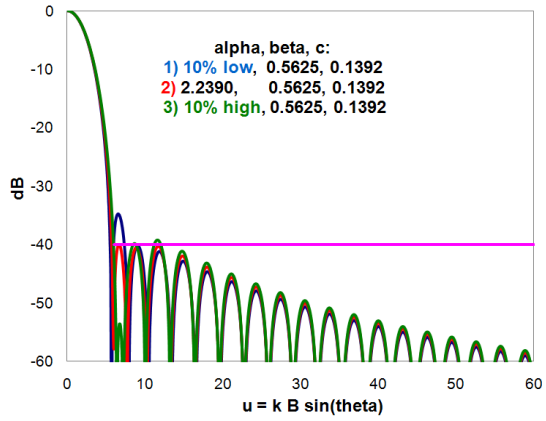

Fig. 4-17. PSO parameter sensitivity, showing variation of radiation pattern when only the 3PS α parameter value is changed from the PSO solution value by ±10%, reproduced courtesy of The Electromagnetics Academy [81].

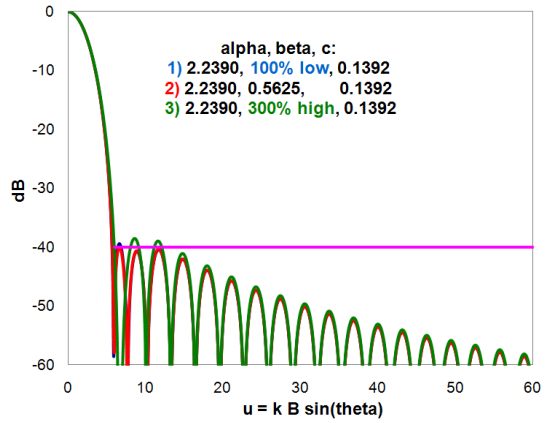

Fig. 4-18. PSO parameter sensitivity, showing variation of radiation pattern when only the 3PS β parameter value is changed by -100% and +300%, reproduced courtesy of The Electromagnetics Academy [81].

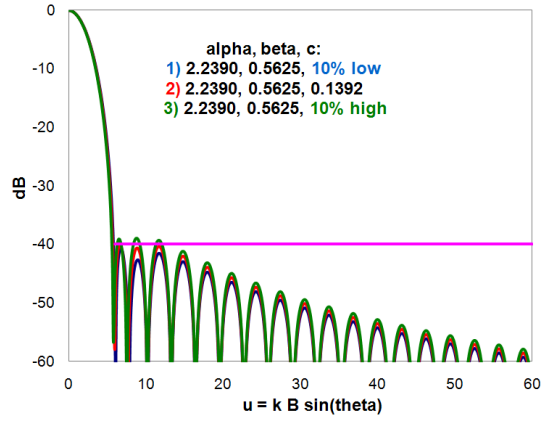

Fig. 4-19. PSO parameter sensitivity, showing variation of radiation pattern when only the 3PS c parameter value is changed from the PSO solution value by ±10%, reproduced courtesy of The Electromagnetics Academy [81].

4.4.5 Examples 5-7: 3PD Maximum Angle Sensitivity with Specified PSLL

PSO examples are presented in Fig. 4-20 - Fig. 4-22 for 3PD distributions with PSLL design goals of respectively -30, -48 and -55 dB, while simultaneously maximizing the relative angle sensitivity, using the fitness function of (4.54). The 3P parameter values for Fig. 4-20 are alpha = 1.9949, beta = 0.0194, and c = 0.0804, in which case a relative angle sensitivity of 79% is achieved with -30 dB PSLL. Those for Fig. 4-21 are alpha = 2.3292, beta = 1.3064, and c = 0.0460, in which case a relative angle sensitivity of 75% is achieved with -38 dB PSLL. The 3P parameter values for Fig. 4-22 are alpha = 0.0318, beta = 8.3484, and c = 0.0031, in which case a relative angle sensitivity of 67% is achieved with -55 dB PSLL. The 3PD distribution can meet even considerably deeper PSLL limits than given by these examples, indicated by Fig. 4-10. These optimal multi-objective solutions are typically found on the edge of a Pareto front. Bayliss [91] reveals that for a difference pattern to realistically achieve maximum relative angle sensitivity with a given maximum PSLL requires that its first sidelobes be of uniform level, and Fig. 4-20 - Fig. 4-22 show that the 3PD distributions determined by PSO with those constraints have that very characteristic.

$$\text{fitness\_16} = \begin{cases} -(\text{relative angle sensitivity}), & \text{if PSLL} \le \text{goal}; \\ 999, & \text{otherwise.} \end{cases} \tag{4.54}$$

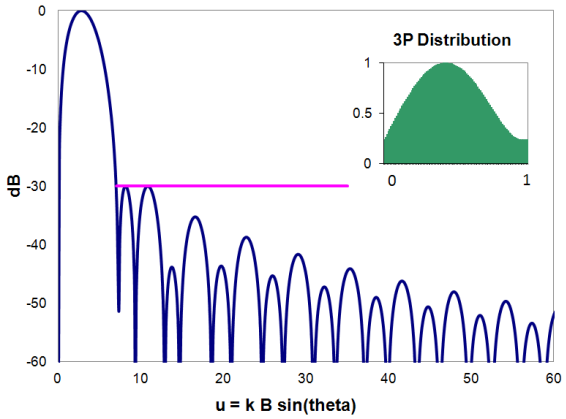

Fig. 4-20. PSO 3PD designed for -30 dB PSLL and maximum relative angle sensitivity. The inset 3PD distribution is shown normalized to its peak height, reproduced courtesy of The Electromagnetics Academy [81].

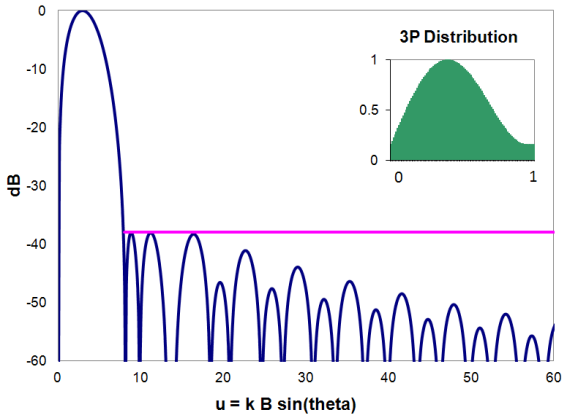

Fig. 4-21. PSO 3PD designed for -38 dB PSLL and maximum relative angle sensitivity. The inset 3PD distribution is shown normalized to its peak height, reproduced courtesy of The Electromagnetics Academy [81].

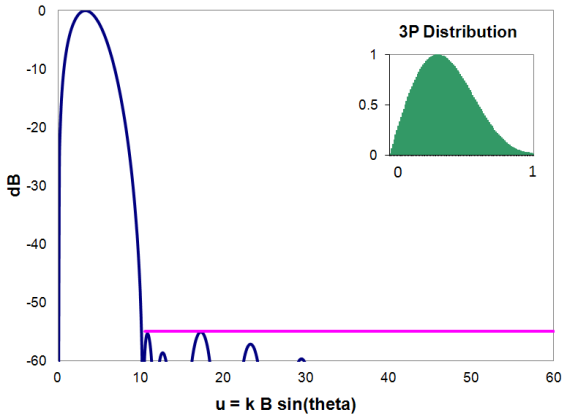

Fig. 4-22. PSO 3PD designed for -55 dB PSLL and maximum relative angle sensitivity. The inset 3PD distribution is shown normalized to its peak height, reproduced courtesy of The Electromagnetics Academy [81].

4.5 CONCLUSION

The 3P distribution is presented for both sum and difference patterns in the context of providing a versatile amplitude distribution model of for an entire class of uniform-phase elliptical antenna apertures. Analytical closed form equations for several characteristics of a general 3PS or 3PD distribution were derived: the far field radiation pattern, taper efficiency, aperture power, asymptotic sidelobe level, and for the 3PD also the relative angle sensitivity. The PSO algorithm was discussed, and references for other metaheuristic optimization methods were given. Several examples of designing 3P distributions by PSO demonstrate that the 3P distribution can meet a range of real-world design constraints. The PSO algorithm converges to a solution in each case with different 3P antenna aperture design constraints. Radiation patterns and distributions for a family of solutions which all satisfy the same requirements were presented, and the sensitivity of each of the 3P parameter values was investigated. The PSO optimized 3P patterns meet peak sidelobe, taper efficiency, and sidelobe mask requirements. The PSO optimized 3P patterns display the ideal characteristic of uniform close-in sidelobe levels when in addition to constraining the optimization by a specified PSLL it is also additionally constrained by maximum taper efficiency, in the case of a sum pattern, or by maximize angle sensitivity in the case of a difference pattern. The versatility of the 3P distribution and PSO's utility as a metaheuristic optimizer combine to provide customized aperture distributions for a versatile range of applications. Material in this chapter has been previously published by the author [81].

CHAPTER 5 CORRUGATED FEEDHORN PATTERNS

Corrugated feedhorns are commonly incorporated into commercial satellite antenna terminals — large Earth-stations that control the satellites, as well as mid-size stationary and portable terminals used for regional communications with the satellite, and of course the small roof-mounted satellite dishes currently used for residential satellite television reception. The corrugated horn provides a high level of polarization purity, beamwidth control, and low loss that contributes to high receive sensitivity. This chapter discusses three methods of calculating the radiation pattern of a corrugated horn, in order of increasing computational complexity: aperture field, spherical wave expansion, and mode matching.

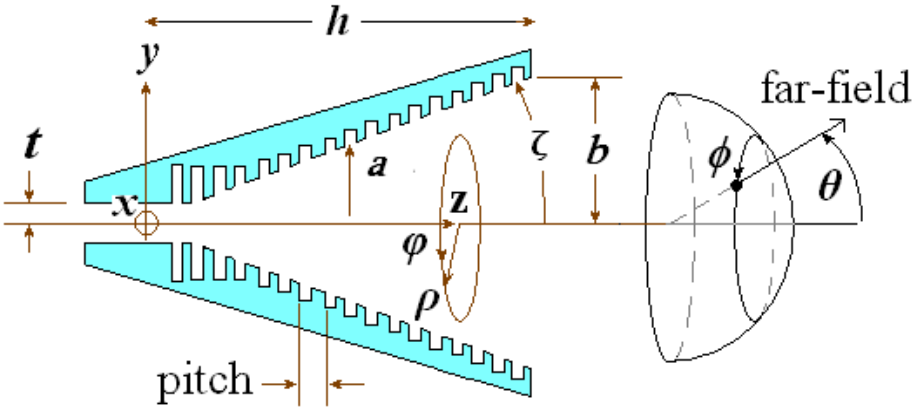

Fig. 5-1. Corrugated-conical horn parameters ($\varphi = \phi = 0$ on positive x-axis), reproduced courtesy of The IEEE [92].

Table 5-1. Far field estimation methods in order of accuracy and computational complexity, reproduced courtesy of The IEEE [92].

1	Aperture Integration (uniform-phase) Closed-form evaluation of (5.15)
2	Aperture Integration augmented by radial phase Numerical integration of (5.14)
3	Spherical Wave Expansion (SWE) Conical surface impedance boundary model (Described in section 9.4.3 of [95].)
4	Numerical Model of corrugated horn geometry Cylindrical mode matching of internal fields, accounting for all corrugations Integral equation, method of moments solution for horn exterior currents

The corrugated horn is typically excited with pure TE_{11} mode at its throat and designed to radiate HE_{11} mode in the horn aperture. These modes are depicted below. Through the length of the corrugated horn the TE_{11} mode ideally gradually transforms into the HE_{11} mode, and a good mode converter jumps from smooth waveguide to approximately half-wave depth corrugations, then gradually reduces the corrugation depth to quarter-wave depth. The characteristic equation, given below in (5.1), where $-E_Z / H_\varphi = j\eta_0 X_{RZ}$, is defined by the boundary conditions of zero φ component of the electrical field at the corrugation wall, and a normalized corrugated wall impedance, X_{RZ}, as seen by a wave with Poynting vector directed perpendicular to and into the corrugated wall.

$$X_{RZ}\left\{\left[\frac{J_n(\gamma a)}{\gamma a}\right]^2\left[1-\left(\frac{\gamma a}{\beta_0 a}\right)^2\right]n^2-\left[J_n'(\gamma a)\right]^2\right\}=\frac{\gamma a}{\beta_0 a}J_n(\gamma a)J_n'(\gamma a) \tag{5.1}$$

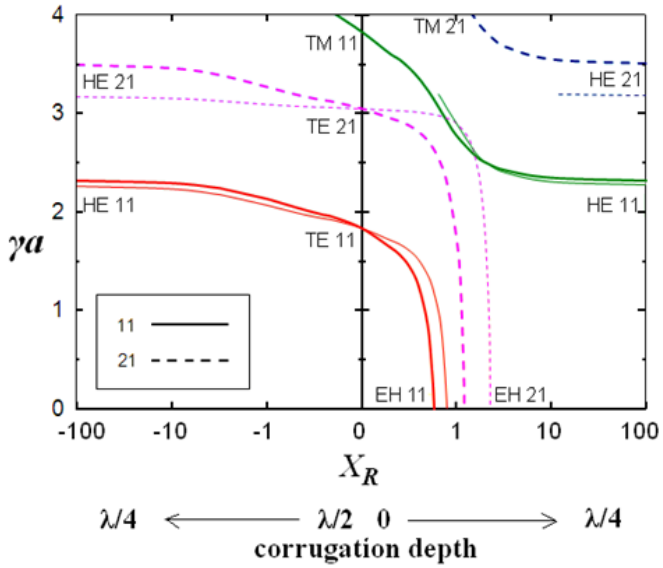

Fig. 5-2. Characteristic Equation Roots for Corrugated Cylindrical Waveguide as a Function of Corrugation Depth.

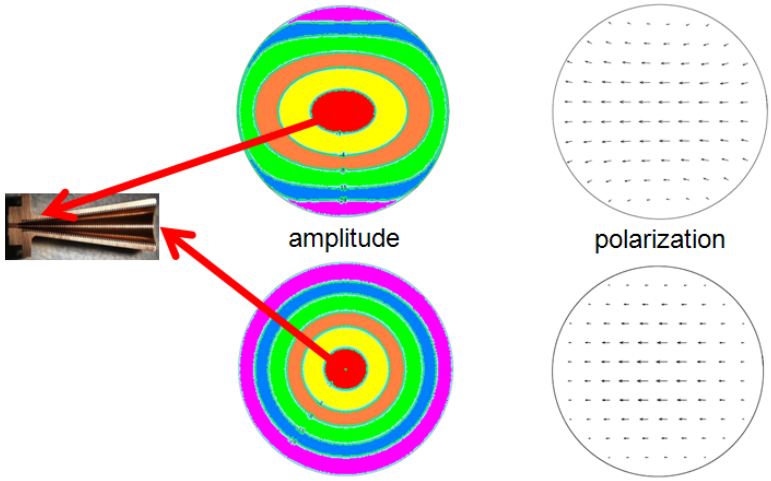

Fig. 5-3. Pure Field Modes at Input (Fig top) and Output (Fig bottom) of Corrugated Horn.

An approximation of the far field radiation pattern of the corrugated-conical horn, by integration of the aperture field, augmented with perimeter-matched quadratic radial phase, is sufficient to establish a baseline design for the feedhorn of a satcom antenna system. The approximated far field patterns compare well to more formal analysis methods, even reasonably so in the main beam with a semi-flare angle as wide as 45 deg for the first two angular modes. The field equations are presented in a compact complex exponential form, from which the components

corresponding to excitation with any polarization sense may be obtained (either sense of circular/elliptical polarization or linear polarization with arbitrary orientation).

5.1 APERTURE FIELD

Aperture field integration provides a rapid means of estimating a feed pattern when the aperture field consists of pure modes, in which case those modes can be integrated in closed-form and the resulting equations evaluated rapidly. An example of such a case is the corrugated horn.

5.1.1 Introduction

Using aperture field with quadratic phase is a popular method for smooth-walled conical and rectangular horns, for far field pattern estimation, and here we investigate the utility of this method for corrugated horns. A simple means for quickly obtaining a reasonable approximation of the far field patterns can be quite valuable for a proposal or project planning. Corrugated-conical horns are commonly used in reflector antenna systems for microwave communication systems, and the design of these systems requires that the performance of the horns be understood reasonably well. Having a low-cost means, with negligible learning curve, of approximating feedhorn performance is useful, at least for planning purposes. Several methods have been investigated for such approximations and are compared in this chapter. Olver, Clarricoats, Kishk and Shafai [95] suggest using aperture field integration with first-order (Taylor) quadratic radial phase – a first-order approximation of the spherical phase implied by the conical flare. We refer to that method as first-order quadratic radial phase (FOQRP). This chapter investigates an alternative quadratic phase function, *perimeter-matched* quadratic radial

phase (PMQRP), which provides an improved approximation of the radiation pattern, especially so for wider flare angles. The prior work apparently presumed small flare angle and did not distinctly consider the PMQRP variation of the quadratic radial phase approximation.

In this section, the basic method of far field determination by far field vector potential is summarized, and we present the results of the PMQRP approximation method for 12 and 45 deg half-flare, conical-corrugated horns for both first and second angular modes. We compare the approximation with more formal methods of analysis, summarized in Table 1.

Analysis of corrugated horns has a rich background. The literature [6], [95]–[124] presents a vast collection of articles on corrugated horns from a variety of perspectives. Minnett and Thomas [96], [97] and [103], Jansen, Jeuken and Lambrechtse [102], James [105], and Clarricoats, Saha, Olver, Kishk and Shafai [98], [99], [107] and [95] address fundamentals. Love [101] offers a full collection of papers on the subject. Sakr [119] presents closed form radiation patterns for uniform-phase aperture, Sinton, Robinson and Ramat-Samii [120] addresses optimized horn profile design, Granet and James [121] overview the general design and Lee [122] addresses field modes and dispersion. In [95], with their Fig. 6.1 and (6.9) and (9.6), Olver, Clarricoats, Kishk and Shafai suggest the use of aperture integration with quadratic phase. They specify use of a first-order quadratic radial phase (FOQRP) function – a 1st term Taylor approximation of the spherical phase function that's implied by the cone that fits inside the horn – to represent the affect of the flare. We consider an alternative PMQRP function instead and find that it yields better main bean pattern estimation, especially for wider flares and for both of the first two angular modes.

This section focuses on the approximation of the circularly polarized (CP) far fields by aperture field integration augmented by quadratic phase. Typically with smooth-walled horns the aperture mode is assumed to be the same as that which excites the horn; although, with corrugated horns the aperture mode is different than the excitation mode. We presume that the corrugated horn has a well designed mode converter (e.g., half-wave depth corrugations at throat tapering to quarter-wave depth in the flare) so that balanced hybrid HE mode dominates in the aperture. Note [110] that the 45 deg half-flare horn can be matched without increasing the depth of the corrugations from quarter wavelength.

We present results from four different analysis methods, identified in Table 1, and find that adding PMQRP to the balanced HE aperture field yields far fields for the main beam in good agreement with more formal analysis methods. This aperture integration analysis effectively models the corrugated-conical horn as a stepped cone consisting of short sections cylindrical waveguide, with general radius a, each supporting a single cylindrical mode. The cylindrical field distributions of the balanced hybrid modes are addressed, and the far field radiation patterns are derived by aperture integration, augmented by radial quadratic phase, and compared with far field patterns determined by Clarricoats' spherical wave expansion (SWE) method for conical horns, as well as cylindrical mode matching (CMM) of the detailed internal geometry of the corrugated horn with integral equation (IE) method of moments solution for the surface currents on the horn exterior.

Both the hybrid HE_{11} and HE_{21} modes are addressed. Corrugated horn HE_{11} radiation patterns are efficient for dual shaped reflector designs where circular symmetry and precise edge illumination control are critical. HE_{21} patterns provide similar efficiency for difference patterns

for single channel monopulse auto-tracking feeds for large ground antennas. All higher angular modes HE_{n1} , n >1, provide an on-axis pattern null; although, HE_{21} uniquely provides tracking error detection in two orthogonal axes, which are typically aligned with the antenna positioner's elevation and cross-elevation axes.

The field equations use rotational polarization (L or R), since this allows compact, general forms. The fields corresponding to linearly polarized excitation are obtained by linear combination of the two senses of rotational polarization.

5.1.2 Aperture Field Radiation Integral

5.1.2.1 Amplitude

Corrugated horns propagate hybrid field modes, and hybrid field modes involve simultaneous propagation of both TEz and TMz modes. Hybrid modes are designated $HE_{nm,}$ or $EH_{nm,}$ where the first index, n, is the angular mode index and represents the number of field cycles for every physical rotation in φ angle, and m is the radial mode index (m^{th} Bessel root), representing the number of field cycles along the radial extent of the waveguide. The HE mode is the sum of TE+TM modes, and the EH mode is their difference, TE–TM.

A well-designed corrugated horn establishes the balanced HE_{11} mode at the horn aperture (and also balanced HE_{21} mode if used for tracking.) Note that a dispersion diagram concerning these modes is presented on page 27 of [107]. The balanced hybrid HE_{11} mode provides purely linearly-polarized transverse fields across the entire aperture, and involves the vector potential amplitudes being related simply through the free-space wave impedance {(10) in [96]}. At the

corrugation boundary the balanced HE fields have only an axial component. What uniquely characterizes the balanced hybrid mode condition is that the E and H vector fields have exactly the same form but with one rotated (90/n) deg in φ from the other, where n is the angular mode index {discussion of Fig. 3(d) in [106]}. This balanced hybrid mode condition naturally occurs well above cutoff with quarter-wavelength corrugation, both of which are typical at the radiating aperture of a large, corrugated horn. Equations (5.2)–(5.5) define the balanced hybrid HE transverse aperture mode fields. To simplify (5.2)–(5.5) the phasor exp[$\pm jn\varphi$] is excluded, where the + corresponds to RCP and minus to LCP, in addition to the $\exp[j\omega t]$ time- and $\exp[-jk_z z]$ axial-propagation phasors. J_ν is the cylindrical Bessel function of the first kind of order ν.

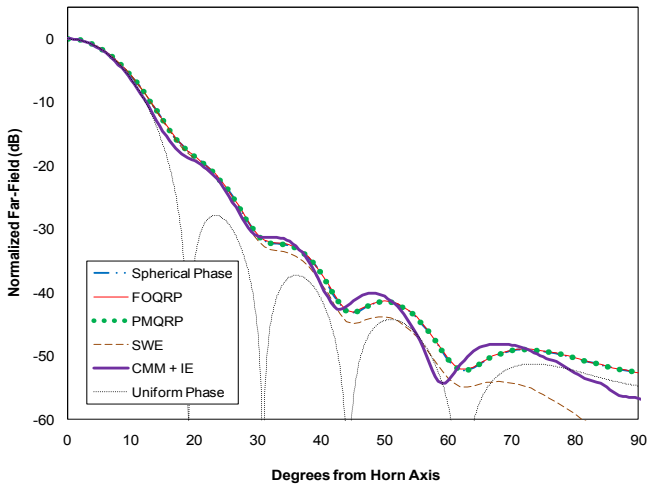

Fig. 5-4. 12-deg half-flare angle HE11 CP co-pol far field by integration of aperture fields augmented by radial phase (22.2 dBi), SWE (22.30 dBi), and cylindrical MM+IE (TICRA CHAMP) numerical modeling of the corrugated horn geometry (22.62 dBi) with 33 corrugations (including 5 in mode converter with linear depth profile), $\beta_0 b = 16.9$, $\beta_0 t = 4.21$, and pitch $\approx \lambda/3$. Excitation is CP TE_{11}. Fig. reproduced courtesy of The IEEE [92].

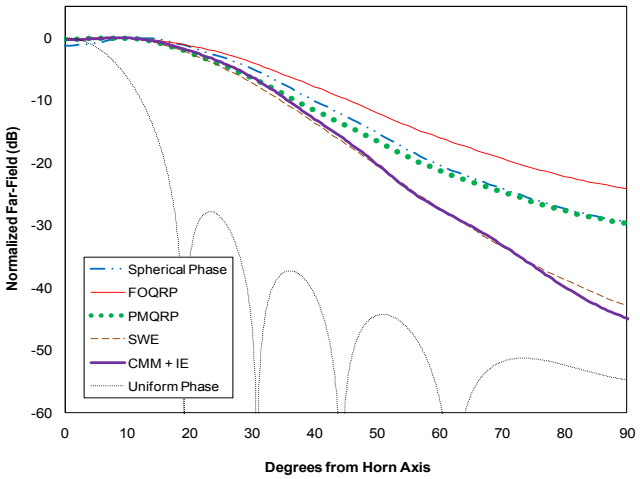

Fig. 5-5. 45-deg half-flare angle HE11 CP co-pol far field by integration of aperture fields augmented by radial phase, SWE (peak 13.54 dBi), and cylindrical MM+IE (TICRA CHAMP) numerical modeling of the corrugated horn geometry (13.12 dBi) with 11 corrugations (including 5 in mode converter with linear depth profile), $\beta_0 b = 16.9$, $\beta_0 t = 4.21$, and pitch $\approx \lambda/5$. Excitation is CP TE_{11}. Fig. reproduced courtesy of The IEEE [92].

$$E_{\rho}^{\mathrm{BAL}} = -(\pm j)(\gamma_{\mathrm{nm}} / \varepsilon)\, J_{n-1}(\gamma_{\mathrm{nm}}\rho) \quad \begin{matrix}\mathrm{L}\\ \mathrm{R}\end{matrix} \tag{5.2}$$

$$H_{\rho}^{\mathrm{BAL}} = -\left(\eta_0 \gamma_{\mathrm{nm}} / \mu\right) J_{n-1}(\gamma_{\mathrm{nm}}\rho) \tag{5.3}$$

$$E_{\varphi}^{\mathrm{BAL}} = +(\gamma_{\mathrm{nm}} / \varepsilon)\, J_{n-1}(\gamma_{\mathrm{nm}}\rho) \tag{5.4}$$

$$H_{\varphi}^{\mathrm{BAL}} = -(\pm j)\left(\eta_0 \gamma_{\mathrm{nm}} / \mu\right) J_{n-1}(\gamma_{\mathrm{nm}}\rho) \quad \begin{matrix}\mathrm{L}\\ \mathrm{R}\end{matrix} \tag{5.5}$$

For the balanced hybrid HE mode the transverse fields relate as

$$E_{\rho} = \pm j\eta_0 H_{\rho} = -(\pm j) E_{\varphi} = \eta_0 H_{\varphi}. \quad \begin{matrix}\mathrm{L}\\ \mathrm{R}\end{matrix} \tag{5.6}$$

The balanced EH modes have the same magnitudes of field coefficients but different signs and with Bessel order $n+1$. The boundary conditions of quarter-wave corrugation on the total fields at the mouth of a large horn aperture, where the balanced hybrid modes are supposed to exist, yield the propagation roots of the characteristic given in (5.7) and (5.8).

$$\gamma_{11} = 2.405 / b, \text{ from } J_0(\gamma_{11} b) = 0 \ \left(\mathrm{HE}_{11} \text{ mode}\right) \tag{5.7}$$

$$\gamma_{21} = 3.832 / b, \text{ from } J_1(\gamma_{21} b) = 0 \ \left(\text{HE}_{21} \text{ mode}\right) \tag{5.8}$$

5.1.2.2 Phase Approximations

In the aperture plane ($z = h$), the radial dependence of the phase, $\chi(\rho)$, of a spherical wave that originates at the apex of the cone, marked by a circled cross in Fig. 5-1, is

$$\chi(\rho) = \beta_0 \left[r(\rho) - r(0) \right], \tag{5.9}$$

$$r(\rho) = \sqrt{h^2 + \rho^2}\,, \tag{5.10}$$

and h is the height of the cone, as indicated in Fig. 5-1. $\chi(\rho)$ is fairly well approximated as a quadratic function,

$$\chi(\rho) \approx u(\rho / b)^2 \tag{5.11}$$

where b is the aperture radius. u represents the quadratic phase at the perimeter of the aperture and is defined, respectively for the two different quadratic functions, as

$$\begin{aligned} u_1 &= \tfrac{1}{2} \beta_0 b \tan\varsigma, && \text{FOQRP;} \\ u_2 &= \beta_0 b \cot\varsigma \left(\sec\varsigma - 1\right), && \text{PMQRP.} \end{aligned} \tag{5.12}$$

ζ is the half-flare angle of the horn. With PMQRP, u is the difference in electrical length between the slant and axial lengths of the cone that fits inside the horn, and thereby matches the spherical and quadratic phase functions at the aperture perimeter. FOQRP effectively matches the spherical and quadratic phase functions only for small ρ values.

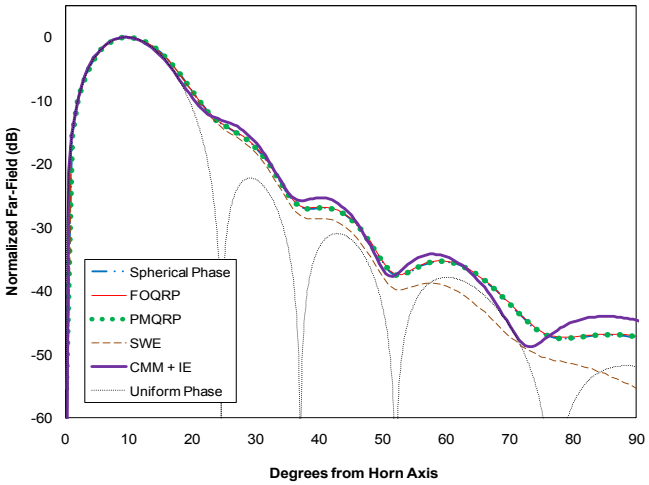

Fig. 5-6. 12-deg half-flare angle HE21 CP co-pol by integration of aperture fields augmented by radial phase (peak 17.1 dBi), SWE (peak 17.19 dBi), and cylindrical MM+IE (MICIAN μWave Wizard) numerical modeling of the corrugated horn geometry (peak 17.17 dBi) with 33 corrugations (including 5 in mode converter with linear depth profile), $\beta_0 b = 16.9$, $\beta_0 t = 4.21$, and pitch $\approx \lambda/3$. Excitation is CP TE21. Fig. reproduced courtesy of The IEEE [92].

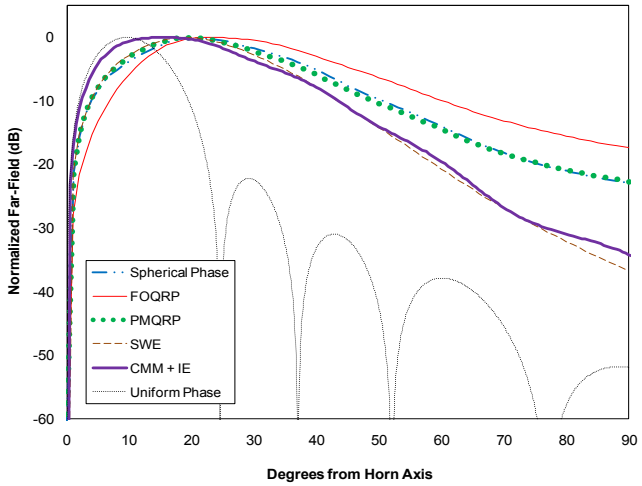

Fig. 5-7. 45-deg half-flare angle HE21 CP co-pol by integration of aperture fields augmented by radial phase, SWE (peak 10.63 dBi), and cylindrical MM+IE (MICIAN μWave Wizard) numerical modeling of the corrugated horn geometry (peak 11.54 dBi) with 11 corrugations (including 5 in mode converter with linear depth profile), $\beta_0 b = 16.9$, $\beta_0 t = 4.21$, and pitch $\approx \lambda/5$. Excitation is CP TE21. Fig. reproduced courtesy of The IEEE [92].

5.1.2.3 Radiation Integral

The far field radiation patterns are estimated by far field vector potentials. The radiated field vector potentials are obtained by integration of the equivalent aperture currents, and we combine the fields due to both the electric and magnetic currents to represent a free-standing aperture with

neither an electric nor a magnetic ground plane. In the far field the vector potentials are proportional to the radiated fields.

The balanced HE mode, far field radiation aperture-integral, including a radial phase term, exp[$j\xi(\rho')$], is given in (5.14). Averaging the far fields due to equivalent electric and magnetic currents for the aperture fields causes the factor of (1+cosθ) / 2. The second Bessel function in (5.14) results from the φ integral, which is done analytically.

$$\xi(\rho') = \begin{cases} \chi(\rho'), & \text{spherical phase;} \\ u(\rho'/b)^2, & \text{quadratic phase.} \end{cases} \tag{5.13}$$

$$\begin{aligned} \mathrm{E}_\phi &= \pm j\,\mathrm{E}_\theta \left\{ \begin{smallmatrix} \mathrm{L} \\ \mathrm{R} \end{smallmatrix} \right\} \\ &= \frac{\gamma\beta_0}{\varepsilon}\left(\frac{\exp[-j\beta_0 r]}{r}\right)\frac{1+\cos\theta}{2} \\ &\cdot \int_0^b J_{n-1}(\gamma\rho')J_{n-1}(\beta_0\rho'\sin\theta) \\ &\cdot \exp\left[j\xi(\rho')\right]\rho' d\rho' \\ &\cdot \exp[\pm jn\phi]j^n \qquad \begin{smallmatrix} \mathrm{L} \\ \mathrm{R} \end{smallmatrix} \end{aligned} \tag{5.14}$$

$$\begin{aligned} \mathrm{E}_\phi^{\,\mathrm{UNIFORM}} &= \pm j\,\mathrm{E}_\theta \left\{ \begin{smallmatrix} \mathrm{L} \\ \mathrm{R} \end{smallmatrix} \right\} \\ &= \frac{\gamma\beta_0}{\varepsilon}\left(\frac{\exp[-j\beta_0 r]}{r}\right)\frac{1+\cos\theta}{2} \\ &\cdot \gamma b^3 J_{n-2}(\gamma b) \\ &\cdot \frac{J_{n-1}[\beta_0 b\sin\theta]}{(\beta_0 b\sin\theta)^2-(\gamma b)^2} \\ &\cdot \exp[\pm jn\phi]j^n \qquad \begin{smallmatrix} \mathrm{L} \\ \mathrm{R} \end{smallmatrix} \end{aligned} \tag{5.15}$$

γ is the radial propagation root at the aperture for mode (*n,m*), and *j* is the square root of minus one. With uniform phase a closed-form (6) is obtained using the Lommel integral formula on

page 337 of [6] and is useful as a check of the numerical integration of (5) when ξ is zero. These far field equations concur with those published by Sakr [119] and reveal that the one arbitrary constant, C, in Sakr's field equations for both HE_{11} and HE_{21} depends on the angular mode index and the root of the characteristic equation.

Note that the observation frame, (θ, ϕ) rotates with both θ and ϕ, with respect to the horn's fixed frame, which affects the observed radiated phase (with respect to the horn's fixed frame) for a rotationally polarized wave. Expressions for linearly (or elliptically) polarized field components are obtained by a linear combination of the field expressions for the two rotational senses and using appropriate coordinate transformation [124] from the (θ, ϕ) observation frame to the horn's fixed frame in which, for example, vertical or horizontal linear polarization may be defined. Adding the balanced hybrid mode field expressions for the two rotational sense, L+R, represents linearly polarized excitation of the horn with the E field in the positive y-axis direction (for the HE_{11} main beam, with the y axis in the ϕ direction with $\phi = 0$).

5.1.3 Far field Results and Comparison of Methods

Fig. 5-4 and Fig. 5-5 reveal how well augmenting the aperture field integration with true spherical or quadratic radial phase approximates the radiated fields for HE_{11} mode (used for communications) in comparison with the SWE and CMM+IE results, and Fig. 5-6 and Fig. 5-7 for HE_{21} mode (used for tracking). All figures represent CP polarization and also present uniform-phase patterns, which have deep nulls that the quadratic phase patterns have filled in. The uniform-phase patterns do well in the main beam with narrow flare angles. With a 12 deg horn the numerical integration of (5) yields good agreement with SWE especially about the main

beam (near-axis), as shown in Fig. 5-4, which also presents the patterns calculated by numerical modeling of the exact geometry of the corrugated horn (by CMM the fields inside the horn and IE solution of the horn exterior currents). The 12 deg horn has thirty-three corrugations, including five for mode converter. The differences that are noticed, mainly off axis, between the aperture integration results and those of the more formal methods are due to the presence of other (higher order) modes other than HE_{11} in the aperture, as well as the aperture phase not being modeled exactly. (The aperture integration and SWE methods also do not account for currents on the horn exterior.) Fig. 5-5 presents similar results for a horn with half-flare angle of 45 deg, eleven total corrugations, and slightly shorter pitch; whereas, all the other horn parameters remain the same as in the previous figure. The figure indicates that among the three aperture integration methods considered, PMQRP provides the best approximation of the SWE or CMM+IE results. Note that an on-axis dip of about one and one quarter dB occurs in the pattern on-axis for the 45 deg half-flare horn using aperture integration with spherical phase; although, the on-axis dip is only about one quarter dB for all the other methods: aperture integration quadratic phase, SWE, and full-wave CMM+IE. The agreement of the aperture integration results with the SWE or CMM+IE results is less with the 45 deg half-flare than the 12 deg since the reasons for the differences, mentioned above, are more pronounced for a wider flare. For increasing flare angle, the aperture integration results – based on modeling the horn as short sections of cylindrical waveguide, each supporting a single cylindrical mode – become less accurate; in which case, method 3 in Table 1, SWE, is a better model. The SWE results presented in the figures satisfy Maxwell's equations in spherical coordinates with the boundary

condition of a conical, anisotropic surface-impedance, as an ideal approximation of the corrugated flare.

Fig. 5-6 and Fig. 5-7 compare the aperture integration with the more formal analysis methods for the second angular (tracking) mode. The agreement is comparable to that for the first angular mode. PMQRP appears to again yield the best approximate results in the main beam.

A typical corrugated horn will have cross-pol patterns with a null on-axis and peaking just outside the main beam shoulder about 10-20 dB below the co-pol pattern level, and follow and tend toward the co-pol pattern farther off axis. Numerical optimization of the corrugated horn geometry (mainly of the mode converter geometry) can reduce the cross-pol level substantially.

5.1.4 Conclusions

Simple equations for the far fields of corrugated-conical horn have been presented and discussed, demonstrating a practical approximation method using aperture field augmented with quadratic phase. It provides good agreement in the main beam with more formal computational analysis techniques, such as SWE and accounting for the complete corrugated horn geometry (CMM + IE). The equations can be used to establish a baseline design of a feedhorn for a satcom antenna.

Aperture integration methods using spherical, and two different quadratic, radial phase functions are compared. PMQRP yields significantly better results than FOQRP. Numerical results for 12 and 45 deg half-flare horns have been presented and discussed. The results suggest that the aperture integration method works well for modest flare angles, and PMQRP works well for moderate flare angles. But for wide flared horns the aperture integration method may not

represent the true aperture fields completely, especially at far, off-axis angles, for which case SWE is a better – yet more numerically complicated – approximate model. A portion of the material presented in this section has been previously published by the author [92].

5.2 SPHERICAL WAVE EXPANSION

The method of spherical wave expansion (SWEX) provides improved accuracy compared to the aperture field method in estimating a horn's radiation pattern, and it also has the ability to represent the pattern at an arbitrary field distance – meaning that it can estimate the horn's near fields just as accurately as its far fields. It does involve a higher computational cost though, compared to AFIM.

The principle involved in modeling a conical horn's radiation fields with SWEX are to assume a pure spherical mode within the horn, and solving Maxwell's equations in spherical coordinates, with the conical horn wall as an impedance boundary condition. The field components have the following forms, as given in [107].

$$E_R\left(R,\theta,\phi\right) = A\frac{\nu\left(\nu+1\right)}{jkR^2}h_\nu^{(2)}\left(kR\right)\,P_\nu^m\left(\cos\theta\right)\cos m\phi \tag{5.16}$$

$$RE_\theta\left(R,\theta,\phi\right) = -Ah_\nu^{(2)}\left(kR\right)\left[\beta P_\nu'^m\left(\cos\theta\right)+\frac{m\bar{\Lambda}}{\sin m\phi}P_\nu^m\left(\cos\theta\right)\right]\cos m\phi \tag{5.17}$$

$$RE_\phi\left(R,\theta,\phi\right) = Ah_\nu^{(2)}\left(kR\right)\left[\bar{\Lambda}P_\nu'^m\left(\cos\theta\right)+\frac{m\beta}{\sin m\phi}P_\nu^m\left(\cos\theta\right)\right]\cos m\phi \tag{5.18}$$

The value of the Bessel function order ν is determined numerically to satisfy the boundary conditions, and with that value the aperture fields (at the cap of the conical horn) are estimated

quite accurately by the single, pure spherical mode, which usually involves an irrational value for ν. The boundary condition equation is different for all three cases of HE11 (corrugated horn), TE, or TM modes (smooth horns). Assuming the HE11 radiated field mode for a corrugated horn, the boundary condition is defined as $f_{\nu+}^{m}(\alpha)=0$, where the function f is defined in general as

$$f_{\nu\pm}^{m}(\theta)=\frac{\partial P_{\nu}^{m}(\cos\theta)}{d\theta}\pm\frac{mP_{\nu}^{m}(\cos\theta)}{\sin\theta}. \tag{5.19}$$

Once the spherical fields at the spherical aperture cap are known, a modal expansion (using integer orders for each expansion mode) projects the radiation pattern to an arbitrary distance from the aperture.

$$\begin{aligned}E_T(R,\theta,\phi)&=\tfrac{A}{2}\left(1+\bar{\Lambda}\right)\hat{a}_{\text{cpol}}\,S_+(R,\theta)\\&\quad+\tfrac{A}{2}\left(1-\bar{\Lambda}\right)\left[\hat{a}_{\text{cpol}}\cos 2\phi+\hat{a}_{\text{Xpol}}\sin 2\phi\right]S_-(R,\theta)\end{aligned} \tag{5.20}$$

$$\bar{\Lambda}=\begin{cases}1:\ \text{HE}\\-1:\ \text{EH}\\0:\ \text{TM}\\\infty:\ \text{TE}\end{cases}\ \text{propagation modes} \tag{5.21}$$

$$\begin{aligned}S_{\pm}(R,\theta)&=h_{\nu}^{(2)}(kR)\,f_{\nu\pm}^{m}(\theta)\ \text{ at cap}\\&=h_{\nu}^{(2)}(kL)\sum\nolimits_{1}^{\infty}C_{n\pm}\,f_{n\pm}^{m}(\theta)\ \text{ outside cap}\end{aligned} \tag{5.22}$$

(modal expansion at spherical cap)

$$\begin{aligned}C_{n\pm}(\alpha,L,R)&=\frac{h_{n}^{(2)}(kR)}{h_{n}^{(2)}(kL)}\frac{(2n+1)(n-m)!}{2n(n+1)(n+m)!}\left[\frac{\sin\alpha}{n(n+1)-\nu(\nu+1)}\right]\cdot\\&\left[n(n+1)P_{n}^{m}(\cos\alpha)f_{\nu\pm}^{m}(\alpha)-\nu(\nu+1)P_{\nu}^{m}(\cos\alpha)f_{n\pm}^{m}(\alpha)\right]\end{aligned} \tag{5.23}$$

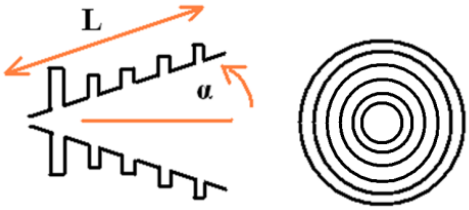

Fig. 5-8. Conical Horn Geometry.

An example comparison of the radiation pattern of a Ku-band corrugated horn, with 10 deg flare angle, calculated using the SWEX method, with the measured pattern is provided below. Note that the SWEX method does not account for currents on the horn exterior surface, which limits its accuracy. The SWEX method estimating a feed horn's pattern is found to be quite accurate within the main beam.

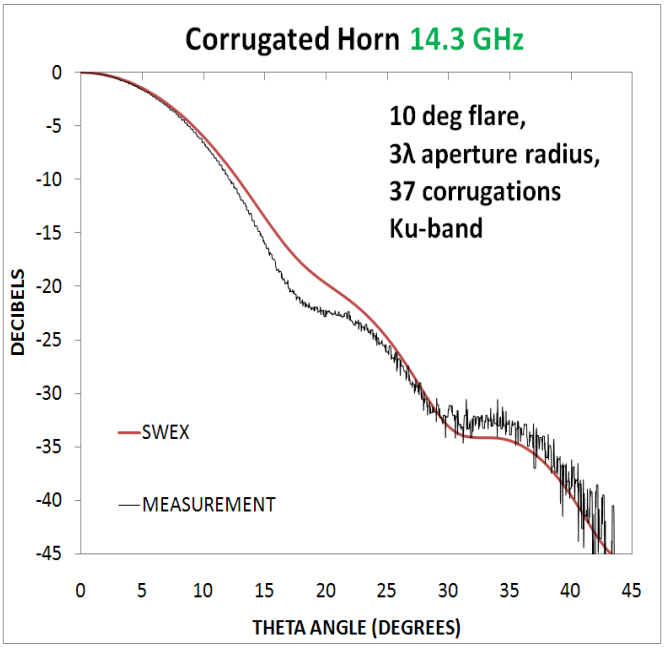

Fig. 5-9. Comparison of Measurement versus SWEX Horn Calculation.

5.3 MODE MATCHING

Cylindrical mode matching represents the horn as a concatenated series of short sections of cylindrical waveguide, indicated in Fig. 5-10 The mode-matching method provides a means to accurately account for the exact geometry of the internal horn geometry, so rather than assuming the conic flare shape of Fig. 5-1, a completely arbitrarily shaped corrugation profile, represented in Fig. 5-10, is considered — arbitrary but assuming at most only a modest flare angle. (The cylindrical mode matching method is limited to analyzing horn semi-flare angles only up to about 45 deg. Circularly symmetric feedhorns with flare angle less than about 40 deg are characterized quite well by cylindrical mode matching. Larger flare angles require spherical mode matching techniques.) A brief User Manual is provided in Appendix 8.7 describing the use of the CYL_MM software program in which these concepts were coded. The CYL_MM program was used to produce the mode-matching results and 3D graphics depicted in this dissertation.

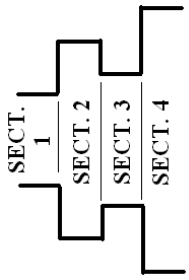

Fig. 5-10. Feedhorn Represented by Short Sections of Cylindrical Waveguide.

Each section of cylindrical waveguide propagates waves, and each junction between sections scatters waves. The sections and junctions are each represented by an s-parameter scattering matrix, and all of the scattering matrices are sequentially cascaded into an overall scattering

matrix that represents the entire feed horn. By the use of the integral equation method-of-moments technique the exterior surface can be accounted for to determine the aperture reflection coefficient for each mode, and that is combined with the s-parameter cascade for the cylindrical sections to provide an improved estimate of the modal coefficients for the aperture fields of the horn. The radiation pattern of the horn can then be calculated using a modal expansion with closed-form far field radiation integrals superimposed for each mode. The horn far fields can then be converted into a spherical wave expansion series to allow the horn fields at any distance to be accurately estimated. The most computationally intensive tasks are the calculation of the scattering matrices for each junction, and the cascading of all the s-parameter matrices for all of the cylindrical sections into a single s-parameter matrix to represent the entire horn.

The scattering parameters for a junction are determined assuming that the smaller section is on the left side in the analysis presented below. The propagation equations for the left and right sides of the junction are first noted below, where the z axis points to the right.

5.3.1 Waveguide Fields

The modal representation of the fields in the cylindrical sections is detailed in the appendix (8.85).

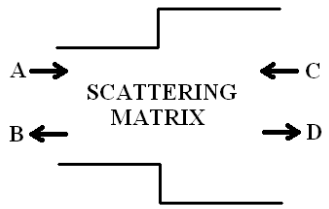

Fig. 5-11. S-parameter Model of the Cylindrical Step Junction.

$$[B] = s'_{11}[A] + s'_{12}[C]$$
$$[D] = s'_{21}[A] + s'_{22}[C] \tag{5.24}$$

LEFT SIDE:

$$E_{\mathrm{SM}} = \sum_i \left\{ A_i \exp[-\gamma_i z] + B_i \exp[\gamma_i z] \right\} e_{i\mathrm{SM}}$$
$$H_{\mathrm{SM}} = \sum_i \left\{ A_i \exp[-\gamma_i z] - B_i \exp[\gamma_i z] \right\} h_{i\mathrm{SM}} \tag{5.25}$$

RIGHT SIDE:

$$E_{\mathrm{LG}} = \sum_i \left\{ D_i \exp[-\gamma_i z] + C_i \exp[\gamma_i z] \right\} e_{i\mathrm{LG}}$$
$$H_{\mathrm{LG}} = \sum_i \left\{ D_i \exp[-\gamma_i z] - C_i \exp[\gamma_i z] \right\} h_{i\mathrm{LG}} \tag{5.26}$$

e_{i} and h_{i} are the cylindrical field distributions for the i^{th} mode, respectively on the smaller (SM) and larger (LG) sides of a particular cylindrical step junction. Continuity of transverse fields across the junction, and mode orthogonality then yields the following system of equations, which are used to solve for the s-parameter matrices. The P, L and R matrices are the mode-interaction (coupling) integrals, for the transverse fields, as defined below, where the row index is *i*, and the column index is *j*. The superscript asterisks symbolize complex conjugation.

$$[P]^T \left[[A] + [B] \right] = [R] \left[[C] + [D] \right] \tag{5.27}$$

$$[L]^* \left[[A] - [B] \right] = [P]^* \left[[D] - [C] \right] \tag{5.28}$$

$$[P]_{ij} = {}_{\mathrm{SM}} I^{\text{Amode, Bmode}}_{\mathrm{L}\,i,\,\mathrm{R}\,j} = \hat{z} \cdot \iint_{\mathrm{SM}} \overline{e}_{i\mathrm{SM}} \times \left(\overline{h}_{j\mathrm{LG}} \right)^* \cdot ds \quad \text{cross-coupling}$$
$$[L]_{ij} = {}_{\mathrm{SM}} I^{\text{Amode, Bmode}}_{\mathrm{L}\,i,\,\mathrm{L}\,j} = \hat{z} \cdot \iint_{\mathrm{SM}} \overline{e}_{i\mathrm{SM}} \times \left(\overline{h}_{j\mathrm{SM}} \right)^* \cdot ds \quad \text{self-coupling left side} \tag{5.29}$$
$$[R]_{ij} = {}_{\mathrm{LG}} I^{\text{Amode, Bmode}}_{\mathrm{R}\,i,\,\mathrm{R}\,j} = \hat{z} \cdot \iint_{\mathrm{LG}} \overline{e}_{i\mathrm{LG}} \times \left(\overline{h}_{j\mathrm{LG}} \right)^* \cdot ds \quad \text{self-coupling right side}$$

The complex conjugation of the magnetic field in the mode interaction integrals of (5.29) is appropriate with circular polarization to cancel the complex temporal and phi phasors

$\exp\left[j\left(\omega t \pm \left(n\phi\right)\right)\right]$ between the electric and magnetic field equations, and consequently complex conjugation appears also in the resulting field matching (5.28) and *s*-parameter equations (5.34)–(5.37). Note that the *s*-parameter values remain the same no matter what polarization the fields have (*e.g.,* linear, circular), and that with linear polarization the complex conjugations of the magnetic fields are not necessary to cancel the complex temporal and phi phasors. (If the conjugations are removed from the mode coupling integrals for linear polarization then they are also respectively removed from the field matching (5.28) and *s*-parameter equations (5.34)–(5.37) as well in order to keep all the equations intact). Only in the case of TE-TE mode interaction do the mode interaction integrals potentially involve a conjugation (when the magnetic fields are conjugated).

In the expressions for *I* below for the various combinations of mode interactions, A and B may each symbolize either L or R (either the left or right side of the step junction), as generalizations of the forms of *I* given in (5.29). (A represents the electric field mode, and B the magnetic field mode.) The lower-case letter *a* is the radius of the smaller of the two cylindrical radii represented in the integral, which means that in the case of $\left[R\right]_{ij}$ it is the radius of the larger of the two radii involved in the step junction. These equations are derived in the appendix (8.196).

$$I_{\mathrm{A,B}}^{\mathrm{TM\text{-}TM}} = \frac{\pi c}{\varepsilon}\begin{cases} \dfrac{a\gamma^{\mathrm{A}}\left(\gamma^{\mathrm{B}}\right)^2 k_z^{\mathrm{A}}/\beta_0}{\left(\gamma^{\mathrm{A}}\right)^2-\left(\gamma^{\mathrm{B}}\right)^2}\left\{J_{n+1}\left(\gamma^{\mathrm{A}}a\right)-\dfrac{\gamma^{\mathrm{A}}a\,J_{n-2}\left(\gamma^{\mathrm{A}}a\right)}{2\left(n-1\right)}\right\}J_n\left(\gamma^{\mathrm{B}}a\right),\ \gamma^{\mathrm{A}}\neq\gamma^{\mathrm{B}}, n\neq 1; \\ \dfrac{a\gamma^{\mathrm{A}}\gamma^{\mathrm{B}}\,k_z^{\mathrm{A}}/\beta_0}{\left(\gamma^{\mathrm{A}}\right)^2-\left(\gamma^{\mathrm{B}}\right)^2}\left\{\gamma^{\mathrm{A}}J_1\left(\gamma^{\mathrm{A}}a\right)J_0\left(\gamma^{\mathrm{B}}a\right)-2\gamma^{\mathrm{B}}J_0\left(\gamma^{\mathrm{A}}a\right)J_1\left(\gamma^{\mathrm{B}}a\right)\right\},\ \gamma^{\mathrm{A}}\neq\gamma^{\mathrm{B}}, n=1; \\ \dfrac{\left(\gamma a\right)^2}{\beta_0}k_z^{\mathrm{L}}J_{n-1}^2\left(\gamma a\right),\ \gamma^{\mathrm{A}}=\gamma^{\mathrm{B}}. \end{cases} \quad (5.30)$$

$$I_{\mathrm{A,B}}^{\mathrm{TM\text{-}TE}} = 0 \tag{5.31}$$

$$I_{\mathrm{A,B}}^{\mathrm{TE\text{-}TM}} = \frac{\pi c}{\varepsilon}\begin{cases} \dfrac{2\gamma^{\mathrm{A}}\gamma^{\mathrm{B}}}{\left(\gamma^{\mathrm{A}}\right)^2-\left(\gamma^{\mathrm{B}}\right)^2}\left\{n\dfrac{\gamma^{\mathrm{A}}}{\gamma^{\mathrm{B}}}J_n\left(\gamma^{\mathrm{A}}a\right)-\gamma^{\mathrm{B}}aJ_{n-1}\left(\gamma^{\mathrm{A}}a\right)\right\}J_n\left(\gamma^{\mathrm{B}}a\right), \gamma^{\mathrm{A}}\neq\gamma^{\mathrm{B}}; \\ \dfrac{\left(\gamma a\right)^2}{2}J_n\left(\gamma a\right)\left\{J_{n+2}\left(\gamma a\right)-J_{n-2}\left(\gamma a\right)\right\},\ \gamma^{\mathrm{A}}=\gamma^{\mathrm{B}}. \end{cases} \tag{5.32}$$

$$I_{\mathrm{A,B}}^{\mathrm{TE\text{-}TE}} = \frac{\pi c}{\varepsilon}\begin{cases} \dfrac{\gamma^{\mathrm{B}}a\left(k_z^{\mathrm{B}}\right)^*/\beta_0}{1-\left(\gamma^{\mathrm{B}}/\gamma^{\mathrm{A}}\right)^2}J_n\left(\gamma^{\mathrm{A}}a\right)\left\{J_{n-1}\left(\gamma^{\mathrm{B}}a\right)-J_{n+1}\left(\gamma^{\mathrm{B}}a\right)\right\},\ \gamma^{\mathrm{A}}\neq\gamma^{\mathrm{B}}; \\ \dfrac{\left(\gamma a\right)^2}{2\beta_0}\left(k_z^{\mathrm{B}}\right)^*\left\{2J_{n-1}^2\left(\gamma a\right)-J_n\left(\gamma a\right)\left[J_{n-2}\left(\gamma a\right)+J_{n+2}\left(\gamma a\right)\right]\right\},\ \gamma^{\mathrm{A}}=\gamma^{\mathrm{B}}. \end{cases} \tag{5.33}$$

5.3.2 Junction S-parameters

The *s*-parameters for the waveguide junction are summarized below in (5.34)–(5.37) and are derived in the appendix (8.179). The row indices of the *s*-parameter matrices represent the output (response) modes, and column indices representing the input (stimulus) modes.

$$\left[S_{11}\right]=\left[L\right]^{\frac{1}{2}}\left[\left[L\right]^*+\left[P\right]^*\left[R\right]^{-1}\left[P\right]^T\right]^{-1}\left[\left[L\right]^*-\left[P\right]^*\left[R\right]^{-1}\left[P\right]^T\right]\left[L\right]^{\frac{-1}{2}}, \tag{5.34}$$

$$\left[S_{12}\right]=\left[L\right]^{\frac{1}{2}}2\left[\left[L\right]^*+\left[P\right]^*\left[R\right]^{-1}\left[P\right]^T\right]^{-1}\left[P\right]^*\left[R\right]^{\frac{-1}{2}}, \tag{5.35}$$

$$\left[S_{21}\right]=\left[R\right]^{\frac{1}{2}}2\left[\left[R\right]+\left[P\right]^T\left[L\right]^{*-1}\left[P\right]^*\right]^{-1}\left[P\right]^T\left[L\right]^{\frac{-1}{2}}, \tag{5.36}$$

and

$$\left[S_{22}\right]=-\left[R\right]^{\frac{1}{2}}\left[\left[R\right]+\left[P\right]^T\left[L\right]^{*-1}\left[P\right]^*\right]^{-1}\left[\left[R\right]-\left[P\right]^T\left[L\right]^{*-1}\left[P\right]^*\right]\left[R\right]^{\frac{-1}{2}}. \tag{5.37}$$

$$\left[R\right]_{ij}^{\frac{1}{2}}=\sqrt{\left|\left[R\right]_{ij}\right|}\ \text{and}\ \left[L\right]_{ij}^{\frac{1}{2}}=\sqrt{\left|\left[L\right]_{ij}\right|} \tag{5.38}$$

See the note regarding the complex conjugations following (5.29). Also note that with circular polarization each reflection (S_{11} or S_{22}) involves a reversal of the sense of rotation: RCP once reflected becomes LCP and vice versa.

Cascading of the *s*-parameters of one junction or section of cylindrical waveguide with the next section's, to produce a combined, single set of *s*-parameters for the cascade as a whole, is accomplished by (5.39)–(5.42), for which a derivation is provided in section 6.3 of [125].

$$\left[S_{11}^{AB}\right]=\left[S_{11}^{A}\right]+\left[S_{12}^{A}\right]\left[\left[I\right]-\left[S_{11}^{B}\right]\left[S_{22}^{A}\right]\right]^{-1}\left[S_{11}^{B}\right]\left[S_{21}^{A}\right] \tag{5.39}$$

$$\left[S_{12}^{AB}\right]=\left[S_{12}^{A}\right]\left[\left[I\right]-\left[S_{11}^{B}\right]\left[S_{22}^{A}\right]\right]^{-1}\left[S_{12}^{B}\right] \tag{5.40}$$

$$\left[S_{21}^{AB}\right]=\left[S_{21}^{B}\right]\left[\left[I\right]-\left[S_{22}^{A}\right]\left[S_{11}^{B}\right]\right]^{-1}\left[S_{21}^{A}\right] \tag{5.41}$$

$$\left[S_{22}^{AB}\right]=\left[S_{22}^{B}\right]+\left[S_{21}^{B}\right]\left[\left[I\right]-\left[S_{22}^{A}\right]\left[S_{11}^{B}\right]\right]^{-1}\left[S_{22}^{A}\right]\left[S_{12}^{B}\right] \tag{5.42}$$

For analysis of a common commercial corrugated horn these matrices are typically of dimension about 100, and the calculations were accomplished with optimized computational efficiency using the matrix subprograms GEMM (BLAS), GESV (LAPACK) and GETRS (LAPACK), the latter of which reuses the factorization from GESV.

The original implementation of the computer code for this arithmetic was tested against results from the literature for two standard test cases: a step junction and a thick iris, as shown in Fig. 5-12. The step junction comparison serves to confirm the validity of the junction s-parameter calculations, and the thick iris comparison serves to confirm the validity of the arithmetic involved in the cascading s-parameter matrices as well. The calculations compare nearly

identically with the published results for the step junction [126] and the thick iris [127], and quite well with results for a three-cavity resonator [128].

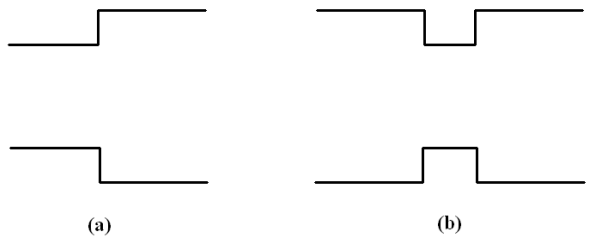

Fig. 5-12. Test Cases: (a) Step Junction, and (b) Thick Iris.

5.3.3 Far Field Modal Radiation Patterns

Once the coefficients of the aperture field modes have been calculated using the mode matching method, the far field radiation pattern can be calculated, for each mode, using the closed-form radiation integrals, given below, that were derived using the aperture field method (combining both the equivalent electric and magnetic current models). The Lommel (8.253) is used to provide a closed-form solution for each of the Bessel product integrals. Appendix 8.3 provides detailed derivations of the fundamentals and field relations used to construct the equations here. The $\pm \frac{L}{R}$ notation indicates the sense of circular polarization: The sign on the top corresponds to left-hand circular and that on the bottom to right-hand circular. Linear polarization is a linear combination of the two circular polarizations. In the following equations the angular and radial cylindrical field mode indices are respectively n and m, and the aperture radius is a. The factor $[R]^{-1/2}$, defined in (5.38) and used in (5.59), representing the final waveguide section at the mouth of the radiating end of the feedhorn, scales $[t_{21}]$ from units of (modal power-normalized) s-parameters into units proportional to field strength for the respective modes in the horn aperture.

Following equations (6-95), (6-101), and (6-102) from [11] the radiated electric far field, $\bar{E}_{ff}$, is proportional to the magnetic and electric vector potentials as given by the equations below, where the magnetic vector potential in the far field is A_{ff}, the electric vector potential F_{ff}, μ free-space permeability, ε free-space permittivity, $\beta_0 = k = 2\pi/\lambda$ is the free space wave number, λ is the wavelength, and ds' the elemental aperture surface area. The vector from the origin in the center of the aperture to a given far field observation point is $\bar{r}(r,\theta,\phi)$, with corresponding unit vector $\hat{r}$.

$$\bar{\bar{E}}_{ff} = \bar{\bar{E}}_{Aff} + \bar{\bar{E}}_{Fff} \approx \left[\bar{\bar{I}} - \hat{r}\hat{r}\cdot\right] j\omega\left(-\bar{A}_{ff} + \eta\,\hat{r}\times\bar{F}_{ff}\right), \tag{5.43}$$

where

$$\bar{A}_{ff} = \frac{\exp[-jkr]}{4\pi r}\mu\iint \bar{J}_{eq}\exp\left[jk(\bar{\rho}'\cdot\hat{r})\right]ds', \tag{5.44}$$

$$\bar{F}_{ff} = \frac{\exp[-jkr]}{4\pi r}\varepsilon\iint \bar{M}_{eq}\exp\left[jk(\bar{\rho}'\cdot\hat{r})\right]ds', \tag{5.45}$$

and

$$\bar{\bar{I}} = \hat{r}\hat{r}\cdot + \hat{\theta}\hat{\theta}\cdot + \hat{\phi}\hat{\phi}\cdot\ . \tag{5.46}$$

$$\begin{aligned} \mathrm{E}_{\theta\ \text{Far-Field}} &\approx -j\beta_0\frac{\exp[-j\beta_0 R]}{4\pi R}\left\{\eta_0\,\mathrm{N}_\theta + \mathrm{L}_\phi\right\} \\ \mathrm{E}_{\phi\ \text{Far-Field}} &\approx -j\beta_0\frac{\exp[-j\beta_0 R]}{4\pi R}\left\{\eta_0\,\mathrm{N}_\phi - \mathrm{L}_\theta\right\} \end{aligned} \tag{5.47}$$

$$\begin{aligned} \bar{\mathrm{N}} &= \iint \bar{J}\exp(j\beta_0\,\bar{r}'\cdot\hat{R})ds';\ \ \bar{J} = \hat{\mathrm{n}}_{\mathrm{ap}}\times\bar{\mathrm{H}} \\ \bar{\mathrm{L}} &= \iint \bar{\mathrm{M}}\exp(j\beta_0\,\bar{r}'\cdot\hat{R})ds';\ \ \bar{\mathrm{M}} = -\hat{\mathrm{n}}_{\mathrm{ap}}\times\bar{\mathrm{E}} \end{aligned} \tag{5.48}$$

$$N_\theta = \pm j^n 2\pi\cos\theta e^{\pm jn\phi}\sum_m\int_0^a \left\{\begin{array}{l} A_m\left[{}_mJ^{TE}_{n-1}J^{\theta}_{n-1} - {}_mJ^{TE}_{n+1}J^{\theta}_{n+1}\right] \\ +B_m\left[{}_mJ^{TM}_{n-1}J^{\theta}_{n-1} + {}_mJ^{TM}_{n+1}J^{\theta}_{n+1}\right] \end{array}\right\}\rho\,d\rho \tag{5.49}$$

$$N_\phi = j^{n+1} 2\pi e^{\pm jn\phi} \sum_m \int_0^a \begin{Bmatrix} A_m \left[{}_m J_{n-1}^{TE} J_{n-1}^{\theta} + {}_m J_{n+1}^{TE} J_{n+1}^{\theta} \right] \\ +B_m \left[{}_m J_{n-1}^{TM} J_{n-1}^{\theta} - {}_m J_{n+1}^{TM} J_{n+1}^{\theta} \right] \end{Bmatrix} \rho \, d\rho \tag{5.50}$$

$$L_\theta = j^{n+1} 2\pi \cos\theta e^{\pm jn\phi} \sum_m \int_0^a \begin{Bmatrix} -D_m \left[{}_m J_{n-1}^{TE} J_{n-1}^{\theta} + {}_m J_{n+1}^{TE} J_{n+1}^{\theta} \right] \\ -E_m \left[{}_m J_{n-1}^{TM} J_{n-1}^{\theta} - {}_m J_{n+1}^{TM} J_{n+1}^{\theta} \right] \end{Bmatrix} \rho \, d\rho \tag{5.51}$$

$$L_\phi = \pm j^n 2\pi e^{\pm jn\phi} \sum_m \int_0^a \begin{Bmatrix} D_m \left[{}_m J_{n-1}^{TE} J_{n-1}^{\theta} - {}_m J_{n+1}^{TE} J_{n+1}^{\theta} \right] + \\ E_m \left[{}_m J_{n-1}^{TM} J_{n-1}^{\theta} + {}_m J_{n+1}^{TM} J_{n+1}^{\theta} \right] \end{Bmatrix} \rho \, d\rho \tag{5.52}$$

$${}_m J_n^{\mathrm{TE}} = J_n\left(\rho \gamma_m^{\mathrm{TE}}\right) \; ; \quad {}_m J_n^{\mathrm{TM}} = J_n\left(\rho \gamma_m^{\mathrm{TM}}\right) \tag{5.53}$$

$$J_n^{\theta} = J_n\left(\rho \beta_0 \sin\theta\right) \tag{5.54}$$

$$A_m = \frac{\gamma_m^{TE} k_{zm}^{TE}}{2\beta_0 \varepsilon \eta_0} t_{21}^{TE} \tag{5.55}$$

$$B_m = \frac{\gamma_m^{TM}}{2\varepsilon \eta_0} t_{21}^{TM} \tag{5.56}$$

$$D_m = \frac{\gamma_m^{TE}}{2\varepsilon} t_{21}^{TE} \tag{5.57}$$

$$E_m = \frac{\gamma_m^{TM} k_{z\,m}^{TM}}{2\beta_0 \varepsilon} t_{21}^{TM} \tag{5.58}$$

$$\left[t_{21}\right] = \left[R\right]^{-1/2} \left[S_{21}\right] \tag{5.59}$$

5.3.4 Comparing Measured and Calculated Far Fields

The Ku-band corrugated horn shown in Fig. 5-13 was analyzed by cylindrical mode matching method, and the results compared to measurement in Fig. 5-14 and Fig. 5-15. The horn achieves 30 dB return loss.

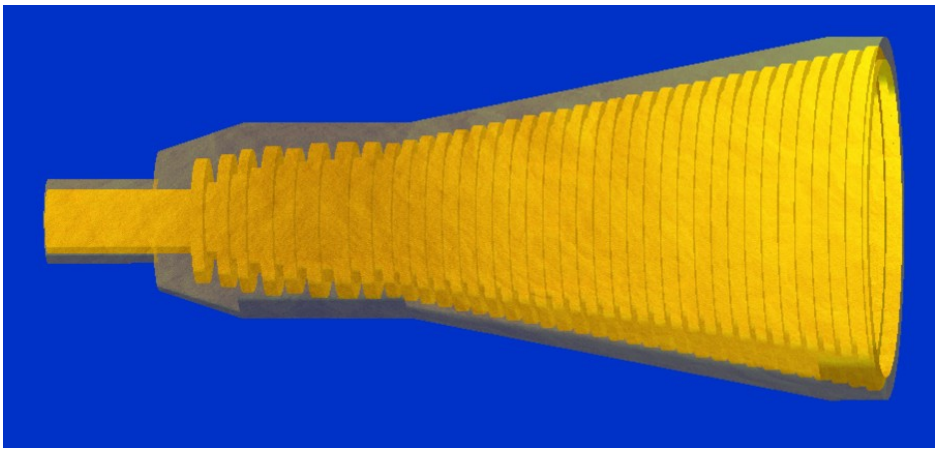

Fig. 5-13. Ku-band corrugated feed horn with 37 corrugations. 3D graphics produced by the ARAM CYL_MM Windows ™ software developed for this dissertation.

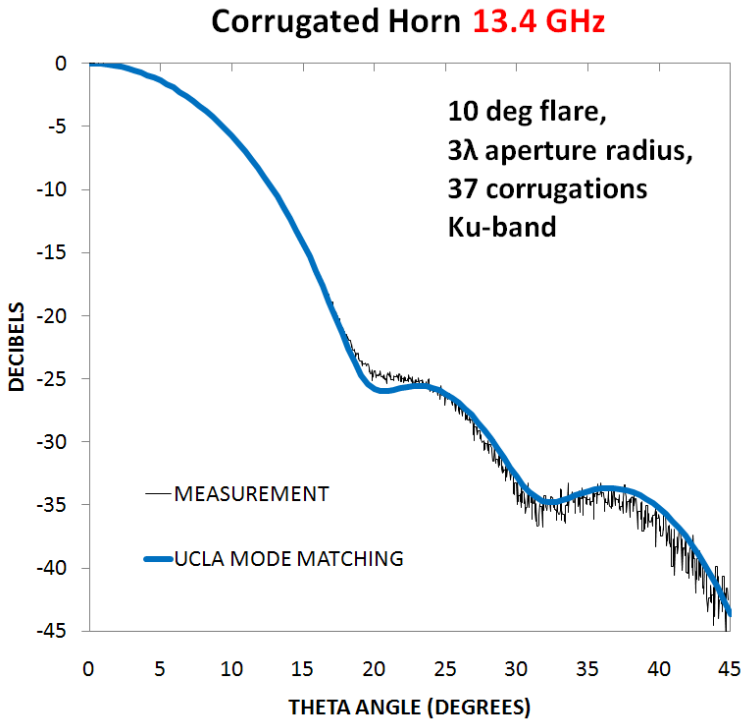

Fig. 5-14 Mode Matching Calculations Compared to Measurement at a 13.4 GHz for horn in Fig. 5-13.

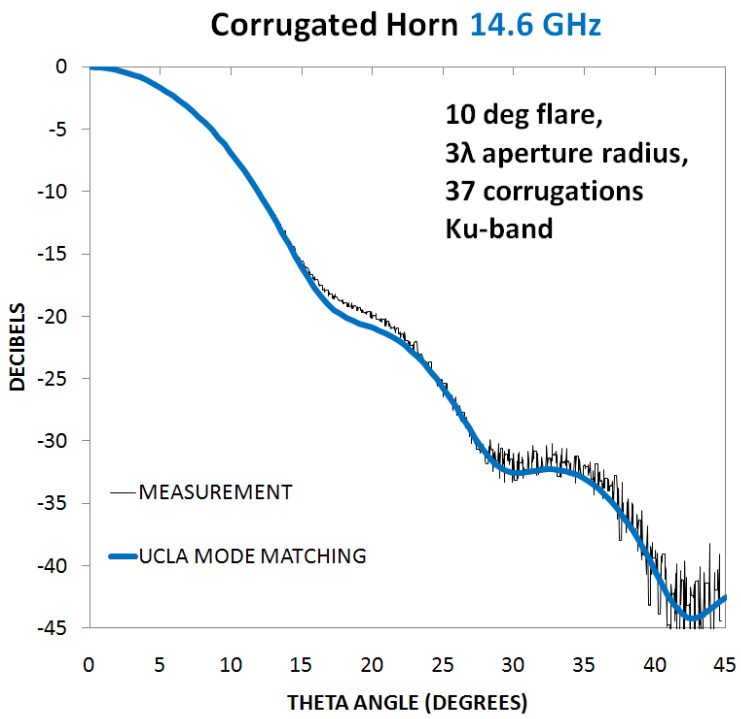

Fig. 5-15. Mode Matching Calculations Compared to Measurement at 14.6 GHz for horn in Fig. 5-13.

The S-band corrugated horn shown in Fig. 5-16 was analyzed using the cylindrical mode matching method, and the results compared with measurements in Fig. 5-17. The horn achieved a return loss of greater than 30 dB.

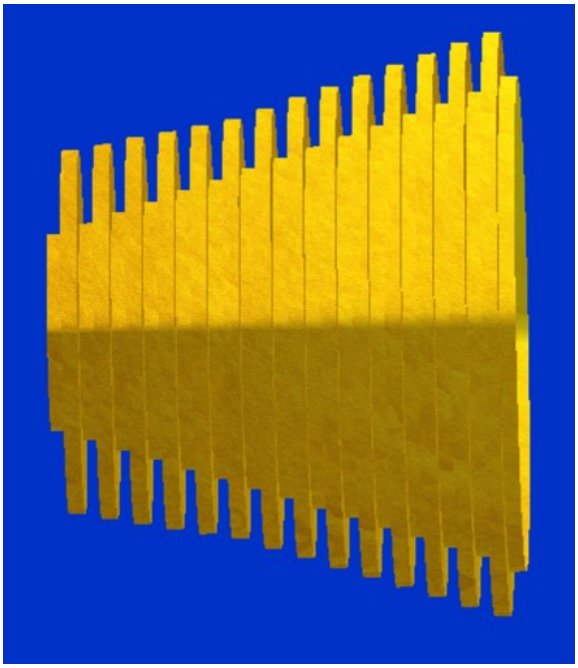

Fig. 5-16. S-band corrugated horn with 14 corrugations. 3D graphics produced by the ARAM CYL_MM Windows ™ software developed for this dissertation.

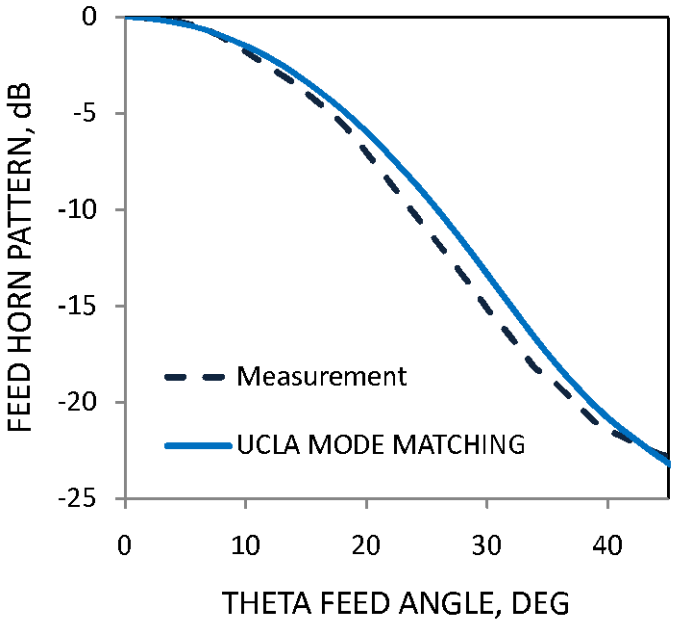

Fig. 5-17. Mode matching calculations compared to measurement at 2.12 GHz for horn in Fig. 5-16.

5.3.5 Computational Speed

The mode-matching method involves a considerable amount of matrix algebra, and it was found that the computation speed of the algorithm is largely determined by the computational efficiency of the matrix math library compiled with the program. See Appendix 8.6. Charts are presented below comparing the speed of the mode matching algorithm with that of a baseline hand-written un-optimized matrix math library used for testing of the original version of this code, and comparing those results also with subsequent versions compiled instead with the AMD ACML or Intel MKL optimized math libraries. The MKL library appears to be the fastest overall and the most robust, in terms of ease of compiling on various platforms and lack of runtime issues such as missing DLLs. For this algorithm on a PC with a 2.4 GHz Intel Core 2 Quad CPU, the MKL library provided an acceleration factor as high as seventy times compared to the un-optimized single-threaded math library. The following charts also show that when using multi-threaded (parallel processing) code the speed improvement is not monotonic when increasing the number of cores (threads). For this mode matching code the optimum number of cores (threads) is between three and four. Results using clMAGMA math library are not presented here because the mode matching calculations practically almost always use modal expansions of order less than a few hundred, and at those sizes of matrices the CPU implementations of the BLAS and LAPACK math routine run considerably faster than the GPU implementation of clMAGMA — clMAGMA is faster only for very large matrices of size in the thousands, in which case clMAGMA would effectively accelerate method of moment problems but not cylindrical mode matching problems.

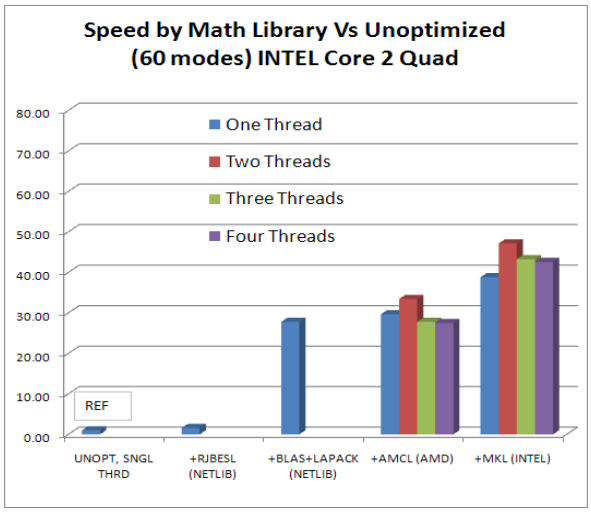

Fig. 5-18. INTEL Core2 Quad Compute Speed versus Math Library with 60 modes.

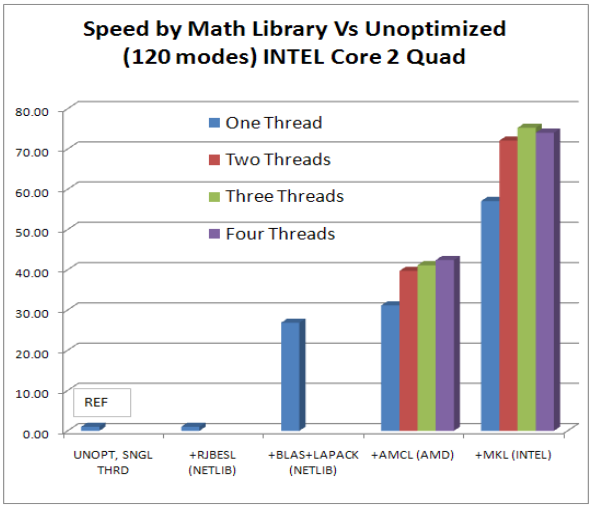

Fig. 5-19. INTEL Core2 Quad Compute Speed versus Math Library with 120 modes.

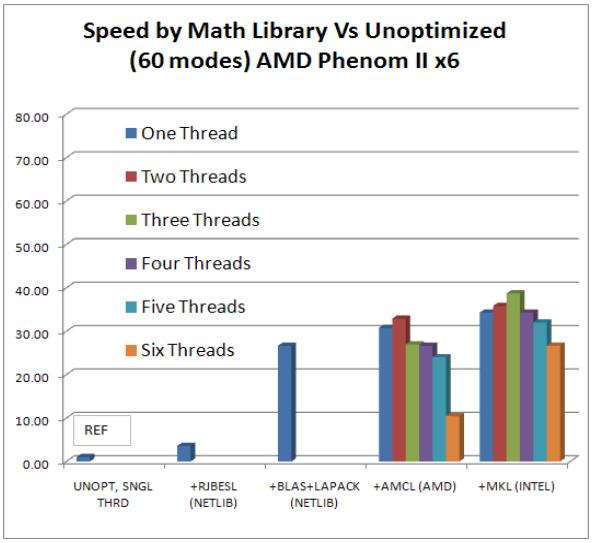

Fig. 5-20. AMD Phenom II-6 Compute Speed versus Math Library with 60 modes

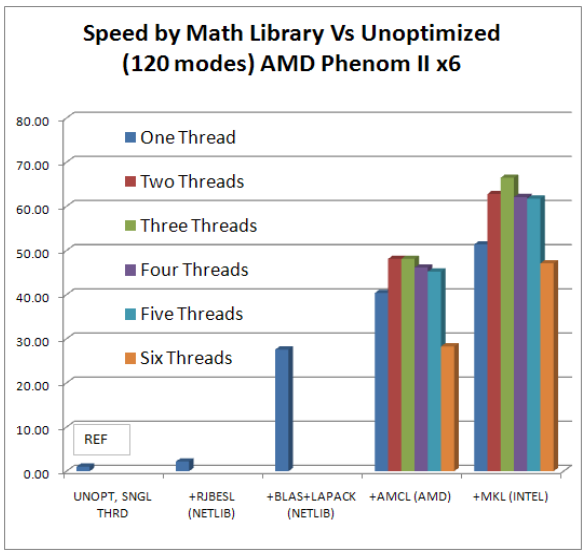

Fig. 5-21. AMD Phenom II-6 Compute Speed Versus Math Library with 120 modes

5.4 PARTICLE SWARM OPTIMIZATION

In this section the design a corrugated horn for a reflector system is accomplished by multi-objective PSO. (Other examples of multi-objective PSO for the design of aperture antennas are provided in section 4.4.) Consider a circularly symmetric Cassegrain dual reflector system operating at 14.3 GHz and fed by a corrugated horn, with the reflector optics designed with a feed edge angle of 17 deg. The following multiple objectives are imposed on the optimization: 1) the horn return loss must be minimized; 2) the reflector optics expects the feed pattern level, dBp1, to drop at 8.18 deg to 4.31 dB below its central peak level; 3) the reflector optics also expects the feed pattern level, dBp2, to drop at 16.36 deg to 18.36 dB below its central peak level; 4) minimize the maximum level of cross-polarization over the entire 17 deg feed angle range (that illuminates the reflector system); and 5) make the horn as short as possible. The fitness function for this optimization is defined for this example in (5.60), where the square of the feed pattern deviation from the goals is amplified to emphasize its importance relative to the

units of the objectives. The optimizer models the geometry of the corrugated feed horn as a horn flare profile over the length of the horn, plus a corrugation depth profile. The horn flare profile is modeled as a balance between both a linear ramp from the starting to the ending radius and a sine squared profile. The optimization chose a balance of 14% linear and 86% sine square flare profile. The first ten corrugation slots from the throat make up the mode converter which initiates the conversion from TE_{11} to HE_{11} mode that is completed by the remainder of the flare, which has corrugations of a constant depth also determined by the optimizer. In this example the horn model is characterized by sixteen parameters that the optimizer juggles and balances throughout the optimization process.

$$\text{fitness} = (\text{return loss}) + 100\left[(\text{dBp1} - 4.31)^2 + (\text{dBp2} - 18.36)^2\right] + \text{maxXpol} + \text{length} \quad (5.60)$$

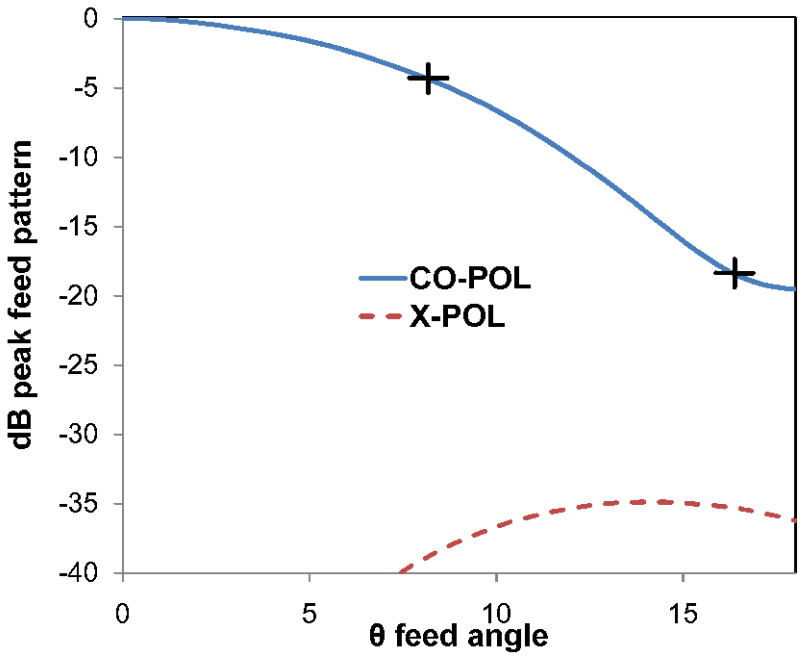

Fig. 5-22. Radiation pattern of feed horn designed by multi-objective PSO.

Fig. 5-22 presents the optimized feed radiation pattern, normalized to its peak amplitude, and the geometry of the optimized horn is provided in Table 5-2. The two "+" crosses within the figure

represent radiation pattern goals set for the optimizer to meet, and the curves show that the radiation pattern of the optimized horn meets those goals quite accurately. The results of this multi-objective PSO corrugated feed horn optimization are a return loss of -119 dB; dBp1 is within 0.05 dB of the target (left cross in the figure), and dBp2 within 0.15 dB (right cross in the figure). The optimization achieves a maximum cross-polarization level -34.9 dBp, with respect to the peak level of the pattern, over the 17 deg range, and the length of the horn is minimized at 24.3 cm.

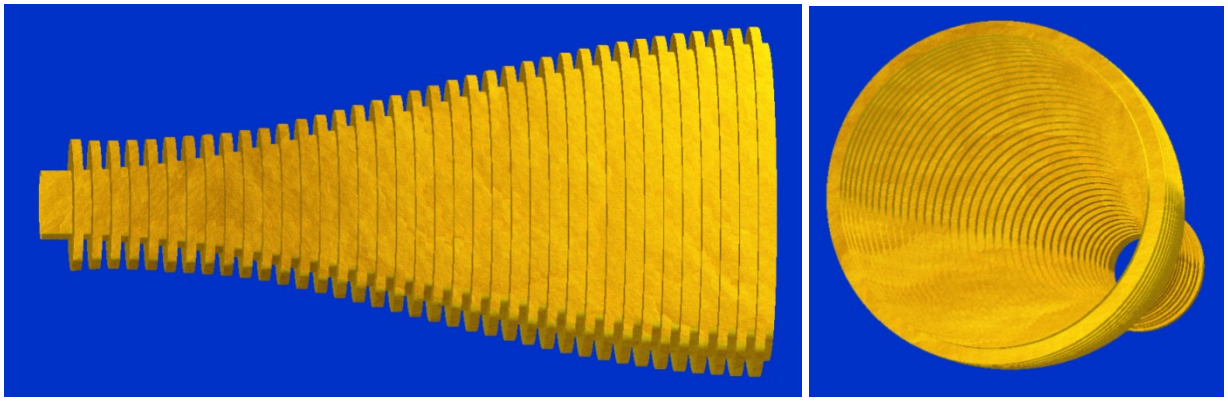

Fig. 5-23. Perspectives of the multi-objective optimized feed horn. 3D graphics produced by the ARAM CYL_MM Windows ™ software developed for this dissertation.

Table 5-2. Geometry (radius, length of the cylindrical sections in cm) of the optimized profiled horn depicted in Fig. 5-23.

1	1.14	1.00	26	2.83	0.32	51	4.19	0.31
2	2.19	0.32	27	2.29	0.31	52	4.87	0.32
3	1.16	0.31	28	2.98	0.32	53	4.33	0.31
4	2.14	0.32	29	2.44	0.31	54	5.00	0.32
5	1.20	0.31	30	3.13	0.32	55	4.46	0.31
6	2.13	0.32	31	2.59	0.31	56	5.13	0.32
7	1.24	0.31	32	3.29	0.32	57	4.59	0.31
8	2.16	0.32	33	2.75	0.31	58	5.25	0.32
9	1.30	0.31	34	3.45	0.32	59	4.71	0.31
10	2.19	0.32	35	2.91	0.31	60	5.36	0.32
11	1.37	0.31	36	3.61	0.32	61	4.82	0.31
12	2.25	0.32	37	3.07	0.31	62	5.46	0.32
13	1.45	0.31	38	3.78	0.32	63	4.92	0.31
14	2.28	0.32	39	3.24	0.31	64	5.55	0.32
15	1.54	0.31	40	3.94	0.32	65	5.01	0.31
16	2.32	0.32	41	3.40	0.31	66	5.63	0.32
17	1.65	0.31	42	4.10	0.32	67	5.09	0.31
18	2.39	0.32	43	3.57	0.31	68	5.70	0.32
19	1.76	0.31	44	4.27	0.32	69	5.16	0.31
20	2.47	0.32	45	3.73	0.31	70	5.76	0.32
21	1.88	0.31	46	4.42	0.32	71	5.22	0.31
22	2.55	0.32	47	3.88	0.31	72	5.80	0.32
23	2.01	0.31	48	4.58	0.32	73	5.26	0.31
24	2.68	0.32	49	4.04	0.31	74	5.83	0.32
25	2.15	0.31	50	4.73	0.32	75	5.29	0.31

5.5 CONCLUSION

This chapter has addressed the design of conical feedhorns using a variety of techniques: aperture field integration method with first-order and also perimeter-matched quadratic radial phase (FOQRP & PMQRP), spherical wave expansion method, and the method of cylindrical mode matching. A comparison of the relative accuracies of each method and also the use of the respective methods as means to trade between accuracy and computational speed is discussed. Measured results are compared with the different computational methods, and the relative merits of each method with respect to the measured data are indicated. The particle swarm optimization method is harnessed to produce an optimized multi-parameter design — with about sixteen

parameters — of a shaped-profile corrugated horn with a combined fitness function that simultaneously minimizes the return loss and radiated cross-polarization component as well as fitting the radiation pattern of the horn to a desired design constraint (for proper illumination of a shaped reflector design).

CHAPTER 6 REFLECTOR RADIATION PATTERNS

Aspects of reflector radiation patterns and their calculation using numerical acceleration methods are discussed in this chapter, including the brute force method of calculating the radiation pattern by Physical Optics (PO), the Gaussian beam method of accelerating the calculation, and an improved version of the Levin quadrature method for asymptotic evaluation of the PO integral, and the application of graphics processors using the OpenCL language. A typical example of a generic offset reflector — the roof-top satellite dish — is shown in Fig. 6-1 below, and a much larger, specialized offset reflector for space application (NASA SMAP soil moisture active passive satellite) is depicted in Fig. 6-2.

Fig. 6-1. Generic Single offset Reflector with Feedhorn and LNA. (Photo from www.ebay.com.)

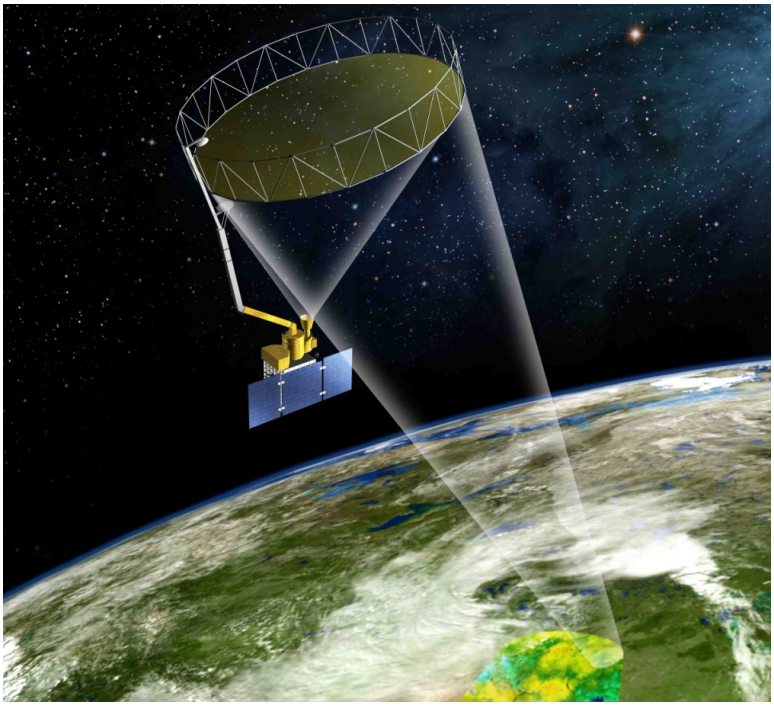

Fig. 6-2. Six meter diameter offset mesh reflector for the NASA SMAP (soil moisture active passive) satellite, expected to launch in 2014, from www.jpl.nasa.gov .

6.1 BRUTE-FORCE PHYSICAL OPTICS

$$\bar{E}(\bar{r})\Big|_{\text{far-field}} = -jk\eta\frac{\exp[-jkr]}{4\pi r}\left\{\theta\hat{\theta}\cdot+\phi\hat{\phi}\cdot\right\}\iint\limits_{\text{reflector}}\bar{J}^{\text{PO}}(\bar{r}\,')\exp\left[jk(\bar{r}\,'\cdot\hat{r})\right]ds', \qquad (6.1)$$

where
$$\bar{J}^{\text{PO}} = \begin{cases} 2\hat{n}\times\bar{H}^{\text{inc}}, \text{ illuminated areas} \\ 0\ , \text{ shadowed areas} \end{cases}. \qquad (6.2)$$

For a single reflector as depicted in Fig. 1-6, the brute force computation of the physical optics integral over the reflector surface involves dividing the aperture into elements of surface area one tenth wavelength on a side and accumulating all the contributions in the far field according to the integrand in (6.1). The integral is calculated independently for each far field observation angle. The current J^{PO}, associated with the elemental patch of aperture surface area represented by the integral of (6.1), is modified to incorporate the Jacobian of the reflector surface shape to account

for the difference between the element of curved reflector surface and that of the flat aperture surface integration area. The polarization orientation of the field illuminating the reflector from the feed at the reflector's focus is that of a Huygens source, given by Ludwig's third definition (which is the ideal feed polarization to create zero cross-polarization radiated from a parabolic reflector). Furthermore, the polarization orientation of the fields radiated in the far field from the reflector system are treated again as that of a Huygens source, with Ludwig's third definition of cross-polarization defining the polarization orientation of the reflector's radiated fields. Some details regarding the relationship between the polarization orientation of the aperture fields and those of the far fields are discussed in Appendix 8.1.

6.2 GAUSSIAN BEAM METHOD

6.2.1 Introduction

The Gaussian beam (GB) method provides a significant computation speed advantage, at the cost of somewhat reduced accuracy, by avoiding the numerical integration of the PO reflector surface integral and instead accounting for the integration of an array of "spot beams" with closed form equations that can be calculated much faster than numerical integration. The GB method uses a pseudo-hexagonal array or cluster of individual Gaussian beamlets to represent the radiation pattern of the feed that illuminates the reflector surface, and accounts for the overall radiation pattern of the reflector by accumulating the individual contributions of each beamlet independently. The representation of the feed pattern by the array of GBs is referred to as a Gaussian beam decomposition of the feed pattern, as depicted in Fig. 6-3 below. The contribution that each GB beamlet makes to the far field radiation pattern of the reflector is

approximated by a closed form equation with the assumption that the reflector surface is smoothly varying and can be approximated by a locally quadratic function within the spot of the reflector surface illuminated by the beamlet.

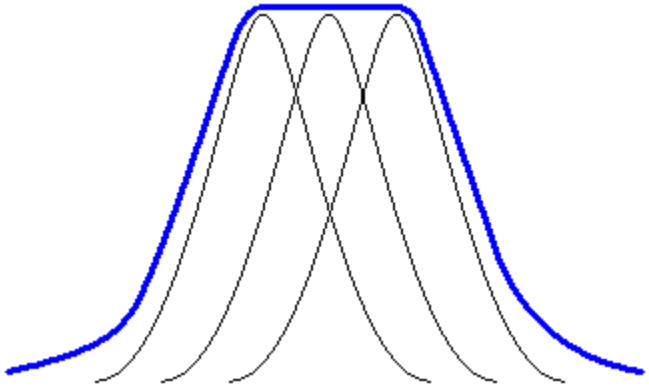

Fig. 6-3. Gaussian beam decomposition of a radiation pattern.

6.2.2 Paraxial Approximation

A Gaussian beam is a paraxial approximation of Maxwell's equations. For the approximation to be accurate the minimum waist of the Gaussian beam, w_0, indicated in Fig. 6-4 below, must be greater than about six wavelengths [129]. With the minimum waist located at the origin the Gaussian beam's field strength, as a function of radius ρ and axial distance z, is given by (6.3). A Gaussian beam is fully characterized by two parameters: the minimum waist and the wavelength.

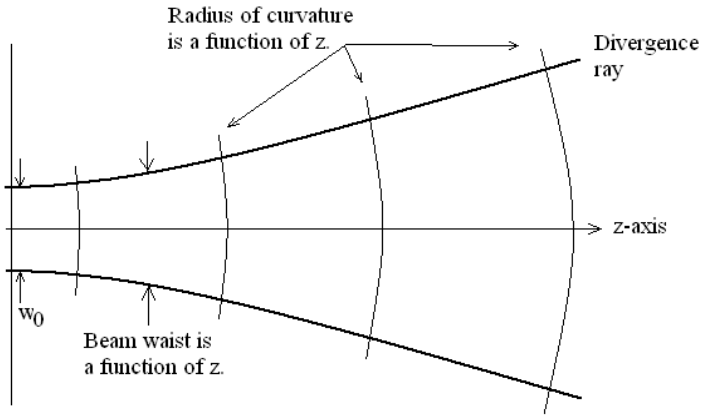

Fig. 6-4 The Gaussian beam is a paraxial solution to Maxwell's equations.

$$GB(\rho,z)=\frac{w_0}{w(z)}\exp\left[-\frac{\rho^2}{w^2(z)}-j\left(k\left\{z+\frac{\rho^2}{2R(z)}\right\}+\xi(z)\right)\right], \tag{6.3}$$

where

$$\text{beam waist, } w(z)=w_0\sqrt{1+\left(\frac{z}{Z_r}\right)^2}, \tag{6.4}$$

$$\text{phase front radius, } R(z)=z\left(1+\left(\frac{Z_r}{z}\right)^2\right), \tag{6.5}$$

$$\xi(z)=\arctan\frac{z}{Z_r}, \tag{6.6}$$

and

$$\text{Rayleigh length, } Z_r=\frac{\pi w_0^2}{\lambda}. \tag{6.7}$$

In order to provide for a smooth decomposition of a feed radiation pattern between the GB axes the GBs are separated by their divergence angle, which in radians is the ratio of the waist to the Rayleigh length.

$$\text{divergence angle } =\frac{w_0}{Z_r} \tag{6.8}$$

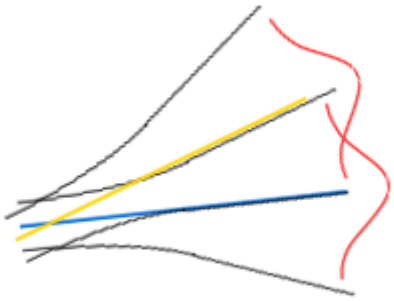

Fig. 6-5. GBs separated in angle by the GB divergence angle.

6.2.3 Spatial distribution of GBs

Separating the GBs uniformly (by their divergence angle) in a hexagonal pattern provides for a smooth, continuous decomposition of a feed radiation pattern in between the GB axes. A deep reflector can span a solid angle up to and even more than a hemisphere, and yet it is not possible to perfectly uniformly distribute a hexagonal pattern over a hemisphere. An approximately hexagonal pattern will reasonably uniformly span a small solid angle, such as what the feed in a dual reflector system might see, but with a single reflector it is effectively not feasible. A suitable alternative is to use a spherical geodesic grid based on an icosahedron tiled with hexagonal cells, as shown in Fig. 6-6 below. The simple construction of this spherical geodesic is described in [130]. The twenty faces of an icosahedron are tiled with the most symmetric tile shape, the hexagon, and projected onto the sphere. In this fashion a great number of hexagonal cells can be nearly uniformly distributed over a sphere: twelve of the cells on the sphere (at the icosahedron vertices) are pentagons rather than hexagons, and the hexagonal cells are slightly larger near the center of the twenty icosahedron faces than near the edges of the faces.

The placement of the GB ray axes on each icosahedron face is done as follows. Let N be the binary power of division. First of all, each of the icosahedron vertices, 12 of them, contains a

GB axis. Depending on the value of N each of the 30 edges of the icosahedron, excluding the endpoints of the edges, contains a number of GB axes: none with N = 0, 1 with N = 1, 3 with N = 2, 7 with N = 3, etc. Inside each face of the icosahedron the number of GB axis points (inside the edges) also depends on N: 1 with N = 0, located in the very center of the face and then projected outward onto the unit sphere, then for each higher N an additional point is added between all points for level (N-1). Inside the face there are 4 points with N = 1, 19 with N = 2, 85 with N = 3, etc. When placing each and every one of these additional GB axis points inside the face, the new point is first located in space at the very midpoint along the dividing line between two existing points, form the prior level (N-1), and then projecting that point radially outward to the surface of the unit sphere, where the new point then resides.

The total number of points (GB axes) distributed on the entire sphere is thereby the sum of 12 vertices plus 30 edges, each containing 2^N-1 points (excluding end points — the vertices), plus 20 icosahedron faces, each containing $4^N + (2^N+1)(2^{L-1}+1)–3(2^N)$ points. Adding these all up, the sphere contains 482 GB axes with N = 2, 1922 GB axes with N = 3, 7682 GB axes with N = 4, and 30722 GB axes with N = 5. Usually only at most one hemisphere is needed for coverage of a reflector, in which case the number of GB axes is have those stated. The baseline angular separation between any two neighboring GBs — this varies slightly across each face of the icosahedron — is $64.3 \text{ deg} / \left(2^{N+1} \sin\left[\pi / 3\right]\right)$, or about 4.6 deg with N = 3.

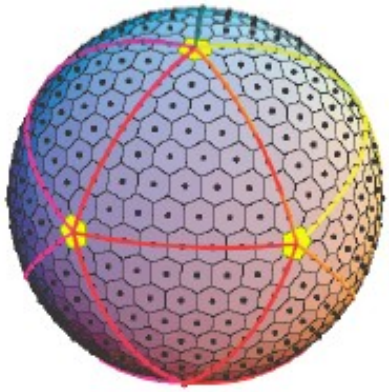

Fig. 6-6. GB axes distributed in spherical geodesic pattern (adapted from [130]). An icosahedron's 20 faces are filled with hexagonal cells, each representing the axis or one GB ray beam. This distributes the GB rays nearly uniformly in solid angle over entire hemisphere.

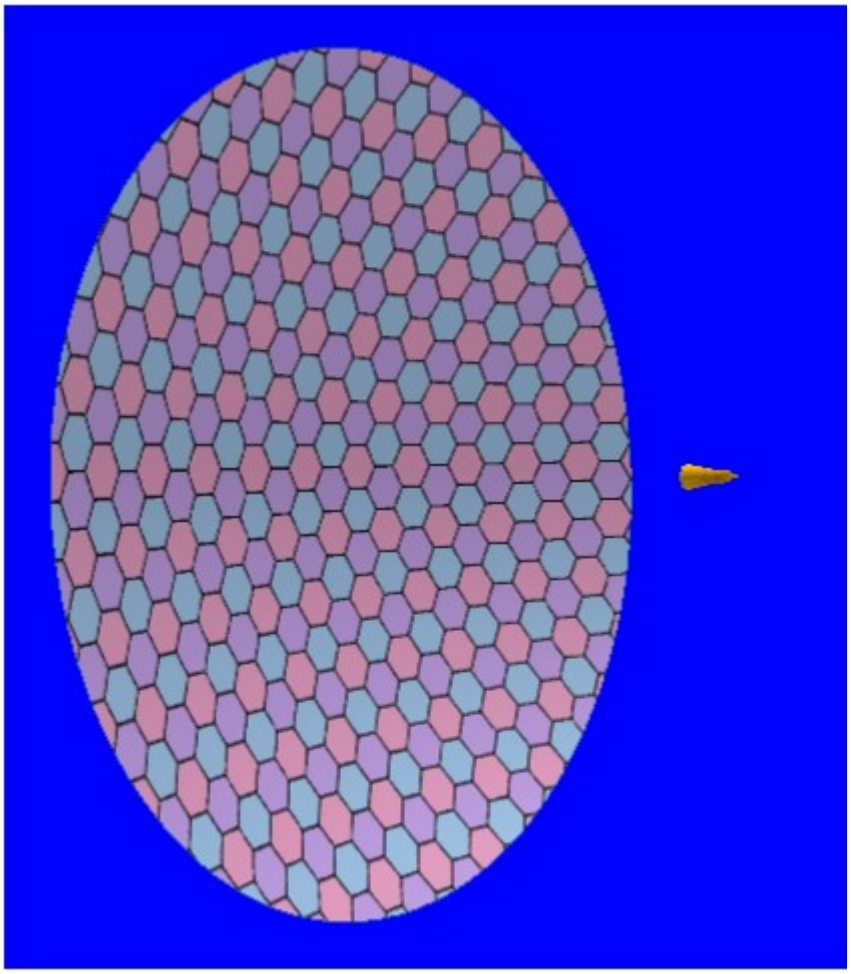

Fig. 6-7. A feedhorn illuminating a reflector from the parabolic focus.

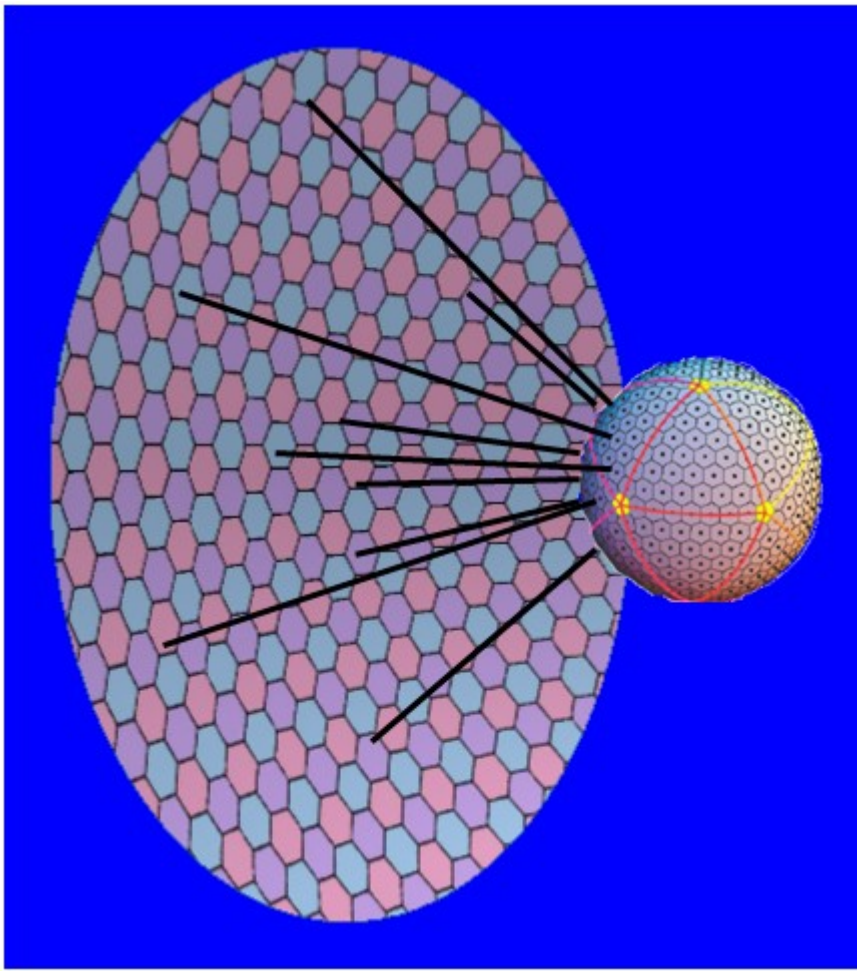

Fig. 6-8. GB rays illuminating the reflector surface, representing a GB decomposition of the radiation pattern from the feedhorn.

6.2.4 GB spot beam and Least Squares method

The contribution to the physical optics integral from each individual Gaussian beamlet is given by

$$\bar{E}(\bar{r})\Big|_{\text{far-field}}^{GB} = -jk\eta\frac{\exp[-jkr]}{4\pi r}\left(\hat{\theta}\hat{\theta}\cdot+\hat{\phi}\hat{\phi}\cdot\right)\iint\limits_{\text{reflector}}\bar{J}_{\text{GB}}^{\text{PO}}(\bar{r}\,')\exp\left[jk\left(\bar{r}\,'\cdot\hat{r}\right)\right]ds'. \qquad (6.9)$$

The physical optics integrand of (6.9) is approximated, within the spot on the reflector surface illuminated by the GB, by the quadratic exponential function

$\hat{p}\exp\left[-a_x x^2 - a_{xy}xy - a_y y^2 - b_x x - b_y y - \gamma\right]$, with the local GB *xy*-plane representing a plane tangent to the reflector surface at the point where the GB axis intersects the reflector surface, with the *x*-axis parallel to the reflector edge, so that

$$\bar{E}(\bar{r})\Big|_{\text{far-field}}^{GB} \approx -jk\eta\frac{\exp[-jkr]}{4\pi r}\hat{p}\iint\limits_{\text{reflector}}\exp\left[-a_x x^2 - a_{xy}xy - a_y y^2 - b_x x - b_y y - \gamma\right]ds' . \qquad (6.10)$$

Each of the coefficients in the argument of the exponential in the integrand of (6.10) may in general be complex valued. An aspect of this approximation is that the vector orientation of the far field contribution from the each GB is altogether assumed to be in a constant direction, $\hat{p}$, across the entire spot on the reflector surface illuminated by the GB beamlet.

The coefficients in (6.10) are estimated by a least-squares method, *e.g.,* the CGELSD or ZGELSD subroutines from www.netlib.org. The six coefficients are determined by simultaneously satisfying, in the least-squares error sense, six simultaneous equations, determined by sampling the far field contribution at six points near the intersection of the GB axis with the reflector surface. The matrix determinant would tend to zero and the condition number to infinity if the six points were chosen symmetrically distributed about a circle; instead, the sample points are taken using a randomized constellation such as shown in Fig. 6-9 below, in order to provide a condition number around 25. The radii indicated in Fig. 6-9 are relative to a normalizing sampling radius made as small as possible to minimize the GB numerical approximation error.

A matrix is singular if its determinant is zero, which happens if its rows or columns are not all linearly independent. If any column of a matrix can be obtained by some linear combination of

the other columns, then the columns are not linearly dependent and the determinant is zero. If the sample points are chosen symmetrically on a circle then one of the columns tends to a linear combination of the others. (Singular value decomposition shows that only one of the singular values tends to zero.) If instead the sampling point locations are randomized then the condition number improves (reduces). The condition number determines how ill-conditioned the matrix is — a zero determinant corresponds to an infinite condition number. If the angles alone are randomized a zero determinant condition is avoided and the condition number improves. If the radii are randomized as well the condition number further improves. Since as noted above only one singular value tends to zero in the singular case of points symmetrically distributed in a circle, a truncated singular value decomposition (TSVD) method [42] could in that case be applied to solve the GB matrix system in spite of the singularity, with a slight compute speed penalty, in which case there would apparently be no need to randomized the sampling point locations.

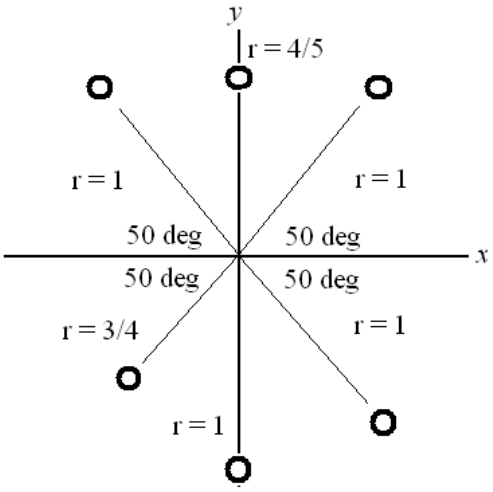

Fig. 6-9. Least-squares sampling point constellation in local GB coordinates on the local reflector surface tangent plane, with the origin representing the point where the GB strikes the reflector surface.

The least squares method (Netlib xGELSD) solves the system of equations in (6.11), where x and y represent the coordinates of the i^{th} point in the constellation of Fig. 6-9 above (in the plane of the local reflector surface tangent), and f_i represent the complex-valued far field contributed by the GB at the i^{th} point in the constellation, corresponding to the integrand of (6.10).

$$\begin{bmatrix} x_1^2 & x_1y_1 & y_1^2 & x_1 & y_1 & 1 \\ x_2^2 & x_2y_2 & y_2^2 & x_2 & y_2 & 1 \\ x_3^2 & x_3y_3 & y_3^2 & x_3 & y_3 & 1 \\ x_4^2 & x_4y_4 & y_4^2 & x_4 & y_4 & 1 \\ x_5^2 & x_5y_5 & y_5^2 & x_5 & y_5 & 1 \\ x_6^2 & x_6y_6 & y_6^2 & x_6 & y_6 & 1 \end{bmatrix} \begin{bmatrix} -a_x \\ -a_{xy} \\ -a_y \\ -b_x \\ -b_y \\ -\gamma \end{bmatrix} = \begin{bmatrix} \ln(f_1) \\ \ln(f_2) \\ \ln(f_3) \\ \ln(f_4) \\ \ln(f_5) \\ \ln(f_6) \end{bmatrix} \tag{6.11}$$

The output of the least squares solution are the coefficients $a_x, a_{xy}, a_y, b_x, b_y, \gamma$, which are incorporated into the closed form solutions below.

6.2.5 Closed form GB Physical Optics PO integral

When a GB lands on the reflector surface far from any reflector edge the GB closed form integral is

$$I = \int_{-\infty}^{\infty}\int_{-\infty}^{\infty} \exp\left[-a_x x^2 - a_{xy}xy - a_y y^2 - b_x x - b_y y - \gamma\right] dxdy = \frac{2\pi \exp\left[\dfrac{a_x b_y^2 - a_{xy} b_x b_y + a_y b_x^2}{4a_x a_y - a_{xy}^2} - \gamma\right]}{\sqrt{4a_x a_y - a_{xy}^2}}, \tag{6.12}$$

where the square root is on the right hand side of the complex plane with phase $\frac{-\pi}{2} < \arg\left(\sqrt{\ }\right) \le \frac{\pi}{2}$.

6.2.6 Edge contribution of GB PO integral

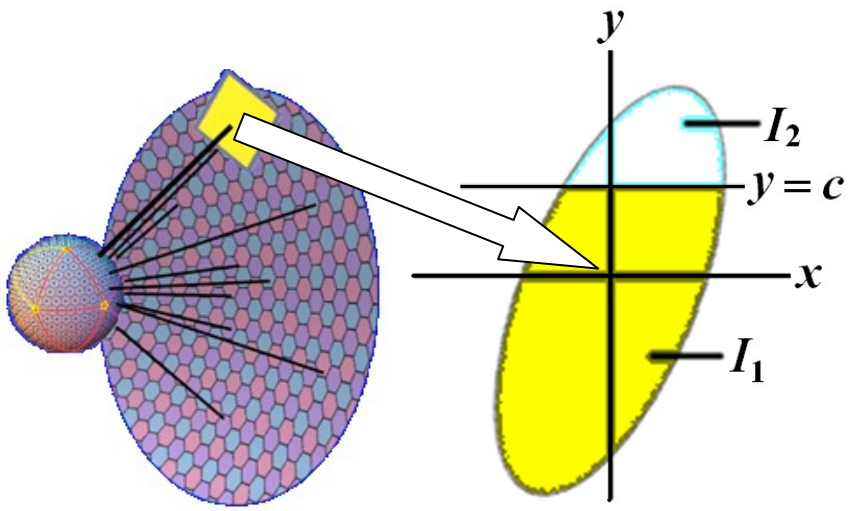

Fig. 6-10. GB illuminating generally oblique local reflector surface tangent plane about local GB origin with edge of reflector located at distance y = c from the point where the GB central axis ray intersects the reflector surface. The diagram on the right represents the spot illuminated by the GB on the local tangent plane.

The diagram on the left of Fig. 6-10 depicts a local reflector surface tangent plane at the point where a GB strikes the reflector surface. The diagram on the right represents the spot illuminated on the tangent plane, at an oblique angle in general, by the GB. The diagram on the right is divided into two regions: I_1, representing the portion of the spot that falls on the reflector surface, and I_2, representing the portion that falls off the reflector edge.

For a GB that is directed close enough to an edge of the reflector to provide significant illumination of the edge, the local GB coordinate system is rotated so that the *x*-axis is parallel to the edge, as depicted in Fig. 6-10, with the edge shown located at $y = c$. Significant illumination of the edge occurs when the GB axis is within about 3 GBangle from the direction to the edge. Fig. 6-10 represents the illumination of the reflector surface by a GB, but the GB does not actually have a sharp contour, as shown in Fig. 6-10; instead, the has a continuous distribution that is concentrated near the center. Note that when the GB strikes the reflector surface at an

oblique angle, as depicted by the elongated ellipse in Fig. 6-10, the peak amplitude of the exponential in the integrand of (6.10) does not occur at the central point where the GB axis strikes the reflector surface. The edge location parameter, *c*, is positive when the GB axis lands on the reflector surface; on the other hand, the edge parameter, *c*, is negative when the GB axis does not intersect the reflector but goes off the edge. The closed form equations for the surface integrals, representing the areas respectively below (I_1) and above (I_2) the edge in Fig. 6-10, are:

$$I_1(c) = \left[I\Big|_{c=\infty} \right] \frac{1}{2} \left[1 - \operatorname{erf} \left[\frac{b_x a_{xy} - 2b_y a_x - c\left(4a_x a_y - a_{xy}^2\right)}{2\sqrt{a_x\left(4a_x a_y - a_{xy}^2\right)}} \right] \right], \tag{6.13}$$

and

$$I_2(c) = \left[I\Big|_{c=\infty} \right] \frac{1}{2} \left[1 + \operatorname{erf} \left[\frac{b_x a_{xy} - 2b_y a_x - c\left(4a_x a_y - a_{xy}^2\right)}{2\sqrt{a_x\left(4a_x a_y - a_{xy}^2\right)}} \right] \right], \tag{6.14}$$

where the square root is on the right hand side of the complex plane with phase $\frac{-\pi}{2} < \arg\left(\sqrt{\ }\right) \le \frac{\pi}{2}$. $I\Big|_{c=\infty}$ represents (6.12).

6.2.6.1 Customized Implementation of the Error Function

The error function, $\operatorname{erf}(\ )$, with complex argument, is used in (6.13) and (6.14) to account for the contribution of the GB to the reflector far field due to the reflector's edge. The GBs that land on the reflector surface more than a few GB waists from the edge reflect nearly entirely in the specular direction, and as a result the diffraction from the reflector edge is determined essentially entirely by the few GBs that illuminate the edge (and primarily those fewer GBs that illuminate the edge at an angle that places the observation point near the diffraction Keller cone). Since the edge contribution can compete in amplitude with the specular component at angles more than a

few GBangle from the specular direction, but the specular component, $[I_{c=\infty}]$ in (6.13) and (6.14) , becomes diminishingly (exponentially) small only a few GBangle from the specular direction, the magnitude of the error function must become extremely exponentially large in amplitude at some observation angles so that its product with the diminishing amplitude of the specular component properly accounts for the edge effect of the PO integral.

The following algorithms presented in Fig. 6-11 and Fig. 6-12 below, are found to provide a fast and sufficiently accurate approximation of the error function with complex argument for use in the GB method. The first presents the basic error function algorithm, and the latter modifies the algorithm so as to provide the exponential z2 as a separate output, *ln_out*, so that it can be summed by the host program with the corresponding exponential in the vanishing specular term and produce a useful result. That exponent ln_out can represent a factor up to the full maximum numerical computing floating value of about 1.0 E 308. If ln_out were not output separately to be summed with the specular term's corresponding exponent, then the exponential in the specular term can become deemed so small by the computer that it is assigned a vanishing zero value, and then its product with the error function is also forced to zero unnecessarily. By treating the exponent of the error function separately in this manner the effective dynamic range of the arithmetic is extended to provide a range useful enough for the GB method computations to account for the effect of the edge.

```
complex<double> erf( complex<double> zin )
{
    complex<double> z, z2;
    complex<double> zouta, zout;
    complex<double> cdtemp;
    double a1, a2;

    if( zin.real() < 0. ) {
        z = -zin;
    } else {
        z = zin;
    }
    z2 = z * z;
    if( abs( z ) < 1 ){
        // M_2_SQRTPI = 2 / sqrt( Pi )
        zouta = M_2_SQRTPI * z * ( 1. - z2 * ( 1./3. -
                z2 * ( 0.1 - z2 * ( 1./42. - z2 * 1./216. ) ) ) );
    } else { // abs( z ) >= 1
        cdtemp = z2 + 1.;
        int j = 0;
        for( int i = 0; i < 12; i++ ) {
        // full series required for accuracy with argument near 0.5-0.9i
        // Using generalized coefficients is faster than a case list.
            cdtemp = ( 12. - j++ * 0.5 ) / cdtemp + 1.;
            cdtemp = ( 12. - j++ * 0.5 ) / cdtemp + z2;
        }
        zouta = 1. - z * ( M_2_SQRTPI / 2. ) * exp( -z2 ) / cdtemp;
    }
    if( zin.real() < 0. ) {
        zout = -zouta;
    } else {
        zout = zouta;
    }
    return zout;
}
```

Fig. 6-11. Algorithm for error function with complex argument.

```
void erf_ln_out( complex<double>* zin, double* constant, double* sign,
                 complex<double>* scale_factor, complex<double>* ln_out )
{
    complex<double> z, z2;
    complex<double> zouta, zout;
    complex<double> cdtemp;
    double a1, a2;

    if( real(*zin) < 0. ) {
        z = -*zin;
    } else {
        z = *zin;
    }
    z2 = z * z;
    if( abs( z ) < 1 ){
        // M_2_SQRTPI = 2 / sqrt( Pi )
        *constant = 0.;
        *scale_factor = M_2_SQRTPI * z * ( 1. - z2 * ( 1. / 3.
                - z2 * ( 0.1 - z2 * ( 1. / 42. - z2 * 1. / 216. ) ) ) );
        *ln_out = 0.;

    } else { // abs( z ) >= 1
        cdtemp = z2 + 1.;
        int j = 0;
        for( int i = 0; i < 12; i++ ) {
        // full series required for accuracy with argument near 0.5-0.9i
        // Using generalized coefficients is faster than a case list.
            cdtemp = ( 12. - j++ * 0.5 ) / cdtemp + 1.;
            cdtemp = ( 12. - j++ * 0.5 ) / cdtemp + z2;
        }
        *constant = 1.;
        *scale_factor = - z * ( M_2_SQRTPI * 0.5 ) / cdtemp;
        *ln_out = -z2;
    }
    if( real(*zin) < 0. ) {
        *sign = -1.;
    } else {
        *sign = +1.;
    }

    // output format:
    // out = sign * ( constant + scale_factor * EXP[ ln_out ] )
}
```

Fig. 6-12. Algorithm for error function with complex argument revised to output exponent (ln_out) separately.

6.2.7 Results

The Gaussian beam method was used to characterize both symmetric and offset single reflector systems, and the results compared to brute force methods.

6.2.7.1 Speed

Compared to brute integration of the PO integral the GB method is 96 times faster for comparable results with a symmetric reflector of 240 wavelengths diameter for far field observation at modest theta angles. This speed is comparable to that reported in [131], [132]. Whereas the brute force calculation of a PO integral for a large antenna pattern cut might take an hour, the same pattern cut calculated using the GB method can take as little as half a minute, depending on the accuracy desired.

6.2.7.2 Symmetric Reflector

Fig. 6-13 shows the comparison of results of both brute force and the GB method for the case of a symmetric reflector of diameter 240 wavelengths, with f/D of 0.5 and Gaussian feed with 12 dB taper. The agreements of the co-polarized and cross-polarized components with brute force are both within a fraction of a decibel over the plotted range.

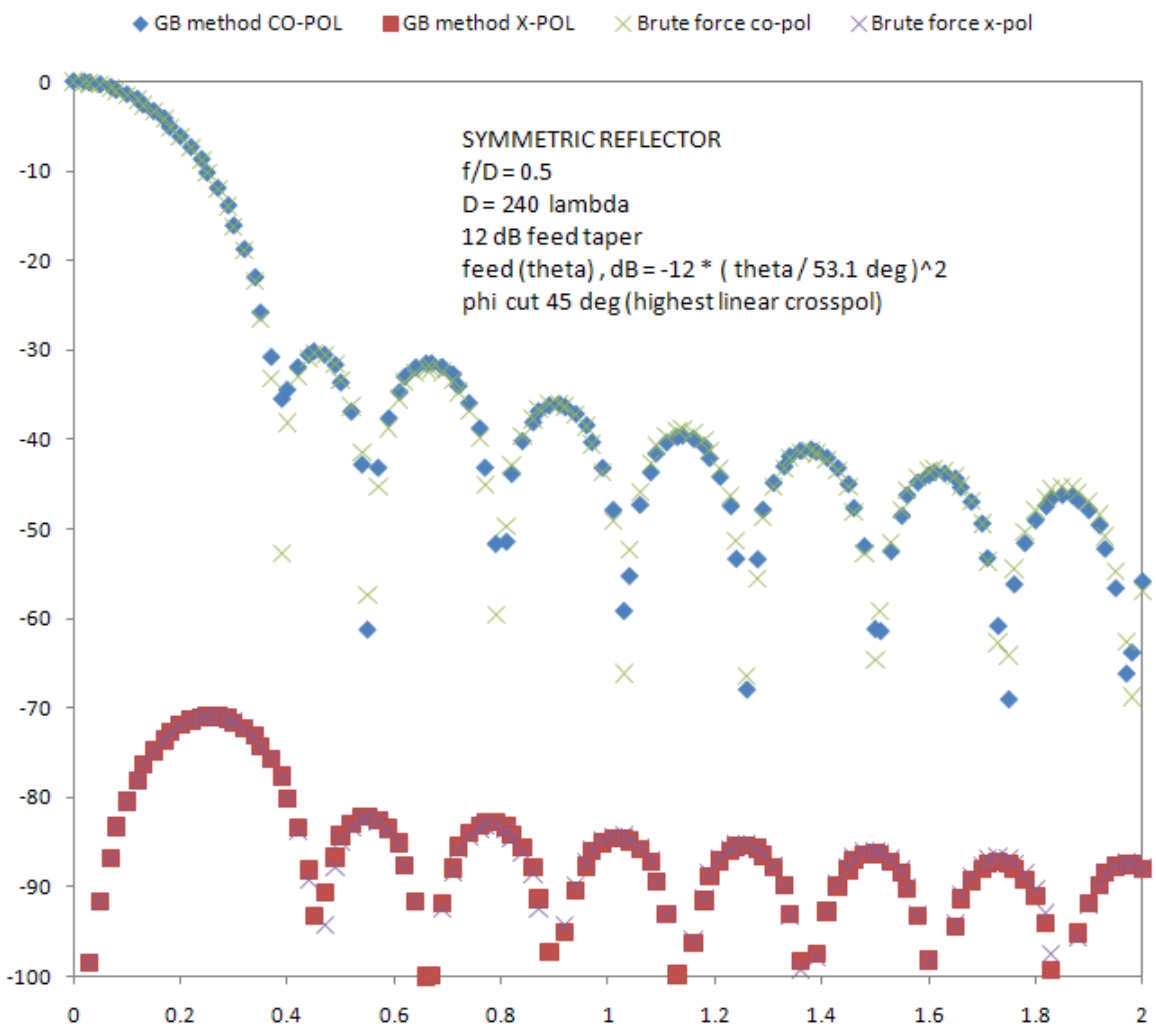

Fig. 6-13. Comparing Gaussian beam and brute force PO methods for symmetric reflector.

6.2.7.3 Offset Reflector

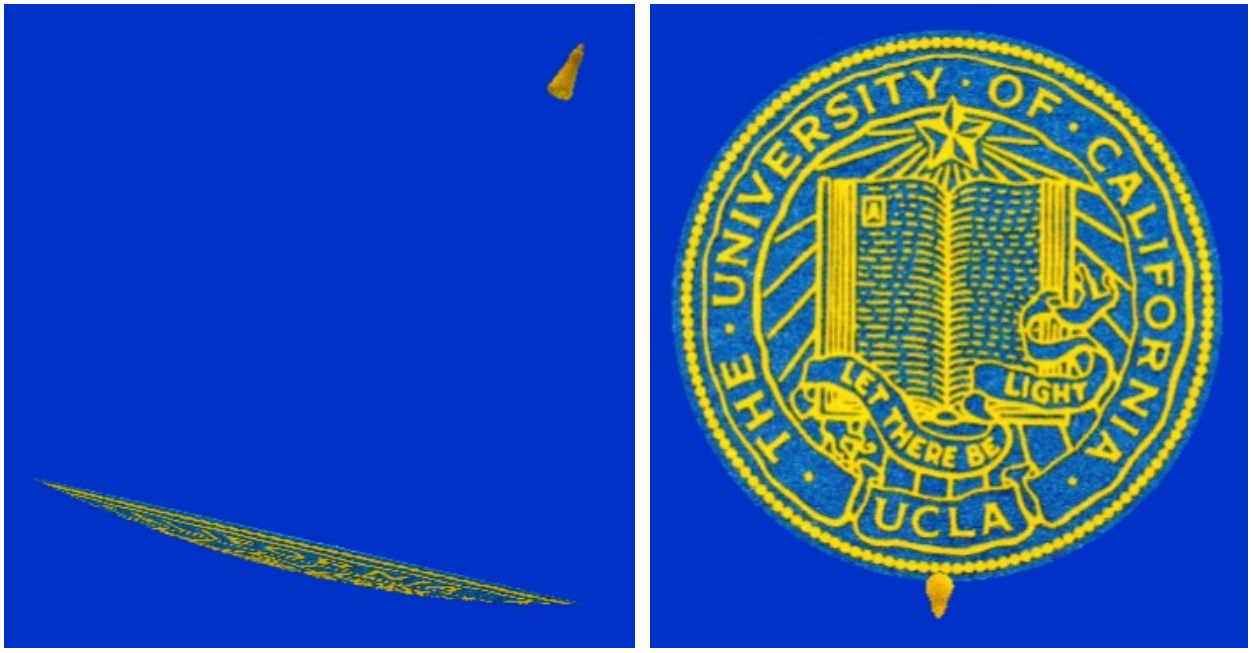

Fig. 6-14. The geometry of the offset reflector system analyzed in Fig. 6-15: The right view is from the main beam direction in the far field (orthographic projection); whereas, the left view is a perspective view from a point near the reflector. 3D graphics produced by the ARAM CYL_MM Windows ™ software developed for this dissertation. The CYL_MM software provides a 3D visualization of the reflector geometry specified in a set of ARAM DUAL reflector analysis software input files.)

Fig. 6-14 shows the offset reflector geometry for the comparison in Fig. 6-15 of brute force and the GB method for the case of an offset reflector of diameter 120 wavelengths, with f/D of 0.5 and Gaussian feed with 12 dB taper. The agreements of the co-polarized and cross-polarized components wrt brute force are both within less than a decibel over the plotted range. In order to achieve this level of accuracy the GB waist had to be adjusted to increase it slightly; although, such an increase tends to degrade the far-out sidelobes. This method appears to require a denser array of GBs for convergence of far-out sidelobes at correspondingly larger angles; e.g., N=3 out to 10 deg, N=4 to 25 deg, N=5 to 50 deg. Better results for the offset reflector were obtained in the cut plane orthogonal to the offset plane than in the offset plane.

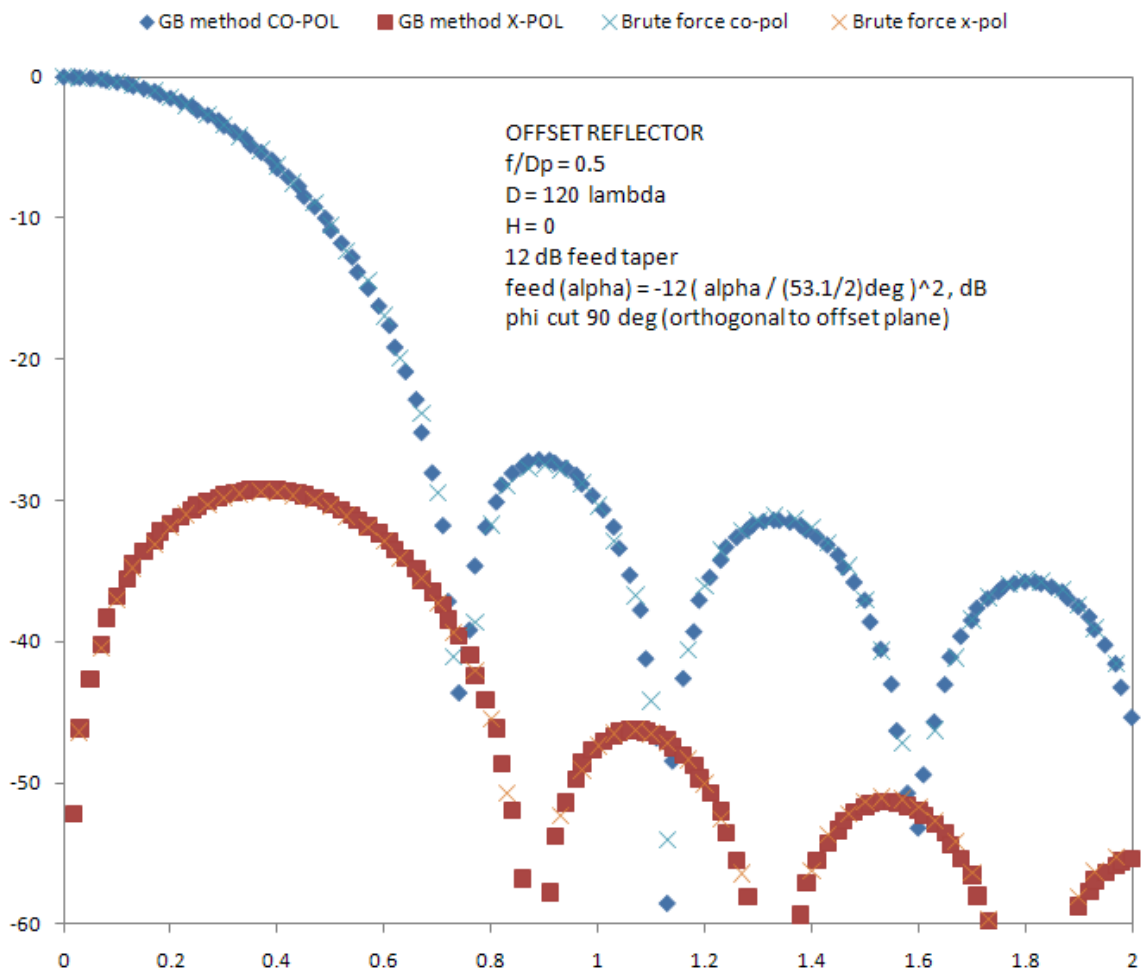

Fig. 6-15. Comparing Gaussian beam and brute force PO methods for the offset reflector depicted in Fig. 6-14, with pattern cut plane orthogonal to the offset plane.

6.2.8 Limitations

Because the GB phase front is parabolic rather than spherical (as a far field solution of Maxwell's equations require) the approximation of a feed's radiation pattern by an array of GBs is limited to a finite range of distance. If a feed pattern is decomposed into an array of GBs at a given distance from the feed, then that decomposition will match the feed pattern reasonably well only out to about ten times the given distance or one tenth closer in. This is indicated in the representative GB array patterns plotted as a function of distance in Fig. 6-16.

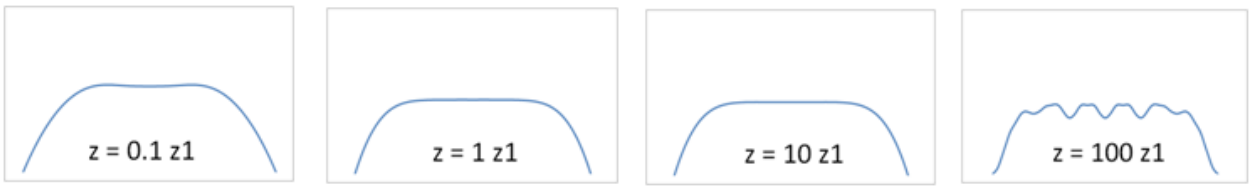

Fig. 6-16. GB array aggregate pattern as a function of distance.

The angle of incidence of the feed's illumination of the reflector surface must be modest. If a feed ray strikes the reflector at a very oblique, near-grazing, angle, then the locally quadratic Gaussian approximation breaks down.

The view angle of the reflector, as seen by the feed, must be significantly larger than the GBangle spacing of the GBs. The GB method assumes that the reflector surface is illuminated by a larger number of GBs.

The paraxial approximation requires that the Gaussian beam waist be larger than approximately six wavelengths [129]. By spacing the GBs by the divergence ray angle (to obtain a smooth decomposition of a radiation pattern), the paraxial approximation then effectively requires that the GB spacing be less than about three degrees; although 5 degrees is acceptable.

$$\text{GBangle} \;=\; \text{ray divergence angle} \approx \frac{w_0}{Z_r} = \frac{\lambda}{\pi w_0}, \text{ for small GBangle} \tag{6.15}$$

$$\frac{1}{6\pi} \text{ rad} \;\approx\; 3 \text{ deg} \tag{6.16}$$

The GB method assumes that the size of the GB spot beam on the reflector surface is minimized, and that condition in conjunction with spacing the GBs by the divergence ray angle establishes (6.17), where w is the GB waist, and GBangle is the angular separation of the GBs.

$$z_1 = \frac{\lambda}{\pi\left(\text{GBangle}\right)^2}, \quad \text{for} \quad \frac{\partial w\left(z, \text{GBangle}\right)}{\partial \text{GBangle}} = 0 \tag{6.17}$$

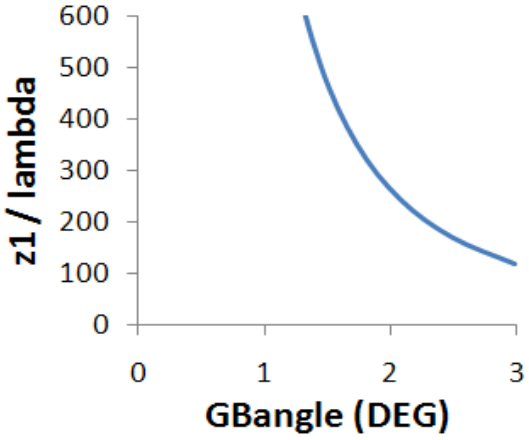

Fig. 6-17. Z1, the minimum distance between feed and reflector as a function of GBangle.

According to Fig. 6-17 the GB method is effectively limited to use with reflector systems with at least 120 wavelengths distance between the feed and the reflector surface, and at that minimum distance the minimum GB spot diameter (twice the waist) on the reflector surface is about twenty wavelengths — with the maximum GBangle of 3 deg. (If smaller GBangle were used the spot illuminated on the reflector surface would be even larger.) If a dual reflector system has less than 120 wavelengths between its feed and subreflector but greater than that between the feed and the equivalent parabola [55], then the GB method can still be applied to the equivalent parabola of the dual reflector system. With a typical ratio of focal length to diameter of 0.4 for reflectors used in communications applications, the GB method is effectively limited to reflectors of diameter larger than 300 wavelengths

6.3 LEVIN METHOD

The Levin method applies to integration over a rectangular domain. The two-dimensional Levin method [33], [35] is a numerical quadrature with the integrand being the product of one term that

slowly varies and an exponential term that can vary rapidly. The Levin method turns the original highly oscillatory integral problem into one of solving a partial differential equation instead. The equivalent partial differential equation is solved using a matrix collocation method, where a grid of points — about ten to thirty on a side — samples both the slowly varying term and the derivative of the exponential argument from the original integrand at a limited number of points. The original Levin method requires a minimum magnitude of phase derivative for convergence. Li [38]–[41] revises Levin's method to alleviate the minimum phase derivative requirement by revealing that the rank of the target matrix allows application of the truncated singular value decomposition method to solve the matrix system with good accuracy in spite of being ill-conditioned, using a Chebyshev differential matrix on Chebyshev-Lobatto nodes. Specifically, Li shows that only the last of the singular values of the target matrix approaches zero when the Levin system is ill-conditioned: The truncated singular value decomposition (TSVD) method reconstructs the system after removing that one, nearly zero-valued singular value and is thereby able to solve the system accurately. Essentially the TSVD solution resolves the problem of the Chebyshev differential matrix being inherently singular, with a zero determinant. Li utilizes a change of integration variable so that the substituted integration limits span from -1 to 1, to correspond with the range of the Chebyshev-Lobatto nodes. Li's two-dimensional method gains a considerable speed advantage over the original Levin method partly by approximating the two-dimensional integral with a cascade of two sets of one-dimensional integrals, at the cost of a slight loss of accuracy due to neglecting some of the terms in the two-dimensional total derivative.

6.3.1 Levin Fundamentals

The fundamentals of the Levin method are explained for the one-dimensional case. Given an original integral of the form

$$I = \int_a^b f(x)\exp\left[ig(x)\right]dx\,, \tag{6.18}$$

which is equivalent to integrating the total derivative of a different compound integrand:

$$I = \int_a^b \tfrac{d}{dx}\left\{p(x)\exp\left[ig(x)\right]\right\}dx\,, \tag{6.19}$$

whereby define the auxiliary function, $p(x)$, by the ordinary differential equation

$$p_x(x) + ig_x(x)\,p(x) = f(x), \quad \text{where } p_x(x) = \tfrac{d}{dx}\,p(x). \tag{6.20}$$

The original one-dimensional integral is equivalent to

$$I = p(b)\exp\left[ig(b)\right] - p(a)\exp\left[ig(a)\right]. \tag{6.21}$$

Thereby the problem of solving the original integral is transformed into one of solving an ordinary differential equation for the auxiliary function, $p(x)$, which can be computed quite rapidly using matrix collocation techniques. If the function is sampled at N points then the size of the matrix system to be solved is N.

Extension to the two-dimensional case is directly analogous. Given the two-dimensional integral

$$I = \int_a^b\int_c^d f(x,y)\exp\left[jq(x,y)\right]dxdy\,, \tag{6.22}$$

which is equivalent to the integral of the total differential of a different compound integrand,

$$I = \int_a^b \int_c^d \frac{\partial^2}{\partial x \partial y} \left\{ p(x,y) \exp\left[jq(x,y) \right] \right\} dxdy \tag{6.23}$$

whereby define the auxiliary function $p(x,y)$ by the partial differential equation

$$p_{xy} + jq_y p_x + jq_x p_y + \left(jq_{xy} - q_x q_y \right) p = f \ . \tag{6.24}$$

Then the original two-dimensional integral is equivalent to

$$\begin{aligned} I = {} & p(b,d) \exp\left[jq(b,d) \right] - p(a,d) \exp\left[jq(a,d) \right] \\ & - p(b,c) \exp\left[jq(b,c) \right] + p(a,c) \exp\left[jq(a,c) \right] \ . \end{aligned} \tag{6.25}$$

Thereby the problem of solving the original integral is transformed into one of solving a partial differential equation for the auxiliary function, $p(x,y)$, which can be solved using matrix collocation techniques. If each dimension is sampled at N points, then the size of the matrix to be solved is N^2. (An NxN matrix is required to uniquely solve the partial differential equation using collocation techniques.)

Note that the compute time for solving a matrix system of size S using LAPACK GESV scales as $O(S^3)$ [www.netlib.org/lapack]. Thus with each dimension sampled at N points the compute time of the one-dimensional case scales as N^3, and that of the two-dimensional case scales as N^6. Li's revision of the Levin method approximates the two-dimensional integral by a cascade of two sets of one-dimensional integrals in order to gain a considerable speed advantage, with a slight loss of accuracy due to the approximation.

Li's two-dimensional revision of the Levin method involves the cascade of two stages of one-dimensional integrals. Assume that the two dimensions of the rectangular domain are sampled respectively by M and N points. Li's first stage involves solving N systems of matrices each of

size M, representing N different one-dimensional integrals over the first variable in the rectangular domain, divided into N strips parallel to that first dimension, each respectively located at the N different sample points of the second dimension. Li's second stage then involves solving two final systems of matrices each of size N, representing one-dimensional integrals over the outer two strips of the rectangular domain, respectively located at the extrema of the sample points in the first dimension. The compute time of Li's revision of Levin's two-dimensional method thereby scales as $(2N^3 + NM^3)$, compared to $(MN)^3$ for the original Levin method. Li's method thereby gains an additional speed advantage for cases in which the integrand varies relative less over one dimension than the other — whereby numerical convergence can be achieved with different minimum M and N.

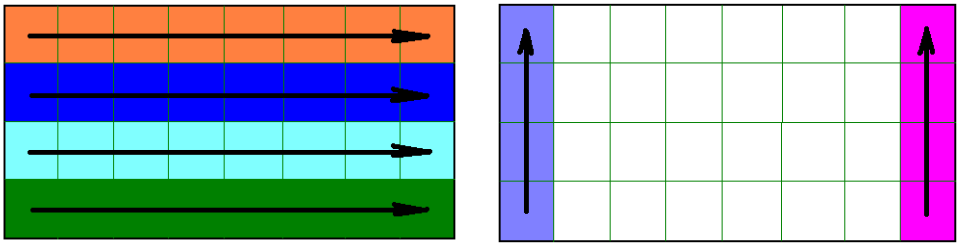

Fig. 6-18. The two stages, left then right, of Li's revision of the Levin 2D integration, respectively along the two dimensions: pictured on the left, with the horizontal bands, are the set of *p*(), and on the right the two vertical bands *r*(), on the left in blue, and *q*(), on the right in pink.

Li's revision of the two-dimensional Levin method is summarized by (6.26)–(6.33).

$$I = \int_a^b \int_c^d f(x,y)\exp\left[jg(x,y)\right]dxdy = \int_c^d \left[\int_a^b f(x,y)\exp\left[jg(x,y)\right]dx\right]dy \tag{6.26}$$

Approximation:

$$I \sim \int_c^d \left[\int_a^b \frac{d}{dx}\left\{p(x,y)\exp\left[jg(x,y)\right]\right\}dx\right]dy, \tag{6.27}$$

where

$$p_x(x,y) + jg_x(x,y)\,p(x,y) = f(x,y). \tag{6.28}$$

Here $p(x,y)$ is solved along strips of x at different y using matrix collocation techniques. Subsequently,

$$I \sim \int_c^d p(b,y)\exp\left[jg(b,y)\right]dy - \int_c^d p(a,y)\exp\left[jg(a,y)\right]dy. \tag{6.29}$$

$$I \sim \int_c^d \frac{d}{dy}\left\{q(y)\exp\left[jg(b,y)\right]\right\}dy - \int_c^d \frac{d}{dy}\left\{r(y)\exp\left[jg(a,y)\right]\right\}dy, \tag{6.30}$$

where
$$q_y(y) + jg_y(b,y)q(y) = p(b,y), \tag{6.31}$$

and
$$r_y(y) + jg_y(a,y)r(y) = p(a,y). \tag{6.32}$$

Here $q(y)$ and $r(y)$ are each solved along their respective strip of y using matrix collocation techniques. Finally,

$$I \sim q(d)\exp\left[jg(b,d)\right] - q(c)\exp\left[jg(b,c)\right] - r(d)\exp\left[jg(a,d)\right] - r(c)\exp\left[jg(a,c)\right]. \tag{6.33}$$

6.3.2 Chebyshev-Lobatto Nodes

Li's revision of the Levin method uses Chebyshev polynomial expansions to provide a computational speed advantage. Chebyshev polynomials of the first kind [133] have the form of (6.34). The Chebyshev polynomials provide faster convergence, in general, than other polynomial series [133], [134].

$$T_n(x) = \cos\left(n\cos^{-1}(x)\right) = \cosh\left(n\cosh^{-1}(x)\right) \tag{6.34}$$

The respective inverse trigonometric identities $\cos^{-1}(z) = \pi/2 + j\ln\left(jz + \sqrt{1-z^2}\right)$ and $\cosh^{-1}(z) = \ln\left(z + j\sqrt{1-z^2}\right)$ help relate the two forms of the Chebyshev polynomials of the first kind.

The computational speed advantage that Li's revision gains is related to the use of the Chebyshev differential matrix, which requires that the function that is represented by a Chebyshev polynomial expansion be sampled at the Chebyshev-Lobatto nodes. The specific locations of the Lobatto nodes are defined in (6.35). The Chebyshev-Lobatto nodes sample the endpoints of the integration interval more densely than the central region.

Lobatto nodes: $$x_k = \cos\left(\frac{\pi k}{N}\right),\ k = 0,1,2...N \tag{6.35}$$

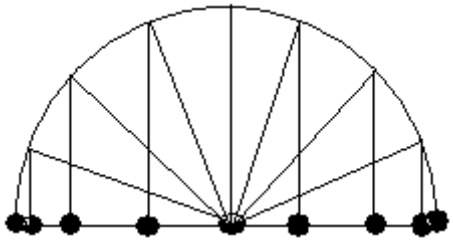

Fig. 6-19. Example set of Chebyshev-Lobatto nodes (line of large dots), showing how they relate to a uniform angular division of the unit circle and that they are more densely populated near the ends.

There are a few choices for implementing the Chebyshev-Lobatto grid system for the Levin+Li quadrature method. A few examples are shown in Fig. 6-20, which displays a) rectilinear integration axes with independent integration limits, b) cylindrical integration axes with independent integration limits, and c) rectilinear integration axes with the limits of the second integration axis being dependent on the first — in this case representing a circular aperture. The first (a) option provides significantly higher numeric quadrature computational efficiency than the others: It has the highest uniformity in its distribution of the grid points; whereas, the other two have their grid points clumped together in areas that do not contribute to convergence of the quadrature. Option (b) has an inefficient clustering of points in its central region as well as on its right side; its quadrature converges but requires substantially higher degree than (a) and thereby provides much lower computational efficiency. Convergence of the first four sidelobes using (b)

requires N on the order of 50; whereas, the grid system of (a) requires only N < 10. The two axes in (c) lose their orthogonality at the left and right sides of the circle, where the two axes become essentially parallel to each other, which hinders the convergence of the quadrature.

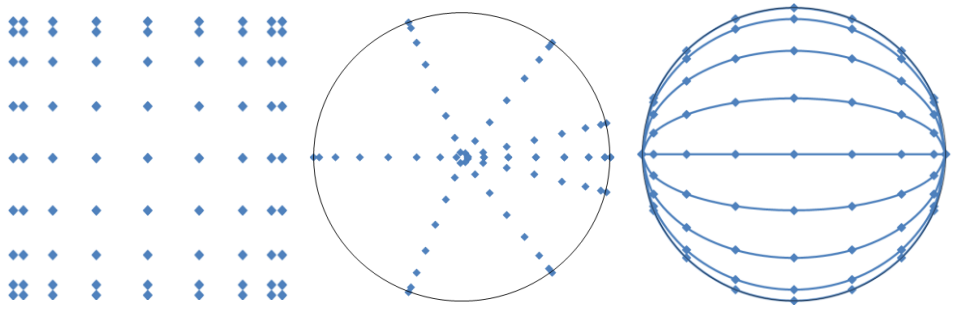

Fig. 6-20. Two-dimensional Chebyshev-Lobatto node grid system options for Levin method: a) independent rectilinear coordinates [x,y], b) independent cylindrical coordinates [ρ,φ], and c) rectilinear with the integration limits of the second integration variable dependent on the first variable [x,y(x)], in this case creating a circular aperture. The first option with independent rectilinear coordinates achieves the Levin quadrature with the highest computational efficiency.

6.3.3 Chebyshev Differential Matrix

The Chebyshev differential matrix, D, assumes a Chebyshev polynomial expansion that is sampled at the Lobatto nodes. The derivative of the Chebyshev polynomial expansion (of some function), sampled at the Lobatto nodes, is simply the matrix product of the differential matrix, D, and the sample vector (of points sampled at the Lobatto nodes).

$$D_{ij} = \begin{cases} \dfrac{2N^2+1}{6}, & i=j=0; \\ -\dfrac{2N^2+1}{6}, & i=j=N; \\ \dfrac{-x_i}{2\sin^2\left(\dfrac{\pi i}{N}\right)}, & i=j\neq 0,N; \\ \dfrac{-c_i}{2c_j}\dfrac{(-1)^{i+j}}{\sin\left(\dfrac{\pi(i+j)}{2N}\right)\sin\left(\dfrac{\pi(i-j)}{2N}\right)}, & i\neq j \end{cases} \tag{6.36}$$

where

$$c_k = \begin{cases} 2, & k = 0, N; \\ 1, & k = 1, 2, \ldots \mathrm{N}-1. \end{cases} \tag{6.37}$$

Table 6-1. Chebyshev differential matrix, $D_{i,j}$

$\frac{2N^2+1}{6}$	$\leftarrow$	$2\frac{(-1)^j}{1-x_j}$	$\rightarrow$	$\frac{1}{2}(-1)^N$
$\uparrow$	$\frac{-x_j}{2\left(1-x_j^2\right)}$	$\leftarrow$	$\frac{(-1)^{i+j}}{x_i - x_j}$	$\uparrow$
$\frac{-1}{2}\frac{(-1)^i}{1-x_i}$	$\uparrow$	$\frac{-x_j}{2\left(1-x_j^2\right)}$	$\downarrow$	$\frac{1}{2}\frac{(-1)^{N+i}}{1+x_i}$
$\downarrow$	$\frac{(-1)^{i+j}}{x_i - x_j}$	$\rightarrow$	$\frac{-x_j}{2\left(1-x_j^2\right)}$	$\downarrow$
$\frac{-1}{2}(-1)^N$	$\leftarrow$	$-2\frac{(-1)^{N+j}}{1+x_j}$	$\rightarrow$	$-\left(\frac{2N^2+1}{6}\right)$

An abbreviated summary of the Chebyshev differential matrix entries is that the off-diagonal values are

$$D_{kj} = \frac{c_k}{c_j}\frac{(-1)^{k+j}}{x_k - x_j}, \quad k, j = 0,1,2\ldots N, k \neq j \ , \tag{6.38}$$

and the diagonal values are a summation of the off-diagonal terms along a given row:

$$D_{kk} = -\sum_{n=0, n\neq k}^{N} D_{kn} \ . \tag{6.39}$$

6.3.4 Collocation Method of Solution

A matrix collocation method is used to solve for the auxiliary function *p*, sampled at the Lobatto nodes, as a key step to obtain the numerical estimate of the integral. By solving the differential

equation for the auxiliary function the oscillatory integral is solved. The original Levin method requires that

$$\left|\mathrm{g}_x\left(x\right)\right|\left|b-a\right| >> 1 \tag{6.40}$$

in order to (solve the matrix equation to) achieve prescribed accuracy. With Li's version of Levin's method (6.20) becomes, in matrix form,

$$\left[\mathrm{A}\right]\left[p\right] = \left[f\right], \tag{6.41}$$

$$\left[\mathrm{A}\right] = \left[\mathrm{D}\right] + i\left[g_x\right] \ . \tag{6.42}$$

[A] is called the target matrix. If (6.40) is not satisfied then the target matrix become ill-conditioned and standard linear matrix methods fail to solve for $p\left(x\right)$. Li found a way around this problem using truncated singular value decomposition by revealing that if [A] is of rank N when well-conditioned then the rank of [A] becomes only N-1 when it is ill-conditioned and only a modest number Chebyshev-Lobatto nodes (< 128) are used on each edge of the integration patch. The singular value decomposition (Golub [135], Sections 2.5.3 and 2.5.6) of [A] is [A] = $[\mathrm{U}][\mathrm{S}][\mathrm{V}]^{\mathrm{H}}$, where all matrices are square of size N+1 (about 10 to 30 < 128). [S] is a diagonal matrix containing a non-increasing ordered list of the singular real values, and [U] and [V] are, in general, complex unitary matrices with columns containing respective the left [U] and right [V] singular vectors. When the target matrix is ill-conditioned, as stated above, only the smallest of the target matrix' singular values becomes nearly zero-valued, and with that knowledge (6.41) is solved accurately using a truncated singular valued decomposition method (TSVD). An example of solving (6.41) by TSVD is

$$\left[p\right] = \left[\mathrm{V}_1\right]\left[\mathrm{S}_1\right]^{-1}\left[\mathrm{U}_1\right]^{\mathrm{H}}\left[f\right], \tag{6.43}$$

where $[S_1]$ is square of size N ([S] with its last row and column removed), and $[U_1]$ and $[V_1]$ are of size N+1 rows by N columns, being respectively [U] and [V] with their last columns removed. A fast TSVD method for solving (6.41) is provided by Chan [42], published when he was a UCLA professor. Chan's method uses a rank-revealing QR factorization and provides a least squares solution while avoiding having to compute the full singular value decomposition.

The procedure for solving the two-dimensional Levin method involves solving N+1 systems each of matrix size N+1, representing the first dimension of integration (e.g., *y*-axis), and then solving two more systems each of matrix size N+1, representing the second dimension of integration (e.g., *x*-axis). The solutions of the first set of N+1 systems are stored as the columns, *j*, of a size (N+1) x (N+1) storage matrix, and the first and the last rows of this storage matrix are subsequently used for the two respectively final system solutions, integrating over the second integration variable. The N+1 equations in the first set are summarized by (6.44), where $-1 \le x_k \le 1$ and $-1 \le y_k \le 1$ are the Chebyshev-Lobatto nodes. (A substitution of the original integration variables is made so integration occurs over the domain of the Lobatto nodes.)

$$\begin{bmatrix} p_x(x_0, y_j) \\ p_x(x_1, y_j) \\ \downarrow \\ p_x(x_N, y_j) \end{bmatrix} + i \begin{bmatrix} g_x(x_0, y_j)\, p(x_0, y_j) \\ g_x(x_1, y_j)\, p(x_1, y_j) \\ \downarrow \\ g_x(x_N, y_j)\, p(x_N, y_j) \end{bmatrix} = \begin{bmatrix} f(x_0, y_j) \\ f(x_1, y_j) \\ \downarrow \\ f(x_N, y_j) \end{bmatrix}. \tag{6.44}$$

The two final systems to be solved, integrating over the second dimension, are summarized by (6.45)–(6.48):

$$\begin{bmatrix} q_y(y_0) \\ q_y(y_1) \\ \downarrow \\ q_y(y_N) \end{bmatrix} + i \begin{bmatrix} g_y(1,y_0)q(y_0) \\ g_y(1,y_1)q(y_1) \\ \downarrow \\ g_y(1,y_N)q(y_N) \end{bmatrix} = \begin{bmatrix} p(1,y_0) \\ p(1,y_1) \\ \downarrow \\ p(1,y_N) \end{bmatrix} \tag{6.45}$$

$$I_1 = q(1)\exp\left[ig(1,1)\right] - q(-1)\exp[ig(1,-1) \tag{6.46}$$

$$\begin{bmatrix} r_y(y_0) \\ r_y(y_1) \\ \downarrow \\ r_y(y_N) \end{bmatrix} + i \begin{bmatrix} g_y(-1,y_0)r(y_0) \\ g_y(-1,y_1)r(y_1) \\ \downarrow \\ g_y(-1,y_N)r(y_N) \end{bmatrix} = \begin{bmatrix} p(-1,y_0) \\ p(-1,y_1) \\ \downarrow \\ p(-1,y_N) \end{bmatrix} \tag{6.47}$$

$$I_2 = r(1)\exp\left[ig(-1,1)\right] - r(-1)\exp[ig(-1,-1) \tag{6.48}$$

Finally, the solution of the two-dimensional numeric quadrature by the Levin method is

$$I = I_1 - I_2 \ . \tag{6.49}$$

If $g_x(x,1) = g_x(x,-1)$, which can hold for far field physical optics integrals with symmetrical reflector systems on principal phi cuts, the matrix systems (6.45) and (6.47) would then represent the same linear system differing only with unique right-hand side column vectors, in which case both systems can be solved simultaneously; e.g., using LAPACK xGESV, to help reduce the overall computational workload.

6.3.5 Truncated Singular Value Decomposition

The two-dimensional Levin solution by Li's method involves first solving N+1 different linear matrix systems of size M+1 (to effectively integrate over the first dimension) — here M and N are the parameters used in defining the order of the Chebyshev differential matrices — and then two more solutions of linear matrix systems of size N+1, to obtain the two-dimensional numeric

quadrature of the original physical optic integral. If the target matrix is well-conditioned, then the TSVD method is not required and the matrix equations may be solved using more traditional matrix methods. In the extreme case of zero phase derivative, $g_x(x) = 0$, then [A] of (6.41) is singular, with zero determinant, and yet the TSVD method solves the matrix system anyway, yielding $p(x) = \int f(x)$ in matrix form (sampled at the Chebyshev-Lobatto nodes). The original Levin method solves a single matrix system of dimension $(N+1)^2$, and also involves additional computations involving a basis function expansion of $p(x)$ that Li's method completely avoids (exploiting the natural properties of the Chebyshev polynomials sampled at the Chebyshev-Lobatto nodes), for which reason the improved Levin method runs considerably faster than the original Levin method.

There may be a way to obviate the need for use of the TSVD altogether: It may be possible to re-derive a variation of the Chebyshev differential matrix for use with the Chebyshev polynomial series expansion whereby the sample points are slightly — perhaps randomly — offset from the Chebyshev-Lobatto nodes. This would decorrelate the sample nodes from an exact correspondence with points sampled at equal angular spacing along a unit circle, and perhaps correspondingly provide for a non-singular differential matrix. This suggestion parallels the reasoning in 6.2.4 regarding the avoidance of a singular sampling matrix for the Gaussian beam method.

6.3.6 Limitations

First of all, Li's revision of the Levin method has somewhat reduced accuracy since it approximates Levin's 2D auxiliary partial differential equation with a two-stage cascade of

several 1D ordinary differential equations. Otherwise, the main restrictions of the use of (Levin's original and) Li's improved version of the Levin method [41] for physical optics applications are that the integration patch should not contain a stationary point with steep phase gradient within the central region of the integration patch, and the integration domain should not contain a resonant point (phase gradient perpendicular to the edge) with steep phase gradient. The issues in these regards are that the Chebyshev-Lobatto points sample the central regions only sparsely, while sampling the terminal regions of the integration domains densely, and sparse sampling is insufficient to capture the integrand content associated with a steep stationary or resonant point. Most accurate numerical quadrature results using Li's version of Levin's method are obtain by identifying the locations of any such stationary and or resonant points in the physical optics structure and choosing to place those points coincident with the corner vertices of the Levin integration patches in those areas. The Levin+Li method yields fast and accurate quadrature of the main beam and first sidelobes of a symmetric reflector using only a single Levin integration patch with only modest node count of N = 8; although convergence of the far-out sidelobes may required considerably higher nodes, perhaps N = 50. The quadrature will converge with much smaller N by locating the integration patch so that the phase gradient — even if small — varies more-or-less monotonically across the patch, as opposed to centering the patch about a pseudo stationary point (with only modest phase gradient): An example of this distinction is modeling a symmetric square reflector with a single Levin patch as opposed to four quarter patches — the main beam and first few sidelobes will converge with only modest node count in either case; although, the far out sidelobes in the latter case will converge with considerably smaller node count than the former.

6.3.7 Practical Application

A practical application of the Levin method is a large reflector system in which pseudo-rectangular patches are built into the structure. Fig. 6-21 shows an example of a large reflector constructed of large pseudo-rectangular subpanels. The physical optics contribution from each panel (or clusters of panels) may be quickly calculated using the Levin method. For example, Fig. 6-22 presents the far field radiation pattern of a square aperture parabolic reflector: The numeric quadrature is completed by the Levin method almost two thousand times faster than brute force with a standard one-tenth wavelength integration patch size. Fig. 6-25 presents the far out sidelobes by Levin+Li and brute force for a different square aperture reflector.

Fig. 6-21. Reflector antenna constructed with large pseudo-rectangular subpanels, from http://www2.l-3com.com/datron/.

6.3.8 Results

The following figures present a comparison of the results of the application the improved Levin method versus brute force for a few single reflector configurations involving symmetric and offset reflector apertures, as well as on- and off-axis feeds. Generally, the Levin method requires a higher order for off-axis feeds than on-axis feeds, and the use of the higher order does slow down the improved Levin calculations a bit. For the close-in sidelobe region of the far field pattern the improved Levin method requires a minimal order (around eight) for convergence with a symmetric reflector aperture. Resonant points must be avoided [35], [41] for convergence of the far-out sidelobes, and this in general means that the phase function over the Levin patch should be more-or-less monotonic to minimize the numerical order required for convergence. The inset graphics in the upper right corner of the following figures indicate the respective reflector models considered, and Fig. 6-25 through Fig. 6-27 in particular use an offset aperture, with one corner on-axis, in order to avoid resonant points within the Levin integration patch.

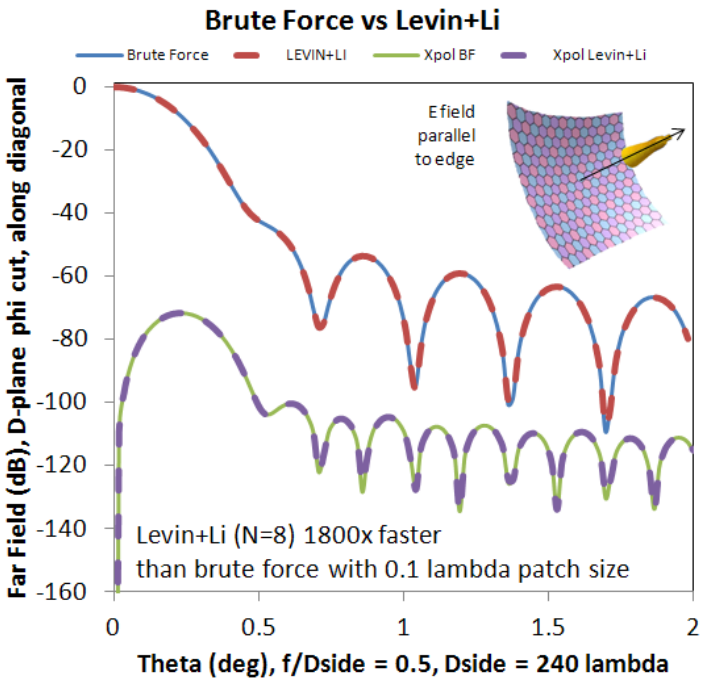

Fig. 6-22. Levin+Li method versus brute force with symmetric aperture and feed on axis: Far field pattern 45 deg cut phi angle, between E- and H-planes, of a square aperture parabolic reflector illuminated by a Gaussian feed with -12 dB feed taper at the center of the aperture edge. The numeric quadrature is completed by the Levin method 1800 times faster than brute force with one-tenth wavelength integration patch size. This uses the grid option (a) indicated in Fig. 6-20. Peak directivity is 57.2 dBi.

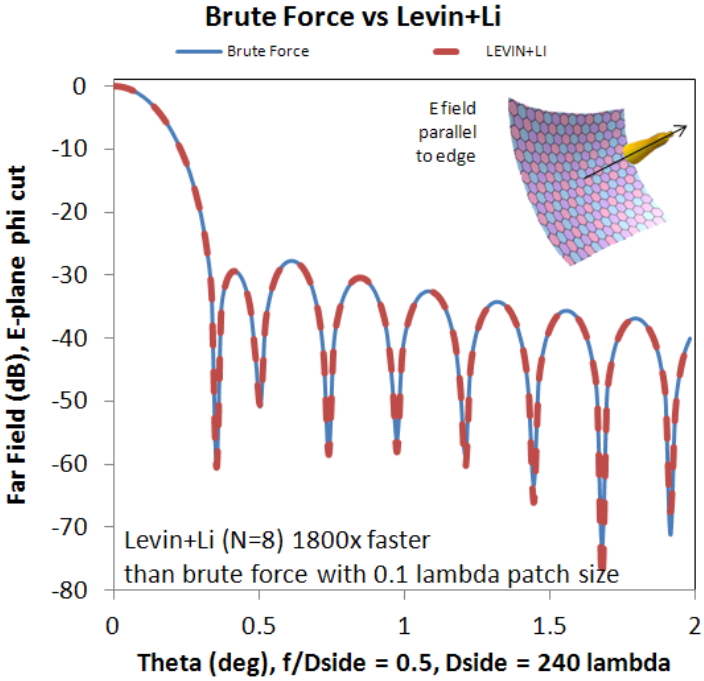

Fig. 6-23. Levin+Li versus brute force close in sidelobes, with symmetric aperture and feed on axis. This represents the same reflector and feed as in Fig. 6-22 but a different φ cut. Peak directivity is 57.2 dBi.

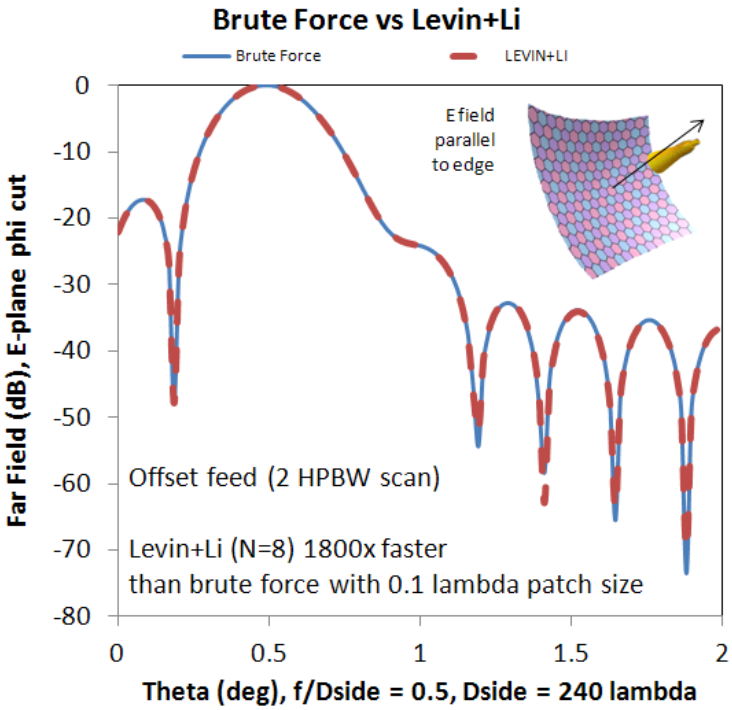

Fig. 6-24. Levin+Li versus brute force close in sidelobes, with symmetric aperture and feed offset for 2 HPBW scan. This represents the same reflector and feed as in Fig. 6-23 but with the feed displaced off-axis. Peak directivity is 56.9 dBi.

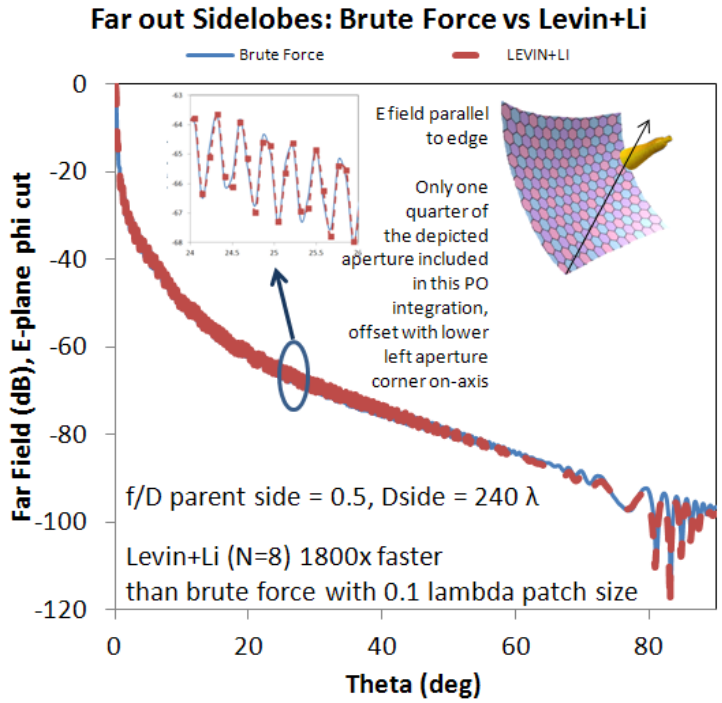

Fig. 6-25. Levin+Li versus brute force far out sidelobes, with offset aperture and feed on axis. This is an offset square aperture with one corner on-axis. The same feed pattern is used here as in Fig. 6-22.

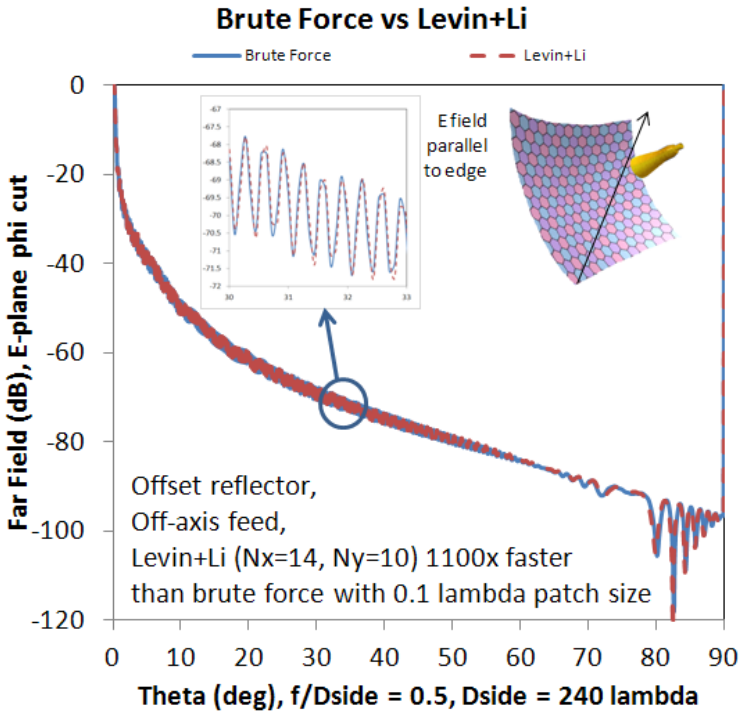

Fig. 6-26. Levin+Li versus brute force far out sidelobes, with offset aperture and feed offset from axis for 0.7 HPBW scan. The same feed pattern is used here as in Fig. 6-22.

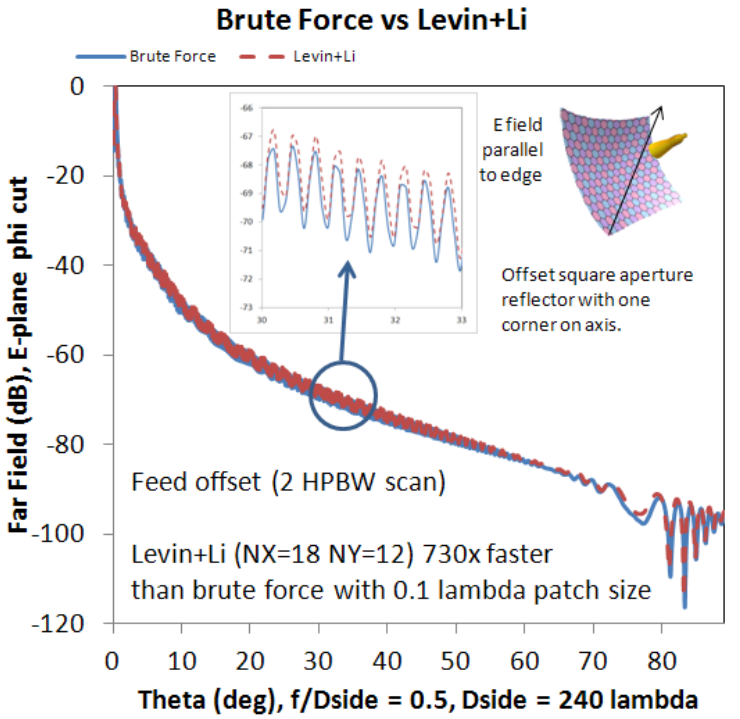

Fig. 6-27. Levin+Li versus brute force far out sidelobes, with offset aperture and feed offset from axis for 2 HPBW scan. The same feed pattern is used here as in Fig. 6-22. The reduced accuracy indicated in the inset plot is believed to be due to the approximation Li makes as identified in (6.27), which becomes more evident with asymmetrical systems such as this case of the feed being displaced significantly off axis.

The acceleration by Levin+Li for the two cases in Fig. 6-22 and Fig. 6-25 of square apertures with 240 wavelengths on a side is almost 2000 times compared to standard brute force with one-tenth wavelength sampling. The acceleration factor increases by the square of the frequency since the compute time of the Levin method is independent of frequency.

6.4 OPENCL GPGPU

The application of the graphics processor to computing antenna radiation patterns provides a substantial acceleration in speed. The same brute force physical optics (PO) code; e.g., a symmetric single reflector of two hundred forty wavelengths diameter, that runs single-threaded C/C++ on an Intel Core 2 Q8200 CPU and compiled to be optimized for speed, runs one hundred times faster when ported to OpenCL and run on AMD HD5850 GPUs hosted by the CPU systems. Porting the code to OpenCL involves opening the processing loops to be run in parallel and some additional code to host the GPU in the CPU system. The ability to accelerate antenna pattern computations by a factor of one hundred provides substantial benefits when many patterns need to be computed repeatedly, such as when optimizing a reflector system. With a GPU many work items ("threads") run in parallel and are grouped into local work groups, each sharing a modest pool of fast, local memory. A GPU has several compute units, and all work items in a work group operate on the same compute unit.

6.4.1 Introduction

GPGPU has proven to speed up scientific computing. In 2008 Peng and Nie [136] reported that their MoM calculations using a GPU (NVIDIA 8800GTX: Brook) ran more than 100x faster

than on a 3 GHz Intel Pentium 4 CPU. Tao, *et al.* [137], also in 2008, reported that their GeForce 6800 Ultra GPU electromagnetic computations were from 30 to several hundred times faster than on a 3.7 GHz Intel Pentium Extreme. And in 2010 a few APS magazine articles cited GPU acceleration versus single-threaded CPU: [138] reports 42x for FDTD (NVIDIA 9500GT GPU: CUDA) versus 1.8 GHz CPU, and [139] reports 50x for MoM (NVIDIA GTX-280 GPU: CUDA) versus 2.2 GHz CPU and anticipates porting the work to OpenCL.

OpenCL is like a multi-lingual interpreter helping to supervise a collection of workers of different languages. The overall operation of the program addressed in this chapter is summarized in Fig. 6-28; wherein, the run time of the number crunching section is to be minimized, and that section can be coded in different languages, but only OpenCL code (a kernel) is designed as a cross-platform language to utilize all of the processing elements in a heterogeneous system.

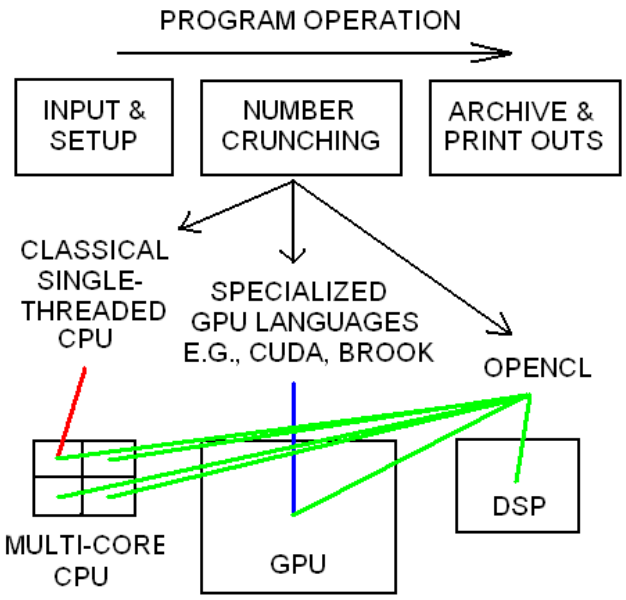

Fig. 6-28. An overview of the operation of the number-crunching computer code addressed here, highlighting the versatility of OpenCL.

This section presents an evaluation of the application of OpenCL language to code a GPU (AMD HD5850, 750 MHz baseline core clock) to calculate the brute force physical optics (PO) radiation patterns of a reflector antenna and compare the compute speed to that of single-threaded CPU code (Intel Core 2 Q8200 2.3 GHz). The HD5850 has 18 compute units (SIMD cores), each with 16 streaming cores (thread processors), each with 5 processing units (stream processors), for a total of 1440 processing units. The 18 compute units each have 32 kB of very fast, local memory shared by all work items in a workgroup. GPU time includes data transfer back to the CPU.

6.4.2 Physical Optics Implementation

The software codes implement the following equations. The far-field PO integral in spherical coordinates is defined in (6.50). The vector to a point on the reflector surface is $\bar{r}'$, the unit vector in the observation direction is $\hat{r}$, the distance to the observation point is r, $k = 2\pi / \lambda$, λ is the wavelength, η is the impedance of free-space, $\hat{n}$ is the reflector surface unit normal vector, $\bar{J}_{\mathrm{PO}} = 2\hat{n} \times \bar{H}_{\mathrm{inc}}$ is the PO reflector surface current from the magnetic field from the feed, and j is the positive square root of negative one with time convention exp[$j\omega t$]. Co- and cross-polarization field orientation is defined by Ludwig's 3rd definition for both the feed and the far-fields.

$$\bar{E}_{far} = \frac{-jk\eta e^{-jkr}}{4\pi r}\left(\hat{\theta}\hat{\theta}\cdot + \hat{\phi}\hat{\phi}\cdot\right)\iint \bar{J}_{\mathrm{PO}}\left(\bar{r}'\right)e^{jk\left(\bar{r}'\cdot\hat{r}\right)}ds' \tag{6.50}$$

The CPU pseudo code: surface area for-loop; feed pattern (Ludwig 3rd); JPO; pattern angle for-loop; co- & x-pol (Ludwig 3rd); propagation phase; accumulator (PO integral); end pattern and surface area loops.

The GPU implements the same functionality in OpenCL, hosted by the CPU. The code is organized with two OpenCL kernels and the host program. Pseudo code of the host program: allocate host memory; initialize OpenCL (identify the GPU, create OpenCL context and two command queues); enqueue (run) the two kernels; transfer the PO pattern data from GPU to CPU to be archived; release OpenCL and host resources. The PO kernel #1 program: identify which elemental surface area the work item represents; feed pattern (Ludwig 3rd); JPO; pattern angle for-loop; co- & x-pol (Ludwig 3rd); propagation phase; store result in local memory; barrier (coordinate work items); first-stage reduction (sum up all contributions from all work items in the work group); barrier; the one head work item in the work group copies the result from local to global memory; barrier; end pattern loop. The final reduction kernel #2 program: identify which PO pattern sample this work item represents; reduce kernel #1's work group contributions for the pattern sample from global memory, with *mem_fence*() between each global memory read; store the result in global memory. Kernel #1 involves 262,144 work items divided into 4096 work groups (64 work items each), with each work item allocated two float complex values of local data shared (LDS) memory, recycled for each pattern point, for a total of 1 kB LDS per work group (32 kB available). Kernel #2 involves 512 work items divided into 64 work groups (8 work items each).

6.4.3 Results and Conclusion

Fig. 6-29 summarizes the results computing the far field PO patterns of a parabolic, symmetric single reflector antenna with a square aperture 240 wavelengths on a side. The f/Dside is 0.5, with linear polarization (parallel to aperture edge). A $\cos^q$ feed pattern is used with q = 2.708 for 12 dB feed taper at the middle of the sides. Using GPU native math functions provides about 20% speed increase of the PO kernel #1 at a cost of a very few hundredths of a dB accuracy. Using the native math the GPU is 130x faster (than single-threaded C/C++ CPU code compiled using MS Visual Studio with the –O2 compiler option to maximize runtime speed), with essentially identical results. The GPU reduction spends about 40% of the GPU compute time. Using the GPU's native math and the manufacturer's over-clocking utility to set the GPU core clock to 1 GHz makes the GPU 170x faster than the CPU, in which case the GPU's (compute time) (clock rate) product is 370x smaller than the CPU's. The significant speed advantage of the GPU can significantly reduce the run time of applications such as the optimization of reflector systems, which repeatedly calculate many patterns.

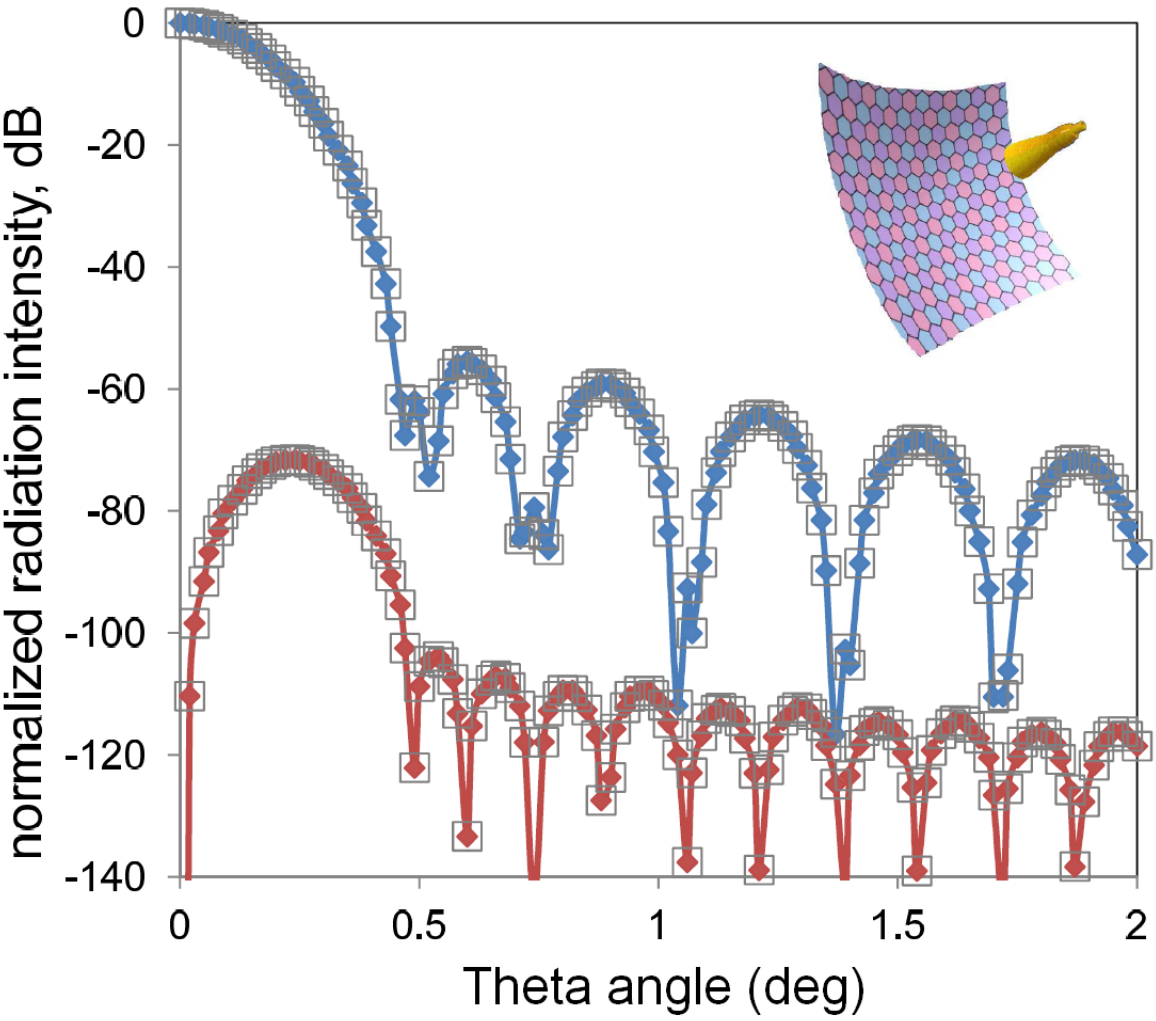

Fig. 6-29. CPU & GPU (open squares) PO co- and cross-pol far field 45 deg phi cuts (between E & H planes, along aperture diagonal) of parabolic reflector with square aperture 240 λ on a side. CPU single-threaded compute time 7.9 sec with 128 pattern points and 0.47 λ integration patch size. GPU compute time 61 ms using GPU native math functions or 77 ms without. The feed pattern is $\cos^q$ with q = 2.708 for -12 dB feed taper at center of aperture side edge.

6.5 CONCLUSION

The method of physical optics, with its reference single-threaded compute speed, is compared to several method of numerical acceleration. The Gaussian beam method employs decomposition of the feed pattern by an angular array of Gaussian beams (paraxial solutions of Maxwell's equations) and a closed-form asymptotic evaluation of the contribution to the overall physical

optics integral by each beam. The improved Levin method utilizes Chebyshev-Lobatto nodes and the Chebyshev differential matrix, along with the truncated singular value decomposition least squares method to provide fast numerical solution of matrix equations that significantly accelerate the computational speed — by up to three orders of magnitude with integration patch size of 240 wavelengths on a side — over pseudo-rectangular patches of single-threaded physical optics integral. The new OpenCL language harnesses the compute power of graphics processors to calculate the very same equations as the brute force physical optics method, except that when ported to OpenCL these same equations run hundreds of times faster on a graphics processor than the reference speed of single-threaded physical optics. A summary comparison of the speeds of these methods is presented in Table 6-2.

Table 6-2. Relative speed comparison of several methods for computing physical optics integral radiation patterns with 1000 point phi cut covering the main beam and first several sidelobes.

METHOD	APERTURE DIAMETER 240 λ	APERTURE DIAMETER 2400 λ	ACCOUNTS FOR REFLECTOR DEPTH?	COMPUTATIONAL MEMORY DEMAND
Brute Force (λ / 10)	1	1	YES	Few MB
Gaussian Beam (N = 3)	6e1	6e3	YES	Few MB
Levin + Li (N = 8)	2e3	2e5	YES	Few MB
BF OpenCL GPU	1e2	1e2 – 1e3	YES	100MB–10GB
FFT2D (λ / 10, CPU)	3e3	2e3	NO	100MB–10GB
Three-Parameter Distrib.	7e6	7e8	NO	Few MB

CHAPTER 7 SYSTEM-LEVEL CHARACTERIZATION

At the system level there are particular performance characteristics that can significantly affect a reflector antenna's performance in a given application, which must be considered and evaluated. Two such characteristics are squint of a circularly polarization beam and the ratio of receive gain to system noise-temperature (G/T). Any squint between the complementary circularly polarized (CP) beams (left-handed LCP and right-handed RCP) causes beam separation that, if unaccounted for, can cause unexpected signal loss in one beam when tracking the other. The G/T of a receiving antenna is basically the bottom-line metric of the antenna's reception capability: It's a key factor included in a communication system's link budget. The higher the G/T is the higher the quality of communications, since high gain and low system noise-temperature promote better reception quality. System noise-temperature is primarily determined by a low-noise amplifier that is often integrated with the reflector's feed horn.

1.1 CP SQUINT

Squint of circularly polarized (CP) beams is a characteristic of an offset reflector antenna system, where the squint occurs in the plane perpendicular to the offset plane. Offset reflectors have the advantage of having no aperture blockage – the feed is offset out of the aperture – but have the side effect of beam squint. Squint is only associated with circular, and not linear, polarization.

The CP squint plane is perpendicular to the offset plane. The LCP and RCP beams squint in opposite directions (which match the directions of the eyes in a cross-eyed face looking in the direction of the reflector's beams) in the squint plane.

Fig. 7-1. Squinted (exaggerated) CP beams from an offset reflector. (Photo from www.ebay.com)

A simple formula that accurately approximates the magnitude of the squint can provide a fast estimate of the effect to help accelerate the analysis of a reflector antenna's characteristics. The CP squint is caused by a natural tilting of the polarization vector across the aperture, which is naturally caused by the offset reflector geometry. With CP a rotational tilt of the polarization is equivalent to either an advance or delay of the propagation phase, depending on the direction of the tilt: left or right. If you were to be able to watch the RCP polarization vector as it illuminated the face of the reflector through its cycles, it would appear to rotate counter-clock-wise. With the offset feed located below the reflector aperture, and looking at the reflector aperture from the far field, the offset reflector geometry naturally causes the polarization vector to tilt like a backslash \ on the left side of the aperture (effectively advancing the phase of the propagation wave) and to tilt like a forward slash / on the right side (effectively delaying the phase of the propagation wave on the right side). These relationships cause the RCP beam to tilt to the left when viewed from behind the reflector (or to the right when viewed from the far field), because a

linear phase gradient across the aperture is equivalent to a beam squint. These same relationships cause the LCP beam to tilt in the opposite direction. The magnitude of the squint can be determined by analyzing the geometry of the polarization tilt across the reflector aperture.

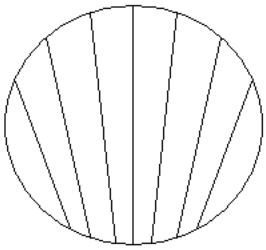

Fig. 7-2. Polarization Tilting Across an Offset Reflector Aperture. (The offset is vertical.)

Rotational matrices provide a simple evaluation of the magnitude of the squint, starting with a reference vector in the polarization reference frame (using Ludwig's 3rd definition of polarization [87]). A rotational matrix is first used to lay a reference polarization vector (unit *y* vector) from the feed down onto the offset reflector surface, with rotation angle θ_S, as depicted in Fig 3.g.i-3. A second rotational matrix is then used to translate the prior resulting vector into the general feedhorn reference frame, with rotation angle ψ. A third rotational matrix, with rotation angle θ_0, then translates the prior result into the main reflector reference frame (with its z-axis parallel to the axis of the parent parabola of the offset reflector). The final result is the Ludwig (3rd) polarization vector *q*, as viewed from the far field.

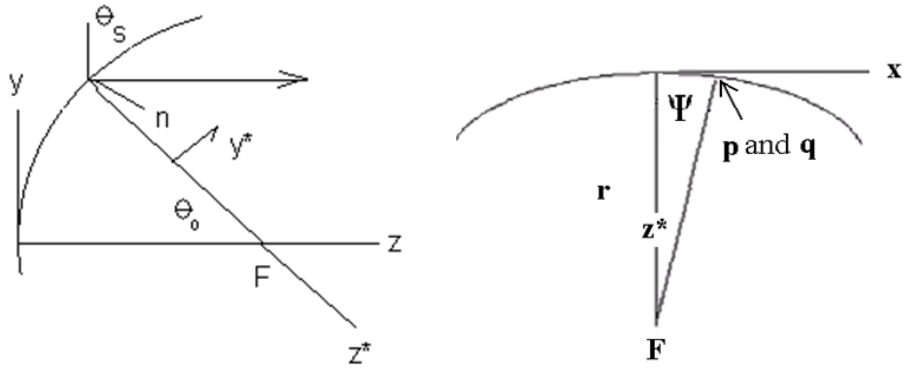

Fig. 7-3. Geometric diagrams for squint calculations.

$$\hat{q}\Big|_{\phi=\pi/2,\,\psi\approx 0} \approx \left[RF_X(-\theta_0)\right]\left[RF_Y(\psi)\right]\left[RV_X(-\theta_S)\right]\begin{bmatrix}0\\1\\0\end{bmatrix} \tag{7.1}$$

$$\hat{q} \approx \begin{bmatrix}\sin\theta_S \sin\psi\\ \cos\theta_S \\ N/A\end{bmatrix} \tag{7.2}$$

The squint angle, assumed small, is then derived through a small-angle approximation of the vector q.

$$\text{Polarization Tilt, } \phi_T = \tan^{-1}\frac{q_X}{q_Y} \approx \tan^{-1}\left[\sin\psi\tan\theta_S\right] \tag{7.3}$$

$$\sin\psi \approx \frac{\Delta x}{r} = \frac{\Delta x(1+\cos\theta_0)}{2\mathrm{f}} \tag{7.4}$$

$$\phi_T\Big|_{\psi\approx 0} \approx \frac{\Delta x(1+\cos\theta_0)}{2\mathrm{f}}\tan\theta_S = \frac{\Delta x\sin\theta_0}{2\mathrm{f}} \tag{7.5}$$

$$\theta_{\text{squint}} = \sin^{-1}\left[\frac{1}{k}\frac{\partial\phi_T}{\partial x}\right] \approx \sin^{-1}\left[\frac{\sin\theta_0}{2k\mathrm{f}}\right] \tag{7.6}$$

This simple equation can be used to quickly and accurately estimate the magnitude of the CP squint from an offset reflector system.

7.1 G/T

Antenna gain-to-system-noise-temperature ratio (G/T) is a key figure of merit in the characterization of an antenna's reception performance. The most practical method of measuring G/T involves the use of a distant signal source of known signal strength. The Sun is a very

distant and strong signal source which has been studied by many organizations to evaluate its signal strength in different frequency bands. Here we evaluate the method, review several published solar flux models, and identify which appears to be the most accurate of those models. G is the antenna gain in decibels, referenced to isotropic gain, and T is the equivalent noise temperature of the receiving system in Kelvin, all at the same receive frequency and referenced to the same point in the antenna system.

The basic relationship involved in measuring an antenna's G/T using the Sun equates Boltzmann's law with the effective aperture size of the antenna, A_{eff}, and the solar flux density, S. Solar radio emission is un-polarized and so includes both polarizations (polarization is always divided into a complementary pair, such as horizontal/vertical or RCP/LCP): Thus an additional factor of two is included in Boltzmann's relation involving the Sun's effective radio noise temperature.

$$k(2\mathrm{T}_{\mathrm{Sun}}) = \mathrm{SA}_{eff} \tag{7.7}$$

The Friis transmission formula relates the effective antenna aperture size to the gain, G, as a function of wavelength. The solar G/T measurement involves taking the ratio of noise power detected by the antenna receive system (including its low-noise amplifier, or LNA) with the antenna pointed at the Sun, then pointed away from the Sun (at "cold sky"), and then comparing the two values. The detected noise power in latter direction (cold sky, pointed away from the Sun) is defined as the system noise power level. This measurement is referred to as a "Y factor."

$$G = \frac{4\pi A_{EFF}}{\lambda^2} \tag{7.8}$$

$$Y_{\text{Sun}} = \frac{T_{\text{Sys}} + T_{\text{Sun}}}{T_{\text{Sys}}}$$
$$T_{\text{Sun}} = T_{\text{Sys}} \left(Y_{\text{Sun}} - 1 \right) \tag{7.9}$$

Two correction factors are introduced to improve the accuracy of the measurement. The intent here is to measure the peak G/T, at the peak of the antenna's main beam, which has a finite beamwidth. Since the Sun is not a point source, and the Sun's radio signal is received over a finite portion of the antenna's beam pattern, a correction factor, K_{HPBW}, is introduced to account for the antenna's half-power beamwidth in relation to the Sun's apparent radio diameter [140]. The Sun's apparent radio diameter is a function of frequency, and this is also accounted for [141] in the determination of the K_{HPBW} correction factor. The solar flux level varies day by day and the high-noon flux value is reported by a number of stations distributed around the world (e.g., National Oceanic and Atmospheric Association). An additional correction factor, K_{ATMOS}, is included to account for the local atmospheric attenuation, which is a function of both the local weather and also the elevation angle of the Sun at the particular hour at which the G/T measurement is taken. The atmospheric attenuation affects the G/T measurement by absorbing a portion of the solar radio flux. An accurate model of the atmospheric attenuation up to 60 GHz is documented by equations found in ITU-R P.676 (*Attenuation by Atmospheric Gases*), P.618 (*Propagation data and prediction methods required for the design of Earth-space telecommunication systems*) and P.453 (*The radio refractive index: its formula and refractivity data*). ITU-R stands for the International Telecommunication Union (ITU), radio communications sector.

All of the factors discussed in the preceding few paragraphs combine to produce the following equation used to measure an antenna's G/T ratio using the Sun:

$$\frac{G}{T_{SYS}} = \frac{\mathrm{K_{HPBW}K_{ATMOS}}}{\mathrm{S}\,\lambda^2}(Y-1)8\pi k \tag{7.10}$$

The solar radio emission spectrum has a characteristic shape as a function of frequency. At high frequencies (far above 10 GHz) the solar spectrum adheres closely to the Planck blackbody radiation model and varies little throughout the sunspot cycle. At frequencies below 10 GHz the solar emission spectrum exceeds the blackbody model, as shown in the figure below, and there is notably strong emission band near 2 GHz during the *active* period. The Sun's radio emission spectrum changes substantially at frequencies below 10 GHz as it passes through the *active* and *quiet* periods of its eleven year sunspot cycle. Some notable models of the solar emission spectrum [142] fail to satisfy the high frequency boundary condition of convergence with the Planck blackbody model. The Daywitt model [141] under/over estimates the solar spectrum for frequencies below/above 5 GHz. Among published solar spectrum models [141]–[143], the emission flux of the *quiet* Sun is represented most accurately by the Kennewell model [143].

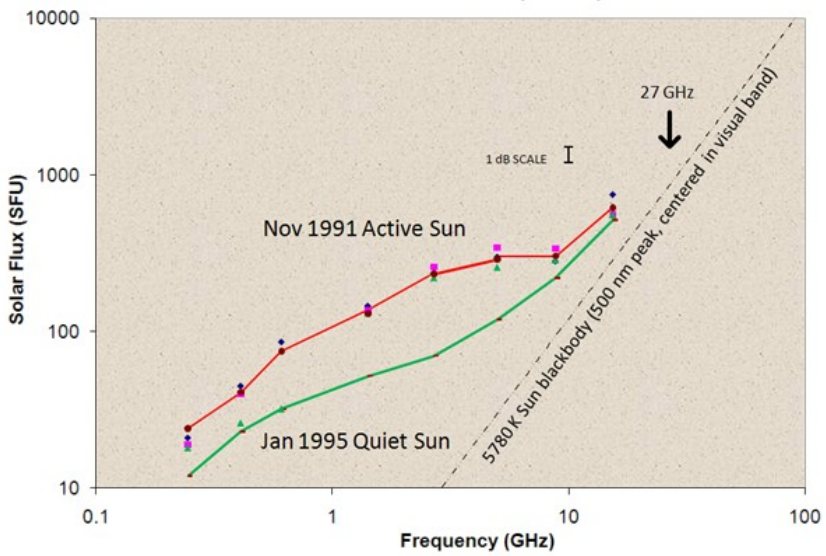

Fig. 7-4. Solar Radio Emission Spectrum: Active and Quiet Phases.

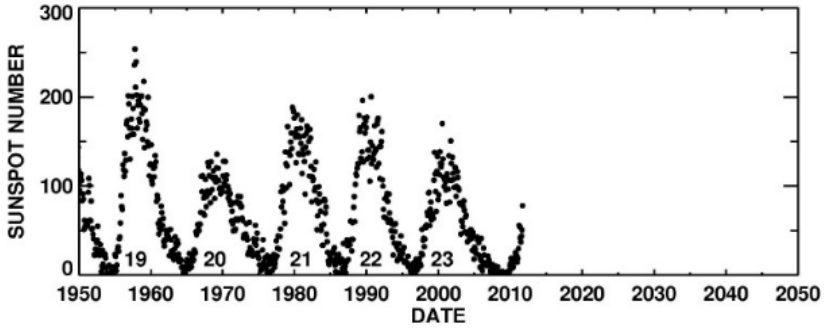

Fig. 7-5. Historical record of the solar sunspot cycle.

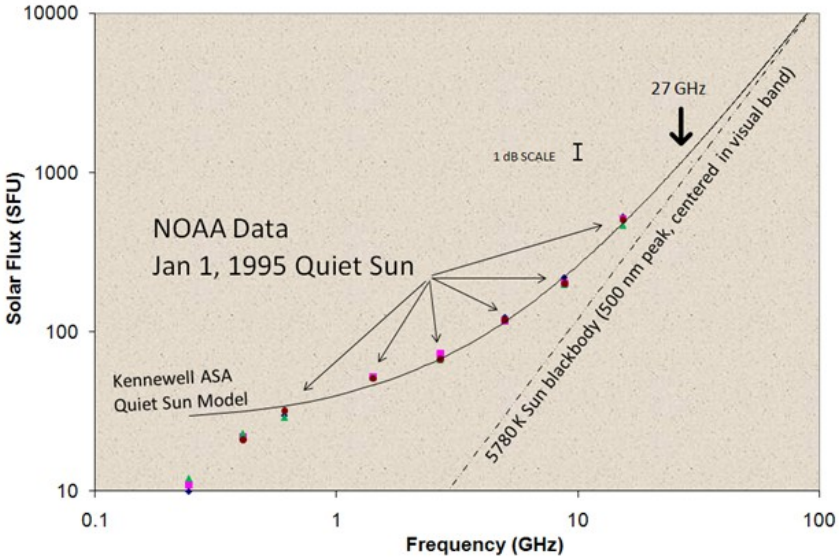

Fig. 7-6. Kennewell Model Compared to NOAA Data of Quiet Sun Phase.

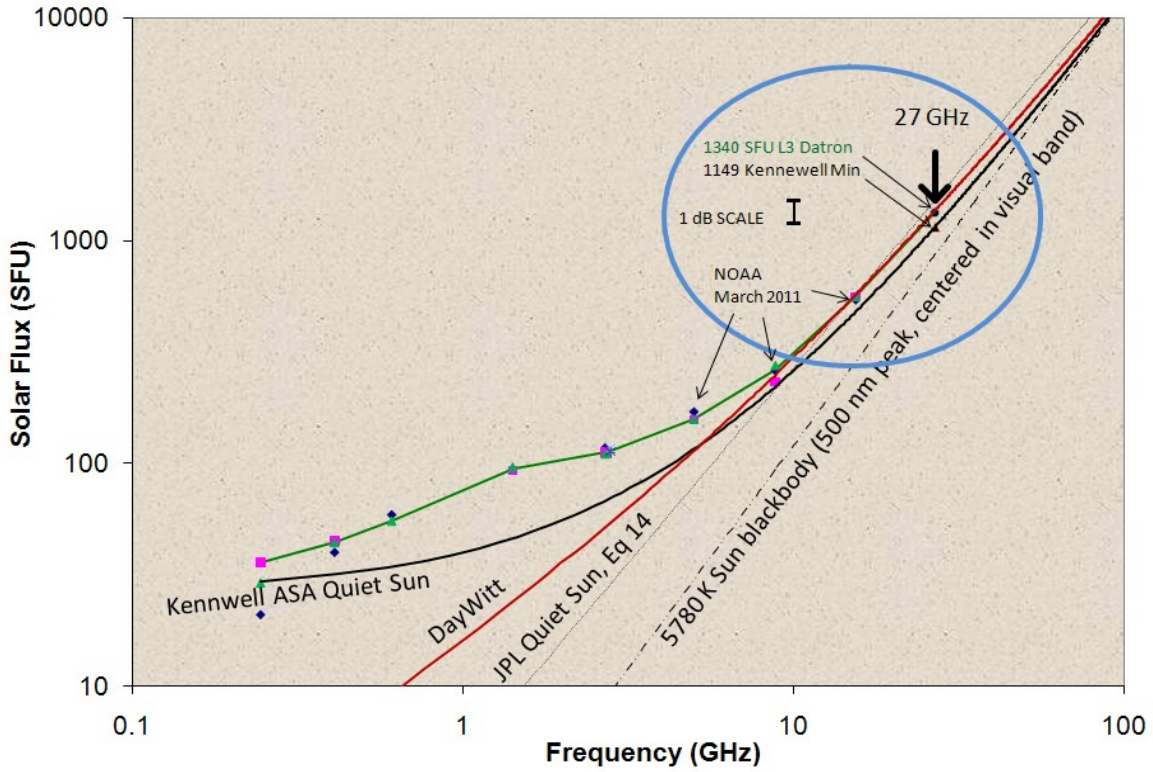

Fig. 7-7. Comparison of Several Models of Solar Spectrum: [Kennewell, Daywitt, Linsky (JPL)] with Typical Data.

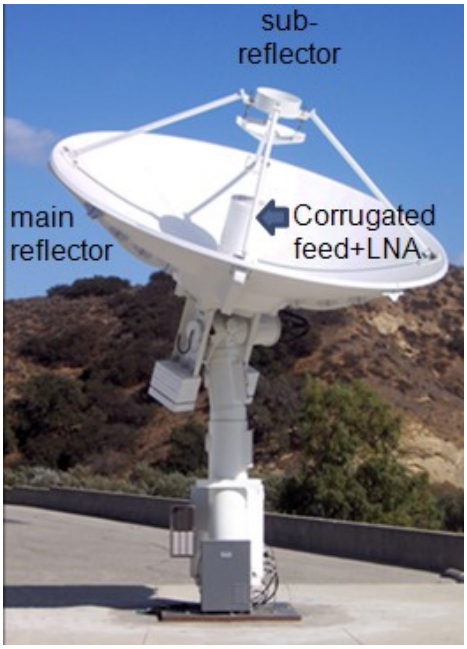

Fig. 7-8. Reflector antennas system used to make the solar measurements. (Photo cleared for public presentation by L-3 Communications [144])

Table 7-1. UCLA/Datron 27 GHz Lunar/Solar Flux Measurements.

2011 March	Moon Diam (deg)	Moon Y (dB)	Moon Temp (K)	Moon EL (deg)	Sun EL (deg)	Sun radio diam	Sun Y (dB)	Sun T (K)	Sun SFU
15	0.534	0.90	205	25	25	0.540	10.07	8160	1240
25	0.523	0.71	232	21	22	0.539	8.92	8880	1350
29	0.500	0.96	206	41	42	0.538	10.62	8710	1320
30	0.496	0.90	199	43	54	0.538	10.59	9030	1370
31	0.493	0.90	192	25	25	0.538	10.59	8710	1320

The columns in Table 7-1 indicating the elevation angles of the moon and sun at the times of the measurements show that the measurements were timed so those elevation angles were nearly identical during each measurement. This was done to try to normalize out the effects of the atmospheric losses due to various weather conditions, and as can be seen by the second row of data the method worked rather well: On March 25, 2011, the weather was overcast with drizzle, and the Y-factors measured with both the moon and the sun were correspondingly low, and yet the effectively measured solar flux level is comparable to the other measurements taken with clear weather.

7.2 CONCLUSION

In this chapter the system-level characteristics of the squint of a circularly polarized beam in an offset reflector configuration and the measurement of receive antenna system gain-to-system-noise-temperature (G/T) ratio are discussed in a manner that helps make the characterization of such system more rapid. A closed-form expression that can be quickly evaluated is derived by considering the polarization tilting across the aperture of an offset reflector system illuminated by a circularly polarized feed. The results of a Ka-band solar flux study are presented that allows

for properly calibration of the solar flux over frequency in order to utilize measurements of the solar flux by an antenna under test (AUT) to quickly estimate the G/T ratio of the AUT. The G/T ratio of a receive system is often considered the bottom-line measure of the quality of the receive antenna. At 27 GHz the solar emission was calibrated by this study at a level of 1340 SFU. This measurement effectively extends the NOAA data with a natural curve, along both the Kennewell ASA and Daywitt quiet Sun spectral models, and projects convergence with the Planck blackbody radiation model, as would be expected.

CHAPTER 8 APPENDICES

The appendices for the individual chapters are gathered altogether here.

8.1 APERTURE FAR FIELD POLARIZATION (3.1)

The following three theoretical (zero cross-polarization) aperture field scenarios address the field orientation in the far field for the aperture cases of magnetic field only, electric field only and balanced TEM with both electric and magnetic fields. Koffman [86] pg 39 states that with (feedhorn) apertures larger than a few wavelengths the far field polarization is similar to that of a Huygens source, for which the θ and ϕ field components are related through $\tan\phi$: That is shown to be the case for a balanced TEM aperture in case 3 below. Thus Ludwig's third definition of polarization [87] — that of a Huygens source — is applied to all apertures considered in this dissertation, feedhorn or reflector, since all apertures in consideration are larger than a few wavelengths with essentially balanced TEM electric and magnetic fields.

1. If a zero cross-polarization planar aperture has purely *y*-directed H_{AP} field only $\left(E_{\text{AP}}=0\right)$, then by the field equivalence principle [2] and using the vector potential [11] to determine the far fields, the orientation of $\bar{E}_{\text{FF}}$ is simply that of $\bar{H}_{\text{AP}}\times\hat{n}_{\text{AP}}$ projected into the far field $\left(\theta,\phi\right)$ view plane. And correspondingly, the orientation of $\bar{H}_{\text{FF}}$ is that

of $\hat{r} \times \bar{E}_{\mathrm{FF}}$. Furthermore, the ratio of the phi- to theta-components of $\bar{E}_{\mathrm{FF}}$ in this H_{AP} case is

$$\frac{E_{\mathrm{FF}\,\phi}}{E_{\mathrm{FF}\,\theta}} = -\sec\theta \tan\phi \tag{8.1}$$

2. If a zero cross-polarization planar aperture has purely *x*-directed E_{AP} field only $\left(H_{\mathrm{AP}} = 0\right)$, then by the field equivalence principle and using the vector potential to determine the far fields, the orientation of $\bar{H}_{\mathrm{FF}}$ is simply that of $\hat{n}_{\mathrm{AP}} \times \bar{E}_{\mathrm{AP}}$ projected into the far field (θ, ϕ) view plane. And correspondingly, the orientation of $\bar{E}_{\mathrm{FF}}$ is that of $\bar{H}_{\mathrm{FF}} \times \hat{r}$. Furthermore, the ratio of the phi- to theta-components of $\bar{E}_{\mathrm{FF}}$ in this E_{AP} case is

$$\frac{E_{FF\,\phi}}{E_{FF\,\theta}} = -\cos\theta \tan\phi \tag{8.2}$$

3. If a zero cross-polarization planar aperture has balanced TEM fields, $\left|\bar{H}_{\mathrm{AP}}\right| = \left|\bar{E}_{\mathrm{AP}}\right| / \eta$, with E field *x*-directed, then by the field equivalence principle and using the vector potential to determine the far fields, the orientation of $\bar{E}_{\mathrm{FF}}$ or $\bar{H}_{\mathrm{FF}}$ is not simply that of $\bar{H}_{\mathrm{AP}} \times \hat{n}_{\mathrm{AP}}$ or $\hat{n}_{\mathrm{AP}} \times \bar{E}_{\mathrm{AP}}$ projected into the far field (θ, ϕ) view plane. Furthermore, the ratio of the phi- to theta-components of $\bar{E}_{\mathrm{FF}}$ is as given in (8.3). Note that $\left|E_\phi / E_\theta\right| = \tan\phi$, or $\left|E_\theta / E_\phi\right| = \tan\phi$, is effectively a definition of a Huygens source, which is what Ludwig's third definition describes.

$$\frac{E_{FF\,\phi}}{E_{FF\,\theta}} = -\tan\phi \tag{8.3}$$

The above relationships are supported by the following arithmetic. For cases 1 and 2 above the electric or magnetic aperture field can be respectively excluded in the following derivations to obtain the respective result for the given case.

The electric far field is obtained with the following steps, according to Equations (6-101a) & (6-102b) of [11], where A_{ff} and F_{ff} are respectively the far field magnetic and electric vector potentials.

$$\bar{E}_{FarField} = \bar{E}_{Aff} + \bar{E}_{Fff} \approx \left[\theta\hat{\theta}\cdot + \phi\hat{\phi}\cdot\right] j\omega\left(-\bar{A}_{ff} + \eta\,\hat{r}\times\bar{F}_{ff}\right) \tag{8.4}$$

$$\bar{A}_{ff} = \mu\iint \bar{J}\,\frac{\exp(-jkr)}{4\pi r}\exp\left(jk(\bar{r}\,'\cdot\hat{r})\right)dS' \tag{8.5}$$

$$\bar{F}_{ff} = \varepsilon\iint \bar{M}\,\frac{\exp(-jkr)}{4\pi r}\exp\left(jk(\bar{r}\,'\cdot\hat{r})\right)dS' \tag{8.6}$$

$$\bar{J} = \hat{n}\times\bar{H}^a \quad \text{and}\ \bar{M} = -\hat{n}\times\bar{E}^a \tag{8.7}$$

$$\bar{E}_{ff} = \frac{jk\exp(-jkr)}{4\pi r}\frac{1}{\sqrt{\mu\varepsilon}}\left[\theta\hat{\theta}\cdot + \phi\hat{\phi}\cdot\right]\iint\left[(-\mu\bar{J}) + \sqrt{\frac{\mu}{\varepsilon}}\,\hat{r}\times(\varepsilon\bar{M})\right]\exp\left(jk(\bar{r}\,'\cdot\hat{r})\right)dS' \tag{8.8}$$

$$\bar{E}_{ff} = \frac{jk\exp(-jkr)}{4\pi r}\left[\theta\hat{\theta}\cdot + \phi\hat{\phi}\cdot\right]\iint\left[\eta\left(-\hat{n}\times\bar{H}^a\right) + \hat{r}\times\left(-\hat{n}\times\bar{E}^a\right)\right]\exp\left(jk(\bar{r}\,'\cdot\hat{r})\right)dS' \tag{8.9}$$

Let $\bar{E}^a = \hat{x}\,Q$, then $\bar{H}^a = \hat{y}\dfrac{Q}{\eta}$ since $\hat{n} = \hat{z}$.

$$\bar{E}_{x\,ff} = \frac{jk\exp(-jkr)}{4\pi r}\left[\theta\hat{\theta}\cdot + \phi\hat{\phi}\cdot\right]\iint\left[\eta\left(-\hat{z}\times\hat{y}\frac{Q}{\eta}\right) + \hat{r}\times\left(-\hat{z}\times\hat{x}Q\right)\right]\exp\left(jk(\bar{r}\,'\cdot\hat{r})\right)dS' \tag{8.10}$$

$$\bar{E}_{x\,ff} = \frac{jk\exp(-jkr)}{4\pi r}\left[\theta\hat{\theta}\cdot + \phi\hat{\phi}\cdot\right]\left(\hat{x} + \hat{r}\times(-\hat{y})\right)\iint Q\exp\left(jk(\bar{r}\,'\cdot\hat{r})\right)dS' \tag{8.11}$$

$$\hat{r} = \hat{x}\sin\theta\cos\phi + \hat{y}\sin\theta\sin\phi + \hat{z}\cos\theta \tag{8.12}$$

$$\hat{r}\times(-\hat{y}) = \hat{x}\cos\theta - \hat{z}\sin\theta\cos\phi \tag{8.13}$$

$$\hat{x} + \hat{r}\times(-\hat{y}) = \hat{x}(1+\cos\theta) - \hat{z}\sin\theta\cos\phi \tag{8.14}$$

$$\hat{x} = \hat{r}\sin\theta\cos\phi + \hat{\theta}\cos\theta\cos\phi - \hat{\phi}\sin\phi \tag{8.15}$$

$$\hat{z} = \hat{r}\cos\theta - \hat{\theta}\sin\theta \tag{8.16}$$

$$\hat{x} + \hat{r}\times(-\hat{y}) = \left[\hat{r}\sin\theta\cos\phi + \hat{\theta}\cos\theta\cos\phi - \hat{\phi}\sin\phi\right](1+\cos\theta) - \left[\hat{r}\cos\theta - \hat{\theta}\sin\theta\right]\sin\theta\cos\phi \tag{8.17}$$

$$\hat{x} + \hat{r}\times(-\hat{y}) = \hat{\theta}\left\{\cos\theta\cos\phi(1+\cos\theta) + \sin^2\theta\cos\phi\right\} - \hat{\phi}\left\{\sin\phi(1+\cos\theta)\right\} + \hat{r}\sin\theta\cos\phi \tag{8.18}$$

Thus when $\bar{E}^a = \hat{x}\,Q$,

$$\hat{x} + \hat{r}\times(-\hat{y}) = (1+\cos\theta)\left[\hat{\theta}\cos\phi - \hat{\phi}\sin\phi\right] + \hat{r}\sin\theta\cos\phi \tag{8.19}$$

and so $$\bar{E}_{x\,ff} = \frac{jk\exp(-jkr)}{4\pi r}(1+\cos\theta)\left[\hat{\theta}\cos\phi - \hat{\phi}\sin\phi\right]\iint Q\exp\left(jk(\bar{r}'\cdot\hat{r})\right)dS' \ . \tag{8.20}$$

Now let $\bar{E}^a = \hat{y}\,Q$, then $\bar{H}^a = -\hat{x}\dfrac{Q}{\eta}$ since $\hat{n} = \hat{z}$.

$$\bar{E}_{y\,ff} = \frac{jk\exp(-jkr)}{4\pi r}\left[\theta\hat{\theta}\cdot + \phi\hat{\phi}\cdot\right]\iint\left[\eta\left(-\hat{z}\times(-\hat{x})\frac{Q}{\eta}\right) + \hat{r}\times\left(-\hat{z}\times\hat{y}Q\right)\right]\exp\left(jk(\bar{r}'\cdot\hat{r})\right)dS' \tag{8.21}$$

$$\bar{E}_{y\,ff} = \frac{jk\exp(-jkr)}{4\pi r}\left[\theta\hat{\theta}\cdot + \phi\hat{\phi}\cdot\right]\left(\hat{y} + \hat{r}\times\hat{x}\right)\iint Q\exp\left(jk(\bar{r}'\cdot\hat{r})\right)dS' \tag{8.22}$$

$$\hat{y} = \hat{r}\sin\theta\sin\phi + \hat{\theta}\cos\theta\sin\phi + \hat{\phi}\cos\phi \tag{8.23}$$

$$\hat{y} + \hat{r}\times\hat{x} = \hat{y}(1+\cos\theta) - \hat{z}\sin\theta\sin\phi = (1+\cos\theta)\left[\hat{\theta}\sin\phi + \hat{\phi}\cos\phi\right] \tag{8.24}$$

Thus when $\bar{E}^a = \hat{y}\,Q$,

$$\bar{E}_{y\,ff} = \frac{jk\exp(-jkr)}{4\pi r}(1+\cos\theta)\left[\hat{\theta}\sin\phi + \hat{\phi}\cos\phi\right]\iint Q\exp\left(jk(\bar{r}'\cdot\hat{r})\right)dS' \tag{8.25}$$

In summary, when the aperture has balanced TEM with both electric and complementary magnetic field,

$$\bar{E}_{ff} = \frac{jk\exp(-jkr)}{4\pi r}(1+\cos\theta)\iint Q\exp\left(jk(\bar{r}'\cdot\hat{r})\right)dS'\begin{cases}\hat{\theta}\cos\phi - \hat{\phi}\sin\phi; & \bar{E}^a = \hat{x}Q \\ \hat{\theta}\sin\phi + \hat{\phi}\cos\phi; & \bar{E}^a = \hat{y}Q\end{cases}. \tag{8.26}$$

The term in the curly brace on the right hand side represents the polarization of a Huygens source, for which Ludwig's third definition of cross-polarization applies.

8.2 THREE-PARAMETER CLOSED-FORM DERIVATIONS (3.1)

This appendix presents the derivations of the closed form equations in Chapter 1.1. Each cited equation below is given, followed by the defining equation, which is then worked into a mathematical form that is solved with reference to either a referenced table of integrals or a symbolic math software program.

Derivation of (4.19), the generalized space factor integral equation:

$$T(\theta,\phi)\Big|_{n=0 \text{ or } 1} = 2\pi abj^n\cos\left[n(\Delta-\Phi)\right]\int_0^1 R(t)J_n(ut)t\,dt \tag{8.27}$$

From (4.17) and (4.18), $$T(\theta,\phi) = I_1\int_0^1 R(t)abt\;dt\,, \tag{8.28}$$

where after substituting $x = \psi - \Phi$,

$$I_1 = \int_0^{2\pi} \left\{ \cos(nx)\cos\left[n(\Phi-\Delta)\right] - \sin(nx)\sin\left[n(\Phi-\Delta)\right] \right\} \exp\left[jut\cos x \right] dx \,. \qquad (8.29)$$

Using [88] (3.915.2), and noting that the term with sine is zero because it's an odd function:

$$I_1 = 2\pi j^n \cos\left[n(\Phi-\Delta)\right] J_n(ut) \qquad (8.30)$$

Q.E.D.

Derivation of (4.31), the space factor of the simplest difference pattern:

$$T_D^{\text{norm}} \Big|_{Q_D = \cos(\psi-\Delta)} = j\pi\cos(\Delta-\Phi)\frac{J_1(u)\mathrm{H}_0(u) - \mathrm{H}_1(u)J_0(u)}{u} \qquad (8.31)$$

From (4.19),

$$T_{\mathrm{D}}^{\text{norm}}(\theta,\phi) = 2j\cos(\Delta-\Phi)\int_0^1 R(t)J_1(ut)t\,dt = \int_0^1 J_1(ut)t\,dt \,. \qquad (8.32)$$

[88] (6.561.1) provides

(6.561.1): $$\int_0^1 x^v J_v(ax)\,dx = 2^{v-1}a^{-v}\pi^{\frac{1}{2}}\Gamma\left(v+\tfrac{1}{2}\right)\left[J_v(a)\mathrm{H}_{v-1}(a) - \mathrm{H}_v(a)J_{v-1}(a)\right], \qquad (8.33)$$

thus $$T_{\mathrm{D}}^{\text{norm}}(\theta,\phi) = 2j\cos(\Delta-\Phi)\left(\frac{\sqrt{\pi}}{u}\Gamma\left(\tfrac{3}{2}\right)\right)\left[J_1(u)\mathrm{H}_0(u) - \mathrm{H}_1(u)J_0(u)\right]. \qquad (8.34)$$

where $\Gamma\left(\frac{3}{2} = \sqrt{\pi}/2\right)$. Q.E.D.

Derivation of (4.33), the 3PS radiation pattern space factor:

$$T_{\mathrm{S}}^{\mathrm{norm}}(u) = 2c\frac{J_1(u)}{u} + (1-c)\frac{2\beta^{\alpha}J_{\alpha+1}\left(\sqrt{u^2-\beta^2}\right)}{I_{\alpha}(\beta)\left(\sqrt{u^2-\beta^2}\right)^{\alpha+1}} \tag{8.35}$$

From (4.19),

$$T_{\mathrm{S}}^{\mathrm{norm}}(\theta) = 2\int_0^1 R(t)J_0(ut)t\,dt = 2\int_0^1 \left\{c + (1-c)\left(\sqrt{1-t^2}\right)^{\alpha}\frac{I_{\alpha}\left(\beta\sqrt{1-t^2}\right)}{I_{\alpha}(\beta)}\right\}J_0(ut)t\,dt \tag{8.36}$$

Consider first the constant term, utilizing [88] (5.52.1):

(5.52.1): $$\int x^{p+1}Z_p(x)\,dx = x^{p+1}Z_{p+1}(x) \tag{8.37}$$

Thereby, $$2c\int_0^1 J_0(ut)t\,dt = 2c\frac{J_1(u)}{u} \tag{8.38}$$

Let I_2 symbolize the second term on the RHS of (8.36), utilizing [88] (6.683.2).

$$I_2 = \frac{2(1-c)}{J_{\alpha}(j\beta)}\int_0^1\left(\sqrt{1-t^2}\right)^{\alpha}J_{\alpha}\left(j\beta\sqrt{1-t^2}\right)J_0(ut)t\,dt \tag{8.39}$$

Then substitute $\sqrt{1-t^2} = \sin x$:

$$I_2 = \frac{2(1-c)}{J_{\alpha}(j\beta)}\int_0^{\pi/2} J_{\alpha}(j\beta\sin x)J_0(u\cos x)\sin^{\alpha+1}x\cos x\,dx \tag{8.40}$$

(6.683.2): $$\int_0^{\pi/2} J_v(z_1\sin x)J_u(z_2\cos x)\sin^{v+1}x\cos^{u+1}x\,dx = \frac{z_1^v z_2^u J_{v+u+1}\left(\sqrt{z_1^2+z_2^2}\right)}{\sqrt{\left(z_1^2+z_2^2\right)^{v+u+1}}} \tag{8.41}$$

Thus $$I_2 = \frac{2(1-c)}{J_\alpha(j\beta)} \frac{(j\beta)^\alpha J_{\alpha+1}\left(\sqrt{u^2-\beta^2}\right)}{\sqrt{\left(u^2-\beta^2\right)^{\alpha+1}}} = (1-c) \frac{2\beta^\alpha J_{\alpha+1}\left(\sqrt{u^2-\beta^2}\right)}{I_\alpha(\beta)\sqrt{\left(u^2-\beta^2\right)^{\alpha+1}}}, \tag{8.42}$$

Q.E.D.

Derivation of (4.35), the 3PS aperture power integral:

$$P_{\text{apS}}^{\text{norm}} = c^2 + 4c(1-c)\frac{I_{\alpha+1}(\beta)}{\beta I_\alpha(\beta)} + \frac{(1-c)^2}{2\alpha+1}\left(1 - \frac{I_{\alpha+1}^2(\beta)}{I_\alpha^2(\beta)}\right) \tag{8.43}$$

The aperture power integral according to (4.24) is

$$P_{\text{apS}} = \int_0^{2\pi}\int_0^1 Q_{\text{S}}^2(t,\psi)abt\,dt\,d\psi\,, \tag{8.44}$$

where $$Q_{\text{S}}(t,\psi) = c + (1-c)\left(\sqrt{1-t^2}\right)^\alpha \frac{I_\alpha\left(\beta\sqrt{1-t^2}\right)}{I_\alpha(\beta)}. \tag{8.45}$$

Thus $$P_{\text{apS}}^{\text{norm}} = 2\int_0^1 \left\{ c + (1-c)\left(\sqrt{1-t^2}\right)^\alpha \frac{I_\alpha\left(\beta\sqrt{1-t^2}\right)}{I_\alpha(\beta)} \right\}^2 t\,dt\,. \tag{8.46}$$

Let $$P_{\text{apS}}^{\text{norm}} \to c^2 + 4\frac{c(1-c)}{J_\alpha(j\beta)} I_3 + \frac{(1-c)^2}{J_\alpha^2(j\beta)} I_4, \tag{8.47}$$

where $$I_3 = \int_0^1 J_\alpha\left(j\beta\sqrt{1-t^2}\right)\left(\sqrt{1-t^2}\right)^\alpha t\,dt\,, \tag{8.48}$$

and $$I_4 = 2\int_0^1 J_\alpha^2\left(j\beta\sqrt{1-t^2}\right)\left(1-t^2\right)^\alpha t\,dt\,. \tag{8.49}$$

I_3 is solved by change of variables $x = j\beta\sqrt{1-t^2}$ to reduce it to the form of (8.37).

$$I_3 = \frac{1}{(j\beta)^{\alpha+2}} \int_0^{j\beta} x^{\alpha+1} J_\alpha(x)\,dx = \frac{J_{\alpha+1}(j\beta)}{j\beta} \tag{8.50}$$

For I_4 let $x = 1 - t^2$ to put it into a form that Maple™ solves:

$$I_4 = \int_0^1 J_\alpha^2\left(j\beta\sqrt{x}\right) x^\alpha dx = \frac{J_\alpha^2(j\beta) + J_{\alpha+1}^2(j\beta)}{2\alpha+1} \tag{8.51}$$

Q.E.D.

Derivation of (4.42), the 3PD radiation pattern space factor:

$$T_{\mathrm{D}}^{\mathrm{norm}} = 2j\cos(\Delta-\Phi)\left\{ c\frac{\pi}{2u}\left[J_1(u)\mathrm{H}_0(u) - \mathrm{H}_1(u)J_0(u)\right] + (1-c)\frac{u\beta^\alpha J_{\alpha+2}\left(\sqrt{u^2-\beta^2}\right)}{I_\alpha(\beta)\left(\sqrt{u^2-\beta^2}\right)^{\alpha+2}}\right\} \tag{8.52}$$

From (4.19), $$T_{\mathrm{D}}^{\mathrm{norm}}(\theta,\phi) = 2j\cos(\Delta-\Phi)\int_0^1 R(t)J_1(ut)t\,dt \tag{8.53}$$

where $$R_{\mathrm{D}}(t) = c + (1-c)t\left(\sqrt{1-t^2}\right)^\alpha \frac{I_\alpha\left(\beta\sqrt{1-t^2}\right)}{I_\alpha(\beta)} \tag{8.54}$$

The first term on the RHS with the *c* coefficient was derived above starting with (8.31). For the second term, define

$$I_5 = \int_0^1 \left\{ t\left(\sqrt{1-t^2}\right)^\alpha \frac{I_\alpha\left(\beta\sqrt{1-t^2}\right)}{I_\alpha(\beta)}\right\} J_1(ut)t\,dt\,. \tag{8.55}$$

Let $t = \sin x$: $$I_5 = \frac{1}{j^\alpha I_\alpha(\beta)} \int_0^{\pi/2} J_1(u\sin x) J_\alpha(j\beta\cos x)\sin^2 x\cos^{\alpha+1} x\,dx \tag{8.56}$$

Utilizing (8.41), $$I_5 = \frac{u\beta^{\alpha} J_{\alpha+2}\left(\sqrt{u^2-\beta^2}\right)}{I_{\alpha}(\beta)\sqrt{\left(u^2-\beta^2\right)^{\alpha+2}}} \tag{8.57}$$

Q.E.D.

Derivation of (4.44), 3PD matching sum pattern space factor:

$$T_{|D|}^{\text{norm}}(0) = 2\left\{\frac{c}{\pi} + (1-c)\sqrt{\frac{2}{\pi}}\frac{I_{\alpha+3/2}(\beta)}{\beta^{3/2} I_{\alpha}(\beta)}\right\} \tag{8.58}$$

From (4.25), $$T_{|D|}^{\text{norm}}(0) = \frac{1}{\pi}\int_0^{2\pi}\int_0^1 R_D(t)\left|\cos(\psi-\Delta)\right| t\, dt d\psi = \frac{4}{\pi}\int_0^1 R_D(t)\, t\, dt \tag{8.59}$$

$$= \frac{4}{\pi}\int_0^1 \left\{c + (1-c)t\left(\sqrt{1-t^2}\right)^{\alpha}\frac{I_{\alpha}\left(\beta\sqrt{1-t^2}\right)}{I_{\alpha}(\beta)}\right\} t dt \tag{8.60}$$

Let $t = \cos\theta$: $$T_{|D|}^{\text{norm}}(0) = \frac{2c}{\pi} + \frac{4(1-c)}{\pi J_{\alpha}(j\beta)}\int_0^{\pi/2} J_{\alpha}(j\beta\sin\theta)\sin^{\alpha+1}\theta\cos^2\theta d\theta \tag{8.61}$$

Using [88] (6.683.6)

(6.683.6): $$\int_0^{\pi/2} J_u(a\sin\theta)(\sin\theta)^{u+1}(\cos\theta)^{2p+1} d\theta = 2^p\Gamma(p+1)a^{-p-1}J_{p+u+1}(a) \tag{8.62}$$

$$T_{|D|}^{\text{norm}}(0) = \frac{2c}{\pi} + \frac{4(1-c)}{\pi J_{\alpha}(j\beta)}\left[2^{\frac{1}{2}}\Gamma\left(\tfrac{3}{2}\right)(j\beta)^{-3/2} J_{\alpha+3/2}(j\beta)\right] \tag{8.63}$$

Q.E.D.

Derivation of (4.45), the 3PD aperture power integral:

$$P_{\text{apD}}^{\text{norm}} = \left\{ \begin{array}{l} \dfrac{c^2}{2} + \dfrac{2c(1-c)}{\beta^{3/2}} \sqrt{\dfrac{\pi}{2}} \dfrac{I_{\alpha+3/2}(\beta)}{I_\alpha(\beta)} \\ \\ + \dfrac{(1-c)^2}{2} \left[\dfrac{1 - \dfrac{I_{\alpha+1}^2(\beta)}{I_\alpha^2(\beta)}}{2\alpha+1} - \dfrac{\beta^{2\alpha}\, {}_2F_3\left(\begin{array}{l} [2\alpha+2, \alpha+1/2]; \\ [2\alpha+1, 2\alpha+3, \alpha+1]; \\ \beta^2 \end{array} \right)}{2^{2\alpha+1}(\alpha+1)\Gamma^2(\alpha+1) I_\alpha^2(\beta)} \right] \end{array} \right\} \tag{8.64}$$

The aperture power integral according to (4.24) is

$$P_{\text{apD}} = \int_0^{2\pi} \int_0^1 Q_{\text{D}}^2(t,\psi) abt\, dt\, d\psi \,, \tag{8.65}$$

where
$$Q_D(t,\psi) = \cos(\psi - \Delta) \left\{ c + (1-c) t \left(\sqrt{1-t^2} \right)^\alpha \frac{I_\alpha\left(\beta\sqrt{1-t^2} \right)}{I_\alpha(\beta)} \right\}. \tag{8.66}$$

Thus
$$P_{\text{apD}}^{\text{norm}} = \int_0^1 \left\{ c + (1-c) t \left(\sqrt{1-t^2} \right)^\alpha \frac{I_\alpha\left(\beta\sqrt{1-t^2} \right)}{I_\alpha(\beta)} \right\}^2 t\, dt \,. \tag{8.67}$$

Let
$$P_{\text{apD}}^{\text{norm}} \to \frac{c^2}{2} + 2 \frac{c(1-c)}{J_\alpha(j\beta)} I_6 + \frac{(1-c)^2}{2 J_\alpha^2(j\beta)} I_7 \,, \tag{8.68}$$

where
$$I_6 = \int_0^1 J_\alpha\left(j\beta\sqrt{1-t^2} \right) \left(\sqrt{1-t^2} \right)^\alpha t^2\, dt \,, \tag{8.69}$$

and
$$I_7 = 2 \int_0^1 J_\alpha^2\left(j\beta\sqrt{1-t^2} \right) \left(1-t^2 \right)^\alpha t^3\, dt \,. \tag{8.70}$$

For I_6 let $x=\sqrt{1-t^2}$ to yield a form that Maple ™ and Mathematica ™ will solve:

$$I_6=\int_0^1 J_\alpha\left(j\beta x\right)x^{\alpha+1}\sqrt{1-x^2}\,dx=\sqrt{\frac{\pi}{2}}\frac{J_{\alpha+3/2}\left(j\beta\right)}{\left(j\beta\right)^{3/2}}. \tag{8.71}$$

For I_7 let $x=1-t^2$: $I_7=\int_0^1 x^\alpha J_\alpha^2\left(j\beta\sqrt{x}\right)dx-\int_0^1 x^{\alpha+1}J_\alpha^2\left(j\beta\sqrt{x}\right)dx\doteq$ (8.72)

From Maple™: $$I_8=\int_0^1 x^\alpha J_\alpha^2\left(j\beta\sqrt{x}\right)dx=\frac{J_\alpha^2\left(j\beta\right)+J_{\alpha+1}^2\left(j\beta\right)}{2\alpha+1} \tag{8.73}$$

Maple™: $$I_9=\frac{\left(j\beta\right)^{2\alpha}\,{}_2F_3\left(\left[2\alpha+2,\alpha+\tfrac{1}{2}\right];\left[2\alpha+1,2\alpha+3,\alpha+1\right];\beta^2\right)}{2^{2\alpha+1}\left(\alpha+1\right)\Gamma^2\left(\alpha+1\right)} \tag{8.74}$$

Q.E.D.

Derivation of (4.49), the slope of the difference pattern:

$$S^{\text{norm}}=\left.\frac{dT_{\text{D}}^{\text{norm}}\left(u\right)}{du}\right|u=0=2j\cos\left(\Delta-\Phi\right)\left\{\frac{c}{6}+\frac{\left(1-c\right)I_{\alpha+2}\left(\beta\right)}{\beta^2 I_\alpha\left(\beta\right)}\right\} \tag{8.75}$$

Recalling (4.42):

$$\frac{T_{\text{D}}^{\text{norm}}\left(u\right)}{2j\cos\left(\Delta-\Phi\right)}=\left\{c\frac{\pi}{2u}\left[J_1\left(u\right)\text{H}_0\left(u\right)-\text{H}_1\left(u\right)J_0\left(u\right)\right]+\left(1-c\right)\frac{u\beta^\alpha J_{\alpha+2}\left(\sqrt{u^2-\beta^2}\right)}{I_\alpha\left(\beta\right)\left(\sqrt{u^2-\beta^2}\right)^{\alpha+2}}\right\} \tag{8.76}$$

Equation (4.27) defines the slope: $$S^{\text{norm}}=\left.\frac{dT_{\text{D}}^{\text{norm}}\left(u\right)}{du}\right|u=0 \tag{8.77}$$

Using either Maple™, Mathematica™ or working out the arithmetic by hand, noting that $\lim_{x\to 0} \mathrm{H}_0(x)/x = 2/\pi$ and $\lim_{x\to 0} \mathrm{H}_1(x)/x^2 = 2/(3\pi)$, yields the given result.

8.3 CYLINDRICAL CORRUGATED HORN FIELDS (CHAPTER 5)

This appendix presents the cylindrical waveguide field equations, along with the corresponding closed-form far fields and directivity, with reference given to Bessel identities that are presented in section 8.4.

8.3.1 Cylindrical Waveguide Fields

Fields within a cylindrical horn are modeled in cylindrical coordinates. General expressions for cylindrical fields propagating in the positive z-axis direction in either left or right (L/R) rotational sense (LCP/RCP) are given below. Phasor representation is used, including exp[$j\omega$t] time- and exp[$-jk_Z z$] axial-propagation phasors (the latter for the cylindrical fields inside the horn); although, the time- and axial-phasor(s) are not explicitly shown. The radian temporal frequency is ω. $k_z(z)$ is the axial wave number and $\gamma(z)$ is the radial wave number, both for propagation within the cylindrical waveguide/horn structure at position z.

The TEz fields are represented by an electrical vector potential, ${}_{\mathrm{C}}\bar{F}$, only with z-axis component, as

$$ {}_{\mathrm{C}}F_Z = F_0 J_n(\gamma\rho)\exp[\pm jn\varphi],\ {}^{\mathrm{L}}_{\mathrm{R}} \tag{8.78}$$

where the left subscript, C, in ${}_{\mathrm{C}}F_Z$ indicates that this vector potential is associated with the fields within the cylindrical horn, modeled in cylindrical coordinates. The electric vector potential is

defined such that the electric flux, $\bar{D} = \varepsilon \bar{E}$, is the negative curl of the electric vector potential. The SI units of $\bar{F}$ in (8.78) are A·s/m.

The TMz fields are represented by a magnetic vector potential, ${}_{\mathrm{C}}\bar{A}$, only with z-axis component, as

$$ {}_{\mathrm{C}}A_Z = F_0 \Lambda \eta_0 J_n(\gamma\rho) \exp[\pm j(n\varphi + \psi)], \quad {}^{\mathrm{L}}_{\mathrm{R}} \tag{8.79} $$

where the left subscript, C, in ${}_{\mathrm{C}}A_Z$ indicates that the vector potential is associated with the fields within the cylindrical horn, modeled in cylindrical coordinates. The magnetic vector potential is defined such that the magnetic flux, $\bar{B} = \mu \bar{H}$, is the curl of the magnetic vector potential. The SI units of $\bar{A}$ in (8.79) are V·s/m. The Λ parameter determines the field mode:

$$ \Lambda = \begin{cases} 0, & \text{TE;} \\ \infty, & \text{TM;} \\ 1, & \text{HE;} \\ -1 & \text{EH.} \end{cases} \tag{8.80} $$

The fields corresponding to the electric and magnetic vector potentials are determined, in general for any coordinate system by (8.81)–(8.84), where the left subscript, C, indicates that the vector potential is associated with the fields within the cylindrical horn, modeled in cylindrical coordinates.

$$ \bar{E}_{\mathbf{F}} = (-1/\varepsilon)\nabla \times {}_{C}\bar{\mathrm{F}}; \tag{8.81} $$

$$ \bar{H}_{\mathbf{F}} = -j\omega {}_{C}\bar{F} - (j/\omega\mu\varepsilon)\nabla(\nabla \cdot {}_{C}\bar{\mathrm{F}}); \tag{8.82} $$

$$ \bar{E}_{\mathbf{A}} = -j\omega {}_{C}\bar{A} - (j/\omega\mu\varepsilon)\nabla(\nabla \cdot {}_{C}\bar{\mathrm{A}}); \tag{8.83} $$

$$\bar{H}_{\mathbf{A}} = (1/\mu)\nabla \times {}_{C}\bar{\mathrm{A}} \,. \tag{8.84}$$

The individual cylindrical field components are presented below derived from the vector potentials above.

$$\begin{aligned} E_{\rho} &= E_{\rho F} + E_{\rho A} \quad {}^{\mathrm{L}}_{\mathrm{R}} \\ &= -(\pm jn/\rho\varepsilon)\ J_n(\gamma\rho)\exp[\pm jn\varphi] \\ &\quad -(\Lambda k_z/\beta_0\varepsilon)\,{}^{\partial}_{\partial\rho}[J_n(\gamma\rho)]\exp[\pm j(n\varphi+\psi)] \end{aligned} \tag{8.85}$$

$$\begin{aligned} E_{\rho} &= -\left(\frac{\Lambda k_z \gamma}{\beta_0 \varepsilon}\right) J_{n-1}(\gamma\rho)\exp[\pm j(n\varphi+\psi)] \\ &\quad + \frac{n}{\rho}\left(\begin{array}{l} \dfrac{\Lambda k_z}{\beta_0\varepsilon}\exp[\pm j(n\varphi+\psi)] \\ -\left(\pm j\dfrac{1}{\varepsilon}\exp[\pm jn\varphi]\right) \end{array}\right) J_n(\gamma\rho) \end{aligned} \tag{8.86}$$

$$\begin{aligned} H_{\rho} &= H_{\rho F} + H_{\rho A} \quad {}^{\mathrm{L}}_{\mathrm{R}} \\ &= -(k_z/\omega\mu\varepsilon)\,{}^{\partial}_{\partial\rho}[J_n(\gamma\rho)]\exp[\pm jn\varphi] \\ &\quad \pm j\left(n/\rho\right)(\Lambda\eta_0/\mu)\,J_n(\gamma\rho)\exp[\pm j(n\varphi+\psi)] \end{aligned} \tag{8.87}$$

$$\begin{aligned} H_{\rho} &= -\left(\frac{k_z \gamma}{\omega\mu\varepsilon}\right) J_{n-1}(\gamma\rho)\exp[\pm jn\varphi] \\ &\quad + \frac{n}{\rho}\left(\begin{array}{l} \pm j\dfrac{\Lambda\eta_0}{\mu}\exp[\pm j(n\varphi+\psi)] \\ +\dfrac{k_z}{\omega\mu\varepsilon}\exp[\pm jn\varphi] \end{array}\right) J_n(\gamma\rho) \end{aligned} \tag{8.88}$$

$$\begin{aligned} E_{\varphi} &= E_{\varphi F} + E_{\varphi A} \quad {}^{\mathrm{L}}_{\mathrm{R}} \\ &= (1/\varepsilon)\,{}^{\partial}_{\partial\rho}[J_n(\gamma\rho)]\exp[\pm jn\varphi] \\ &\quad -\left(\pm j\right)(n/\rho)\,(\Lambda k_z/\beta_0\varepsilon)\,J_n(\gamma\rho)\exp[\pm j(n\varphi+\psi)] \end{aligned} \tag{8.89}$$

$$E_\varphi = \left(\frac{\gamma}{\varepsilon}\right) J_{n-1}(\gamma\rho)\exp[\pm jn\varphi] - \frac{n}{\rho}\begin{pmatrix} \pm j\dfrac{\Lambda k_z}{\beta_0\varepsilon}\exp[\pm j(n\varphi+\psi)] \\ +\dfrac{1}{\varepsilon}\exp[\pm jn\varphi] \end{pmatrix} J_n(\gamma\rho) \tag{8.90}$$

$$\begin{aligned} H_\varphi &= H_{\varphi F} + H_{\varphi A} \quad \begin{matrix}\mathrm{L}\\ \mathrm{R}\end{matrix} \\ &= -(\pm j)(n/\rho)\,(k_z/\omega\mu\varepsilon)\,J_n(\gamma\rho)\exp[\pm jn\varphi] \\ &\quad -(\Lambda\eta_0/\mu)\,\tfrac{\partial}{\partial\rho}[J_n(\gamma\rho)]\exp[\pm j(n\varphi+\psi)] \end{aligned} \tag{8.91}$$

$$H_\varphi = -\left(\frac{\Lambda\eta_0\gamma}{\mu}\right) J_{n-1}(\gamma\rho)\exp[\pm j(n\varphi+\psi)] + \frac{n}{\rho}\begin{pmatrix} \dfrac{\Lambda\eta_0}{\mu}\exp[\pm j(n\varphi+\psi)] \\ -(\pm j)\dfrac{k_z}{\omega\mu\varepsilon}\exp[\pm jn\varphi] \end{pmatrix} J_n(\gamma\rho) \tag{8.92}$$

$$\begin{aligned} E_Z &= E_{ZA} \quad \begin{matrix}\mathrm{L}\\ \mathrm{R}\end{matrix} \\ &= -j\omega\frac{\gamma^2}{\beta_0^2}\Lambda\eta_0\ \mathrm{J_n}(\gamma\rho)\exp[\pm j(n\varphi+\psi)] \end{aligned} \tag{8.93}$$

$$\begin{aligned} H_Z &= H_{ZF} \quad \begin{matrix}\mathrm{L}\\ \mathrm{R}\end{matrix} \\ &= -j\omega\frac{\gamma^2}{\beta_0^2}\,\mathrm{J_n}(\gamma\rho)\exp[\pm jn\varphi] \end{aligned} \tag{8.94}$$

8.3.2 HE mode Far fields and Directivity

In this section closed form equations for the HE balanced hybrid mode far fields in spherical coordinates, (r,θ,ϕ), are derived for the cylindrical feedhorn. (The difference between these far field equations and those presented in section 5.3.3 are that in this section the assumption is specifically made that the aperture fields represent balanced HE modes, for which with circular

polarization the H and E fields are related as given in (8.102) — in section 5.3.3 the fields are not in general balanced but may represent any combination of TE or TM modes). Far field vector potentials $\bar{A}$ and $\bar{F}$ are defined and then the far fields are determined from the far field vector potentials. Apostrophes are given to the arguments associated with the source fields within the horn aperture, to distinguish them from the arguments associated with the location of the point at which the far fields are to be evaluated. The aperture currents, $\bar{M}$ and $\bar{J}$, equivalent to the horn aperture fields, are assigned components in cylindrical coordinates, and the far field integrals, $\bar{L}$ and $\bar{N}$, assigned components in spherical coordinates.

$$\begin{aligned}\begin{Bmatrix}\bar{A}\\ \bar{F}\end{Bmatrix} &= \begin{Bmatrix}\mu\int G(\bar{r},\bar{r}\,')\bar{J}_{aperture}(\bar{r})dv'\\ \varepsilon\int G(\bar{r},\bar{r}\,')\bar{M}_{aperture}(\bar{r})dv'\end{Bmatrix}\\ &\approx \begin{Bmatrix}\mu\\ \varepsilon\end{Bmatrix}\frac{e^{-j\beta_0 r}}{4\pi r}\begin{Bmatrix}\bar{N}\\ \bar{L}\end{Bmatrix}\ \text{in spherical far - field}\end{aligned} \tag{8.95}$$

$$\bar{N} = \iint\left(\bar{J} - \left(\bar{J}\cdot\hat{r}\right)\hat{r}\right)\exp(j\beta_0\,\bar{r}\,'\cdot\hat{r})ds';\ \bar{J} = \hat{\mathrm{n}}_{\mathrm{ap}}\times\bar{H} \tag{8.96}$$

$$\bar{L} = \iint\left(\bar{M} - \left(\bar{M}\cdot\hat{r}\right)\hat{r}\right)\exp(j\beta_0\,\bar{r}\,'\cdot\hat{r})ds';\ \bar{M} = -\hat{\mathrm{n}}_{\mathrm{ap}}\times\bar{E} \tag{8.97}$$

$$\begin{aligned}\begin{Bmatrix}\bar{E}_{\mathbf{A}}\\ \bar{H}_{\mathbf{F}}\end{Bmatrix} &= -j\omega\begin{Bmatrix}\bar{A}\\ \bar{F}\end{Bmatrix} - \frac{j\omega}{\beta_0^2}\nabla\nabla\cdot\begin{Bmatrix}\bar{A}\\ \bar{F}\end{Bmatrix}\\ &\approx -j\omega\begin{Bmatrix}\bar{A}\\ \bar{F}\end{Bmatrix},\end{aligned} \tag{8.98}$$

since in the far field limit what becomes effectively a plane wave has essentially zero divergence.

Thus
$$\begin{Bmatrix}\bar{E}_{\mathbf{A}}\ \text{Far-field}\\ \bar{H}_{\mathbf{F}}\ \text{Far-field}\end{Bmatrix} \approx -j\omega\begin{Bmatrix}\mu\\ \varepsilon\end{Bmatrix}\frac{e^{-j\beta_0 r}}{4\pi r}\begin{Bmatrix}\bar{N}\\ \bar{L}\end{Bmatrix}. \tag{8.99}$$

Vector summation of the E field directly due to $\bar{N}$ along with that corresponding to the free-space H field due to $\bar{L}$ yields the electric far fields as

$$\mathrm{E}_{\theta\ \text{Far-Field}} = -j\beta_0 \frac{\exp(-j\beta_0 r)}{4\pi r}\left\{ \eta_0 \mathrm{N}_\theta + \mathrm{L}_\phi \right\}, \tag{8.100}$$

and

$$\mathrm{E}_{\phi\ \text{Far-Field}} = -j\beta_0 \frac{\exp(-j\beta_0 r)}{4\pi r}\left\{ \eta_0 \mathrm{N}_\phi - \mathrm{L}_\theta \right\}. \tag{8.101}$$

For balanced hybrid mode we have

$$\bar{E} = \pm \mathrm{j}\,\eta_0 \bar{H}, \quad {}^{\mathrm{L}}_{\mathrm{R}} \tag{8.102}$$

Thus

$$\bar{J} = \pm\left(j / \eta_0 \right)\bar{M}, \quad {}^{\mathrm{L}}_{\mathrm{R}} \tag{8.103}$$

and

$$\bar{N} = \pm\left(j / \eta_0 \right)\bar{L}. \quad {}^{\mathrm{L}}_{\mathrm{R}} \tag{8.104}$$

The effect of an extended PEC flange (or ground plane) about the aperture would be estimated using two times $\bar{L}$ and zero $\bar{N}$ (since the PEC causes $\bar{J} = 0$, by the field equivalence principle and imaging theory), and the effect of an extended PMC flange using two times $\bar{N}$ and zero $\bar{L}$ (since the PMC causes $\bar{M} = 0$). By involving both $\bar{N}$ and $\bar{L}$ an average between the two types of flanges is obtained, which can be considered an approximation of an absence of any flange about the aperture.

The equivalent magnetic current at the exit aperture of the horn for balanced hybrid mode is given by

$$\bar{M} = -\hat{\mathrm{n}}_{\mathrm{ap}} \times \bar{E} = \hat{\rho}' \mathrm{E}_{\varphi'} - \hat{\varphi}' \mathrm{E}_{\rho'}\ . \tag{8.105}$$

$$\mathrm{M}_{\rho'} = \mathrm{E}_{\varphi'} = \frac{\gamma}{\varepsilon} J_{n-1}(\gamma\rho')\exp[\pm jn\varphi'] \ \begin{matrix}\mathrm{L}\\ \mathrm{R}\end{matrix} \tag{8.106}$$

$$\begin{aligned}\mathrm{M}_{\varphi'} &= -\mathrm{E}_{\rho'} \\ &= \frac{\gamma}{\varepsilon} J_{n-1}(\gamma\rho')\exp[\pm j(n\varphi' + \tfrac{\pi}{2})] \ \begin{matrix}\mathrm{L}\\ \mathrm{R}\end{matrix}\end{aligned} \tag{8.107}$$

$$\bar{\mathrm{r}}' = \hat{\mathrm{x}}\rho'\cos\varphi' + \hat{y}\rho'\sin\varphi' \tag{8.108}$$

$$\hat{r} = \hat{x}\sin\theta\cos\varphi + \hat{y}\sin\theta\sin\varphi + \hat{z}\cos\theta \tag{8.109}$$

Consider $\bar{L}$:

$$\begin{aligned}\mathrm{L}_\theta = \int_0^{2\pi}\int_0^b [\hat{\theta}\cdot\bar{M}]\exp[j\beta_0\rho'\sin\theta\cos(\phi-\varphi')] \\ \cdot\rho' d\rho' d\varphi'\end{aligned} \tag{8.110}$$

$$\begin{aligned}\mathrm{L}_\phi = \int_0^{2\pi}\int_0^b [\hat{\phi}\cdot\bar{M}]\exp[j\beta_0\rho'\sin\theta\cos(\phi-\varphi')] \\ \cdot\rho' d\rho' d\varphi'\end{aligned} \tag{8.111}$$

$$\hat{\theta}\cdot\hat{\rho}' = \cos\theta\cos(\phi-\varphi') \tag{8.112}$$

$$\hat{\theta}\cdot\hat{\varphi}' = \cos\theta\sin(\phi-\varphi') \tag{8.113}$$

$$\hat{\phi}\cdot\hat{\rho}' = -\sin(\phi-\varphi') \tag{8.114}$$

$$\hat{\phi}\cdot\hat{\varphi}' = \cos(\phi-\varphi') \tag{8.115}$$

For LCP:

$$\begin{aligned}\mathrm{L}_\theta = \frac{\gamma}{\varepsilon}\int\int \left(\begin{array}{c}\cos\theta\cos(\phi-\varphi')J_{n-1}(\gamma\rho') \\ \cdot\exp[jn\varphi'] \\ +\cos\theta\sin(\phi-\varphi')J_{n-1}(\gamma\rho') \\ \cdot\exp[j(n\varphi'+\pi/2)]\end{array}\right) \\ \cdot\exp[j\beta_0\rho'\sin\theta\cos(\phi-\varphi')]\rho' d\rho' d\varphi'\end{aligned} \tag{8.116}$$

$$= \frac{\gamma}{\varepsilon}\cos\theta \iint J_{n-1}(\gamma\rho')\exp\left[j\beta_0\rho'\sin\theta\cos(\phi-\varphi')\right] \cdot \exp\left[\pm j\left\{\phi+(n-1)\varphi'\right\}\right]\rho' d\rho' d\varphi';\ \begin{matrix}\mathrm{L}\\ \mathrm{R}\end{matrix} \tag{8.117}$$

$$\mathrm{L}_\phi = \frac{\gamma}{\varepsilon}\int\int \begin{pmatrix} -\sin(\phi-\varphi')J_{n-1}(\gamma\rho') \\ \quad \cdot\exp[jn\varphi'] \\ +\cos(\phi-\varphi')J_{n-1}(\gamma\rho') \\ \quad \cdot\exp[j(n\varphi'+\pi/2)] \end{pmatrix} \cdot\exp[j\beta_0\rho'\sin\theta\cos(\phi-\varphi')]\rho' d\rho' d\varphi' \tag{8.118}$$

$$= \frac{\gamma}{\varepsilon}\iint J_{n-1}(\gamma\rho')\exp\left[j\beta_0\rho'\sin\theta\cos(\phi-\varphi')\right] \cdot\exp\left[\pm j\left\{\phi+(n-1)\varphi'+\pi/2\right\}\right]\rho' d\rho' d\varphi';\ \begin{matrix}\mathrm{L}\\ \mathrm{R}\end{matrix} \tag{8.119}$$

For HE_{11} LCP:

$$\mathrm{L}_\theta = \frac{\gamma}{\varepsilon}\cos\theta\exp[j\phi] \cdot\int_0^b J_0(\gamma\rho')2\pi J_0(\beta_0\rho'\sin\theta)\rho' d\rho' \tag{8.120}$$

$$\mathrm{L}_\phi = \frac{\gamma}{\varepsilon}\exp[j(\phi+\pi/2)] \cdot\int_0^b J_0(\gamma\rho')2\pi J_0(\beta_0\rho'\sin\theta)\rho' d\rho' \tag{8.121}$$

Use the Lommel integral formula (8.253).

$$\mathrm{L}_\theta^{11} = 2\pi b(\gamma_{11}b)^2 J_1(\gamma_{11}b)/\varepsilon \cdot\frac{J_0(\beta_0 b\sin\theta)}{(\gamma_{11}b)^2-(\beta_0 b\sin\theta)^2} \cdot\cos\theta\exp\left[\pm j\phi\right]\ \begin{matrix}\mathrm{L}\\ \mathrm{R}\end{matrix} \tag{8.122}$$

$$\mathrm{L}_\phi^{11} = 2\pi b(\gamma_{11}b)^2 J_1(\gamma_{11}a)/\varepsilon \cdot\frac{J_0(\beta_0 b\sin\theta)}{(\gamma_{11}a)^2-(\beta_0 b\sin\theta)^2} \cdot(\pm j)\exp\left[\pm j\phi\right]\ \begin{matrix}\mathrm{L}\\ \mathrm{R}\end{matrix} \tag{8.123}$$

With balanced HE mode the E and H fields have identical forms but with one rotated (90 / n) deg in φ from the other, thus

$$\bar{N} = \pm\left(j / \eta_0\right)\bar{L}_{\ \frac{\mathrm{L}}{\mathrm{R}}}. \tag{8.124}$$

The HE_{11} far fields for the uniform-phase flat circular horn aperture are thereby as follows.

$$\begin{aligned} \mathrm{E}_{\theta}^{\ 11} &= \beta_0 b\,(\gamma_{11}^{ap} b)^2 J_1(\gamma_{11}^{ap} b)/\varepsilon \\ &\cdot\left(\frac{1+\cos\theta}{2}\right)\frac{J_0[\beta_0 b\sin\theta]}{(\gamma_{11}^{ap} b)^2-(\beta_0 b\sin\theta)^2} \\ &\cdot\frac{e^{-j\beta_0 r}}{r}\left(\pm\exp\left[\pm j\phi\right]\right)\ \ \mathrm{HE}_{\ \frac{\mathrm{L}}{\mathrm{R}}} \end{aligned} \tag{8.125}$$

$$\begin{aligned} \mathrm{E}_{\phi}^{\ 11} &= \beta_0 b\,(\gamma_{11}^{ap} b)^2 J_1(\gamma_{11}^{ap} b)/\varepsilon \\ &\cdot\left(\frac{1+\cos\theta}{2}\right)\frac{J_0[\beta_0 b\sin\theta]}{(\gamma_{11}^{ap} b)^2-(\beta_0 b\sin\theta)^2} \\ &\cdot\frac{e^{-j\beta_0 r}}{r}\,j\exp\left[\pm j\phi\right]\ \ \mathrm{HE}_{\ \frac{\mathrm{L}}{\mathrm{R}}} \end{aligned} \tag{8.126}$$

For HE_{21} LCP:

$$\begin{aligned} \mathrm{L}_{\theta} &= \frac{\gamma}{\varepsilon}\cos\theta\int\int J_1(\gamma\rho')\exp\left[j(\phi+\varphi')\right] \\ &\cdot\exp\left[j\beta_0\rho'\sin\theta\cos(\phi-\varphi')\right] \\ &\cdot\rho' d\rho' d\varphi' \end{aligned} \tag{8.127}$$

$$\begin{aligned} &= \frac{\gamma}{\varepsilon}\cos\theta\exp[j2\phi] \\ &\cdot\int_0^b J_1(\gamma\rho')\,j2\pi J_1(\beta_0\rho'\sin\theta)\rho' d\rho' \end{aligned} \tag{8.128}$$

$$\begin{aligned} \mathrm{L}_{\phi} &= \frac{\gamma}{\varepsilon}\int\int J_1(\gamma\rho')\exp\left[j\left(\phi+\varphi'+\pi/2\right)\right] \\ &\cdot\exp\left[j\beta_0\rho'\sin\theta\cos(\phi-\varphi')\right] \\ &\cdot\rho' d\rho' d\varphi' \end{aligned} \tag{8.129}$$

$$= \frac{\gamma}{\varepsilon} j \exp[j2\phi] \cdot \int_0^b J_1(\gamma\rho') j2\pi J_1(\beta_0 \rho' \sin\theta) \rho' d\rho' \tag{8.130}$$

Use the Lommel integral formula (8.253).

$$\mathrm{L}_\theta^{21} = 2\pi b(\gamma_{21}b)^2 J_0(\gamma_{21}b)/\varepsilon \cdot \frac{J_1(\beta_0 b\sin\theta)}{(\gamma_{21}b)^2 - (\beta_0 b\sin\theta)^2} \cdot \cos\theta\left(\mp \qquad \pm j2\phi\right] \ {}^{\mathrm{L}}_{\mathrm{R}} \tag{8.131}$$

$$\mathrm{L}_\phi^{21} = 2\pi b(\gamma_{21}b)^2 J_0(\gamma_{21}b)/\varepsilon \cdot \frac{J_1(\beta_0 b\sin\theta)}{(\gamma_{21}b)^2 - (\beta_0 b\sin\theta)^2} \cdot \exp\left[\pm j2\phi\right] \ {}^{\mathrm{L}}_{\mathrm{R}} \tag{8.132}$$

$$\bar{N} = \pm\left(j/\eta_0\right)\bar{L} \ {}^{\mathrm{L}}_{\mathrm{R}} \tag{8.133}$$

The HE_{21} far fields for the uniform-phase flat circular horn aperture are thereby as follows.

$$\mathrm{E}_\theta^{21} = \beta_0 b\,(\gamma_{21}^{ap}b)^2 J_0(\gamma_{21}^{ap}b)/\varepsilon \cdot \left(\frac{1+\cos\theta}{2}\right)\frac{J_1[\beta_0 b\sin\theta]}{(\gamma_{21}^{ap}b)^2 - (\beta_0 b\sin\theta)^2} \cdot \frac{e^{-j\beta_0 r}}{r}\left(-\exp\left[\pm j2\varphi\right]\right) \ \mathrm{HE} \ {}^{\mathrm{L}}_{\mathrm{R}} \tag{8.134}$$

$$\mathrm{E}_\phi^{21} = \beta_0 b\,(\gamma_{21}^{ap}b)^2 J_0(\gamma_{21}^{ap}b)/\varepsilon \cdot \left(\frac{1+\cos\theta}{2}\right)\frac{J_1[\beta_0 b\sin\theta]}{(\gamma_{21}^{ap}b)^2 - (\beta_0 b\sin\theta)^2} \cdot \frac{e^{-j\beta_0 r}}{r}\left(\pm\exp\left[\pm j2\phi\right]\right) \ \mathrm{HE} \ {}^{\mathrm{L}}_{\mathrm{R}} \tag{8.135}$$

The directivity of HE_{11}, HE_{21} or any mode, is defined as the ratio of the total power on a sphere (radius observation distance) uniformly illuminated with the field radiated in the chosen direction at the observation distance, to the total power in the transverse field integrated over either the aperture, as given by

$$D(\theta,\phi) = \frac{4\pi r^2 \left|\bar{E}_{\text{far-field}}(\theta,\phi)\right|^2}{\iint\limits_{\text{aperture}} \left|\bar{E}^{\text{transverse}}_{\text{aperture}}\right|^2_{\text{peak}} dA}, \tag{8.136}$$

or over the far field sphere (yielding the same result in either case). Note that the aperture phase efficiency due to radial quadratic phase is about 85% for both the HE_{11} and HE_{21} modes with horn half-flare angle about 12 deg; whereas, with a 45 deg horn half-flare angle the phase efficiency drops to about 10%.

The aperture taper efficiency, η_{taper}, which for HE_{11} is about 69%, is defined as

$$\eta_{\text{taper}} = \frac{\left[\iint |E| dA\right]^2}{A_{\text{ap}} \iint |E|^2 dA}, \tag{8.137}$$

$$\eta^{HE_{11}}_{\text{taper}} = \frac{4}{(\gamma_{11} b)^2}. \tag{8.138}$$

8.3.3 Field Mode Matching at Waveguide Junction

Fig. 8-1 depicts a general waveguide step junction, with the smaller end on the left side, used in this section to derive the field matching matrix equations (5.27) and (5.28), which are repeated

here in (8.139) and (8.140). The axial propagation z-axis vector and the junction surface normal, $\hat{n}$, are both defined to point to the right in Fig. 8-1.

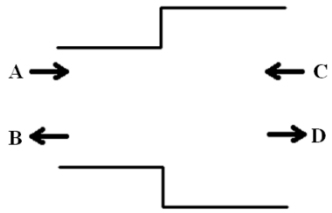

Fig. 8-1 Cylindrical Waveguide Step Junction

$$[P]^T\big[[A]+[B]\big]=[R]\big[[C]+[D]\big] \tag{8.139}$$

$$[L]^*\big[[A]-[B]\big]=[P]^*\big[[D]-[C]\big] \tag{8.140}$$

Equations (8.139) and (8.140) above summarize the field matching relations and are derived in the following discussion below. The asterisks symbolize complex conjugation. The tangential fields on either side of the junction plane are given by the following modal expansions, in reference to (5.25) and (5.26), where N_{SM} modes are assigned to the smaller waveguide on the left side, and N_{LG} modes assigned to the larger right side. A practical rule of thumb for computations is that a sufficient number of modes to include for each section is proportional to the respective radii.

$$\bar{E}_t^{\mathrm{SM}}=\sum_{n=1}^{N_{\mathrm{SM}}}\left(a_n+b_n\right)\bar{e}_n^{\mathrm{SM}} \tag{8.141}$$

$$\bar{H}_t^{\mathrm{SM}}=\sum_{n=1}^{N_{\mathrm{SM}}}\left(a_n-b_n\right)\bar{h}_n^{\mathrm{SM}} \tag{8.142}$$

$$\bar{E}_t^{\mathrm{LG}}=\sum_{m=1}^{N_{\mathrm{LG}}}\left(d_m+c_m\right)\bar{e}_m^{\mathrm{LG}} \tag{8.143}$$

$$\bar{H}_t^{\mathrm{LG}} = \sum_{m=1}^{N_{\mathrm{LG}}} \left(d_m - c_m\right) \bar{h}_m^{\mathrm{LG}} \tag{8.144}$$

The mode sets are assumed to be orthogonal as given in (8.145), which holds for the fields in the complete waveguide cross section on either side of the junction: S = LG or SM.

$$\iint_{\mathrm{S}} \bar{e}_i^{\mathrm{S}} \times \left(\bar{h}_j^{\mathrm{S}}\right)^* \cdot \hat{n} dS = \begin{cases} \neq 0, & i = j; \\ = 0, & i \neq j. \end{cases} \tag{8.145}$$

Let $$\left[L\right]_{ij} = \iint_{\mathrm{SM}} \bar{e}_i^{\mathrm{SM}} \times \left(\bar{h}_j^{\mathrm{SM}}\right)^* \cdot \hat{n} dS\,, \tag{8.146}$$

and $$\left[R\right]_{ij} = \iint_{\mathrm{LG}} \bar{e}_i^{\mathrm{LG}} \times \left(\bar{h}_j^{\mathrm{LG}}\right)^* \cdot \hat{n} dS\,. \tag{8.147}$$

A cross-coupling integral is designated as *P*.

$$\left[P\right]_{ij} = \iint_{\mathrm{SM}} \bar{e}_i^{\mathrm{SM}} \times \left(\bar{h}_j^{\mathrm{LG}}\right)^* \cdot \hat{n}\, dS \tag{8.148}$$

Consider the electric field boundary equation (EFBC) on the larger side of the junction and the magnetic field boundary equation (MFBC) on the smaller side.

EFBC: $$\hat{n} \times \bar{E}^{LG} = \begin{cases} 0, & \rho > \rho_{\mathrm{SM}}; \\ \hat{n} \times \bar{E}^{\mathrm{SM}}, & \rho \le \rho_{\mathrm{SM}}. \end{cases} \tag{8.149}$$

MFBC: $$\hat{n} \times \bar{H}^{LG} = \hat{n} \times \bar{H}^{\mathrm{SM}}, \ \rho \le \rho_{\mathrm{SM}} \tag{8.150}$$

Dotting the left hand side of the EFBC with a the complex conjugate of a single magnetic field mode on the larger side, utilizing (8.153), and accounting for mode orthogonality we find

$$\iint_{\mathrm{LG}} \left(\hat{n} \times \bar{E}^{\mathrm{LG}}\right) \cdot \left(\bar{h}_j^{\mathrm{LG}}\right)^* dS = \left(c_j + d_j\right)\left[R\right]_{jj}\,. \tag{8.151}$$

Exercising the EFBC and since the transverse electric field at the junction is zero along the junction wall,

$$\begin{aligned}\iint_{\mathrm{LG}}\left(\hat{n}\times\bar{E}^{\mathrm{LG}}\right)\cdot\left(\bar{h}_j^{\mathrm{LG}}\right)^* dS &= \iint_{\mathrm{SM}}\left(\hat{n}\times\bar{E}^{\mathrm{SM}}\right)\cdot\left(\bar{h}_j^{\mathrm{LG}}\right)^* dS \\ &= \sum_{n=1}^{N_{\mathrm{SM}}}\left(a_n+b_n\right)\iint_{\mathrm{SM}}\bar{e}_n^{\mathrm{SM}}\times\left(\bar{h}_j^{\mathrm{LG}}\right)^*\cdot\hat{n}\,dS\end{aligned}, \tag{8.152}$$

where use is made of the vector identify

$$\left(\bar{A}\times\bar{B}\right)\cdot\bar{C}=\left(\bar{C}\times\bar{A}\right)\cdot\bar{B}=\left(\bar{B}\times\bar{C}\right)\cdot\bar{A}\,. \tag{8.153}$$

Combining (8.151), (8.152) and (8.148):

$$\sum_{n=1}^{N_{\mathrm{SM}}}\left(a_n+b_n\right)[P]_{nj}=[R]_{jj}\left(c_j+d_j\right), \tag{8.154}$$

which is represented in matrix form, with both sides having matrix size $N_{\mathrm{LG}}\times 1$, by

$$[P]^T\left[[A]+[B]\right]=[R]\left[[C]+[D]\right] \tag{8.155}$$

Dotting the left hand side of the MFBC with a single electric field mode on the smaller side, accounting for mode orthogonality, and referring to (5.25), (5.26), (8.153), and (8.148) yields

$$\iint_{\mathrm{SM}}\left(\hat{n}\times\left(\bar{H}^{\mathrm{LG}}\right)^*\right)\cdot\bar{e}_i^{\mathrm{SM}}dS=-\sum_{m=1}^{N_{\mathrm{LG}}}\left(d_m-c_m\right)^*\iint_{\mathrm{SM}}\left(\bar{e}_i^{\mathrm{SM}}\times\left(\bar{h}_m^{\mathrm{LG}}\right)^*\right)\cdot\hat{n}\,dS=-\sum_{m=1}^{N_{\mathrm{LG}}}\left(d_m-c_m\right)^*[P]_{im}\,. \tag{8.156}$$

Combining (8.146), the MFBC (8.150), and (8.153) yields

$$\iint_{\mathrm{SM}}\left(\hat{n}\times\left(\bar{H}^{LG}\right)^*\right)\cdot\bar{e}_i^{\mathrm{SM}}dS=-\left(a_i-b_i\right)^*\iint_{\mathrm{SM}}\left(\bar{e}_i^{\mathrm{SM}}\times\left(\bar{h}_i^{\mathrm{SM}}\right)^*\right)\cdot\hat{n}\,dS=-\left(a_i-b_i\right)^*[L]_{ii}\,. \tag{8.157}$$

Thus
$$[L]_{ii}(a_i - b_i)^* = \sum_{m=1}^{N_{\mathrm{LG}}} [P]_{im}(d_m - c_m)^*, \tag{8.158}$$

or
$$[L]_{ii}^*(a_i - b_i) = \sum_{m=1}^{N_{\mathrm{LG}}} [P]_{im}^*(d_m - c_m), \tag{8.159}$$

which is represented in matrix form, with both sides having matrix size $N_{\mathrm{SM}} \times 1$, by

$$[L]^*\big[[A]-[B]\big] = [P]^*\big[[D]-[C]\big]. \tag{8.160}$$

See the note regarding the complex conjugations following (5.29).

8.3.4 Junction *S*-Parameters

In this section the *s*-parameters of the waveguide junction, (5.34)–(5.37), are derived, with shorthand that excludes some of the matrix brackets. First pseudo-*s'*-parameter are derived, which relate the in-going and out-going modal voltages on the two sides of the junction, and then from those the true *S*-parameters are derived by accounting the different wave impedances of each mode. (Microwave *S*-parameters are defined to relate in- and out-going root power, and are not just ratio of voltages.)

Isolating $[B]$ in (8.155) provides

$$B = P^{\mathrm{T\text{-}1}} R(C + D) - A. \tag{8.161}$$

Substituting (8.161) into (8.160) yields (8.162), where superscript "T-1" reads "inverse of the transpose,"

$$P^*(D - C) = L^*\left\{A - \left[P^{\mathrm{T\text{-}1}} R(C + D) - A\right]\right\}, \tag{8.162}$$

or $$\left[P^{*}+L^{*}P^{\mathrm{T}\text{-}1}R\right]D=2L^{*}A+\left[P^{*}-L^{*}P^{\mathrm{T}\text{-}1}R\right]C\,, \tag{8.163}$$

or $$\left[P^{\mathrm{T}}L^{*-1}P^{*}+R\right]D=2P^{\mathrm{T}}A+\left[P^{\mathrm{T}}L^{*-1}P^{*}-R\right]C\,. \tag{8.164}$$

Since $$[D]=[s'_{21}][A]+[s'_{22}][C]\,, \tag{8.165}$$

where the *s'* are the pseudo– *s*-parameters that relate only the modal voltages between the ports, then

$$[s'_{21}]=2\left[R+P^{\mathrm{T}}L^{*-1}P^{*}\right]^{-1}P^{\mathrm{T}}\,, \tag{8.166}$$

and $$[s'_{22}]=-\left[R+P^{\mathrm{T}}L^{*-1}P^{*}\right]^{-1}\left[R-P^{\mathrm{T}}L^{*-1}P^{*}\right]. \tag{8.167}$$

Furthermore, now isolating $[D]$ in (8.155) provides

$$D=R^{-1}P^{\mathrm{T}}\left(A+B\right)-C\,. \tag{8.168}$$

Substituting (8.168) into (8.160) yields

$$P^{*}\left(\left[R^{-1}P^{\mathrm{T}}\left(A+B\right)-C\right]-C\right)=L^{*}\left\{A-B\right\}, \tag{8.169}$$

or $$\left[P^{*}R^{-1}P^{\mathrm{T}}+L^{*}\right]B=\left[L^{*}-P^{*}R^{-1}P^{\mathrm{T}}\right]A+2P^{*}C\,. \tag{8.170}$$

Since $$[B]=[s'_{11}][A]+[s'_{12}][C]\,, \tag{8.171}$$

then $$[s'_{11}]=\left[L^{*}+P^{*}R^{-1}P^{\mathrm{T}}\right]^{-1}\left[L^{*}-P^{*}R^{-1}P^{\mathrm{T}}\right], \tag{8.172}$$

and $$[s'_{12}]=2\left[L^{*}+P^{*}R^{-1}P^{\mathrm{T}}\right]^{-1}P^{*}\,. \tag{8.173}$$

The pseudo-*s'*-parameters relate the in- and out-going modal voltages according to (8.174),

$$\begin{bmatrix}[B]\\ [D]\end{bmatrix}=\begin{bmatrix}[s'_{11}] & [s'_{12}]\\ [s'_{21}] & [s'_{22}]\end{bmatrix}\begin{bmatrix}[A]\\ [C]\end{bmatrix}; \tag{8.174}$$

although the pseudo-*s'*-parameters $[s']$ do not in general have the properties of the conservation of power and reciprocity, stated in (8.175) and (8.176), where *p* is the output port and *q* the input (stimulus) port, which are defined properties of microwave *s*-parameters for a lossless passive network such as the presumed perfectly electrically conductive (PEC) metallic corrugated feedhorn structure in consideration here. The reason the pseudo-*s'*-parameters do not represent conservation of power or reciprocity is that the waveguide modes each have different wave impedances. The true *s*-parameters, here symbolized as capital $[S]$ and defined in (8.177), are obtained from $[s']$ by first normalizing [145] the input columns (right matrix multiplication) by the square root of the self-coupling power integrals for the cylindrical waveguide at the input port ($[\ ]^{\frac{-1}{2}}$ matrices), and subsequently scaling the output rows (left matrix multiplication) by the square root of the self-coupling power integrals ($[\ ]^{\frac{1}{2}}$ matrices) for the cylindrical waveguide at the output port.

Given mode *j* stimulating port q: $$\sum_i \sum_p \left| \left[s_{pq} \right]_{ij} \right|^2 = 1 . \tag{8.175}$$

Passive network reciprocity: $$s_{pq} = s_{pq} . \tag{8.176}$$

$$\left[S_{pq} \right] = \left[\text{out}_p \right]^{\frac{1}{2}} \left[s'_{pq} \right] \left[\text{in}_q \right]^{\frac{-1}{2}} , \tag{8.177}$$

where $$\left[\text{in}\right]^{\frac{1}{2}}_{ij} = \begin{cases} \sqrt{\left[\text{in}\right]_{ii}}, & i = j; \\ 0, & i \neq j. \end{cases} \text{ and } \left[\text{out}\right]^{\frac{1}{2}}_{ij} = \begin{cases} \sqrt{\left[\text{out}\right]_{ii}}, & i = j; \\ 0, & i \neq j. \end{cases} \tag{8.178}$$

$[\text{in}]$ and $[\text{out}]$ each represent the self-coupling matrix for the respective input and output ports for the given *s*-parameter: either $[L]$ or $[R]$.

Thereby the true microwave *s*-parameters for the junction, relating the in- and out-going root power between the ports, are summarized in (8.179)–(8.182).

$$[S_{11}] = [L]^{\frac{1}{2}} \left[[L]^{*} + [P]^{*} [R]^{-1} [P]^{T} \right]^{-1} \left[[L]^{*} - [P]^{*} [R]^{-1} [P]^{T} \right] [L]^{\frac{-1}{2}}, \tag{8.179}$$

$$[S_{12}] = [L]^{\frac{1}{2}} 2 \left[[L]^{*} + [P]^{*} [R]^{-1} [P]^{T} \right]^{-1} [P]^{*} [R]^{\frac{-1}{2}}, \tag{8.180}$$

$$[S_{21}] = [R]^{\frac{1}{2}} 2 \left[[R] + [P]^{T} [L]^{*-1} [P]^{*} \right]^{-1} [P]^{T} [L]^{\frac{-1}{2}}, \tag{8.181}$$

and

$$[S_{22}] = -[R]^{\frac{1}{2}} \left[[R] + [P]^{T} [L]^{*-1} [P]^{*} \right]^{-1} \left[[R] - [P]^{T} [L]^{*-1} [P]^{*} \right] [R]^{\frac{-1}{2}}. \tag{8.182}$$

$$[R]^{\frac{1}{2}}_{ij} = \sqrt{\left| [R]_{ij} \right|} \text{ and } [L]^{\frac{1}{2}}_{ij} = \sqrt{\left| [L]_{ij} \right|} \tag{8.183}$$

Note the absolute value operation on each matrix element of the self-coupling matrices in (8.183)

.

Note that pseudo-*s'*-parameters, $[s']$, represent the modal voltages, which are proportional to field strength for any given mode, but the true *s*-parameters $[S]$ are not; so to convert from $[S]$ to field strength, $[S]$ must be left-matrix multiplied by $[\text{out}]^{\frac{-1}{2}}$, where *out* represents the port at which the field strength values are desired, either $[R]^{\frac{-1}{2}}$ or $[L]^{\frac{-1}{2}}$.

8.3.5 Mode Interaction Coupling Integrals

In the following four sections the mode interaction coupling integral (8.184), for cylindrical waveguide is derived for the four combinations of fields in the junction plane: transverse magnetic to transverse magnetic (TM-TM), transverse magnetic to transverse electric (TM-TE),

transverse electric to transverse magnetic (TE-TM) and transverse electric to transverse electric (TE-TE). The junction model used here has the smaller diameter, *a*, on the left, larger, *b,* on the right, and the coupling integral is defined as the junction plane surface integral of the cross product of the electric field on the left and the magnetic field on the right side of the junction, dotted with the surface normal vector. (If an actual junction subsequently in consideration has its larger waveguide on the left then the resulting *s*-parameters calculated with this junction model can be simply transposed.) The field polarization in these equations is circular, where the upper sign in the "$\pm$" and "$\mp$" symbols each represents the polarity for left circular polarization, and the lower sign represents that for right circular polarization: $\frac{\mathrm{L}}{\mathrm{R}}$. The phase shift between the two linearly polarized components that make up the circularly polarized wave is assumed to be 90 deg, $\psi = \pi / 2$, to provide for zero circular cross polarization. The assumption is made that the angular modal index is the same for the field modes on both sides of the junction, and the radial modal indices for the left and right sides are respectively *p* and *q*. Cylindrical coordinates are used to represent the fields, with the cylindrical *z*-axis pointing to the right (into the larger waveguide). Only the axial *z*-component of the field cross product is considered since the mode matching only involves the fields tangential to the junction plane. The coupling integral involves the difference between the product of the rho component of the e-field on the smaller left side and the complex conjugate of the phi component of the h-field on the larger right side and the product of the phi component of the e-field on the smaller side and the complex conjugate of the rho component of the h-field on the larger right side. β_0 is the free-space wave number, and k_z is the propagation wave number in the axial direction for the given mode, where $\beta_0^2 = k_z^2 + \gamma^2$.

Note that γ is a function of angular modal index, the radial modal index, the field mode (TM, TE) and the cylindrical waveguide radius.

$$I_{\mathrm{SM}\,p,\mathrm{LG}\,q} = \hat{z}\cdot\iint_{\mathrm{SM}} \overline{e}_{\mathrm{SM}\,p}\times\left(\overline{h}_{\mathrm{LG}\,q}\right)^{*} ds = \iint_{\mathrm{SM}} e_{\mathrm{SM}\,p\,\rho}\left(h_{\mathrm{LG}\,q\,\varphi}\right)^{*} - e_{\mathrm{SM}\,p\,\varphi}\left(h_{\mathrm{LG}\,q\,\rho}\right)^{*} ds \qquad (8.184)$$

8.3.5.1 TM-TM Mode Coupling Integral

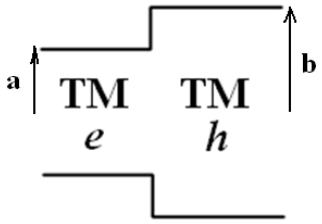

Fig. 8-2 Junction with TM-TM modes: Coupling *e* field on left with *h* field on right.

Consider the fields on both sides of the TM-TM junction for the mode coupling integral (8.184): electric field on left and magnetic on right. From (8.86) and (8.90) for transverse magnetic mode (TM: $\Lambda=\infty$), the rho and phi components of the electric field on the left side of the junction are given as follows.

$$E_{\mathrm{SM}\,\rho} = -\left(\frac{k_z\gamma}{\beta_0\varepsilon}\right)J_{n-1}(\gamma\rho)\exp[\pm j(n\varphi+\psi)] + \frac{n}{\rho}\left(\frac{k_z}{\beta_0\varepsilon}\exp[\pm j(n\varphi+\psi)]\right)J_n(\gamma\rho)\,{}^{\mathrm{L}}_{\mathrm{R}}, \qquad (8.185)$$

or

$$E_{\mathrm{SM}\,\rho} = \frac{k_z^{\mathrm{SM}}\gamma_m^{\mathrm{SM}}}{2\beta_0\varepsilon}\left\{-J_{n-1}(\gamma_m^{\mathrm{SM}}\rho)+J_{n+1}(\gamma_m^{\mathrm{SM}}\rho)\right\}\exp[\pm j(n\varphi+\psi)]\,{}^{\mathrm{L}}_{\mathrm{R}}, \qquad (8.186)$$

utilizing the Bessel identity of (8.250),

and

$$E_{\mathrm{SM}\,\varphi} = -(\pm j)\frac{n}{\rho}\frac{k_z}{\beta_0\varepsilon}\exp[\pm j(n\varphi+\psi)]J_n(\gamma\rho)\,{}^{\mathrm{L}}_{\mathrm{R}}, \qquad (8.187)$$

or

$$E_{\mathrm{SM}\,\varphi} = -(\pm j)\frac{k_z^{\mathrm{SM}}}{2\beta_0\varepsilon}\left\{J_{n-1}(\gamma^{\mathrm{SM}}\rho)+J_{n+1}(\gamma^{\mathrm{SM}}\rho)\right\}\exp[\pm j(n\varphi+\psi)]\,{}^{\mathrm{L}}_{\mathrm{R}}. \qquad (8.188)$$

From (8.88) and (8.92) for transverse magnetic mode (TM: $\Lambda = \infty$), the rho and phi component of the magnetic field on the right side of the junction are

$$H_{\mathrm{LG}\,\rho} = \pm j \frac{n}{\rho} \frac{\eta_0}{\mu} \exp[\pm j(n\varphi + \psi)] J_n(\gamma\rho)\, {}^{\mathrm{L}}_{\mathrm{R}}, \tag{8.189}$$

or

$$H_{\mathrm{LG}\,\rho} = \pm j \frac{\eta_0}{2\mu} \left\{ J_{n-1}(\gamma_q^{\mathrm{LG}}\rho) + J_{n+1}(\gamma_q^{\mathrm{LG}}\rho) \right\} \exp[\pm j(n\varphi + \psi)]\, {}^{\mathrm{L}}_{\mathrm{R}}, \tag{8.190}$$

and

$$H_{\mathrm{LG}\,\varphi} = -\frac{\eta_0 \gamma}{\mu} J_{n-1}(\gamma\rho) \exp[\pm j(n\varphi + \psi)] + \frac{n}{\rho} \left(\frac{\eta_0}{\mu} \exp[\pm j(n\varphi + \psi)] \right) J_n(\gamma\rho)\, {}^{\mathrm{L}}_{\mathrm{R}}, \tag{8.191}$$

or

$$H_{\mathrm{LG}\,\varphi} = \frac{\eta_0 \gamma}{2\mu} \left\{ -J_{n-1}(\gamma^{\mathrm{LG}}\rho) + J_{n+1}(\gamma^{\mathrm{LG}}\rho) \right\} \exp[\pm j(n\varphi + \psi)]\, {}^{\mathrm{L}}_{\mathrm{R}}. \tag{8.192}$$

Consider the two terms of the axial component of the cross product, where superscripts L and SM both refer to the left, smaller side of the junction and R and LG to the right, larger side.

$$\begin{aligned} & E_\rho^{\mathrm{SM}} \left(H_\phi^{\mathrm{LG}} \right)^* - E_\phi^{\mathrm{SM}} \left(H_\rho^{\mathrm{LG}} \right)^* \\ & \qquad = \frac{\gamma^{\mathrm{SM}} \gamma^{\mathrm{LG}} k_z^{\mathrm{SM}} c}{2\beta_0 \varepsilon} \left\{ J_{n-1}\left(\gamma^{\mathrm{SM}}\rho\right) J_{n-1}\left(\gamma^{\mathrm{LG}}\rho\right) + J_{n+1}\left(\gamma^{\mathrm{SM}}\rho\right) J_{n+1}\left(\gamma^{\mathrm{LG}}\rho\right) \right\} \end{aligned} \tag{8.193}$$

$$I_{\mathrm{SM}\,p,\mathrm{LG}\,q} = \hat{z} \cdot \iint_{\mathrm{SM}} \overline{e}_{\mathrm{SM}\,p} \times \left(\overline{h}_{\mathrm{LG}\,q} \right)^* ds \tag{8.194}$$

When $\gamma^{\mathrm{L}} \neq \gamma^{\mathrm{R}}$ the integral is solved in closed form using the Lommel integral (8.253).

$$I_{\mathrm{L}\,p,\mathrm{R}\,q}^{\text{TM-TM}} \Bigg|_{\gamma^{\mathrm{L}} \neq \gamma^{\mathrm{R}}} = \frac{\pi c}{\beta_0 \varepsilon} \gamma^{\mathrm{L}} \gamma^{\mathrm{R}} k_z^{\mathrm{L}} \left\{ \begin{aligned} & \frac{\gamma^{\mathrm{R}} a J_{n-1}\left(\gamma^{\mathrm{L}} a\right) J_{n-2}\left(\gamma^{\mathrm{R}} a\right) - \gamma^{\mathrm{L}} a J_{n-2}\left(\gamma^{L} a\right) J_{n-1}\left(\gamma^{\mathrm{R}} a\right)}{\left(\gamma^{\mathrm{L}}\right)^2 - \left(\gamma^{\mathrm{R}}\right)^2} \\ & + \frac{\gamma^{\mathrm{R}} a J_{n+1}\left(\gamma^{\mathrm{L}} a\right) J_n\left(\gamma^{\mathrm{R}} a\right)}{\left(\gamma^{\mathrm{L}}\right)^2 - \left(\gamma^{\mathrm{R}}\right)^2} \end{aligned} \right\} \tag{8.195}$$

Equation (8.195) simplifies when $n \neq 1$ to

$$I^{\text{TM-TM}}_{\text{L}\,p,\text{R}\,q}\Big|_{\substack{n\neq 1,\\ \gamma^{\text{L}}\neq\gamma^{\text{R}}}} = \left(\frac{\pi c}{\beta_0\,\varepsilon}\right)\frac{\gamma^{\text{L}} a\, k_z^{\text{L}}}{\left(\gamma^{\text{L}}/\gamma^{\text{R}}\right)^2-1} J_n\left(\gamma^{\text{R}} a\right)\left\{J_{n+1}\left(\gamma^{\text{L}} a\right)-\frac{\gamma^{\text{L}} a\, J_{n-2}\left(\gamma^{\text{L}} a\right)}{2(n-1)}\right\}, \quad (8.196)$$

and when $n=1$ it simplifies instead to

$$I^{\text{TM-TM}}_{\text{L}\,p,\text{R}\,q}\Big|_{\substack{n=1,\\ \gamma^{\text{L}}\neq\gamma^{\text{R}}}} = \left(\frac{\pi c}{\beta_0\,\varepsilon}\right)\frac{a\gamma^{\text{L}}\gamma^{\text{R}}\, k_z^{\text{L}}}{\left(\gamma^{\text{L}}\right)^2-\left(\gamma^{\text{R}}\right)^2}\left\{\gamma^{\text{L}}\, J_1\left(\gamma^{\text{L}} a\right)J_0\left(\gamma^{\text{R}} a\right)-2\gamma^{\text{R}}\, J_0\left(\gamma^{\text{L}} a\right)J_1\left(\gamma^{\text{R}} a\right)\right\}. \quad (8.197)$$

When $\gamma^{\text{L}}=\gamma^{\text{R}}$ the integral is solved using (8.257).

$$I^{\text{TM-TM}}_{\text{L}\,p,\text{R}\,q}\Big|_{\gamma^{\text{L}}=\gamma^{\text{R}}} = \frac{\pi c}{\beta_0\,\varepsilon}(\gamma a)^2\, k_z^{\text{L}} J_{n-1}^2(\gamma a) \quad (8.198)$$

Note that for TM mode $J_n\left(\gamma^{\text{L}} a\right)=J_n\left(\gamma^{\text{R}} b\right)=0$, $J_{n-1}\left(\gamma^{\text{L}} a\right)=-J_{n+1}\left(\gamma^{\text{L}} a\right)$, and $J_{n-1}\left(\gamma^{\text{R}} b\right)=-J_{n+1}\left(\gamma^{\text{R}} b\right)$. In the case of self-coupling (b=a) of different modes ([L] and [R] matrix off-diagonals) the TM-TM coupling integral is identically zero, as shown below.

Consider the numerator of the term in large braces in (8.195), as given in (8.199), for the self-coupling integrals. The double-crossed terms are zero-valued (TM mode). The single-crossed terms are zero-valued (TM mode) only in the case of the self-coupling integrals (for [L] and [R]) but not for the general case of the general junction mode coupling integrals for [P], as defined in (5.29).

numerator

$$= \gamma^{\mathrm{R}} a \left[J_{n-1}\left(\gamma^{\mathrm{L}} a\right) J_{n-2}\left(\gamma^{\mathrm{R}} a\right) + J_{n+1}\left(\gamma^{\mathrm{L}} a\right) \cancel{J_n\left(\gamma^{\mathrm{R}} a\right)} \right] \tag{8.199}$$
$$-\gamma^{\mathrm{L}} a \left[J_{n-2}\left(\gamma^{\mathrm{L}} a\right) J_{n-1}\left(\gamma^{\mathrm{R}} a\right) + \cancel{J_n\left(\gamma^{\mathrm{L}} a\right)} J_{n+1}\left(\gamma^{\mathrm{R}} a\right) \right]$$

$$= \gamma^{\mathrm{R}} a \left\{ \left[J_{n-2}\left(\gamma^{\mathrm{L}} a\right) + \cancel{J_n\left(\gamma^{\mathrm{L}} a\right)} \right] \frac{\gamma^{\mathrm{L}} a}{2(n-1)} \right\} J_{n-2}\left(\gamma^{\mathrm{R}} a\right) \tag{8.200}$$
$$-\gamma^{\mathrm{L}} a J_{n-2}\left(\gamma^{\mathrm{L}} a\right) \left\{ \left[J_{n-2}\left(\gamma^{\mathrm{R}} a\right) + J_n\left(\gamma^{\mathrm{R}} a\right) \right] \frac{\gamma^{\mathrm{R}} a}{2(n-1)} \right\}$$

$$= -\frac{\gamma^{\mathrm{L}} a \gamma^{\mathrm{R}} a}{2(n-1)} J_{n-2}\left(\gamma^{\mathrm{L}} a\right) \cancel{J_n\left(\gamma^{\mathrm{R}} a\right)} \tag{8.201}$$

$$= \text{zero for self-coupling} \tag{8.202}$$

8.3.5.2 TM-TE Mode Coupling Integral

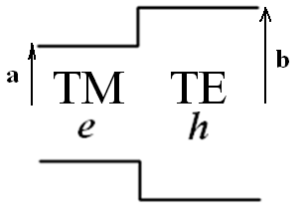

Fig. 8-3 Junction with TM-TE modes: Coupling *e* field on left with *h* field on right.

Consider the fields on both sides of the TM-TE junction for the mode coupling integral (8.184): electric field on left and magnetic on right. From (8.186) and (8.188) for transverse magnetic mode (TM: $\Lambda = \infty$), the rho and phi components of the electric field on the left side of the junction are given as follows.

$$E_{\mathrm{SM}\,\rho} = \frac{k_z^{\mathrm{SM}} \gamma_m^{\mathrm{SM}}}{2\beta_0 \varepsilon} \left\{ -J_{n-1}(\gamma_m^{\mathrm{SM}} \rho) + J_{n+1}(\gamma_m^{\mathrm{SM}} \rho) \right\} \exp[\pm j(n\varphi + \psi)]_{\mathrm{R}}^{\mathrm{L}}, \tag{8.203}$$

$$E_{\mathrm{SM}\varphi} = -(\pm j)\frac{k_z^{\mathrm{SM}}}{2\beta_0\varepsilon}\left\{J_{n-1}(\gamma^{\mathrm{SM}}\rho)+J_{n+1}(\gamma^{\mathrm{SM}}\rho)\right\}\exp[\pm j(n\varphi+\psi)]\,{}_{\mathrm{R}}^{\mathrm{L}}\,. \tag{8.204}$$

From (8.88) and (8.92) for transverse electric mode (TE: $\Lambda = 0$), the rho and phi component of the magnetic field on the right side of the junction are

$$H_{\mathrm{LG}\,\rho} = -\frac{k_z\gamma}{\omega\mu\varepsilon}J_{n-1}(\gamma\rho)\exp[\pm jn\varphi] + \frac{n}{\rho}\left(\frac{k_z}{\omega\mu\varepsilon}\exp[\pm jn\varphi]\right)J_n(\gamma\rho)\,{}_{\mathrm{R}}^{\mathrm{L}}\,, \tag{8.205}$$

or
$$H_{\mathrm{LG}\rho} = \pm j\frac{c\gamma^{\mathrm{LG}}k_z^{\mathrm{LG}}}{2\beta_0\,\varepsilon}\left\{J_{n-1}(\gamma^{\mathrm{LG}}\rho)-J_{n+1}(\gamma^{\mathrm{LG}}\rho)\right\}\exp[\pm j\left(n\varphi+\psi\right)]\,{}_{\mathrm{R}}^{\mathrm{L}}\,, \tag{8.206}$$

and
$$H_{\mathrm{LG}\varphi} = \quad -(\pm j)\frac{n}{\rho}\left(\frac{k_z}{\omega\mu\varepsilon}\exp[\pm jn\varphi]\right)J_n(\gamma\rho)\,, \tag{8.207}$$

or
$$H_{\mathrm{LG}\varphi} = \frac{-c\gamma^{\mathrm{LG}}k_z^{\mathrm{LG}}}{2\beta_0\,\varepsilon}\left\{J_{n-1}(\gamma^{\mathrm{LG}}\rho)+J_{n+1}(\gamma^{\mathrm{LG}}\rho)\right\}\exp[\pm j\left(n\varphi+\psi\right)]\,{}_{\mathrm{R}}^{\mathrm{L}}\,. \tag{8.208}$$

Consider the two terms of the axial component of the cross product, where superscripts L and SM both refer to the left, smaller side of the junction and R and LG to the right, larger side.

$$\begin{aligned} &E_\rho^{\mathrm{SM}}\left(H_\phi^{\mathrm{LG}}\right)^* - E_\phi^{\mathrm{SM}}\left(H_\rho^{\mathrm{LG}}\right)^* \\ &\qquad = \frac{\gamma^{\mathrm{SM}}\gamma^{\mathrm{LG}}k_z^{\mathrm{SM}}\left(k_z^{\mathrm{LG}}\right)^* c}{2\beta_0^2\,\varepsilon}\left\{J_{n-1}\left(\gamma^{\mathrm{SM}}\rho\right)J_{n-1}\left(\gamma^{\mathrm{LG}}\rho\right)-J_{n+1}\left(\gamma^{\mathrm{SM}}\rho\right)J_{n+1}\left(\gamma^{\mathrm{LG}}\rho\right)\right\} \end{aligned} \tag{8.209}$$

$$I_{\mathrm{SM}\,p,\mathrm{LG}q} = \hat{z}\cdot\iint_{\mathrm{SM}}\overline{e}_{\mathrm{SM}\,p}\times\left(\overline{h}_{\mathrm{LG}\,q}\right)^* ds \tag{8.210}$$

When $\gamma^{\mathrm{L}} \neq \gamma^{\mathrm{R}}$ the integral is solved in closed form using the Lommel integral (8.253).

$$I_{\mathrm{L}\,p,\mathrm{R}\,q}^{\text{TM-TE}}\Bigg|_{\gamma^{\mathrm{L}}\neq\gamma^{\mathrm{R}}} = \frac{\pi c}{\beta_0^2\,\varepsilon}\gamma^{\mathrm{L}}\gamma^{\mathrm{R}}k_z^{\mathrm{L}}\left(k_z^{\mathrm{R}}\right)^*\left\{\begin{array}{l}\dfrac{\gamma^{\mathrm{R}}a\,J_{n-1}\left(\gamma^{\mathrm{L}}a\right)J_{n-2}\left(\gamma^{\mathrm{R}}a\right)-\gamma^{\mathrm{L}}a\,J_{n-2}\left(\gamma^{\mathrm{L}}a\right)J_{n-1}\left(\gamma^{\mathrm{R}}a\right)}{\left(\gamma^{\mathrm{L}}\right)^2-\left(\gamma^{\mathrm{R}}\right)^2}\\ -\dfrac{\gamma^{\mathrm{R}}a\,J_{n+1}\left(\gamma^{\mathrm{L}}a\right)J_{n}\left(\gamma^{\mathrm{R}}a\right)-\gamma^{\mathrm{L}}a\,J_{n}\left(\gamma^{\mathrm{L}}a\right)J_{n+1}\left(\gamma^{\mathrm{R}}a\right)}{\left(\gamma^{\mathrm{L}}\right)^2-\left(\gamma^{\mathrm{R}}\right)^2}\end{array}\right\}$$
$$= 0 \quad \forall n,p,q \tag{8.211}$$

If $\gamma^{\mathrm{L}}=\gamma^{\mathrm{R}}$ the integral is solved using (8.257), and again is identically zero.

$$I_{\mathrm{L}\,p,\mathrm{R}\,q}^{\text{TM-TE}}\Bigg|_{\gamma^{\mathrm{L}}=\gamma^{\mathrm{R}}} = 0 \tag{8.212}$$

Note that for TM mode $J_n\left(\gamma^{\mathrm{L}}a\right)=0$, and $J_{n-1}\left(\gamma^{\mathrm{L}}a\right)=-J_{n+1}\left(\gamma^{\mathrm{L}}a\right)$. For TE mode $J_{n-1}\left(\gamma^{\mathrm{R}}b\right)=J_{n+1}\left(\gamma^{\mathrm{R}}b\right)$. For all mode combinations the TM-TE coupling integral is identically zero: TM mode in the smaller section does not couple at all to TE mode in the larger section. The proof of zero coupling, in general, is given here, starting with the numerator of (8.211), using $J_{n-1}\left(\gamma^{\mathrm{L}}a\right)=-J_{n+1}\left(\gamma^{\mathrm{L}}a\right)$, where $\gamma^{\mathrm{L}}a$ is a (TM) Bessel zero, $J_n\left(\gamma^{\mathrm{L}}a\right)=0$, and also using the Bessel identity (8.250).

$$\begin{aligned}\text{numerator} \rightarrow\ & \gamma^{\mathrm{R}}a\left[J_{n-1}\left(\gamma^{\mathrm{L}}a\right)J_{n-2}\left(\gamma^{\mathrm{R}}a\right)-J_{n+1}\left(\gamma^{\mathrm{L}}a\right)J_{n}\left(\gamma^{\mathrm{R}}a\right)\right]\\ & -\gamma^{\mathrm{L}}a\left[J_{n-2}\left(\gamma^{\mathrm{L}}a\right)J_{n-1}\left(\gamma^{\mathrm{R}}a\right)-\cancel{J_{n}\left(\gamma^{\mathrm{L}}a\right)}J_{n+1}\left(\gamma^{\mathrm{R}}a\right)\right]\end{aligned} \tag{8.213}$$

$$\begin{aligned}&=\gamma^{\mathrm{R}}a\left[J_{n-1}\left(\gamma^{\mathrm{L}}a\right)\left\{J_{n-2}\left(\gamma^{\mathrm{R}}a\right)+J_{n}\left(\gamma^{\mathrm{R}}a\right)\right\}\right]\\ &-\gamma^{\mathrm{L}}a\left[J_{n-2}\left(\gamma^{\mathrm{L}}a\right)J_{n-1}\left(\gamma^{\mathrm{R}}a\right)\right]\end{aligned} \tag{8.214}$$

$$= \gamma^{\mathrm{R}} a \left[J_{n-1}\left(\gamma^{\mathrm{L}} a\right) \left\{ \frac{2(n-1)}{\gamma^{\mathrm{R}} a} J_{n-1}\left(\gamma^{\mathrm{R}} a\right) \right\} \right] - \gamma^{\mathrm{L}} a \left[J_{n-2}\left(\gamma^{\mathrm{L}} a\right) J_{n-1}\left(\gamma^{\mathrm{R}} a\right) \right] \tag{8.215}$$

$$= 2(n-1) J_{n-1}\left(\gamma^{\mathrm{L}} a\right) J_{n-1}\left(\gamma^{\mathrm{R}} a\right) - \gamma^{\mathrm{L}} a J_{n-2}\left(\gamma^{\mathrm{L}} a\right) J_{n-1}\left(\gamma^{\mathrm{R}} a\right) \tag{8.216}$$

$$= 2(n-1) \left\{ \left[J_{n-2}\left(\gamma^{\mathrm{L}} a\right) + \cancel{J_n\left(\gamma^{\mathrm{L}} a\right)} \right] \frac{\gamma^{\mathrm{L}} a}{2(n-1)} \right\} J_{n-1}\left(\gamma^{\mathrm{R}} a\right) - \gamma^{\mathrm{L}} a J_{n-2}\left(\gamma^{\mathrm{L}} a\right) J_{n-1}\left(\gamma^{\mathrm{R}} a\right) \tag{8.217}$$

$$= \gamma^{\mathrm{L}} a J_{n-2}\left(\gamma^{\mathrm{L}} a\right) J_{n-1}\left(\gamma^{\mathrm{R}} a\right) - \gamma^{\mathrm{L}} a J_{n-2}\left(\gamma^{\mathrm{L}} a\right) J_{n-1}\left(\gamma^{\mathrm{R}} a\right) \tag{8.218}$$

$$\text{numerator} = 0; \ \text{Q.E.D.} \tag{8.219}$$

8.3.5.3 TE-TM Mode Coupling Integral

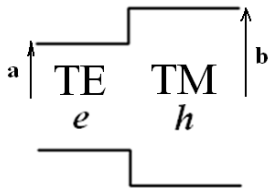

Fig. 8-4 Junction with TE-TM modes: Coupling *e* field on left with *h* field on right.

Consider the fields on both sides of the TE-TM junction for the mode coupling integral (8.184): electric field on left and magnetic on right. From (8.86) and (8.90) for transverse electric mode (TE: $\Lambda = 0$), the rho and phi components of the electric field on the left side of the junction are given as follows.

$$E_{\mathrm{SM}\,\rho} = -(\pm j) \frac{n}{\rho} \left(\frac{1}{\varepsilon} \exp[\pm jn\varphi] \right) J_n(\gamma\rho)^{\frac{\mathrm{L}}{\mathrm{R}}}, \tag{8.220}$$

or

$$E_{\mathrm{SM}\,\rho} = \frac{-\gamma^{\mathrm{SM}}}{2\varepsilon} \left\{ J_{n-1}(\gamma^{\mathrm{SM}}\rho) + J_{n+1}(\gamma^{\mathrm{SM}}\rho) \right\} \exp[\pm j(n\varphi + \psi)]^{\frac{\mathrm{L}}{\mathrm{R}}}, \tag{8.221}$$

utilizing the Bessel identity of (8.250),

and $$E_{\mathrm{SM}\,\varphi} = \left(\frac{\gamma}{\varepsilon}\right) J_{n-1}(\gamma\rho)\exp[\pm jn\varphi] + \frac{n}{\rho}\left(-\frac{1}{\varepsilon}\exp[\pm jn\varphi]\right) J_n(\gamma\rho)\ {}_{\mathrm{R}}^{\mathrm{L}}, \tag{8.222}$$

or $$E_{\mathrm{SM}\,\varphi} = -(\pm j)\frac{\gamma^{\mathrm{SM}}}{2\varepsilon}\left\{J_{n-1}(\gamma^{\mathrm{SM}}\rho) - J_{n+1}(\gamma^{\mathrm{SM}}\rho)\right\}\exp[\pm j(n\varphi+\psi)]\ {}_{\mathrm{R}}^{\mathrm{L}}. \tag{8.223}$$

From (8.190) and (8.192) the transverse magnetic mode (TM: $\Lambda = \infty$) rho and phi component of the magnetic field on the right side of the junction are

$$H_{\mathrm{LG}\,\rho} = \pm j\frac{\eta_0}{2\mu}\left\{J_{n-1}(\gamma_q^{\mathrm{LG}}\rho) + J_{n+1}(\gamma_q^{\mathrm{LG}}\rho)\right\}\exp[\pm j(n\varphi+\psi)]\ {}_{\mathrm{R}}^{\mathrm{L}}, \tag{8.224}$$

and $$H_{\mathrm{LG}\,\varphi} = \frac{\eta_0\gamma^{\mathrm{LG}}}{2\mu}\left\{-J_{n-1}(\gamma^{\mathrm{LG}}\rho) + J_{n+1}(\gamma^{\mathrm{LG}}\rho)\right\}\exp[\pm j(n\varphi+\psi)]\ {}_{\mathrm{R}}^{\mathrm{L}}. \tag{8.225}$$

Consider the two terms of the axial component of the cross product, where superscripts L and SM both refer to the left, smaller side of the junction and R and LG to the right, larger side.

$$\begin{aligned} &E_\rho^{\mathrm{SM}}\left(H_\phi^{\mathrm{LG}}\right)^* - E_\phi^{\mathrm{SM}}\left(H_\rho^{\mathrm{LG}}\right)^* \\ &\qquad = \frac{\gamma^{\mathrm{SM}}\gamma^{\mathrm{LG}}c}{2\varepsilon}\left\{J_{n-1}\left(\gamma^{\mathrm{SM}}\rho\right)J_{n-1}\left(\gamma^{\mathrm{LG}}\rho\right) - J_{n+1}\left(\gamma^{\mathrm{SM}}\rho\right)J_{n+1}\left(\gamma^{\mathrm{LG}}\rho\right)\right\} \end{aligned} \tag{8.226}$$

$$I_{\mathrm{SM}\,p,\mathrm{LG}\,q} = \hat{z}\cdot\iint_{\mathrm{SM}} \bar{e}_{\mathrm{SM}\,p}\times\left(\bar{h}_{\mathrm{LG}\,q}\right)^* ds \tag{8.227}$$

When $\gamma^{\mathrm{L}} \neq \gamma^{\mathrm{R}}$ the integral is solved in closed form using the Lommel integral (8.253).

$$I^{\text{TE-TM}}_{\text{L}\,p,\text{R}\,q}\Bigg|_{\gamma^{\text{L}}\neq\gamma^{\text{R}}} = \frac{\pi c}{\varepsilon}\gamma^{\text{L}}\gamma^{\text{R}}\left\{\begin{array}{l}\dfrac{\gamma^{\text{R}}a\,J_{n-1}\left(\gamma^{\text{L}}a\right)J_{n-2}\left(\gamma^{\text{R}}a\right)-\gamma^{\text{L}}a\,J_{n-2}\left(\gamma^{\text{L}}a\right)J_{n-1}\left(\gamma^{\text{R}}a\right)}{\left(\gamma^{\text{L}}\right)^2-\left(\gamma^{\text{R}}\right)^2} \\ -\dfrac{\gamma^{\text{R}}a\,J_{n+1}\left(\gamma^{\text{L}}a\right)J_{n}\left(\gamma^{\text{R}}a\right)-\gamma^{\text{L}}a\,J_{n}\left(\gamma^{\text{L}}a\right)J_{n+1}\left(\gamma^{\text{R}}a\right)}{\left(\gamma^{\text{L}}\right)^2-\left(\gamma^{\text{R}}\right)^2}\end{array}\right\} \quad (8.228)$$

Equation (8.228) simplifies to

$$I^{\text{TE-TM}}_{\text{L}\,p,\text{R}\,q}\Bigg|_{\gamma^{\text{L}}\neq\gamma^{\text{R}}} = \frac{\pi c}{\varepsilon}\frac{2\gamma^{\text{L}}\gamma^{\text{R}}}{\left(\gamma^{\text{L}}\right)^2-\left(\gamma^{\text{R}}\right)^2}\left\{n\frac{\gamma^{\text{L}}}{\gamma^{\text{R}}}J_n\left(\gamma^{\text{L}}a\right)-\gamma^{\text{R}}a\,J_{n-1}\left(\gamma^{\text{L}}a\right)\right\}J_n\left(\gamma^{\text{R}}a\right) \quad (8.229)$$

If coincidentally $\gamma^{\text{L}}=\gamma^{\text{R}}$ the integral is solved using (8.257). Since the two sides have different modes (TE and TM) it would have to be a peculiar ratio of the two waveguide radii to cause the two gammas to become equal.

$$I^{\text{TE-TM}}_{\text{L}\,p,\text{R}\,q}\Bigg|_{\gamma^{\text{L}}=\gamma^{\text{R}}} = \frac{\pi c}{2\varepsilon}\left(\gamma a\right)^2 J_n\left(\gamma a\right)\left\{J_{n+2}\left(\gamma a\right)-J_{n-2}\left(\gamma a\right)\right\} \quad (8.230)$$

Note that for TM mode $J_n\left(\gamma^{\text{L}}a\right)=0$, and $J_{n-1}\left(\gamma^{\text{L}}a\right)=-J_{n+1}\left(\gamma^{\text{L}}a\right)$. For TE mode $J_{n-1}\left(\gamma^{\text{L}}a\right)=J_{n+1}\left(\gamma^{\text{L}}a\right)$. In the case of self-coupling (*b*=*a*) of different modes ([L] and [R] matrix off-diagonals) the coupling integral is identically zero, which can be shown by manipulating (8.228) using the above noted relations in addition to Bessel identity (8.250), as given below.

Consider the numerator of the term in large braces in (8.228), as given in (8.231) for the self-coupling integrals. The single-crossed terms are zero-valued (TM mode) only in the case of the self-coupling integrals (for [L] and [R]) but not for the general case of the general junction mode coupling integrals for [P], as defined in (5.29).

$$\begin{aligned}&\text{numerator}\\&=\gamma^{\mathrm{R}}a\left[J_{n-1}\left(\gamma^{\mathrm{L}}a\right)J_{n-2}\left(\gamma^{\mathrm{R}}a\right)-J_{n+1}\left(\gamma^{\mathrm{L}}a\right)J_{n}\left(\gamma^{\mathrm{R}}a\right)\right]\\&-\gamma^{\mathrm{L}}a\left[J_{n-2}\left(\gamma^{\mathrm{L}}a\right)J_{n-1}\left(\gamma^{\mathrm{R}}a\right)-J_{n}\left(\gamma^{\mathrm{L}}a\right)J_{n+1}\left(\gamma^{\mathrm{R}}a\right)\right]\end{aligned} \tag{8.231}$$

$$=\gamma^{\mathrm{R}}a\left[J_{n-1}\left(\gamma^{\mathrm{L}}a\right)J_{n-2}\left(\gamma^{\mathrm{R}}a\right)\right]-\gamma^{\mathrm{L}}a\left[J_{n-1}\left(\gamma^{\mathrm{R}}a\right)\left\{J_{n-2}\left(\gamma^{\mathrm{L}}a\right)+J_{n}\left(\gamma^{\mathrm{L}}a\right)\right\}\right] \tag{8.232}$$

$$=\gamma^{\mathrm{R}}a\left[J_{n-1}\left(\gamma^{\mathrm{L}}a\right)J_{n-2}\left(\gamma^{\mathrm{R}}a\right)\right]-\gamma^{\mathrm{L}}a\left[J_{n-1}\left(\gamma^{\mathrm{R}}a\right)\left\{J_{n-1}\left(\gamma^{\mathrm{L}}a\right)\frac{2(n-1)}{\gamma^{\mathrm{L}}a}\right\}\right] \tag{8.233}$$

$$=\gamma^{\mathrm{R}}a\left[J_{n-1}\left(\gamma^{\mathrm{L}}a\right)J_{n-2}\left(\gamma^{\mathrm{R}}a\right)\right]-\gamma^{\mathrm{R}}a\left[\left\{J_{n-2}\left(\gamma^{\mathrm{R}}a\right)+J_{n}\left(\gamma^{\mathrm{R}}a\right)\right\}J_{n-1}\left(\gamma^{\mathrm{L}}a\right)\right] \tag{8.234}$$

$$=\gamma^{\mathrm{R}}aJ_{n-1}\left(\gamma^{\mathrm{L}}a\right)\cancel{J_{n}\left(\gamma^{\mathrm{R}}a\right)}=0\text{ for self-coupling} \tag{8.235}$$

8.3.5.4 TE-TE Mode Coupling Integral

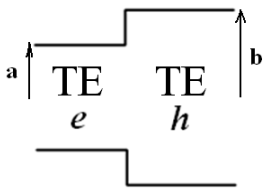

Fig. 8-5 Junction with TE-TE modes: Coupling *e* field on left with *h* field on right.

Consider the fields on both sides of the TE-TE junction for the mode coupling integral (8.184): electric field on left and magnetic on right. From (8.221) and (8.223) for transverse electric

mode (TE: $\Lambda = 0$), the rho and phi components of the electric field on the left side of the junction are given as follows.

$$E_{\mathrm{SM}\,\rho} = \frac{-\gamma^{\mathrm{SM}}}{2\varepsilon}\left\{J_{n-1}(\gamma^{\mathrm{SM}}\rho) + J_{n+1}(\gamma^{\mathrm{SM}}\rho)\right\}\exp[\pm j\left(n\varphi + \psi\right)]\,{}^{\mathrm{L}}_{\mathrm{R}}\,, \tag{8.236}$$

$$E_{\mathrm{SM}\,\varphi} = -\left(\pm j\right)\frac{\gamma^{\mathrm{SM}}}{2\varepsilon}\left\{J_{n-1}(\gamma^{\mathrm{SM}}\rho) - J_{n+1}(\gamma^{\mathrm{SM}}\rho)\right\}\exp[\pm j\left(n\varphi + \psi\right)]\,{}^{\mathrm{L}}_{\mathrm{R}}\,. \tag{8.237}$$

From (8.206) and (8.208) for transverse magnetic mode (TE: $\Lambda = 0$), the rho and phi component of the magnetic field on the right side of the junction are

$$H_{\mathrm{LG}\,\rho} = \pm j\frac{c\gamma^{\mathrm{LG}}k_z^{\mathrm{LG}}}{2\beta_0\,\varepsilon}\left\{J_{n-1}(\gamma^{\mathrm{LG}}\rho) - J_{n+1}(\gamma^{\mathrm{LG}}\rho)\right\}\exp[\pm j\left(n\varphi + \psi\right)]\,{}^{\mathrm{L}}_{\mathrm{R}}\,, \tag{8.238}$$

and

$$H_{\mathrm{LG}\,\varphi} = \frac{-c\gamma^{\mathrm{LG}}k_z^{\mathrm{LG}}}{2\beta_0\,\varepsilon}\left\{J_{n-1}(\gamma^{\mathrm{LG}}\rho) + J_{n+1}(\gamma^{\mathrm{LG}}\rho)\right\}\exp[\pm j\left(n\varphi + \psi\right)]\,{}^{\mathrm{L}}_{\mathrm{R}}\,. \tag{8.239}$$

Consider the two terms of the axial component of the cross product, where superscripts L and SM both refer to the left, smaller side of the junction and R and LG to the right, larger side.

$$\begin{aligned} &E_\rho^{\mathrm{SM}}\left(H_\phi^{\mathrm{LG}}\right)^* - E_\phi^{\mathrm{SM}}\left(H_\rho^{\mathrm{LG}}\right)^* \\ &\qquad = \frac{c\gamma^{\mathrm{SM}}\gamma^{\mathrm{LG}}\left(k_z^{\mathrm{LG}}\right)^*}{2\beta_0\,\varepsilon}\left\{J_{n-1}\left(\gamma^{\mathrm{SM}}\rho\right)J_{n-1}\left(\gamma^{\mathrm{LG}}\rho\right) + J_{n+1}\left(\gamma^{\mathrm{SM}}\rho\right)J_{n+1}\left(\gamma^{\mathrm{LG}}\rho\right)\right\} \end{aligned} \tag{8.240}$$

$$I_{\mathrm{SM}\,p,\mathrm{LG}\,q} = \hat{z}\cdot\iint\limits_{\mathrm{SM}}\overline{e}_{\mathrm{SM}\,p}\times\left(\overline{h}_{\mathrm{LG}\,q}\right)^* ds \tag{8.241}$$

When $\gamma^{\mathrm{L}} \neq \gamma^{\mathrm{R}}$ the integral is solved in closed form using the Lommel integral (8.253).

$$I^{\text{TE-TE}}_{\text{L}\,p,\text{R}\,q}\Bigg|_{\gamma^{\text{L}}\neq\gamma^{\text{R}}} = \frac{\pi c\gamma^{\text{L}}\gamma^{\text{R}}\left(k_z^{\text{R}}\right)^*}{\beta_0\,\varepsilon}\left\{\begin{aligned}&\frac{\gamma^{\text{R}}a\,J_{n-1}\left(\gamma^{\text{L}}a\right)J_{n-2}\left(\gamma^{\text{R}}a\right)-\gamma^{\text{L}}a\,J_{n-2}\left(\gamma^{\text{L}}a\right)J_{n-1}\left(\gamma^{\text{R}}a\right)}{\left(\gamma^{\text{L}}\right)^2-\left(\gamma^{\text{R}}\right)^2}\\ &+\frac{\gamma^{\text{R}}a\,J_{n+1}\left(\gamma^{\text{L}}a\right)J_{n}\left(\gamma^{\text{R}}a\right)-\gamma^{\text{L}}a\,J_{n}\left(\gamma^{\text{L}}a\right)J_{n+1}\left(\gamma^{\text{R}}a\right)}{\left(\gamma^{\text{L}}\right)^2-\left(\gamma^{\text{R}}\right)^2}\end{aligned}\right\} \quad (8.242)$$

Equation (8.242) simplifies to

$$I^{\text{TE-TE}}_{\text{L}\,p,\text{R}\,q}\Bigg|_{\gamma^{\text{L}}\neq\gamma^{\text{R}}} = \left(\frac{\pi c}{\beta_0\,\varepsilon}\right)\frac{\gamma^{\text{R}}a\left(k_z^{\text{R}}\right)^*}{1-\left(\gamma^{\text{R}}/\gamma^{\text{L}}\right)^2}J_n\left(\gamma^{\text{L}}a\right)\left\{J_{n-1}\left(\gamma^{\text{R}}a\right)-J_{n+1}\left(\gamma^{\text{R}}a\right)\right\}. \quad (8.243)$$

When $\gamma^{\text{L}}=\gamma^{\text{R}}$ the integral is solved using (8.257).

$$I^{\text{TE-TE}}_{\text{L}\,p,\text{R}\,q}\Bigg|_{\gamma^{\text{L}}=\gamma^{\text{R}}} = \frac{\pi c(\gamma a)^2}{2\beta_0\,\varepsilon}\left(k_z^{\text{R}}\right)^*\left\{2J_{n-1}^2(\gamma a)-J_n(\gamma a)\left[J_{n-2}(\gamma a)+J_{n+2}(\gamma a)\right]\right\} \quad (8.244)$$

Note the complex conjugation of k_z^R in (8.243) and (8.244), and see the note regarding complex conjugation depending on field polarization following (5.29). For TE mode $J_{n-1}\left(\gamma^{\text{L}}a\right)=J_{n+1}\left(\gamma^{\text{L}}a\right)$, and $J_{n-1}\left(\gamma^{\text{R}}b\right)=J_{n+1}\left(\gamma^{\text{R}}b\right)$. In the case of self-coupling (*b*=*a*) of different modes ([L] or [R] matrix off-diagonals) the coupling integral is identically zero, which can be shown by manipulating (8.242) using the above relations in addition to Bessel identity (8.250).

Consider the numerator of the term in large braces in (8.242), as given in (8.245) for the self-coupling integrals.

$$\begin{aligned}\text{numerator} = {} & \gamma^{\mathrm{R}} a\left[J_{n-1}\left(\gamma^{\mathrm{L}} a\right) J_{n-2}\left(\gamma^{\mathrm{R}} a\right) + J_{n+1}\left(\gamma^{\mathrm{L}} a\right) J_n\left(\gamma^{\mathrm{R}} a\right)\right] \\ & - \gamma^{\mathrm{L}} a\left[J_{n-2}\left(\gamma^{\mathrm{L}} a\right) J_{n-1}\left(\gamma^{\mathrm{R}} a\right) + J_n\left(\gamma^{\mathrm{L}} a\right) J_{n+1}\left(\gamma^{\mathrm{R}} a\right)\right]\end{aligned} \tag{8.245}$$

$$\begin{aligned} & = \gamma^{\mathrm{R}} a\left[J_{n-1}\left(\gamma^{\mathrm{L}} a\right)\left\{J_{n-2}\left(\gamma^{\mathrm{R}} a\right) + J_n\left(\gamma^{\mathrm{R}} a\right)\right\}\right] \\ & -\gamma^{\mathrm{L}} a\left[J_{n-1}\left(\gamma^{\mathrm{R}} a\right)\left\{J_{n-2}\left(\gamma^{\mathrm{L}} a\right) + J_n\left(\gamma^{\mathrm{L}} a\right)\right\}\right]\end{aligned} \tag{8.246}$$

$$= \gamma^{\mathrm{R}} a\left[J_{n-1}\left(\gamma^{\mathrm{L}} a\right)\left\{J_{n-1}\left(\gamma^{\mathrm{R}} a\right)\frac{2(n-1)}{\gamma^{\mathrm{R}} a}\right\}\right] - \gamma^{\mathrm{L}} a\left[J_{n-1}\left(\gamma^{\mathrm{R}} a\right)\left\{J_{n-1}\left(\gamma^{\mathrm{L}} a\right)\frac{2(n-1)}{\gamma^{\mathrm{L}} a}\right\}\right] \tag{8.247}$$

$$= 0 \text{ for self-coupling integrals} \tag{8.248}$$

8.4 BESSEL IDENTITIES (CHAPTER 8)

$$F_n\left(x\right) = \frac{x\frac{\partial}{\partial x}\left[J_n\left(x\right)\right]}{J_n\left(x\right)} \tag{8.249}$$

$$J_\nu(x) = \left[J_{\nu-1}(x) + J_{\nu+1}(x)\right] {}^{x}\!/_{2\nu} \tag{8.250}$$

$$\tfrac{\partial}{\partial\rho}[J_n(\gamma\rho)] = \gamma J_{n-1}(\gamma\rho) - J_n(\gamma\rho)\, {}^{n}\!/_{\rho} \tag{8.251}$$

$$J_{-n}(x) = (-1)^n J_n(x);\ n \text{ an integer} \tag{8.252}$$

Lommel Integral formula [6], pg 337:

$$\int_0^x J_n(\alpha x) J_n(\nu x) x dx = \frac{x}{\alpha^2 - \nu^2}\begin{pmatrix} J_n(\alpha x)\frac{\partial}{\partial x} J_n(\nu x) - \\ J_n(\nu x)\frac{\partial}{\partial x} J_n(\alpha x) \end{pmatrix} \tag{8.253}$$

From [146] (11.3.20), (11.3.32) and (11.3.34) respectively, the following integrals are obtained.

$$\int_0^z t\, J_0(t)\, dt = z\, J_1(z) \tag{8.254}$$

$$\int_0^z t\, J_{n-1}^2(t)\, dt = 2\sum_{k=0}^{\infty}(n+2k) J_{n+2k}^2(z) \tag{8.255}$$

$$\int_0^z t\, J_0^2(t)\, dt = \frac{z^2}{2}\left[J_0^2(z) + J_1^2(z)\right] \tag{8.256}$$

From [88] (5.54.2) the following integral is obtained.

$$\int Z_n^2(at)\, t\, dt = \frac{t^2}{2}\left\{Z_n^2(at) - Z_{n-1}(at) Z_{n+1}(at)\right\} \tag{8.257}$$

From [88] (6.561.1) the following integral is obtained.

$$\int_0^z t\, J_1(t)\, dt = \frac{\pi}{2} z\left[J_1(z)\mathrm{H}_0(z) + J_0(z)\mathrm{H}_1(z)\right] \tag{8.258}$$

$H_v(z)$ is the Struve function, used to compute the aperture taper efficiency of the second angular mode, which is greater than that of the first angular mode.

$$\mathrm{H}_0(z) = \sum_{k=0}^{\infty} \frac{(-1)^k (z/2)^{2k+1}}{\pi \prod_{i=0}^{k} (i + 1/2)^2} \tag{8.259}$$

$$\mathrm{H}_1(z) = \sum_{k=0}^{\infty} \frac{(-1)^k (z/2)^{2k+2}}{(k+3/2)\pi \prod_{i=0}^{k} (i + 1/2)^2} \tag{8.260}$$

The code used to calculate Bessel functions of the first kind, $J_v(x)$, was adapted to C language from the FORTRAN code provided online by Netlib: http://www.netlib.org/specfun/rjbesl, which provides a speed/precision tradeoff — using the NSIG and RTNSIG parameters — and applies to non-negative real order Bessel with non-negative real argument. The following code for calculating the above Struve functions was adapted to C language from the special function code in FORTRAN found online at the following Internet hyperlink: http://jin.ece.illinois.edu/routines/routines.html. It is relatively fast with sufficient accuracy.

```
#include <math.h>
/*
C
C       ===================================================
C       Purpose: This program computes Struve function
C                H0(x) using subroutine STVH0
C       Input :  x   --- Argument of H0(x)
C       Output:  H0(x)
C       Example:
C                   x          H0(x)
C                 ----------------------
C                   0.0       .00000000
C                   5.0      -.18521682
C                  10.0       .11874368
C                  15.0       .24772383
C                  20.0       .09439370
C                  25.0      -.10182519
C       ===================================================
C
*/
float struve_h0( float X ) {
#define myabs(x) ( x < 0 ? (-x) : ( x ) )
#define SQ(x) ((x)*(x))
/*
C       ============================================
C       Purpose: Compute Struve function H0(x)
C       Input :  x   --- Argument of H0(x) ( x ò 0 )
C       Output:  SH0 --- H0(x)
C       ============================================
*/
            int K, KM;
        double PI=acos(-1.);//3.141592653589793;
        double S=1.0;
        double R=1.0;
            double A0, T, T2, P0, Q0, TA0, BY0;

            double dtemp;
```

```
         if (X <= 20.0) {
            A0=2.0*X / PI;
            for( K=1; K<=60; K++ ) {
               R=-R*X/(2.0*K+1.0)*X/(2.0*K+1.0);
               S=S+R;
               if ( myabs(R) < myabs(S)*1.0e-12 ) break;
            }
            return(A0*S);
         } else {
            KM=(0.5*(X+1.0));
            if (X>=50.0) KM=25;
            for( K=1; K<=KM; K++ ) {
                   dtemp = ((2.0*K-1.0)/X);
               R=-R*SQ(dtemp);
               S=S+R;
               if ( myabs(R) < myabs(S) * 1.0e-12 ) break;
            }
            T=4/X;
            T2=SQ(T);
            P0=((((-.37043e-5*T2+.173565e-4)*T2-.487613e-4)
               *T2+.17343e-3)*T2-.1753062e-2)*T2+.3989422793;
            Q0=T*(((((.32312e-5*T2-.142078e-4)*T2+.342468e-4)*
               T2-.869791e-4)*T2+.4564324e-3)*T2-.0124669441);
            TA0=X-0.25*PI;
            BY0=2./sqrt(X)*(P0*sin(TA0)+Q0*cos(TA0));
            return(2./(PI*X)*S+BY0);
         }
}

/*
C
C       ======================================================
C       Purpose: This program computes Struve function
C                H1(x) using subroutine STVH1
C       Input :  x   --- Argument of H1(x)
C       Output:  H1(x)
C       Example:
C                   x          H1(x)
C                  ----------------------
C                    0.0       .00000000
C                    5.0       .80781195
C                   10.0       .89183249
C                   15.0       .66048730
C                   20.0       .47268818
C                   25.0       .53880362
C       ======================================================
C
*/
float struve_h1( float X ) {
#define myabs(x) ( x < 0 ? (-x) : ( x ) )
#define SQ(x) ((x)*(x))
/*
C       ============================================
C       Purpose: Compute Struve function H1(x)
C       Input :  x   --- Argument of H1(x) ( x ò 0 )
```

```
C       Output:  SH1 --- H1(x)
C       ========================================
*/
            int K, KM;
        double PI=acos(-1.);//3.141592653589793;
        double S;
        double R;
            double A0, T, T2, P1, Q1, TA1, BY1;

            double dtemp;
//        IMPLICIT DOUBLE PRECISION (A-H,O-Z)
        R=1.0;
        if (X<=20.0) {
           S=0.0;
           A0=-2.0/PI;
           for( K=1; K<=60; K++) {
              R=-R*X*X/(4.0*K*K-1.0);
              S=S+R;
              if ( myabs(R) < myabs(S) * 1.0e-12) break;
           }
           return(A0*S);
        } else {
           S=1.0;
           KM=0.5*X;
           if (X>50.0) KM=25;
           for( K=1; K<=KM; K++ ) {
              R=-R*(4.0*K*K-1.0)/(X*X);
              S=S+R;
              if ( myabs(R) < myabs(S)*1.0e-12 ) break;
           }
           T=4.0/X;
           T2=SQ(T);
           P1=((((.42414e-5*T2-.20092e-4)*T2+.580759e-4)*T2
              -.223203e-3)*T2+.29218256e-2)*T2+.3989422819;
           Q1=T*(((((-.36594e-5*T2+.1622e-4)*T2-.398708e-4)*
              T2+.1064741e-3)*T2-.63904e-3)*T2+.0374008364);
           TA1=X-0.75*PI;
           BY1=2.0/sqrt(X)*(P1*sin(TA1)+Q1*cos(TA1));
           return(2.0/PI*(1.0+S/(X*X))+BY1);
        }
}
```

8.5 METHODS OF STEEPEST DECENT PATH AND OF STATIONARY PHASE (CHAPTER 1)

Consider a function, $f(z)$, of complex variable *z,* that is analytic over a given line integral contour domain and a line integral of that function of the following form:

$$I = \int_{\text{SDP}} F(z)\exp\left[\xi f(z)\right]dz\,, \tag{8.261}$$

where ξ is large positive real. Let there be a stationary (saddle) point at z_x, and with a Taylor expansion of the argument of the exponential, let

$$f(z) = f(z_s) + \frac{(z-z_s)^2}{2} f''(z_s)\,. \tag{8.262}$$

Then
$$I = F(z_s)\exp\left[\xi f(z_s)\right] \int_{\text{SDP}} \exp\left[\frac{\xi(z-z_s)^2}{2} f''(z_s)\right]dz\,, \tag{8.263}$$

and the saddle-point surface on which the steepest descent path (SDP) exists is defined by constant $\text{Im}\{f(z)\}$. Thus

$$\text{Re}\{f(z)\} - \text{Re}\{f(z_s)\} \approx \frac{(z-z_s)^2}{2} f''(z_s) \tag{8.264}$$

must be negative real along the SDP. Let

$$z - z_s = s\exp\left[j\psi\right]. \tag{8.265}$$

Consider the line passing through the saddle-point and parallel to the SDP at that point:

$$z(s,\psi) - z_s = s\exp\left[j\psi\right], \tag{8.266}$$

where s is real, and ψ is the angle, with respect to the x-axis, of the direction that the SDP passes through the saddle-point.

$$\frac{\partial z}{\partial s} = \exp[j\psi] \tag{8.267}$$

Then
$$\xi\frac{(z-z_s)^2}{2}f''(z_s)=\xi\frac{s^2}{2}\exp[j2\psi]f''(z_s)$$
$$=-\xi\frac{s^2}{2}\{-\exp[j2\psi]f''(z_s)\} \tag{8.268}$$

Define ψ so that
$$-\exp[j2\psi]f''(z_s)=|f''(z_s)|. \tag{8.269}$$

Note that ψ is chosen so $-\exp[j2\psi]$ cancels out the phase of $f''(z_s)$.

Thus
$$I_{\text{SDP}}=F(z_s)\exp[\xi f(z_s)]\int_{\text{SDP}}\exp\left[\frac{-\xi P}{2}s^2+j\psi\right]ds \tag{8.270}$$

$$I_{\text{SDP}}=F(z_s)\exp[\xi f(z_s)+j\psi]\int_{-\varepsilon}^{\varepsilon}\exp\left[\frac{-\xi P}{2}s^2\right]ds \tag{8.271}$$

Since
$$\int_{-\infty}^{\infty}\exp[-ax^2]dx=\sqrt{\frac{\pi}{a}},\quad a \text{ real}>0, \tag{8.272}$$

finally,
$$\boxed{I_{\text{SDP}}=\int_C F(z)\exp[\xi f(z)]dz\approx\sqrt{\frac{2\pi}{\xi|f''(z_s)|}}F(z_s)\exp[\xi f(z_s)+j\psi_{\text{SDP}}]}, \tag{8.273}$$

where of the two candidate values for ψ the correct one defines the direction through the saddle-point for the SDP contour integral — from the lower to the upper integration limit — with the shortest total contour path length. This is analogous to Fermat's principle for optics, which states that a stationary point is defined by minimum total optical path length.

Similarly, the saddle-point surface for the Method of Stationary Phase (MSP) technique is defined by constant $\text{Im}\{f(z)\}$,

$$\boxed{I_{\text{MSP}}\approx F(z_s)\sqrt{\frac{2\pi}{\xi|f''(z_s)|}}\exp\left[\xi f(z_s)+j\left(\psi'_{\text{MSP}}\pm\frac{\pi}{4}\text{sgn}\left[\text{Im}\{f''(z_s)\exp[j2\psi'_{\text{MSP}}]\}\right]\right)\right]} \tag{8.274}$$

where ψ'_{MSP} is chosen so that

$$\mathrm{Re}\left\{\exp\left[j2\psi'_{\mathrm{MSP}}\right]f''(z_s)\right\}=0\,. \tag{8.275}$$

Consider the proper choice of ψ_{SDP} when applying the method of SDP to the following integral:

$$I=\int_0^\infty \exp\left[-a\left(\frac{z^2}{2}-z\right)\right]dz\ ;\ a\in\text{real}>0 \tag{8.276}$$

$$=\int \exp\left[a\,f(z)\right]dz \tag{8.277}$$

$$=\sqrt{\frac{2\pi}{a}}\exp\left[\frac{a}{2}\right]\left\{\frac{1+\mathrm{erf}\sqrt{a/2}}{2}\right\}\,. \tag{8.278}$$

For large a,

$$\lim_{a\to\infty} I(a)=\sqrt{\frac{2\pi}{a}}\exp\left[\frac{a}{2}\right]. \tag{8.279}$$

$$\begin{aligned} &f(z)=-\left(z^2/2-z\right)\ ;\ f(z_s)=1/2\\ &f'(z)=1-z\qquad\quad ;\ z_s=1+j0\\ &f''(z)=\rho e^{j\theta}=-1\quad ;\ \theta=\pi\\ &\psi_{SDP}=-\theta/2\pm\pi/2=0\text{ or }-\pi. \end{aligned} \tag{8.280}$$

According to Cauchy theory of complex variables, the above integral is independent of the contour path through the z-plane between the fixed integration limits, since the integrand is analytic. Thus the same integral result is obtained whether or not the integration contour passes through any particular point; e.g., a stationary point. If the integration contour does pass through the stationary point then the integral is independent of the direction the contour takes through that or any other point.

Path independence no longer applies though, when the integral is approximated by the MSP or SDP asymptotic methods, because MSP and SDP only consider the contribution in the

immediate vicinity of the stationary point. Applying the SDP method to the above example: the two candidate solutions are $\psi_{SDP} = 0, -\pi$, and the correct result, (8.279), is obtained by SDP, according to (8.274), only with $\psi = 0$. If the contour path were taken in the opposite direction, with $\psi_{SDP} = -\pi$, then the SDP result would be in error by a factor of -1. In order to utilize the incorrect $\psi_{SDP} = -\pi$ angle the contour path would have to take a significant detour in the complex plane so as to go past the stationary point, then turn back around to pass backwards through the saddle point, then detour again to finally head in the direction of the upper limit of the integration: Such detours extend the total contour path length and produce the wrong integral result. This is illustrated in Fig. 8-6.

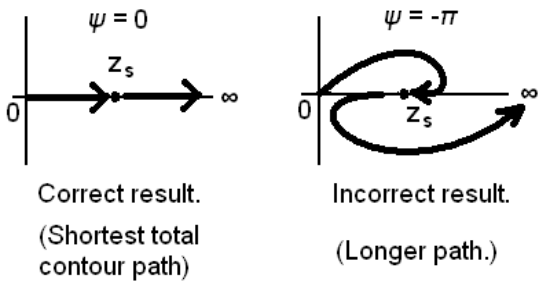

Fig. 8-6. An analogy of Fermat's principle, of shortest path length, determines the proper choice of the two candidate values of ψ for SDP or MSP, given the fixed integration end points.

As an interesting example of the application of the SDP method to integrals involving a saddle point, consider the following two integrals, which upon initial inspection might seem to produce the same result, because the values of the respective integrands behave the same as the respective (straight-line) contour path is traveled; although, use of the SDP (or MSP) method produces distinctly different results for the two integrals.

$$ {}_1I = \int_{-\infty \exp[j\pi/4]}^{+\infty \exp[j\pi/4]} \exp\left[z^2\right] dz \tag{8.281} $$

$$ {}_2I = \int_{-\infty}^{+\infty} \exp\left[jz^2\right] dz \tag{8.282} $$

Applying the SDP method to both integrals produces distinct results, which agree with Mathematica™ and Maple™.

$$ {}_1I_{\mathrm{SDP}} = \sqrt{\pi}\exp\left[j\pi/2\right] \tag{8.283} $$

$$ {}_2I_{\mathrm{SDP}} = \sqrt{\pi}\exp\left[j\pi/4\right] \tag{8.284} $$

8.6 USE OF DIFFERENT MATH LIBRARIES (CHAPTER 5)

This appendix summarizes the differences between using the different math libraries in different versions of the cylindrical mode matching (CYL_MM) computer program distinguished by their use of different math libraries but otherwise being functionally identical: custom hand-written math library, Netlib, ACML and MKL. The different versions of CYL_MM each involve a main program that does not call any BLAS or LAPACK functions from the math library, supported by subroutines that do call routines from the math library. All the versions except the original one using the hand-written library share the same main program. (The one using the hand-written library was eventually abandoned and lost main-program compatibility somewhere during the evolution of the program development.) The Microsoft Visual Studio™ (2008) integrated development environment (IDE) setup is the same and shared by all CYL_MM program versions, so the differences are mainly in the VS2008 project linker additional dependency settings that are specified in the particular VS2008 solution (IDE) file, and for the ACML cases also distinguished by some unique differences in the content of the subroutines that call BLAS and LAPACK routines.

8.6.1 Custom Hand-Written cmath.h Math Libraries

A) At top of subroutine file:

```
#include "cmmath.h"
```

B) Declarations at top of inside subroutine: nothing in particular.

C) Example BLAS and LAPACK calls:

None: Matrix A is inverted, then left multiplied with the b vector.

8.6.2 Netlib - BLAS (e.g. xGEMM) & LAPACK (e.g. xGESV)

VS2008 setup: Tools / Options / VC++ Directories /

Include: c:\Program Files\CLAPACK\INCLUDE

Libraries: c:\Program Files\CLAPACK\lib

Project / Properties ... / Linker / input / additional dependencies

libf2c.lib // My C calls are converted to FORTRAN calls that linker ties to math lib.

blas.lib

lapack.lib

In source codes that call on Netlib:

A) Declarations outside subroutine:

```
// for BLAS & CLAPACK
namespace lapack {
  extern "C" {
#include "f2c.h"
#undef abs
#include "clapack.h"
  }
}
```

B) Declarations at top of inside subroutine:

```
// vars for BLAS ZGEMM, matrix multiply
char z_transa, z_transb;
lapack::integer  z_m, z_n, z_k;
complex<double> alpha, beta;
lapack::doublecomplex * z_alpha = (lapack::doublecomplex *) &alpha, *
z_beta = (lapack::doublecomplex *) &beta;
lapack::integer z_lda, z_ldb, z_ldc;
lapack::doublecomplex * z_a, * z_b, * z_c;
// vars unique for CLAPACK ZGESV, solve linear matrix eq
lapack::integer z_nrhs;
lapack::integer z_ipiv[maxArrayTotLenSqr];
lapack::integer z_info;
```

C) Example BLAS and LAPACK calls

```
zgemm_( &z_transa, &z_transb, &z_m, &z_n, &z_k, z_alpha, z_a, &z_lda,
z_b, &z_ldb, z_beta, z_c, &z_ldc );
zgesv_( &z_n, &z_nrhs, z_a, &z_lda, z_ipiv, z_b, &z_ldb, &z_info );
```

8.6.3 ACML Single Threaded

The ACML library is not directly compatible with the Netlib library as MKL is, so the subroutine that calls the ACML library routines (BLAS / LAPACK) has to be slightly revised from the Netlib standard convention to match either the ACML FORTRAN or C calling convention. Here the choice was made to use the FORTRAN convention, to be pseudo compatible with the Netlib standard FORTRAN calling convention, as used in the prior case.

VS2008 setup: Tools / Options / VC++ Directories /

Include: c:\AMD\acml4.4.0\ifort32\include

Libraries: c:\AMD\acml4.4.0\ifort32\lib

// Intel compiler files (ifconsol.lib, etc. required to link ACML lib):

c:\Program Files\Intel\Composer XE 2013\compiler\lib\ia32

Project / Properties ... / Linker / input / additional dependencies

libacml.lib

libacml_dll.lib

In source codes that calls BLAS or LAPACK:

A) Declarations outside subroutine:

```
// AMD ACML BLAS/LAPACK excerpt from acml.h
extern "C" {
typedef struct
{
  double real, imag;
} doublecomplex;
// all ACML routines called in subr must be declared here
extern void ZGEMM(char *transa, char *transb, int *m, int *n, int *k,
doublecomplex *alpha, doublecomplex *a, int *lda, doublecomplex *b, int *ldb,
doublecomplex *beta, doublecomplex *c, int *ldc, int transa_len, int
transb_len);
extern void ZGESV(int *n, int *nrhs, doublecomplex *a, int *lda, int
*ipiv, doublecomplex *b, int *ldb, int *info);
extern void ZGETRS(char *trans, int *n, int *nrhs, doublecomplex *a, int
*lda, int *ipiv, doublecomplex *b, int *ldb, int *info, int trans_len);
//      From ACML Doc / acml.txt:
//   * The FORTRAN interface names are appended by an underscore (except
//     for the Windows 32-bit and 64-bit Microsoft C/Intel Fortran
//     version of ACML, where FORTRAN interface names are distinguished
//     from C by being upper case rather than lower case - this is the
//     default for the Intel Fortran compiler)
}
   Some of the ACML Fortran calls for BLAS (ZGEMM & ZGETRS) have
additional arguments
(,ione,ione or ,ione added respectively to end of ZGEMM/ZGETRS arg lists,
where ione is defined as int ione=1,
```

```
      and is not of pointer type but value in the arg list, to specify length
of char string inputs) which do not appear
      in Netlib's LAPACK Fortran calls or documentation.
```

A2) Alternative to the above is:

```
      Include the whole acml header file, putting it in its own namespace
avoids conflict with <complex>:
      namespace acml {
        acml.h
      }
and replacing declarations using doublecomplex with acml::doublecomplex instead
```

B) Declarations at top of inside subroutine:

```
      int ione = 1; // See note in (A) above.
      // vars for BLAS ZGEMM, matrix multiply
      char z_transa, z_transb;
      int  z_m, z_n, z_k;
      complex<double> alpha, beta;
      doublecomplex  *  z_alpha  =  (doublecomplex  *)  &alpha,  *  z_beta  =
(doublecomplex *) &beta;
      int z_lda, z_ldb, z_ldc;
      doublecomplex * z_a, * z_b, * z_c;
      // vars unique for CLAPACK ZGESV, solve linear matrix eq
      int z_nrhs;
      int z_ipiv[maxArrayTotLenSqr];
      int z_info;
```

C) Example BLAS and LAPACK calls

```
      ZGEMM( &z_transa, &z_transb, &z_m, &z_n, &z_k, z_alpha, z_a, &z_lda, z_b,
&z_ldb, z_beta, z_c, &z_ldc, ione, ione );
      ZGESV( &z_n, &z_nrhs, z_a, &z_lda, z_ipiv, z_b, &z_ldb, &z_info );
```

8.6.4 ACML Multi-Threaded (Parallel)

VS2008 setup: Tools / Options / VC++ Directories /

Include: c:\AMD\acml4.4.0\ifort32_mp\lib

Libraries: c:\AMD\acml4.4.0\ifort32_mp\lib

// Intel compiler files (ifconsol.lib, etc. required to link ACML lib):

c:\Program Files\Intel\Composer XE 2013\compiler\lib\ia32

Project / Properties ... / Linker / input / additional dependencies

libacml_mp.lib

libacml_mp_dll.lib

In source codes that call on BLAS or LAPACK:

A) Declarations outside subroutine: Same as for ACML single-threaded case.

B) Declarations at top of inside subroutine: Same as for ACML single-threaded case.

C) Example BLAS and LAPACK calls: Same as for ACML single-threaded case.

See section 0 below regarding control of how many parallel threads to use.

8.6.5 MKL Single Threaded

The MKL library is directly compatible with the Netlib library, so no change is required to be made to the code, only to the Visual Studio solution file, to direct the linker to link the BLAS and LAPACK libraries from MKL instead of Netlib.

VS2008 setup: Tools / Options / VC++ Directories /

Include: None: (MKL is fully integrated into Visual Studio.)

Libraries: None: (MKL is fully integrated into Visual Studio.)

Project / Properties ... / Linker / input / additional dependencies

libf2c.lib // Just like my Netlib case, my C calls are converted to FORTRAN calls that linker ties to math lib.

mkl_intel_c_dll.lib

mkl_sequential_dll.lib

mkl_core_dll.lib

In source codes that call on BLAS or LAPACK:

A) Declarations outside subroutine: Same as for Netlib case.

B) Declarations at top of inside subroutine: Same as for Netlib case.

C) Example BLAS and LAPACK calls: Same as for Netlib case.

Note that nowhere in the code is there a #include "mkl.h," because -- for code compatibility with Netlib math lib – BLAS or LAPACK routines are called using the F2C convention, and the VS linker is directed to link to MKL-provided FORTRAN BLAS/LAPACK subroutines rather than Netlib's.

8.6.6 MKL Multi-Threaded (Parallel)

The MKL library is directly compatible with the Netlib library, so no change is required to be made to the code, only to the Visual Studio solution file, to direct the linker to link the BLAS and LAPACK libraries from MKL instead of Netlib.

VS2008 setup: Tools / Options / VC++ Directories /

Include: None: (MKL is fully integrated into Visual Studio.)

Libraries: None: (MKL is fully integrated into Visual Studio.)

Project / Properties ... / Linker / input / additional dependencies

libf2c.lib // Just like my Netlib case, my C calls are converted to FORTRAN calls that linker ties to math lib.

mkl_intel_c_dll.lib

mkl_intel_thread_dll.lib

mkl_core_dll.lib

libiomp5md.lib

In source codes that call on BLAS or LAPACK:

A) Declarations outside subroutine: Same as for single thread.

B) Declarations at top of inside subroutine: Same as for single thread.

C) Example BLAS and LAPACK calls: Same as for single thread.

Note that nowhere in the code is there a #include "mkl.h," because -- for code compatibility with Netlib math lib – BLAS or LAPACK routines are called using the F2C convention, and the VS linker is directed to link to MKL-provided FORTRAN BLAS/LAPACK subroutines rather than Netlib's.

8.6.7 Specifying the Number of Parallel OpenMP Threads to Use

For the ACML or MKL parallel multi-threaded versions (that use OpenMP to multi-thread), there is ability to control the maximum number of threads that will be used on a system (up to the max available):

ACML thread control: To specify how many threads a code compiled with the ACML MP parallel library uses, set Environment Variable OMP_NUM_THREADS to the desired number of threads.

MKL thread control: To specify how many threads a code compiled with the MKL parallel library uses, set Environment Variable MKL_NUM_THREADS to the desired number of threads.

8.7 ARAM CYL-MM SOFTWARE USER MANUAL (CHAPTER 5)

8.7.1 Input and output files

The CYL_MM program provides cylindrical mode-matching analysis for an axially symmetric feedhorn of arbitrary geometry. It receives its feedhorn geometry specification from an input file with the file name extension .aram1, and provides outputs in text and graphical windows (2D & 3D) as well as an archival output text file with .txt file name extension. The F1 key pops up a help menu that summarizes all the features available to the user. The 3D graphics window will display the feedhorn along with any reflector system geometry specified by dual.dat1 and dual.dat2 DUAL program input files placed in the same directory where the .aram1 corrugated horn file resides. (Exceptions are that the Jacobi-Bessel shaped surface and the array feeds are not yet implemented in the code for viewing.) Thereby the CYL_MM 3D graphics window serves as a DUAL geometry 3D viewer for any single or dual reflector system of either Cassegrain or Gregorian geometry: The CYL_MM corrugated horn is rendered in 3D along with the reflectors. There is an input flag that directs the program to not produce any windows: This flag is intended for use in optimization runs, for which the results of the cylindrical mode matching analysis are desired from the program's output .txt file as rapidly as possible, to minimize the optimization cycle time. At the completion of the optimization the .aram1 file may be run by the CYL_MM program (with that input flag reset) to view the optimized geometry in 3D.

The CYL_MM program opens two windows: a text and 2D window on top, and a separate 3D window below. The far field pattern of the corrugated horn (geometry specified in the .aram1

file) is shown in 2D on the right side of the top CYL_MM window and is also output to the out.txt file that is generated by the program in the same directory where the .aram1 file is launched from.

Fig. 8-7. Example display of DUAL reflector geometry with super quadratic main and subreflector apertures, (peculiarly stubby Cassegrain system for example only) along with the feedhorn. 3D graphics produced by the ARAM CYL_MM Windows ™ software developed for this dissertation.

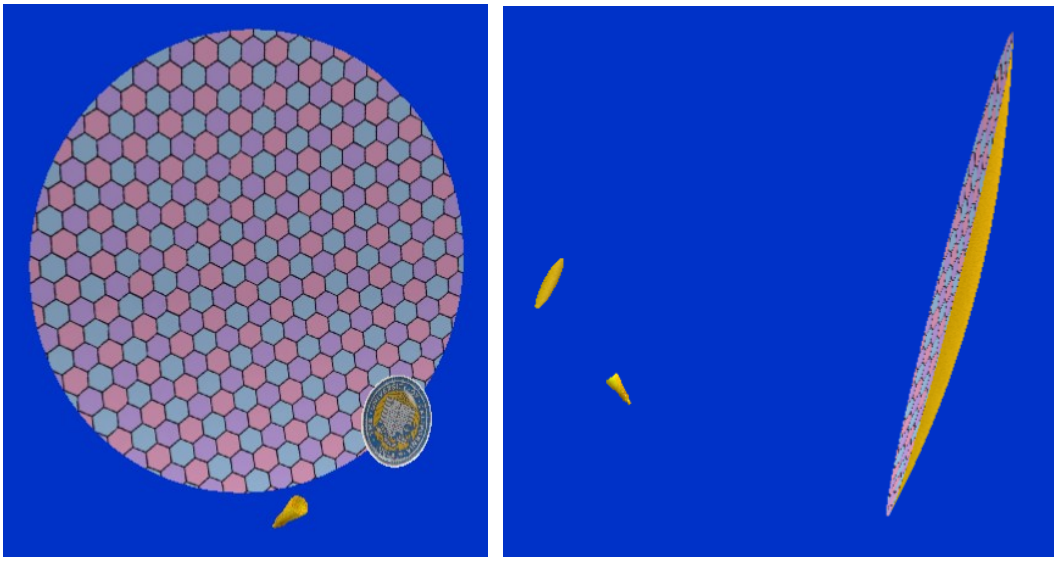

Fig. 8-8. Two views of the ARAM CYL_MM software's display of the DUAL reflector geometry for the Cassegrain dual reflector example given in the ARAM DUAL reflector analysis software User Manual.

The .aram1 input file name extension is intended to be the first of possibly a number of Windows™ registered file type extensions associated with perhaps a suite of programs to be

developed by the UCLA ARAM group in the future. Examples are provided below of an input file and corresponding output file for the analysis, by the CYL_MM program, of a Ku band corrugated horn.

1. Input file

```
Header info line 1: Ku feed horn
Header info line 2: 13.4-14.0 & 14.6-15.2 GHz
Header info line 3:
cm      dimensional units ("cm" or "m" or "in")
13.7e9  center freq, Hz
0.6e9   bandwidth, Hz
1       angular mode index
20       # radial modes
1       excitation radial mode(add #RadialModes to any TM mode index)
1       1= # radial modes a function of radius
0.0     zero radius mode # factor
1       exponent of mode # by radius function
0       1=list evanescent s-params
1       excitation port for field plots (1 or 2)
10      max modes to plot
90      deg far-field plot angular range
40      dBp far-field plot range
0       1= linear polarized far fields, 0= circular polarized
0      X rotation (deg pitch)
0       Y rotation (deg yaw)
0       Z rotation (deg roll)
0       translation in X
0       translation in Y
0       translation in Z
0       eyeZ (camera location: positive is into the screen) If zero will be set
to suitable value by progrma.
0            1= Do not display any windows, and quit right after completing
calculations and closing output file.
1.143000000  5.334065000   [radius, length] of individual cylindrical sections
2.231266063  0.431362055   that make up the feed horn's circularly symmetric
1.369237585  0.484680063   geometry, starting from throat end of horn.
2.379078291  0.432026747
1.689551967  0.300178455
2.549185548  0.359478097
1.881546587  0.499689568
2.665961572  0.468863812
#   9.2         8.1       You can comment out lines by inserting the # charcter
at the beginning of the line.
1.983033046  0.309883861
2.597460002  0.461565309
2.10693065   0.398105751
2.771475583  0.499814026
2.177723683  0.473708024
2.181959175  0.334563418
2.760138067  0.378552181
2.298577754  0.236324718
#   9.2         8.1       You can comment out lines by inserting the # charcter
at the beginning of the line.
2.880992138  0.378552181
```

```
2.419431825   0.236324718
3.001846209   0.378552181
3.406116563   0.378552181
3.14455625    4.236324718
3.726970634   0.378552181
3.265410321   0.236324718
3.847824705   0.378552181
3.386264392   0.236324718
3.968678776   0.378552181
3.507118463   0.236324718
4.089532847   0.378552181
3.627972534   0.236324718
4.210386918   0.378552181
3.748826605   0.236324718
4.331240989   0.378552181
3.869680676   0.236324718
4.45209506    0.378552181
3.990534747   0.236324718
4.572949131   0.378552181
4.111388818   0.236324718
4.693803202   0.378552181
4.232242889   0.236324718
4.814657273   0.378552181
4.35309696    0.236324718
4.935511343   0.378552181
4.473951031   0.236324718
5.056365414   0.378552181
4.594805102   0.236324718
5.177219485   0.378552181
4.715659173   0.236324718
5.298073556   0.378552181
4.836513244   0.236324718
5.418927627   0.378552181
4.957367314   0.236324718
5.539781698   0.378552181
5.078221385   0.236324718
5.660635769   0.378552181
5.199075456   0.236324718
5.78148984    0.378552181
5.319929527   0.236324718
5.902343911   0.378552181
5.440783598   0.236324718
6.023197982   0.378552181
5.561637669   0.236324718
6.144052053   0.378552181
5.68249174    0.236324718    A blank line (not commented out) starts a separate,
optional section to specify the exterior horn surface:
       A "blank" line is defined as any line that begins with "white space,"
which includes space or tab.
1.5    0       [radius, axial location (wrt horn throat end)]
1.5    4       These represent cardinal points that define the curve
2.5    4       of the external body of the horn.
3.5    7
3.5    13
6.5    28
6.5    30.03003
```

2. Example Output File (created by the CYL_MM program in response to the above file):

```
Header info line 1: Ku feed horn
```

```
Header info line 2: 13.4-14.0 & 14.6-15.2 GHz
Header info line 3:

 1.37e+010 Hz center freq (13.7 GHz)

 6e+008 Hz freq bandwidth (0.6 GHz)

Angular mode index = 1
# radial modes max = 20
Excitation mode = TE 1,1
modes_by_radius = 1
zero_rad_mode_num_factor = 0
mode_num_by_rad_func_pwr = 1
list_evanescent_s_params = 0

plotExcitePort = 1
modes2plot = 10

far-field angular range (deg) = 90
far-field dBp range = 40
Far Field polarization = 0
Default worldRotX = 0 degrees pitch
Default worldRotY = 0 degrees yaw
Default worldRotZ = 0 degrees roll
Default worldTransX = 0
Default worldTransY = 0
Default worldTransZ = 0
Default eyeZ camera view point = 0
Quit right after completing calculations flag = 0

Internal horn cylindrical geometry:
Sect   1: radius (cm)=        1.143, length (cm)=      5.33406
Sect   2: radius (cm)=      2.23127, length (cm)=     0.431362
Sect   3: radius (cm)=      1.36924, length (cm)=      0.48468
Sect   4: radius (cm)=      2.37908, length (cm)=     0.432027
Sect   5: radius (cm)=      1.68955, length (cm)=     0.300178
Sect   6: radius (cm)=      2.54919, length (cm)=     0.359478
Sect   7: radius (cm)=      1.88155, length (cm)=      0.49969
Sect   8: radius (cm)=      2.66596, length (cm)=     0.468864
Sect   9: radius (cm)=      1.98303, length (cm)=     0.309884
Sect  10: radius (cm)=      2.59746, length (cm)=     0.461565
Sect  11: radius (cm)=      2.10693, length (cm)=     0.398106
Sect  12: radius (cm)=      2.77148, length (cm)=     0.499814
Sect  13: radius (cm)=      2.17772, length (cm)=     0.473708
Sect  14: radius (cm)=      2.18196, length (cm)=     0.334563
Sect  15: radius (cm)=      2.76014, length (cm)=     0.378552
Sect  16: radius (cm)=      2.29858, length (cm)=     0.236325
Sect  17: radius (cm)=      2.88099, length (cm)=     0.378552
Sect  18: radius (cm)=      2.41943, length (cm)=     0.236325
Sect  19: radius (cm)=      3.00185, length (cm)=     0.378552
Sect  20: radius (cm)=      3.40612, length (cm)=     0.378552
Sect  21: radius (cm)=      3.14456, length (cm)=      4.23632
Sect  22: radius (cm)=      3.72697, length (cm)=     0.378552
Sect  23: radius (cm)=      3.26541, length (cm)=     0.236325
Sect  24: radius (cm)=      3.84782, length (cm)=     0.378552
Sect  25: radius (cm)=      3.38626, length (cm)=     0.236325
Sect  26: radius (cm)=      3.96868, length (cm)=     0.378552
Sect  27: radius (cm)=      3.50712, length (cm)=     0.236325
Sect  28: radius (cm)=      4.08953, length (cm)=     0.378552
Sect  29: radius (cm)=      3.62797, length (cm)=     0.236325
Sect  30: radius (cm)=      4.21039, length (cm)=     0.378552
Sect  31: radius (cm)=      3.74883, length (cm)=     0.236325
```

```
Sect  32: radius (cm)=      4.33124, length (cm)=     0.378552
Sect  33: radius (cm)=      3.86968, length (cm)=     0.236325
Sect  34: radius (cm)=       4.4521, length (cm)=     0.378552
Sect  35: radius (cm)=      3.99053, length (cm)=     0.236325
Sect  36: radius (cm)=      4.57295, length (cm)=     0.378552
Sect  37: radius (cm)=      4.11139, length (cm)=     0.236325
Sect  38: radius (cm)=       4.6938, length (cm)=     0.378552
Sect  39: radius (cm)=      4.23224, length (cm)=     0.236325
Sect  40: radius (cm)=      4.81466, length (cm)=     0.378552
Sect  41: radius (cm)=       4.3531, length (cm)=     0.236325
Sect  42: radius (cm)=      4.93551, length (cm)=     0.378552
Sect  43: radius (cm)=      4.47395, length (cm)=     0.236325
Sect  44: radius (cm)=      5.05637, length (cm)=     0.378552
Sect  45: radius (cm)=      4.59481, length (cm)=     0.236325
Sect  46: radius (cm)=      5.17722, length (cm)=     0.378552
Sect  47: radius (cm)=      4.71566, length (cm)=     0.236325
Sect  48: radius (cm)=      5.29807, length (cm)=     0.378552
Sect  49: radius (cm)=      4.83651, length (cm)=     0.236325
Sect  50: radius (cm)=      5.41893, length (cm)=     0.378552
Sect  51: radius (cm)=      4.95737, length (cm)=     0.236325
Sect  52: radius (cm)=      5.53978, length (cm)=     0.378552
Sect  53: radius (cm)=      5.07822, length (cm)=     0.236325
Sect  54: radius (cm)=      5.66064, length (cm)=     0.378552
Sect  55: radius (cm)=      5.19908, length (cm)=     0.236325
Sect  56: radius (cm)=      5.78149, length (cm)=     0.378552
Sect  57: radius (cm)=      5.31993, length (cm)=     0.236325
Sect  58: radius (cm)=      5.90234, length (cm)=     0.378552
Sect  59: radius (cm)=      5.44078, length (cm)=     0.236325
Sect  60: radius (cm)=       6.0232, length (cm)=     0.378552
Sect  61: radius (cm)=      5.56164, length (cm)=     0.236325
Sect  62: radius (cm)=      6.14405, length (cm)=     0.378552
Sect  63: radius (cm)=      5.68249, length (cm)=     0.236325

Horn exterior surface cardinal points.
Point #   1: radius (cm)=          1.5, axial location (cm)=            0
Point #   2: radius (cm)=          1.5, axial location (cm)=            4
Point #   3: radius (cm)=          2.5, axial location (cm)=            4
Point #   4: radius (cm)=          3.5, axial location (cm)=            7
Point #   5: radius (cm)=          3.5, axial location (cm)=           13
Point #   6: radius (cm)=          6.5, axial location (cm)=           28
Point #   7: radius (cm)=          6.5, axial location (cm)=        30.03
Header info line 1: Ku feed horn
Header info line 2: 13.4-14.0 & 14.6-15.2 GHz
Header info line 3:

 1.37e+010 Hz center freq (13.7 GHz)

 6e+008 Hz freq bandwidth (0.6 GHz)

Angular mode index = 1
# radial modes max = 20
Excitation mode = TE 1,1
modes_by_radius = 1
zero_rad_mode_num_factor = 0
mode_num_by_rad_func_pwr = 1
list_evanescent_s_params = 0

plotExcitePort = 1
modes2plot = 10

far-field angular range (deg) = 90
far-field dBp range = 40
```

```
Far Field polarization = 0
Default worldRotX = 0 degrees pitch
Default worldRotY = 0 degrees yaw
Default worldRotZ = 0 degrees roll
Default worldTransX = 0
Default worldTransY = 0
Default worldTransZ = 0
Default eyeZ camera view point = 0
Quit right after completing calculations flag = 0

Internal horn cylindrical geometry:
Sect   1: radius (cm)=        1.143, length (cm)=      5.33406
Sect   2: radius (cm)=      2.23127, length (cm)=     0.431362
Sect   3: radius (cm)=      1.36924, length (cm)=      0.48468
Sect   4: radius (cm)=      2.37908, length (cm)=     0.432027
Sect   5: radius (cm)=      1.68955, length (cm)=     0.300178
Sect   6: radius (cm)=      2.54919, length (cm)=     0.359478
Sect   7: radius (cm)=      1.88155, length (cm)=      0.49969
Sect   8: radius (cm)=      2.66596, length (cm)=     0.468864
Sect   9: radius (cm)=      1.98303, length (cm)=     0.309884
Sect  10: radius (cm)=      2.59746, length (cm)=     0.461565
Sect  11: radius (cm)=      2.10693, length (cm)=     0.398106
Sect  12: radius (cm)=      2.77148, length (cm)=     0.499814
Sect  13: radius (cm)=      2.17772, length (cm)=     0.473708
Sect  14: radius (cm)=      2.18196, length (cm)=     0.334563
Sect  15: radius (cm)=      2.76014, length (cm)=     0.378552
Sect  16: radius (cm)=      2.29858, length (cm)=     0.236325
Sect  17: radius (cm)=      2.88099, length (cm)=     0.378552
Sect  18: radius (cm)=      2.41943, length (cm)=     0.236325
Sect  19: radius (cm)=      3.00185, length (cm)=     0.378552
Sect  20: radius (cm)=      3.40612, length (cm)=     0.378552
Sect  21: radius (cm)=      3.14456, length (cm)=      4.23632
Sect  22: radius (cm)=      3.72697, length (cm)=     0.378552
Sect  23: radius (cm)=      3.26541, length (cm)=     0.236325
Sect  24: radius (cm)=      3.84782, length (cm)=     0.378552
Sect  25: radius (cm)=      3.38626, length (cm)=     0.236325
Sect  26: radius (cm)=      3.96868, length (cm)=     0.378552
Sect  27: radius (cm)=      3.50712, length (cm)=     0.236325
Sect  28: radius (cm)=      4.08953, length (cm)=     0.378552
Sect  29: radius (cm)=      3.62797, length (cm)=     0.236325
Sect  30: radius (cm)=      4.21039, length (cm)=     0.378552
Sect  31: radius (cm)=      3.74883, length (cm)=     0.236325
Sect  32: radius (cm)=      4.33124, length (cm)=     0.378552
Sect  33: radius (cm)=      3.86968, length (cm)=     0.236325
Sect  34: radius (cm)=       4.4521, length (cm)=     0.378552
Sect  35: radius (cm)=      3.99053, length (cm)=     0.236325
Sect  36: radius (cm)=      4.57295, length (cm)=     0.378552
Sect  37: radius (cm)=      4.11139, length (cm)=     0.236325
Sect  38: radius (cm)=       4.6938, length (cm)=     0.378552
Sect  39: radius (cm)=      4.23224, length (cm)=     0.236325
Sect  40: radius (cm)=      4.81466, length (cm)=     0.378552
Sect  41: radius (cm)=       4.3531, length (cm)=     0.236325
Sect  42: radius (cm)=      4.93551, length (cm)=     0.378552
Sect  43: radius (cm)=      4.47395, length (cm)=     0.236325
Sect  44: radius (cm)=      5.05637, length (cm)=     0.378552
Sect  45: radius (cm)=      4.59481, length (cm)=     0.236325
Sect  46: radius (cm)=      5.17722, length (cm)=     0.378552
Sect  47: radius (cm)=      4.71566, length (cm)=     0.236325
Sect  48: radius (cm)=      5.29807, length (cm)=     0.378552
Sect  49: radius (cm)=      4.83651, length (cm)=     0.236325
Sect  50: radius (cm)=      5.41893, length (cm)=     0.378552
Sect  51: radius (cm)=      4.95737, length (cm)=     0.236325
```

```
Sect  52: radius (cm)=      5.53978, length (cm)=     0.378552
Sect  53: radius (cm)=      5.07822, length (cm)=     0.236325
Sect  54: radius (cm)=      5.66064, length (cm)=     0.378552
Sect  55: radius (cm)=      5.19908, length (cm)=     0.236325
Sect  56: radius (cm)=      5.78149, length (cm)=     0.378552
Sect  57: radius (cm)=      5.31993, length (cm)=     0.236325
Sect  58: radius (cm)=      5.90234, length (cm)=     0.378552
Sect  59: radius (cm)=      5.44078, length (cm)=     0.236325
Sect  60: radius (cm)=       6.0232, length (cm)=     0.378552
Sect  61: radius (cm)=      5.56164, length (cm)=     0.236325
Sect  62: radius (cm)=      6.14405, length (cm)=     0.378552
Sect  63: radius (cm)=      5.68249, length (cm)=     0.236325

Horn exterior surface cardinal points.
Point #   1: radius (cm)=          1.5, axial location (cm)=            0
Point #   2: radius (cm)=          1.5, axial location (cm)=            4
Point #   3: radius (cm)=          2.5, axial location (cm)=            4
Point #   4: radius (cm)=          3.5, axial location (cm)=            7
Point #   5: radius (cm)=          3.5, axial location (cm)=           13
Point #   6: radius (cm)=          6.5, axial location (cm)=           28
Point #   7: radius (cm)=          6.5, axial location (cm)=        30.03

Number of modes on each side of each junction determined by respective radii.
numModesInput = 6

Step   1: rad_L =    1.143, rad_R =    2.231, len_R=    0.431, #modes=   3:  7
Step   2: rad_L =    2.231, rad_R =    1.369, len_R=    0.485, #modes=   7:  4
Step   3: rad_L =    1.369, rad_R =    2.379, len_R=    0.432, #modes=   4:  7
Step   4: rad_L =    2.379, rad_R =    1.690, len_R=    0.300, #modes=   7:  5
Step   5: rad_L =    1.690, rad_R =    2.549, len_R=    0.359, #modes=   5:  8
Step   6: rad_L =    2.549, rad_R =    1.882, len_R=    0.500, #modes=   8:  6
Step   7: rad_L =    1.882, rad_R =    2.666, len_R=    0.469, #modes=   6:  8
Step   8: rad_L =    2.666, rad_R =    1.983, len_R=    0.310, #modes=   8:  6
Step   9: rad_L =    1.983, rad_R =    2.597, len_R=    0.462, #modes=   6:  8
Step  10: rad_L =    2.597, rad_R =    2.107, len_R=    0.398, #modes=   8:  6
Step  11: rad_L =    2.107, rad_R =    2.771, len_R=    0.500, #modes=   6:  9
Step  12: rad_L =    2.771, rad_R =    2.178, len_R=    0.474, #modes=   9:  7
Step  13: rad_L =    2.178, rad_R =    2.182, len_R=    0.335, #modes=   7:  7
Step  14: rad_L =    2.182, rad_R =    2.760, len_R=    0.379, #modes=   7:  8
Step  15: rad_L =    2.760, rad_R =    2.299, len_R=    0.236, #modes=   8:  7
Step  16: rad_L =    2.299, rad_R =    2.881, len_R=    0.379, #modes=   7:  9
Step  17: rad_L =    2.881, rad_R =    2.419, len_R=    0.236, #modes=   9:  7
Step  18: rad_L =    2.419, rad_R =    3.002, len_R=    0.379, #modes=   7:  9
Step  19: rad_L =    3.002, rad_R =    3.406, len_R=    0.379, #modes=   9: 11
Step  20: rad_L =    3.406, rad_R =    3.145, len_R=    4.236, #modes=  11: 10
Step  21: rad_L =    3.145, rad_R =    3.727, len_R=    0.379, #modes=  10: 12
Step  22: rad_L =    3.727, rad_R =    3.265, len_R=    0.236, #modes=  12: 10
Step  23: rad_L =    3.265, rad_R =    3.848, len_R=    0.379, #modes=  10: 12
Step  24: rad_L =    3.848, rad_R =    3.386, len_R=    0.236, #modes=  12: 11
Step  25: rad_L =    3.386, rad_R =    3.969, len_R=    0.379, #modes=  11: 12
Step  26: rad_L =    3.969, rad_R =    3.507, len_R=    0.236, #modes=  12: 11
Step  27: rad_L =    3.507, rad_R =    4.090, len_R=    0.379, #modes=  11: 13
Step  28: rad_L =    4.090, rad_R =    3.628, len_R=    0.236, #modes=  13: 11
Step  29: rad_L =    3.628, rad_R =    4.210, len_R=    0.379, #modes=  11: 13
Step  30: rad_L =    4.210, rad_R =    3.749, len_R=    0.236, #modes=  13: 12
Step  31: rad_L =    3.749, rad_R =    4.331, len_R=    0.379, #modes=  12: 14
Step  32: rad_L =    4.331, rad_R =    3.870, len_R=    0.236, #modes=  14: 12
Step  33: rad_L =    3.870, rad_R =    4.452, len_R=    0.379, #modes=  12: 14
Step  34: rad_L =    4.452, rad_R =    3.991, len_R=    0.236, #modes=  14: 12
Step  35: rad_L =    3.991, rad_R =    4.573, len_R=    0.379, #modes=  12: 14
Step  36: rad_L =    4.573, rad_R =    4.111, len_R=    0.236, #modes=  14: 13
Step  37: rad_L =    4.111, rad_R =    4.694, len_R=    0.379, #modes=  13: 15
```

```
Step  38: rad_L =    4.694, rad_R =    4.232, len_R=    0.236, #modes=  15: 13
Step  39: rad_L =    4.232, rad_R =    4.815, len_R=    0.379, #modes=  13: 15
Step  40: rad_L =    4.815, rad_R =    4.353, len_R=    0.236, #modes=  15: 14
Step  41: rad_L =    4.353, rad_R =    4.936, len_R=    0.379, #modes=  14: 16
Step  42: rad_L =    4.936, rad_R =    4.474, len_R=    0.236, #modes=  16: 14
Step  43: rad_L =    4.474, rad_R =    5.056, len_R=    0.379, #modes=  14: 16
Step  44: rad_L =    5.056, rad_R =    4.595, len_R=    0.236, #modes=  16: 14
Step  45: rad_L =    4.595, rad_R =    5.177, len_R=    0.379, #modes=  14: 16
Step  46: rad_L =    5.177, rad_R =    4.716, len_R=    0.236, #modes=  16: 15
Step  47: rad_L =    4.716, rad_R =    5.298, len_R=    0.379, #modes=  15: 17
Step  48: rad_L =    5.298, rad_R =    4.837, len_R=    0.236, #modes=  17: 15
Step  49: rad_L =    4.837, rad_R =    5.419, len_R=    0.379, #modes=  15: 17
Step  50: rad_L =    5.419, rad_R =    4.957, len_R=    0.236, #modes=  17: 16
Step  51: rad_L =    4.957, rad_R =    5.540, len_R=    0.379, #modes=  16: 18
Step  52: rad_L =    5.540, rad_R =    5.078, len_R=    0.236, #modes=  18: 16
Step  53: rad_L =    5.078, rad_R =    5.661, len_R=    0.379, #modes=  16: 18
Step  54: rad_L =    5.661, rad_R =    5.199, len_R=    0.236, #modes=  18: 16
Step  55: rad_L =    5.199, rad_R =    5.781, len_R=    0.379, #modes=  16: 18
Step  56: rad_L =    5.781, rad_R =    5.320, len_R=    0.236, #modes=  18: 17
Step  57: rad_L =    5.320, rad_R =    5.902, len_R=    0.379, #modes=  17: 19
Step  58: rad_L =    5.902, rad_R =    5.441, len_R=    0.236, #modes=  19: 17
Step  59: rad_L =    5.441, rad_R =    6.023, len_R=    0.379, #modes=  17: 19
Step  60: rad_L =    6.023, rad_R =    5.562, len_R=    0.236, #modes=  19: 18
Step  61: rad_L =    5.562, rad_R =    6.144, len_R=    0.379, #modes=  18: 20
Step  62: rad_L =    6.144, rad_R =    5.682, len_R=    0.236, #modes=  20: 18

Far Field patterns (deg, dB): CP [co-, x-pol]
 0.00    0.00 -199.00
 0.91   -0.03  -59.58
 1.82   -0.13  -47.60
 2.73   -0.29  -40.67
 3.64   -0.52  -35.84
 4.55   -0.81  -32.17
 5.45   -1.17  -29.25
 6.36   -1.60  -26.87
 7.27   -2.10  -24.89
 8.18   -2.67  -23.24
 9.09   -3.31  -21.84
10.00   -4.02  -20.67
10.91   -4.81  -19.68
11.82   -5.68  -18.86
12.73   -6.64  -18.19
13.64   -7.68  -17.66
14.55   -8.82  -17.24
15.45  -10.06  -16.95
16.36  -11.42  -16.75
17.27  -12.91  -16.66
18.18  -14.55  -16.65
19.09  -16.36  -16.74
20.00  -18.39  -16.91
20.91  -20.69  -17.16
21.82  -23.36  -17.49
22.73  -26.57  -17.89
23.64  -30.58  -18.37
24.55  -35.68  -18.91
25.45  -39.26  -19.52
26.36  -36.58  -20.20
27.27  -33.62  -20.94
28.18  -31.73  -21.74
29.09  -30.58  -22.60
30.00  -29.92  -23.52
30.91  -29.62  -24.49
```

31.82	-29.58	-25.53
32.73	-29.75	-26.61
33.64	-30.11	-27.75
34.55	-30.63	-28.94
35.45	-31.28	-30.17
36.36	-32.07	-31.45
37.27	-32.98	-32.77
38.18	-34.00	-34.13
39.09	-35.13	-35.52
40.00	-36.34	-36.94
40.91	-37.61	-38.36
41.82	-38.92	-39.78
42.73	-40.19	-41.18
43.64	-41.36	-42.53
44.55	-42.34	-43.81
45.45	-43.09	-44.99
46.36	-43.61	-46.06
47.27	-43.92	-46.99
48.18	-44.13	-47.79
49.09	-44.28	-48.47
50.00	-44.44	-49.03
50.91	-44.65	-49.50
51.82	-44.91	-49.90
52.73	-45.24	-50.25
53.64	-45.65	-50.55
54.55	-46.11	-50.82
55.45	-46.64	-51.08
56.36	-47.23	-51.33
57.27	-47.85	-51.57
58.18	-48.50	-51.81
59.09	-49.17	-52.06
60.00	-49.84	-52.32
60.91	-50.49	-52.60
61.82	-51.10	-52.90
62.73	-51.66	-53.21
63.64	-52.17	-53.55
64.55	-52.62	-53.91
65.45	-53.01	-54.29
66.36	-53.34	-54.70
67.27	-53.64	-55.13
68.18	-53.91	-55.59
69.09	-54.16	-56.07
70.00	-54.40	-56.57
70.91	-54.65	-57.09
71.82	-54.91	-57.64
72.73	-55.18	-58.20
73.64	-55.47	-58.78
74.55	-55.78	-59.37
75.45	-56.11	-59.97
76.36	-56.46	-60.58
77.27	-56.83	-61.19
78.18	-57.23	-61.79
79.09	-57.65	-62.38
80.00	-58.08	-62.94
80.91	-58.53	-63.46
81.82	-59.00	-63.93
82.73	-59.49	-64.33
83.64	-59.98	-64.65
84.55	-60.49	-64.88
85.45	-61.00	-65.00
86.36	-61.51	-65.02
87.27	-62.02	-64.94

```
88.18  -62.52  -64.77
89.09  -62.99  -64.52
90.00  -63.43  -64.22

********
******** S-Parameters
********

S11: response to excitation mode TE 1, 1:
TE 1, 1 (prop) =  -31.0 dB @   61 deg,   0.1%P, |V|=   0.028

S21: response to excitation mode TE 1, 1:
TE 1, 1 (prop) =   -1.7 dB @   71 deg,  67.9%P, |V|=   0.824
TE 1, 2 (prop) =   -7.7 dB @   66 deg,  16.9%P, |V|=   0.411
TE 1, 3 (prop) =  -27.4 dB @   94 deg,   0.2%P, |V|=   0.043
TE 1, 4 (prop) =  -48.4 dB @  -70 deg,   0.0%P, |V|=   0.004
TE 1, 5 (prop) =  -57.9 dB @  115 deg,   0.0%P, |V|=   0.001
TM 1, 1 (prop) =   -9.5 dB @   61 deg,  11.1%P, |V|=   0.334
TM 1, 2 (prop) =  -15.0 dB @ -100 deg,   3.2%P, |V|=   0.178
TM 1, 3 (prop) =  -22.3 dB @ -100 deg,   0.6%P, |V|=   0.076
TM 1, 4 (prop) =  -33.4 dB @   21 deg,   0.0%P, |V|=   0.021

S12: response to excitation mode TE 1, 1:
TE 1, 1 (prop) =   -1.7 dB @   71 deg,  67.9%P, |V|=   0.824

S22: response to excitation mode TE 1, 1:
TE 1, 1 (prop) =  -14.4 dB @  -47 deg,   3.7%P, |V|=   0.191
TE 1, 2 (prop) =   -8.7 dB @  170 deg,  13.4%P, |V|=   0.366
TE 1, 3 (prop) =  -11.6 dB @ -125 deg,   6.9%P, |V|=   0.263
TE 1, 4 (prop) =  -31.8 dB @  -28 deg,   0.1%P, |V|=   0.026
TE 1, 5 (prop) =  -45.3 dB @  146 deg,   0.0%P, |V|=   0.005
TM 1, 1 (prop) =  -13.2 dB @   57 deg,   4.8%P, |V|=   0.219
TM 1, 2 (prop) =  -15.9 dB @ -121 deg,   2.6%P, |V|=   0.161
TM 1, 3 (prop) =  -22.6 dB @   99 deg,   0.6%P, |V|=   0.074
TM 1, 4 (prop) =  -30.3 dB @   15 deg,   0.1%P, |V|=   0.031

Port 1: sum of power from excitation =   1.000, or 0.000 dB
Port 2: sum of power from excitation =   1.000, or 0.000 dB

Total run time = 0.92 seconds.
```

8.7.2 Software Installation

The serial number required for installation of the CYL_MM setup program (setup.exe with its associated arch6.msi file) is currently seven ones followed by one zero. A copy of the ARAM CYL_MM Windows ™ program is available to members of the UCLA ARAM group headed by Prof. Rahmat-Samii for student use. The CYL_MM installation setup files, source code, and example files are archived on the ARAM workstations “fat-man” and “jen” in the directory C:\CYL_MM. The CYL_MM program produced all the feedhorn mode-matching results and

the feedhorn and reflector 3D graphics depicted in this dissertation. The CYL_MM program provides 3D visualization of the ARAM DUAL reflector analysis DOS program's geometry, and the ARAM DUAL program, with user manual and source code, is archived on fat-man and jen in the directory C:\DUAL.

CHAPTER 9 REFERENCES

[1] S. A. Schelkunoff, "Some Equivalence Theorems of Electromagnetics and Their Application to Radiation Problems," *Bell Syst. Tech. J.*, vol. 15, no. 1, pp. 92–112, 1936.

[2] S. R. Rengarajan and Y. Rahmat-Samii, "The field equivalence principle: illustration of the establishment of the non-intuitive null fields," *IEEE Antennas Propag. Mag.*, vol. 42, no. 4, pp. 122 –128, Aug. 2000.

[3] S. R. Rengarajan, "Errata [to 'The field equivalence principle: Illustration of the establishment of the non-intuitive null fields [Education]']," *IEEE Antennas Propag. Mag.*, vol. 43, no. 1, pp. 134–134, Feb. 2001.

[4] A. J. Booysen, "Aperture theory and the equivalence principle," *IEEE Antennas Propag. Mag.*, vol. 45, no. 3, pp. 29 – 40, Jun. 2003.

[5] A. Dodd, "An Acre of Glass – The History of the Telescope," *Ezine @rticles*, 2009. .

[6] S. Silver, *Microwave Antenna Theory and Design*. New York: McGraw-Hill, 1949.

[7] W. A. Imbriale, "Evolution of the large Deep Space Network antennas," *IEEE Antennas Propag. Mag.*, vol. 33, no. 6, pp. 7–19, 1991.

[8] A. W. Love (Editor), *Reflector Antennas*. John Wiley & Sons, Inc., 1978.

[9] V. Jamnejad-Dailami and Y. Rahmat-Samii, "Some important geometrical features of conic-section-generated offset reflector antennas," *IEEE Trans. Antennas Propag.*, vol. 28, no. 6, pp. 952–957, 1980.

[10] Y. Rahmat-Samii and A. Densmore, "A history of reflector antenna development: Past, present and future," in *Microwave and Optoelectronics Conference (IMOC), 2009 SBMO/IEEE MTT-S International*, 2009, pp. 17–23.

[11] C. Balanis, *Advanced Engineering Electromagnetics*. Wiley, 1989.

[12] R. J. Burkholder and T.-H. Lee, "Adaptive sampling for fast physical optics numerical integration," *IEEE Trans. Antennas Propag.*, vol. 53, no. 5, pp. 1843 – 1845, May 2005.

[13] Y. Rahmat-Samii and R. Cheung, "Nonuniform sampling techniques for antenna applications," *IEEE Trans. Antennas Propag.*, vol. 35, no. 3, pp. 268–279, Mar. 1987.

[14] A. D. Craig and P. D. Simms, "Fast integration techniques for reflector antenna pattern analysis," *Electron. Lett.*, vol. 18, no. 2, pp. 60 –62, 1982.

[15] Y. Rahmat-Samii, "A comparison between GO/aperture-field and physical-optics methods of offset reflectors," *IEEE Trans. Antennas Propag.*, vol. 32, no. 3, pp. 301–306, Mar. 1984.

[16] P. T. Lam, S.-W. Lee, C. Hung, and R. Acosta, "Strategy for reflector pattern calculation: Let the computer do the work," *IEEE Trans. Antennas Propag.*, vol. 34, no. 4, pp. 592–595, Apr. 1986.

[17] A. Zeidaabadi, Z. Hossein, and H. Mirmohammad-Sadeghi, "A Fast Method to Compute Radiation Fields of Shaped Reflector Antennas by FFT," in *Advanced Microwave and Millimeter Wave Technologies Semiconductor Devices Circuits and Systems*, M. Mukherjee, Ed. InTech, 2010.

[18] A. Boag and E. Michielssen, "A fast physical optics (FPO) algorithm for double-bounce scattering," *IEEE Trans. Antennas Propag.*, vol. 52, no. 1, pp. 205 – 212, Jan. 2004.

[19] C. Parrot, D. Millot, C. Letrou, and A. Boag, "A distributed memory MultiLevel fast Physical Optics algorithm," in *3rd European Conference on Antennas and Propagation, 2009. EuCAP 2009*, 2009, pp. 141 –144.

[20] C. Letrou and A. Boag, "An MLPO algorithm for fast evaluation of the focal plane fields of reflector antennas," in *2012 6th European Conference on Antennas and Propagation (EUCAP)*, 2012, pp. 3436 –3437.

[21] Y. Rahmat-Samii, "Jacobi-Bessel analysis of reflector antennas with elliptical apertures," *IEEE Trans. Antennas Propag.*, vol. 35, no. 9, pp. 1070 – 1074, Sep. 1987.

[22] Y. Li, "A further research on the Jacobi-Bessel series method in analysis of reflector antenna," *J. Electron. China*, vol. 4, no. 1, pp. 11–19, 1987.

[23] Dah-Weih Duan, "PO/PTD Diffraction synthesis of Array-Fed Reflector Antennas for Satellite and Radar Applications," Ph.D. Dissertation, UCLA, Los Angeles, CA, 1992.

[24] V. Jamnejad, "A new integration scheme for application to the analysis of reflector antennas," in *Antennas and Propagation Society International Symposium, 1984*, 1984, vol. 22, pp. 380 – 384.

[25] A. Ludwig, "Computation of radiation patterns involving numerical double integration," *IEEE Trans. Antennas Propag.*, vol. 16, no. 6, pp. 767 – 769, Nov. 1968.

[26] A. C. Ludwig, "Comments on the accuracy of the 'Ludwig' integration algorithm," *IEEE Trans. Antennas Propag.*, vol. 36, no. 4, pp. 578 –579, Apr. 1988.

[27] R. J. Pogorzelski, "The Ludwig integration algorithm for triangular subregions," *Proc. IEEE*, vol. 73, no. 4, pp. 837 – 838, Apr. 1985.

[28] M. L. X. Dos Santos and N. R. Rabelo, "On the Ludwig integration algorithm for triangular subregions," *Proc. IEEE*, vol. 74, no. 10, pp. 1455–1456, 1986.

[29] W. Meng, W. Nan, and L. Changhong, "Problem of singularity in Ludwig's algorithm," *Microw. Opt. Technol. Lett.*, vol. 49, no. 2, pp. 400–403, 2007.

[30] G. D. Crabtree, "A numerical quadrature technique for physical optics scattering analysis," *IEEE Trans. Magn.*, vol. 27, no. 5, pp. 4291 – 4294, Sep. 1991.

[31] B. M. Park, Y. Rahmat-Samii, and D. W. Duan, "On Crabtree's BQSP technique for significant reduction of integration points in analyzing reflector antennas," in *Antennas and Propagation Society International Symposium, 1994. AP-S. Digest*, 1994, vol. 1, pp. 229 – 232 vol.1.

[32] R. J. Pogorzelski, "Quadratic phase integration using a Chebyshev expansion," *IEEE Trans. Antennas Propag.*, vol. 33, no. 5, pp. 563–566, May 1985.

[33] D. Levin, "Procedures for computing one- and two-dimensional integrals of functions with rapid irregular oscillations," *Math. Comput.*, vol. 38, no. 158, pp. 531–538, 1982.

[34] D. Levin, "Fast integration of rapidly oscillatory functions," *J. Comput. Appl. Math.*, vol. 67, no. 1, pp. 95–101, Feb. 1996.

[35] A. C. Durgun and M. Kuzuoglu, "Computation of physical optics integral by Levin's integration algorithm," *Prog. Electromagn. Res. M*, vol. 6, pp. 59–74, 2009.

[36] S. Xiang, "On the Filon and Levin methods for highly oscillatory integral," *J. Comput. Appl. Math.*, vol. 208, no. 2, pp. 434–439, Nov. 2007.

[37] E. M. E. Elbarbary and S. M. El-Sayed, "Higher order pseudospectral differentiation matrices," *Appl. Numer. Math.*, vol. 55, no. 4, pp. 425–438, Dec. 2005.

[38] J. Li, X. Wang, T. Wang, and C. Shen, "Delaminating quadrature method for multi-dimensional highly oscillatory integrals," *Appl. Math. Comput.*, vol. 209, no. 2, pp. 327–338, Mar. 2009.

[39] J. Li, X. Wang, T. Wang, and S. Xiao, "An improved Levin quadrature method for highly oscillatory integrals," *Appl. Numer. Math.*, vol. 60, no. 8, pp. 833–842, Aug. 2010.

[40] J. Li, X. Wang, T. Wang, S. Xiao, and M. Zhu, "On an improved-Levin oscillatory quadrature method," *J. Math. Anal. Appl.*, vol. 380, no. 2, pp. 467–474, Aug. 2011.

[41] J. Li, X. Wang, and L. Qu, "Calculation of Physical Optics Integrals Over NURBS Surface Using a Delaminating Quadrature Method," *IEEE Trans. Antennas Propag.*, vol. 60, no. 5, pp. 2388 –2397, May 2012.

[42] T. F. Chan and P. C. Hansen, “Computing Truncated Singular Value Decomposition Least Squares Solutions by Rank Revealing QR-factorizations,” *SIAM J Sci Stat Comput*, vol. 11, no. 3, pp. 519–530, May 1990.

[43] U. T. Ehrenmark, “A three-point formula for numerical quadrature of oscillatory integrals with variable frequency,” *J. Comput. Appl. Math.*, vol. 21, no. 1, pp. 87–99, Jan. 1988.

[44] F. Saez de Adana, *Practical applications of asymptotic techniques in electromagnetics*. Boston: Artech House, 2011.

[45] J. Zhang, W. M. Yu, X. Y. Zhou, and T. J. Cui, “Efficient Evaluation of the Physical-Optics Integrals for Conducting Surfaces Using the Uniform Stationary Phase Method,” *IEEE Trans. Antennas Propag.*, vol. 60, no. 5, pp. 2398 –2408, May 2012.

[46] F. Vico-Bondia, M. Ferrando-Bataller, and A. Valero-Nogueira, “A New Fast Physical Optics for Smooth Surfaces by Means of a Numerical Theory of Diffraction,” *IEEE Trans. Antennas Propag.*, vol. 58, no. 3, pp. 773–789, Mar. 2010.

[47] F. Vico, M. Ferrando, E. Alfonso, and D. Sanchez, “A new fast physical optics method for very large parabolic surfaces with polygonal contour,” in *2007 IEEE Antennas and Propagation Society International Symposium*, 2007, pp. 3896–3899.

[48] C. Delgado, J. M. Gomez, and M. F. Catedra, “Analytical Field Calculation Involving Current Modes and Quadratic Phase Expressions,” *IEEE Trans. Antennas Propag.*, vol. 55, no. 1, pp. 233–240, Jan. 2007.

[49] J. Zhang, B. Xu, and T. J. Cui, “An Alternative Treatment of Saddle Stationary Phase Points in Physical Optics for Smooth Surfaces,” *IEEE Trans. Antennas Propag.*, vol. 62, no. 2, pp. 986–991, Feb. 2014.

[50] Y. M. Wu, L. J. Jiang, W. E. I. Sha, and W. C. Chew, “The Numerical Steepest Descent Path Method for Calculating Physical Optics Integrals on Smooth Conducting Quadratic Surfaces,” *IEEE Trans. Antennas Propag.*, vol. 61, no. 8, pp. 4183–4193, Aug. 2013.

[51] Y. Wu, L. Jiang, and W. C. Chew, “An efficient method for computing hightly oscillatory physical optics integral,” *Prog. Electromagn. Res.*, vol. 127, pp. 211–257, 2012.

[52] H.-H. Chou and H.-T. Chou, “Fast SDM for shaped reflector antenna synthesis via patch decompositions in PO integrals,” *Prog. Electromagn. Res.*, vol. 92, pp. 361–375, 2009.

[53] M. Albani, “Boundary Diffracted Wave and Incremental Geometrical Optics: A Numerically Efficient and Physically Appealing Line-Integral Representation of Radiation Integrals. Aperture Scalar Case,” *IEEE Trans. Antennas Propag.*, vol. 59, no. 2, pp. 586–594, Feb. 2011.

[54] M. Arias-Acuña, A. García-Pino, and O. Rubiños-López, “Fast Far Field Computation of Single and Dual Reflector Antennas,” *J. Eng.*, vol. 2013, Mar. 2013.

[55] W. V. T. Rusch, J. Prata, A., Y. Rahmat-Samii, and R. A. Shore, "Derivation and application of the equivalent paraboloid for classical offset Cassegrain and Gregorian antennas," *IEEE Trans. Antennas Propag.*, vol. 38, no. 8, pp. 1141 –1149, Aug. 1990.

[56] T. Veldhuizen, "Expression Templates," *C Rep.*, vol. 7, pp. 26–31, 1995.

[57] A. Breglia, A. Capozzoli, C. Curcio, and A. Liseno, "CUDA Expression Templates for Electromagnetic Applications on GPUs [EM Programmer's Notebook]," *IEEE Antennas Propag. Mag.*, vol. 55, no. 5, pp. 156–166, Oct. 2013.

[58] D. Goddeke, "Fast and Accurate Finite-Element Multigrid Solvers for PDE Simulations on GPU Clusters," Dissertation, Technical University of Dortmund, North Rhine-Westphalia, Germany, 2010.

[59] J. S. Asvestas, "The physical-optics integral and computer graphics," *IEEE Trans. Antennas Propag.*, vol. 43, no. 12, pp. 1459–1460, 1995.

[60] J. Sanders and E. Kandrot, *CUDA by Example: An Introduction to General-Purpose GPU Programming*, 1st ed. Addison-Wesley Professional, 2010.

[61] I. Buck, T. Foley, D. Horn, J. Sugerman, K. Fatahalian, M. Houston, and P. Hanrahan, "Brook for GPUs: stream computing on graphics hardware," *ACM Trans Graph*, vol. 23, no. 3, pp. 777–786, Aug. 2004.

[62] B. Gaster, L. Howes, D. R. Kaeli, P. Mistry, and D. Schaa, *Heterogeneous Computing with OpenCL*, 1st ed. Morgan Kaufmann, 2011.

[63] D. Göddeke, R. Strzodka, and S. Turek, "Performance and accuracy of hardware-oriented native-, emulated-and mixed-precision solvers in FEM simulations," *Int J Parallel Emerg Distrib Syst*, vol. 22, no. 4, pp. 221–256, Jan. 2007.

[64] J. D. Owens, D. Luebke, N. Govindaraju, M. Harris, J. Krüger, A. E. Lefohn, and T. J. Purcell, "A Survey of General-Purpose Computation on Graphics Hardware," *Comput. Graph. Forum*, vol. 26, no. 1, pp. 80–113, Mar. 2007.

[65] E. Anderson, Z. Bai, C. Bischof, S. Blackford, J. Demmel, J. Dongarra, J. D. Croz, A. Greenbaum, S. Hammarling, A. McKenney, and D. Sorensen, *LAPACK Users' Guide*. SIAM, 1987.

[66] X.-S. Yang, *Introduction to Mathematical Optimization: From Linear Programming to Metaheuristics*. Cambridge International Science Publishing, 2008.

[67] M. Dorigo, M. Birattari, and T. Stutzle, "Ant colony optimization," *IEEE Comput. Intell. Mag.*, vol. 1, no. 4, pp. 28–39, 2006.

[68] M. D. Gregory, Z. Bayraktar, and D. H. Werner, "Fast Optimization of Electromagnetic Design Problems Using the Covariance Matrix Adaptation Evolutionary Strategy," *IEEE Trans. Antennas Propag.*, vol. 59, no. 4, pp. 1275–1285, 2011.

[69] Y. Rahmat-Samii and E. Michielssen, *Electromagnetic optimization by genetic algorithms*. J. Wiley, 1999.

[70] S. Karimkashi and A. A. Kishk, "Invasive Weed Optimization and its Features in Electromagnetics," *IEEE Trans. Antennas Propag.*, vol. 58, no. 4, pp. 1269 –1278, Apr. 2010.

[71] J. Kennedy and R. Eberhart, "Particle swarm optimization," in *, IEEE International Conference on Neural Networks, 1995. Proceedings*, 1995, vol. 4, pp. 1942 –1948.

[72] J. Robinson and Y. Rahmat-Samii, "Particle swarm optimization in electromagnetics," *IEEE Trans. Antennas Propag.*, vol. 52, no. 2, pp. 397 – 407, Feb. 2004.

[73] M. Chen, "Second Generation Particle Swarm Optimization," in *IEEE Congress on Evolutionary Computation, 2008. CEC 2008. (IEEE World Congress on Computational Intelligence)*, 2008, pp. 90–96.

[74] S. Xu, Y. Rahmat-Samii, and D. Gies, "Shaped-reflector antenna designs using particle swarm optimization: An example of a direct-broadcast satellite antenna," *Microw. Opt. Technol. Lett.*, vol. 48, no. 7, pp. 1341–1347, 2006.

[75] G. G. Yen and W.-F. Leong, "Dynamic Multiple Swarms in Multiobjective Particle Swarm Optimization," *IEEE Trans. Syst. Man Cybern. Part Syst. Hum.*, vol. 39, no. 4, pp. 890–911, 2009.

[76] S. K. Goudos, Z. D. Zaharis, D. G. Kampitaki, I. T. Rekanos, and C. S. Hilas, "Pareto Optimal Design of Dual-Band Base Station Antenna Arrays Using Multi-Objective Particle Swarm Optimization With Fitness Sharing," *IEEE Trans. Magn.*, vol. 45, no. 3, pp. 1522–1525, 2009.

[77] W. Youhua, Y. Weili, and Z. Guansheng, "Adaptive simulated annealing for the optimal design of electromagnetic devices," *IEEE Trans. Magn.*, vol. 32, no. 3, pp. 1214–1217, 1996.

[78] A. Fanni, A. Manunza, M. Marchesi, and F. Pilo, "Tabu Search metaheuristics for global optimization of electromagnetic problems," *IEEE Trans. Magn.*, vol. 34, no. 5, pp. 2960–2963, 1998.

[79] S. Mostaghim and J. Teich, "Covering Pareto-optimal fronts by subswarms in multi-objective particle swarm optimization," in *Congress on Evolutionary Computation, 2004. CEC2004*, 2004, vol. 2, pp. 1404–1411 Vol.2.

[80] Y. Jin and B. Sendhoff, "Pareto-Based Multiobjective Machine Learning: An Overview and Case Studies," *IEEE Trans. Syst. Man Cybern. Part C Appl. Rev.*, vol. 38, no. 3, pp. 397 – 415, May 2008.

[81] A. Densmore and Y. Rahmat-Samii, “Three-parameter elliptical aperture distributions for sum and difference antenna patterns using particle swarm optimization,” *Prog. Electromagn. Res.*, vol. 143, pp. 709–743, 2013.

[82] D.-W. Duan and Y. Rahmat-Samii, “A generalized three-parameter (3-P) aperture distribution for antenna applications,” *IEEE Trans. Antennas Propag.*, vol. 40, no. 6, pp. 697–713, 1992.

[83] R. C. Hansen, “Array pattern control and synthesis,” *Proc. IEEE*, vol. 80, no. 1, pp. 141–151, 1992.

[84] R. F. Collin and F. J. Zucker, *Antenna Theory*, 2 vols. McGraw-Hill Companies, The, 1969.

[85] R. S. Elliott, *Antenna Theory and Design*. New Jersey: Englewood Cliffs, 1981.

[86] I. Koffman, “Feed polarization for parallel currents in reflectors generated by conic sections,” *IEEE Trans. Antennas Propag.*, vol. 14, no. 1, pp. 37–40, 1966.

[87] A. Ludwig, “The definition of cross polarization,” *IEEE Trans. Antennas Propag.*, vol. 21, no. 1, pp. 116 – 119, Jan. 1973.

[88] I. S. Gradshteyn and I. M. Ryzhik, *Table of Integrals, Series and Products*, 2nd ed. Academic Press Inc., 1980.

[89] S. A. Schelkunoff, “A Mathematical Theory of Linear Arrays,” *Bell Syst. Tech. J.*, vol. 22, no. 1, pp. 80–107, Jan. 1943.

[90] T. T. Taylor, “Design of circular apertures for narrow beamwidth and low sidelobes,” *IRE Trans. Antennas Propag.*, vol. 8, no. 1, pp. 17–22, 1960.

[91] E. T. Bayliss, “Design of Monopulse Antenna Difference Patterns with Low Sidelobes*,” *Bell Syst. Tech. J.*, vol. 47, no. 5, pp. 623–650, 1968.

[92] A. Densmore, Y. Rahmat-Samii, and G. Seck, “Corrugated-Conical Horn Analysis Using Aperture Field With Quadratic Phase,” *IEEE Trans. Antennas Propag.*, vol. 59, no. 9, pp. 3453 –3457, Sep. 2011.

[93] G. Yanchang and L. Nanzhi, “A three-parameter distribution for difference pattern,” in *Antennas and Propagation Society International Symposium, 1993. AP-S. Digest*, 1993, pp. 1594 –1597 vol.3.

[94] “Code of Federal Regulations, Title 47 Telecommunications, Chapter 1 Federal Communications Commission, Subchapter B Common Carrier Services, Part 25 Satellite Communications, Subpart C Technical Standards, Section 25.209 Antenna Performance Standards.” U.S. Government Printing Office.

[95] A. D. Olver, P. J. B. Clarricoats, A. A. Kishk, and L. Shafai, *Microwave horns and feeds*. New York: IEEE Press, 1994.

[96] H. Minnett and B. Thomas, "A method of synthesizing radiation patterns with axial symmetry," *IEEE Trans. Antennas Propag.*, vol. 14, no. 5, pp. 654 – 656, Sep. 1966.

[97] B. M. Thomas, "Theoretical performance of prime-focus paraboloids using cylindrical hybrid-mode feeds," *Proc. Inst. Electr. Eng.*, vol. 118, no. 11, pp. 1539 –1549, Nov. 1971.

[98] P. J. B. Clarricoats and P. K. Saha, "Propagation and radiation behaviour of corrugated feeds. Part 1: Corrugated-waveguide feed," *Proc. Inst. Electr. Eng.*, vol. 118, no. 9, pp. 1167 –1176, Sep. 1971.

[99] P. J. B. Clarricoats and P. K. Saha, "Propagation and radiation behaviour of corrugated feeds. Part 2: Corrugated-conical-horn feed," *Proc. Inst. Electr. Eng.*, vol. 118, no. 9, pp. 1177 –1186, Sep. 1971.

[100] P. D. Potter, "Efficient Antenna Systems: A New Computer Program for the Design and Analysis of High-Performance Conical Feedhorns," *JPL Tech. Rep. 32-1526*, vol. 13, no. Nov and Dec, pp. 92–107, 1972.

[101] A. Love, *Electromagnetic Horn Antennas*. IEEE Press, 1976.

[102] J. K. M. Jansen, M. E. J. Jeuken, and C. W. Lambrechtse, "The scalar feed," in *Electromagnetic Horn Antennas*, New York: IEEE Press, 1976, p. 453.

[103] B. Thomas, "Design of corrugated conical horns," *IEEE Trans. Antennas Propag.*, vol. 26, no. 2, pp. 367 – 372, Mar. 1978.

[104] B. M. Thomas and H. C. Minnett, "Modes of propagation in cylindrical waveguides with anisotropic walls," *Proc. Inst. Electr. Eng.*, vol. 125, no. 10, pp. 929 –932, Oct. 1978.

[105] G. L. James, "Analysis and Design of TE11-to-HE11 Corrugated Cylindrical Waveguide Mode Converters," *IEEE Trans. Microw. Theory Tech.*, vol. 29, no. 10, pp. 1059 – 1066, Oct. 1981.

[106] G. James, "Propagation and radiation properties of corrugated cylindrical coaxial waveguides," *IEEE Trans. Antennas Propag.*, vol. 31, no. 3, pp. 477 – 483, May 1983.

[107] P. J. B. Clarricoats and A. D. Olver, *Corrugated Horns for Microwave Antennas*. Institution of Electrical Engineers, 1984.

[108] D. Hoppe, "Propagation and Radiation Characteristics of a Multimoded Corrugated Waveguide Feedhorn," *TDA Prog. Rep.*, vol. 42–82, no. April-June, pp. 57–67, 1985.

[109] C. Knop, Y.-B. Cheng, and E. Ostertag, "On the fields in a conical horn having an arbitrary wall impedance," *IEEE Trans. Antennas Propag.*, vol. 34, no. 9, pp. 1092 – 1098, Sep. 1986.

[110] A. D. Olver and J. Xiang, "Wide angle corrugated horns analysed using spherical modal-matching," *Microw. Antennas Propag. IEE Proc. H*, vol. 135, no. 1, pp. 34 – 40, Feb. 1988.

[111] P.-S. Kildal, "Artificially soft and hard surfaces in electromagnetics," *IEEE Trans. Antennas Propag.*, vol. 38, no. 10, pp. 1537 –1544, Oct. 1990.

[112] R. Padman and J. A. Murphy, "Radiation patterns of 'scalar' lightpipes," *Infrared Phys.*, vol. 31, no. 5, pp. 441–446, 1991.

[113] J. A. Murphy and R. Padman, "Radiation patterns of few-moded horns and condensing lightpipes," *Infrared Phys.*, vol. 31, no. 3, pp. 291–299, 1991.

[114] R. R. Collmann and F. M. Landstorfer, "Calculation of the field radiated by horn-antennas using the mode-matching method," *IEEE Trans. Antennas Propag.*, vol. 43, no. 8, pp. 876 –880, Aug. 1995.

[115] C. Granet, "Profile options for feed horn design," in *Microwave Conference, 2000 Asia-Pacific*, 2000, pp. 1448 –1451.

[116] B. Maffei, P. A. R. Ade, C. E. Tucker, E. Wakui, R. J. Wylde, J. A. Murphy, and R. M. Colgan, "Shaped Corrugated Horns for Cosmic Microwave Background Anisotropy Measurements," *Int. J. Infrared Millim. Waves*, vol. 21, no. 12, pp. 2023–2033, 2000.

[117] J. A. Murphy, R. Colgan, C. O'Sullivan, B. Maffei, and P. Ade, "Radiation patterns of multi-moded corrugated horns for far-IR space applications," *Infrared Phys. Technol.*, vol. 42, no. 6, pp. 515–528, Dec. 2001.

[118] H. S. Lee and H. J. Eom, "Radiation From a Corrugated Circular Waveguide With a Flange," *J. Electromagn. Waves Appl.*, vol. 16, no. 9, pp. 1255–1274, 2002.

[119] L. Sakr, "The higher order modes in the feeds of the satellite monopulse tracking antennas," in *Electrotechnical Conference, 2002. MELECON 2002. 11th Mediterranean*, 2002, pp. 453 – 457.

[120] S. Sinton, J. Robinson, and Y. Rahmat-Samii, "Standard and micro Genetic Algorithm optimization of profiled corrugated horn antennas," *Microw. Opt. Technol. Lett.*, vol. 35, no. 6, pp. 449–453, 2002.

[121] C. Granet and G. L. James, "Design of corrugated horns: a primer," *IEEE Antennas Propag. Mag.*, vol. 47, no. 2, pp. 76 – 84, Apr. 2005.

[122] H. S. Lee, "Dispersion Relation of Corrugated Circular Waveguides," *J. Electromagn. Waves Appl.*, vol. 19, no. 10, pp. 1391–1406, 2005.

[123] E. Gleeson, J. A. Murphy, B. Maffei, W. Lanigan, J. Brossard, G. Cahill, E. Cartwright, S. E. Church, J. Hinderks, E. Kirby, and C. O'Sullivan, "Corrugated waveguide band edge filters for CMB experiments in the far infrared," *Infrared Phys. Technol.*, vol. 46, no. 6, pp. 493–505, Aug. 2005.

[124] Y. Rahmat-Samii, "Useful coordinate transformations for antenna applications," *IEEE Trans. Antennas Propag.*, vol. 27, no. 4, pp. 571 – 574, Jul. 1979.

[125] A. K. Bhattacharyya, *Active Phased Array Antenna*. Hoboken, NJ: John Wiley & Sons, Inc., 2006.

[126] W. J. English, "The Circular Waveguide Step-Discontinuity Mode Transducer (Short Papers)," *IEEE Trans. Microw. Theory Tech.*, vol. 21, no. 10, pp. 633 – 636, Oct. 1973.

[127] R. W. Scharstein and A. T. Adams, "Thick circular iris in a TE11 mode circular waveguide," *IEEE Trans. Microw. Theory Tech.*, vol. 36, no. 11, pp. 1529 –1531, Nov. 1988.

[128] R. Thabet and M. L. Riabi, "Design of Metallic Cylindrical Waveguide Bandpass Filters Using Genetic Algorithm Optimization," in *Proceedings of PIERS 2009 in Moscow*, Moscow, Russia, 2009, pp. 1549–1554.

[129] P. Varga and P. Török, "The Gaussian wave solution of Maxwell's equations and the validity of scalar wave approximation," *Opt. Commun.*, vol. 152, no. 1–3, pp. 108–118, Jun. 1998.

[130] D. A. Randall, T. D. Ringler, R. P. Heikes, P. Jones, and J. Baumgardner, "Climate modeling with spherical geodesic grids," *Comput. Sci. Eng.*, vol. 4, no. 5, pp. 32–41, 2002.

[131] H.-T. Chou and P. H. Pathak, "Uniform asymptotic solution for electromagnetic reflection and diffraction of an arbitrary Gaussian beam by a smooth surface with an edge," *Radio Sci.*, vol. 32, no. 4, pp. 1319–1336, 1997.

[132] H.-T. Chou, P. H. Pathak, and R. J. Burkholder, "Novel Gaussian beam method for the rapid analysis of large reflector antennas," *IEEE Trans. Antennas Propag.*, vol. 49, no. 6, pp. 880 –893, Jun. 2001.

[133] L. C. Andrews, *Special functions for engineers and applied mathematicians*. Macmillan, 1985.

[134] J. P. Boyd and R. Petschek, "The Relationships Between Chebyshev, Legendre and Jacobi Polynomials: The Generic Superiority of Chebyshev Polynomials and Three Important Exceptions," *J. Sci. Comput.*, vol. 59, no. 1, pp. 1–27, Apr. 2014.

[135] G. H. Golub and C. F. Van Loan, *Matrix computations*. Baltimore: Johns Hopkins University Press, 1996.

[136] S. Peng and Z. Nie, "Acceleration of the Method of Moments Calculations by Using Graphics Processing Units," *IEEE Trans. Antennas Propag.*, vol. 56, no. 7, pp. 2130 –2133, Jul. 2008.

[137] Y.-B. Tao, H. Lin, and H. J. Bao, "From CPU to GPU: GPU-based electromagnetic computing (GPUECO)," *Prog. Electromagn. Res.*, vol. 81, pp. 1–19, 2008.

[138] D. De Donno, A. Esposito, L. Tarricone, and L. Catarinucci, “Introduction to GPU Computing and CUDA Programming: A Case Study on FDTD [EM Programmer’s Notebook],” *Antennas Propag. Mag. IEEE*, vol. 52, no. 3, pp. 116 –122, Jun. 2010.

[139] E. Lezar and D. B. Davidson, “GPU-Accelerated Method of Moments by Example: Monostatic Scattering,” *IEEE Antennas Propag. Mag.*, vol. 52, no. 6, pp. 120 –135, Dec. 2010.

[140] H. Ko, “On the determination of the disk temperature and the flux density of a radio source using high-gain antennas,” *IRE Trans. Antennas Propag.*, vol. 9, no. 5, pp. 500 – 501, Sep. 1961.

[141] W. C. Daywitt, *A preliminary investigation into using the sun as a source for G/T measurements (NBSIR 84-3015)*. Boulder, Colorado: U.S. Dept. of Commerce, National Bureau of Standards, 1984.

[142] J. L. Linsky, “A recalibration of the quiet Sun millimeter spectrum based on the Moon as an absolute radiometric standard,” *Sol. Phys.*, vol. 28, no. 2, pp. 409–418, Feb. 1973.

[143] J. A. Kennewell, “Solar radio interference to satellite downlinks,” in *Antennas and Propagation, 1989. ICAP 89., Sixth International Conference on (Conf. Publ. No.301)*, 1989, pp. 334 –339 vol.2.

[144] A. Densmore, G. Seck, and Y. Rahmat-Samii, “Ka-Band Solar Flux Study for G/T Measurements,” presented at the URSI National Radio Science Meeting, Univ. Colorado at Boulder, 2012.

[145] D. J. Hoppe, “Modal analysis applied to circular, rectangular, and coaxial waveguides,” *Jet Propuls. Lab. TDA Prog. Rep.*, vol. (July-Sept) 42–95, pp. 89–96, Sep. 1988.

[146] M. Abramowitz, *Handbook of Mathematical Functions, With Formulas, Graphs and Mathematical Tables*, Reprint. United States Government Printing, 1972.